Hugo Heidy Miyasato

Modeling of the Clutch Squeal Phenomenon and Practical Possibilities for its Mitigation

Modelagem do Fenômeno de Squeal de Embreagens e Possibilidades Práticas para sua Atenuação

41/2015

CAMPINAS
2015

UNIVERSIDADE ESTADUAL DE CAMPINAS
FACULDADE DE ENGENHARIA MECÂNICA

Hugo Heidy Miyasato

Modeling of the Clutch Squeal Phenomenon and Practical Possibilities for its Mitigation

Modelagem do Fenômeno de Squeal de Embreagens e Possibilidades Práticas para sua Atenuação

Doctoral Thesis presented to the School of Mechanical Engineering of the University of Campinas in partial fulfillment of the requirements for the degree of Doctor in Mechanical Engineering, in the Area of Solid Mechanics and Mechanical Design.

Tese de Doutorado apresentada à Faculdade de Engenharia Mecânica da Universidade Estadual de Campinas como parte dos requisitos exigidos para obtenção do título de Doutor em Engenharia Mecânica, na Área de Mecânica dos Sólidos e Projeto Mecânico.

Orientador: Prof. Dr. Milton Dias Junior
Coorientador:

ESTE EXEMPLAR CORRESPONDE À VERSÃO FINAL DA DISSERTAÇÃO DEFENDIDA PELO ALUNO Hugo Heidy Miyasato, E ORIENTADO PELO PROF. DR. Milton Dias Junior.

.....
ASSINATURA DO ORIENTADOR

CAMPINAS
2015

Ficha catalográfica
Universidade Estadual de Campinas
Biblioteca da Área de Engenharia e Arquitetura
Elizangela Aparecida dos Santos Souza - CRB 8/8098

M699m

Miyasato, Hugo Heidy, 1986-
Modeling of the clutch squeal phenomenon and practical possibilities for its mitigation / Hugo Heidy Miyasato. – Campinas, SP : [s.n.], 2015.

Orientador: Milton Dias Junior.
Tese (doutorado) – Universidade Estadual de Campinas, Faculdade de Engenharia Mecânica.

1. Automóveis - Vibração. 2. Dinâmica das máquinas - Modelos Matemáticos. 3. Mecânica - Vibração. 4. Atrito. I. Dias Junior, Milton,1961-. II. Universidade Estadual de Campinas. Faculdade de Engenharia Mecânica. III. Título.

Informações para Biblioteca Digital

Título em outro idioma: Modelagem do fenômeno de squeal de embreagens e possibilidades práticas para sua atenuação
Palavras-chave em inglês:
Automobiles - Vibration
Dynamics of machines - Mathematical Models
Mechanics - Vibration
Friction
Área de concentração: Mecânica dos Sólidos e Projeto Mecânico
Titulação: Doutor em Engenharia Mecânica
Banca examinadora:
Milton Dias Junior [Orientador]
Katia Lucchesi Cavalca Dedini
Robson Pederiva
Sérgio Junichi Idehara
Rodrigo Nicoletti
Data de defesa: 27-02-2015
Programa de Pós-Graduação: Engenharia Mecânica

UNIVERSIDADE ESTADUAL DE CAMPINAS

FACULDADE DE ENGENHARIA MECÂNICA

COMISSÃO DE PÓS-GRADUAÇÃO EM ENGENHARIA MECÂNICA

DEPARTAMENTO DE SISTEMAS INTEGRADOS

TESE DE DOUTORADO

Modeling of the Clutch Squeal Phenomenon and Practical Possibilities for its Mitigation

Modelagem do Fenômeno de Squeal de Embreagens e Possibilidades Práticas para sua Atenuação

Autor: Hugo Heidy Miyasato

Orientador: Prof. Dr. Milton Dias Junior

A Banca Examinadora composta pelos membros abaixo aprovou essa Tese:

Prof. Dr. Milton Dias Junior, Presidente
DSI/FEM/UNICAMP

Profa. Dra. Katia Lucchesi Cavalca Dedini
DSI/FEM/UNICAMP

Prof. Dr. Robson Pederiva
DSI/FEM/UNICAMP

Prof. Dr. Sérgio Junichi Idehara
UFSC/Joinville

Prof. Dr. Rodrigo Nicoletti
USP/EESC/ São Carlos

Campinas, 27 de fevereiro de 2015.

Dedico este trabalho ao meu pai, Sr. Hermes Hideyas Miyasato, minha mãe, Sra. Massako Shono Miyasato e minha irmã, Erica Saemi Miyasato.

Agradecimentos

Esse é o único ponto no qual o autor pode colocar seus pensamentos nesse texto de conteúdo técnico. Se injustiças forem cometidas, peço desculpas.

Primeiramente, quero agradecer aos meus pais, Hermes Hideyas Miyasato e Massako Shono Miyasato pelas oportunidades na vida, carinho, conselhos e pelo exemplo. Agradeço a minha irmã Erica Saemi Miyasato pela amizade e conselhos.

Quero agradecer ao meu orientador, professor Milton Dias Junior pela amizade ao longo desses anos que se passaram desde a iniciação científica, mestrado e doutorado. Sempre que possível, complartilhou de sua experiência e abriu portas para que eu pudesse me aprimorar tanto técnica quanto pessoalmente. Muito obrigado.

Agradeço a Vinícius Gabriel Segala Simionatto pela amizade e parceria por toda essa jornada, por um caminho tortuoso e difícil. Desejo aqui muita força e bons votos para todos seus projetos futuros.

Agradeço aos amigos e colegas de curso que tanto me ajudaram e pelo convívio e aprendizado no período de graduação, com um agradecimento para Helói Francisco Gentil Genari e Felipe Sversut Arsioli. Agradeço também a todos os familiares que me apoiaram nos momentos mais difíceis. Agradeço ao professor Robson Pederiva pelos aprendizado no período de PED. Reservo minha gratidão à professora Katia Lucchesi Cavalca Dedini por todo o apoio em diversos momentos cruciais.

Agradeço a Douglas Vinícius Lemes e a Leandro Tadeu Roldão Perestrelo por acreditarem no trabalho realizado, buscarem o crescimento do conhecimento comum e pelo aprendizado. Agradeço a Leandro Perestrelo por gentilmente permitir a utilização e modificação de figuras do seu material didático, que aqui foram utilizadas como base para a maior parte das ilustrações e descrições técnicas.

Quero agradecer à Capes pelo suporte e financiamento. Agradeço à UNICAMP pelo ensino. Agradeço a Mauro Romera, Maurício Oliveira de Sant'Anna e a Rosângelo Wilterson Aparecido Ferreira pela colaboração, disposição e ajuda nas atividades experimentais. Agradeço a Fábio Menegatti de Melo pelo convívio, apoio e conversas no dia-a-dia do laboraório.

Agradeço à ZF do Brasil por todo o apoio ao longo do trabalho. Agradeço toda ajuda, atenção e esforço de Lucas Aurélio, Giezel Dias da Trindade Junior, Armando Kawaoku e João Arthur Cavalcanti Silva.

Agradeço ao futuro leitor que se interessar por esse trabalho e lê-lo.

I don't like work, - no man does - but I like what is in the work, - the chance to find yourself. Your own reality - for yourself, not for others - what no other man can ever know. They can only see the mere show, and never can tell what it really means.

Joseph Conrad

Resumo

O trem de potência é um sistema complexo, uma vez que envolve a interação entre componentes tais como o motor, a embreagem, a transmissão e as rodas. Diversos fenômenos de ruído, vibração e sua severidade (NVH) podem surgir durante o seu funcionamento (*judder, clonk, shuffle, rattle,* etc.). O *squeal* de embreagens é um fenômeno relativamente novo desse sistema e ele surge como um ruído de tom único, especialmente em situações de partida na fase de modulação da embreagem.

Componentes tais como as molas *cushion*, membrana e de retrocesso foram modeladas a fim de permitir a criação de diferentes projetos e combinações em termos de posição e propriedades físicas. Um mecanismo de estabilização para a placa de pressão foi testado numericamente para servir como uma alternativa para o sistema quando não existem possibilidades de modificações nos seus parâmetros.

Discos de embreagens reais contêm imperfeições devido à utilização, tolerâncias da manufatura, etc. Para levar esses fatos em consideração, um elemento rotativo de rigidez/amortecimento viscoso com atrito foi criado para representar as molas *cushion* e suportar distribuições arbitrárias ao longo do perímetro do disco, permitindo que cada elemento tenha suas próprias características. A suposição de amortecimento viscoso introduziu termos relacionados à velocidade de rotação do disco de embreagem na matriz de rigidez. Simulações com pequenos erros de posicionamento nas molas *cushion* geraram acoplamento entre a vibração axial da placa de pressão e seus deslocamentos angulares.

A mola membrana foi modelada como uma alavanca, permitindo a introdução de medições. Isso foi importante para identificar regiões de rigidez negativa e positiva, explicando sua interação com uma curva de *cushion* real. As molas de retrocesso foram modeladas, resultando numa representação matricial na qual foi possível gerar termos de rigidez positiva fora da diagonal principal.

Finalmente, o mecanismo de estabilização para o sistema consistiu de outro disco conectado à placa de pressão. Quando as propriedades do dispositivo foram ajustadas apropriadamente, ele foi efetivo em uma situação de *veering*. Nessa condição, as coordenadas de ambos os discos foram combinadas nas formas modais, causando movimentos de *wobbling* fora de fase que resultaram em dissipação de energia nos elementos de conexão.

Palavras Chave: *squeal* de embreagens, trem de potência, NVH

Abstract

The powertrain is a complex system, once that it involves the interaction between components such as the engine, the clutch, the transmission and the wheels. Several noise, vibration and harshness (NVH) phenomena may appear during its operation (judder, clonk, shuffle, rattle, etc.). Clutch squeal is a relatively new phenomenon of this system and it appears as a single tone noise, especially on a drive-off condition on the modulation phase of the clutch.

Components such as the cushion, diaphragm and leaf springs were modelled to allow the creation of different designs and combinations in terms of position or physical properties. A stabilization device for the pressure plate was numerically tested to serve as an alternative to the system when there are no practical possibilities of modifications on its parameters.

Real clutch discs contain imperfections due to usage, manufacturing tolerances, etc. To take these facts into consideration, a rotating stiffness/viscous damper element with friction was created to represent the cushion springs and support arbitrary distributions along the perimeter of the disc, allowing each element to have its own characteristics. The assumption of viscous damping introduced terms related to the clutch disc rotating speed on the stiffness matrix. Simulations with small position errors on the cushion spring generated coupling between the pressure plate axial vibration and its angular displacements.

The diaphragm spring was modelled as a lever, allowing the introduction of measurements. It was important to identify regions of negative and positive stiffness, explaining its interaction with a real cushion curve. The leaf springs were modelled, which resulted on a matrix representation where it was possible to generate positive stiffness terms out of its main diagonal.

Finally, the stabilization device for the system consisted of another disc connected to the pressure plate. When the device properties were properly adjusted, it was affective in a situation of veering. In this condition, the coordinates of both discs were combined on the mode shapes, causing out of phase wobbling motions, that resulted on energy dissipation on the connection elements.

Keywords: clutch squeal, powertrain, NVH

Lista de Ilustrações

Lista de Tabelas

Lista de Abreviaturas e Siglas

Letras latinas

a - diaphragm spring lever constant, distance bellow the centre of gravity of the pressure plate
b - diaphragm spring lever constant
c - element viscous damping constant
cg - representation for $\cos\gamma$
cp - representation for $\cos\psi_i$
d - distance above the centre of gravity of the pressure plate
$[C]$ - damping matrix
F - force
G,$[G]$ - centre of gravity, gyroscopic matrix
h - half of the plate height
$[H_1]$,$[H_2]$ - extra inertial contribution on the gyroscopic and stiffness matrices
I - inertia, simplification for the inertia around x and y axis
Im - imaginary part of complex number
j - complex number constant
k - element stiffness constant
l - inclined stiffness distance from the centre of gravity
$[K]$ - stiffness matrix
m - pressure plate mass
$[M], M$ - mass matrix, moment
N - normal load
O - origin of the inertial reference system, origin of the disc
$\{p\}$ - state space array
Q - contact point
r - position vector
R,$[R]$ - contact radius, rotation matrices
Re - real part of complex number
sg - representation for $\sin\gamma$
sp - representation for $\sin\psi_i$
t - time

V - speed
X - eigenvector position
z - vertical displacement of the plate

Letras Gregas

γ - flywheel rotating speed
θ - clutch disc rotating speed, angular positions of the mass of the vibration absorber
α - pressure plate angular displacement
β - pressure plate angular displacement
ψ_i - element relative position
ω - angular speed
μ - friction coefficient
λ - eigenvalue
Δ - parameter for the solution of a second order equation, elastic deformation, variation on parameters
ϕ - phase angle
ν - unitary tangential speed
ρ - angular position od diaphragm spring
ε - positioning angle of the connecting element of the vibration absorber
σ - eigenvalue real part
ϖ - eigenvalue imaginary part

Superescritos
$'$ - indication of array modelled with the rotating speed on global coordinates
* - complex conjugate term

Subscritos

0 - localization of an array on the global reference frame
$above$ - stiffness value above the stability range using the stabilization device
$bellow$ - stiffness value bellow the stability range using the stabilization device
$cushion$ - related to the cushion spring
c - damping effort
$cons$ - constant friction force or moments
d - clutch disc
$device$ - related to the stabilization device for the pressure plate
dp,m - terms related to the diaphragm spring
e - static position
i - ith element, force, moment, mode shape
in - inner radius
fr - friction effort
k - elastic effort
$lower\ limit$ - lower limit of the stability range using the stabilization device
mov - effort due to the moving viscous damper element
out - outer radius
$plate$ - related to the pressure plate
r - terms related to the leaf spring
$stable$ - stiffness value within the stability range using the stabilization device
sys - system matrices
t - tangential stiffness
t_{rel} - tangential speed
$upper\ limit$ - upper limit of the stability range using the stabilization device
z - vertical direction
x - angular speed/accelerations on x axis on Cardan coordinates
y - angular speed/accelerations on y axis on Cardan coordinates
y - angular speed/accelerations on z axis on Cardan coordinates
xx - inertia around x axis on Cardan coordinates
yy - inertia around y axis on Cardan coordinates
zz - inertia around z axis on Cardan coordinates

x' - angular speed/accelerations on x axis with the rotating speed on global coordinates

y' - angular speed/accelerations on y axis with the rotating speed on global coordinates
y' - angular speed/accelerations on z axis with the rotating speed on global coordinates
$x'x'$ - inertia around x axis with the rotating speed on global coordinates
$y'y'$ - inertia around y axis with the rotating speed on global coordinates
$z'z'$ - inertia around z axis with the rotating speed on global coordinates
var - variable friction force or moments

Abreviações

C - configuration with clutch cover only for modal analysis
CSC - Concentric Slave Cylinder
FCPD - configuration with flywheel, clutch cover and pressure plate for modal analysis
FCP- - configuration with flywheel, clutch cover without pressure plate for modal analysis
FCP+ - configuration with flywheel, clutch cover wit pressure plate for modal analysis
FRF - Frequency Response Function
NVH - Noise Vibration and Harshness
P - configuration with pressure plate only for modal analysis

Contents

1 Introduction

The powertrain or driveline is a complex system, involving the interaction of different components (engine, gearbox, tires, etc.) during its operation. Each one of them has its particular features, (technical names, working principles, design possibilities, manufacturing tolerances, etc.). Combine these variables and put this large set into proper operation is a very difficult task, once that problems may emerge only on the last stages of design. Even worse, they can happen after the customer has already acquired the product. Clutch squeal is a relatively new subject of study on the area, once that the first scientific publication found (Wickramarachi *et al.*, 2005) dates back only 10 years from the date of conclusion of this thesis.

1.1 Clutch squeal/Eek technical description

The phenomenon can have different names depending on the manufacturer or country. From the start, it is important to inform that part of the works refer to "Eek" (Wickramarachi *et al.* (2005), Freitag *et al.* (2010), Drozdetskaya *et al.* (2011), Fidlin *et al.* (2011)) while some specify the term "clutch squeal" (Hervé *et al.* (2008b), Hervé *et al.* (2008a), and Hervé *et al.* (2009)). This thesis will attain to the last term due to the fact that this is the terminology used by the known circle of contacts from the industry.

A squeal occurrence during a drive-off is presented on Fig. 1.1 during the phase of modulation of the clutch disc. There is a very high relative rotating speed between the engine flywheel and the transmission. The phenomenon can be noticed as a frequency component of 280 Hz (Fig. 1.1(b)), measured by an accelerometer inside the gearbox. The squeal event in this case lasted for 2.4s. (Kinkaid *et al.*, 2003) stated that literature agree on brake squeals on a distinct frequencies for the same brake system. As far as the practical knowledge of the author goes, little deviations happened on the occurrence of clutch squeals, in this case, approximately between 278-281 Hz. From the mentions of clutch squeal found in literature (Chapter 3), experimental data is scarce (Wickramarachi *et al.*, 2005).

Table 1.1 contains the frequency ranges clearly determined by the papers. Based on this, it is possible to observe that they are much lower than the ones reported for brake squeal (above 1000 Hz according to Kinkaid *et al.* (2003)). Besides that, Hervé *et al.* (2009) mentioned on the introduction of their work that clutch squeal frequencies could be higher than 1000 kHz. A wider range of occurrence from 250 to 500 Hz could be related to the fact that there is no further

description of the vehicles, for example, if they were lightweight or heavy duty ones.

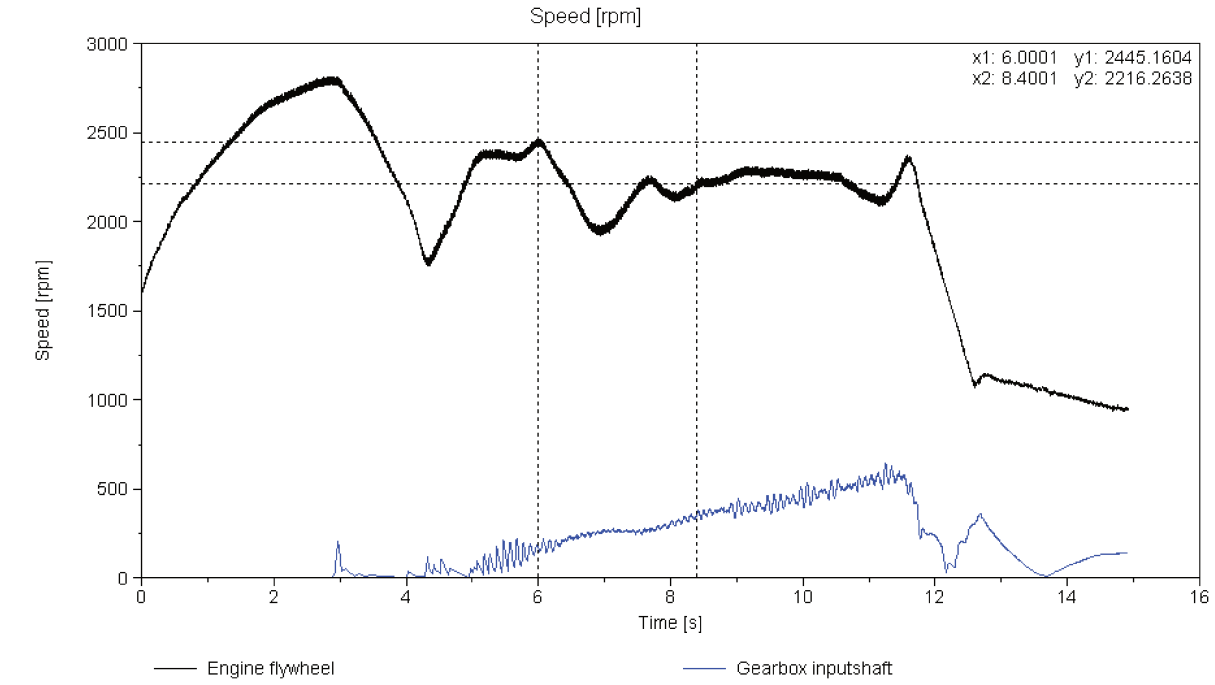

(a)

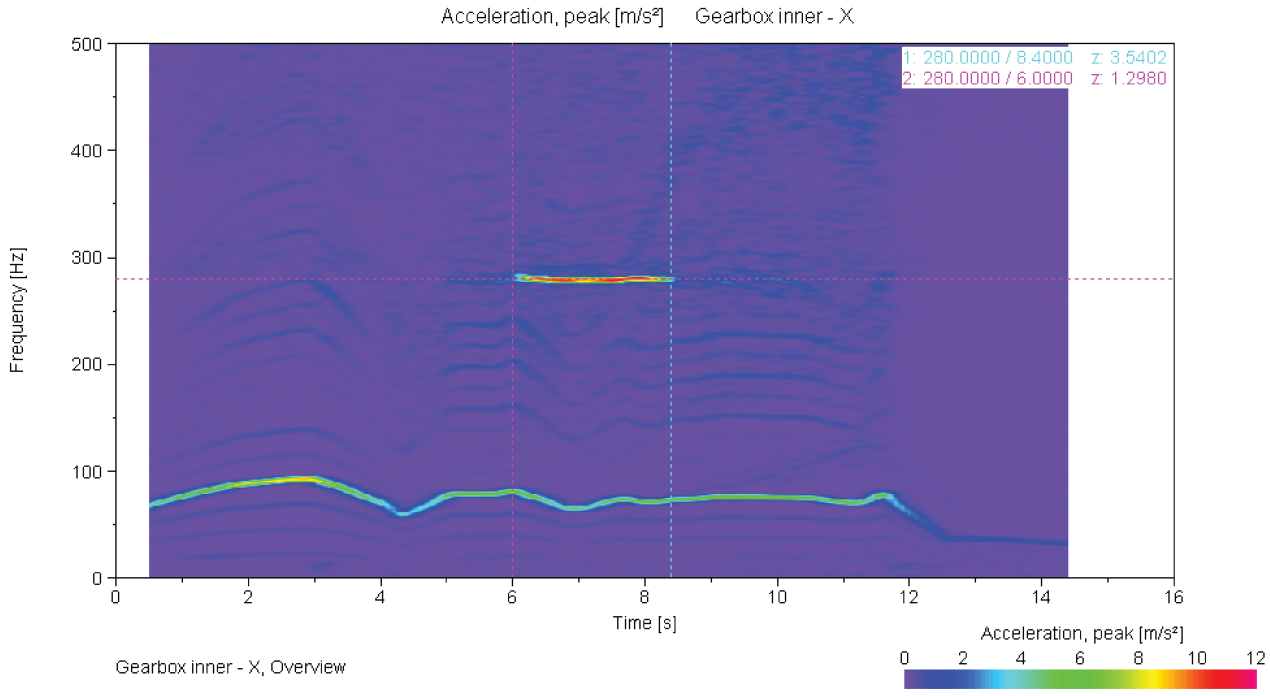

(b)

Figure 1.1: Rotating speeds on a squeal occurrence (Fig. 1.1(a)) and acceleration on the gearbox during the event (Fig. 1.1(b)) for a passenger car.

Table 1.1: Clutch squeal/eek frequency reange found in literature.

Frequency [Hz]	**250**	**300**	**350**	**400**	**450**	**500**
Wickramarachi *et al.* (2005)						
Freitag *et al.* (2010)						
Drozdetskaya *et al.* (2011)						
Fidlin *et al.* (2011)						
This thesis						

Figure 1.2 contains the cumulative sum of clutch squeal events obtained from a real vehicular test. Here occurs a threshold for the squealing events, meaning that it is necessary to change some system parameters from their original post manufacturing stage up to a "state" where the instability can take place.

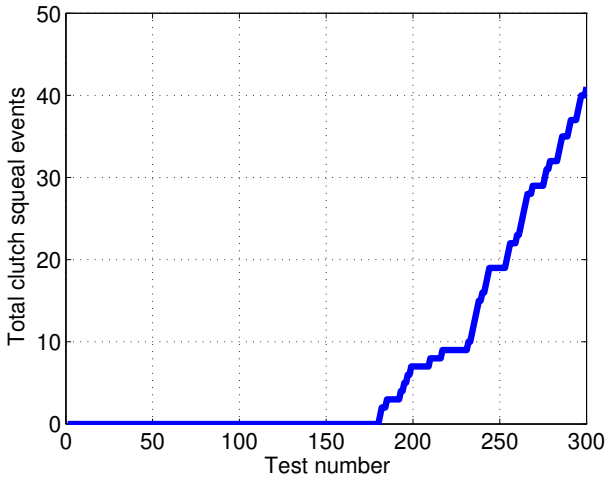

Figure 1.2: Experimental occurrence of clutch squeal events for a passenger car.

1.2 Clutch squeal in relation to other powertrain Noise, Vibration and Harshness (NVH) phenomena

Figure 1.3 shows a scheme organizing the main powertrain Noise, Vibration and Harshness (NVH) phenomena. Some phenomena occur when the transmission is either in idle, when the vehicle is still with engine on, or with engaged gear, in a situation of torque transmission to the wheels. The clutch facings may be sliding in relation to the pressure plate/flywheel. By such distinction, phenomena with a fully coupled clutch can be modelled as pure torsional vibration problems:

- shuffle and clunk/clonk (Krenz (1985), Crowther *et al.* (2005), Menday *et al.* (1999), Simionatto (2011))
- creeping
- gear rattle (Singh *et al.* (1989), Wang *et al.* (2001), Kim and Singh (2001), Brancati *et al.* (2005), Miyasato (2011), Simionatto (2015))
- clap and start/stop

The occurrence of NVH phenomena are related to both system and operational conditions. With this idea, a vehicle susceptible to some phenomenon must be excited by the proper input. Some events are found during drive-off, like *judder* (Albers and Herbst (1998), Centea *et al.* (2001), Perestrelo (2013)) while others are found with stable loads (*creeping, rattle*). The generation of torque pulses may result on *clonk/clunk* or *clap*. Natural frequencies of the powertrain may be excited either by rotating speed orders (*rattle*) or torque pulses (*shuffle*).

The final distinction is made on the annoying subjective aspects for the driver or passengers. Some are most critical in terms of vehicle oscillations (*judder*,*shuffle*) while others are basically related to the noise generated by impacts on the gears. But they are not only acoustic problems, once that they are all generated by some vibration behaviour.

By this whole classification, one can define clutch squeal from Fig. 1.3 as "*a phenomenon that happens with a combination of engaged gear+sliding clutch on a drive-off situation, resulting in a single tone noise for the driver*".

1.3 Thesis objective

This thesis has the following objectives:

1. Explore the differences between two hypotheses for the representation the pressure plate and cushion springs, adopting relative motion and viscous damping dissipation.
2. Create a rotating stiffness/viscous damper element with friction that supports arbitrary distributions along the perimeter of the pressure plate. Verify the behaviour of the system with errors on the cushion spring.
3. Give realistic features to the model and develop possibilities for squeal mitigation, providing a theoretical basis for the use of the leaf springs and the creation of a mechanical device for the stabilization of the pressure plate.

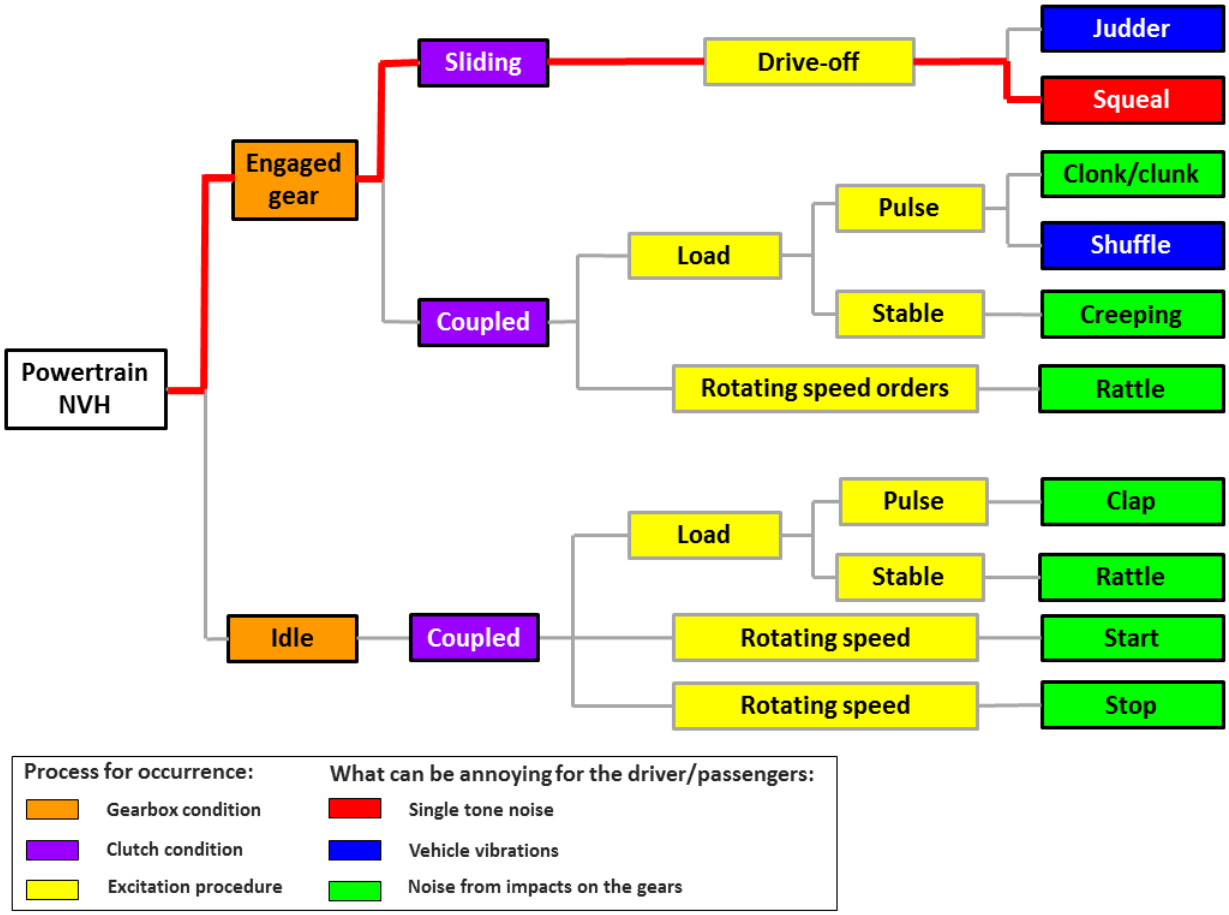

Figure 1.3: Powertrain phenomenon description.

1.4 Thesis outline

Figure 1.4 presents the knowledge areas. The chapters are grouped in terms of background, theoretical development, element possibilities and application.

1.4.1 Background

Chapter 2 contains the basic principles of the clutch system technology. The necessary technical terms and working principles are provided to give a better comprehension of the literature. Chapter 3 describes the papers on the matter available up to the date of conclusion of this thesis, grouping them based on common characteristics, and pointing the differences. The analysis on Section 3.4 will result on the model with the following hypotheses, that impact the rest of the work:

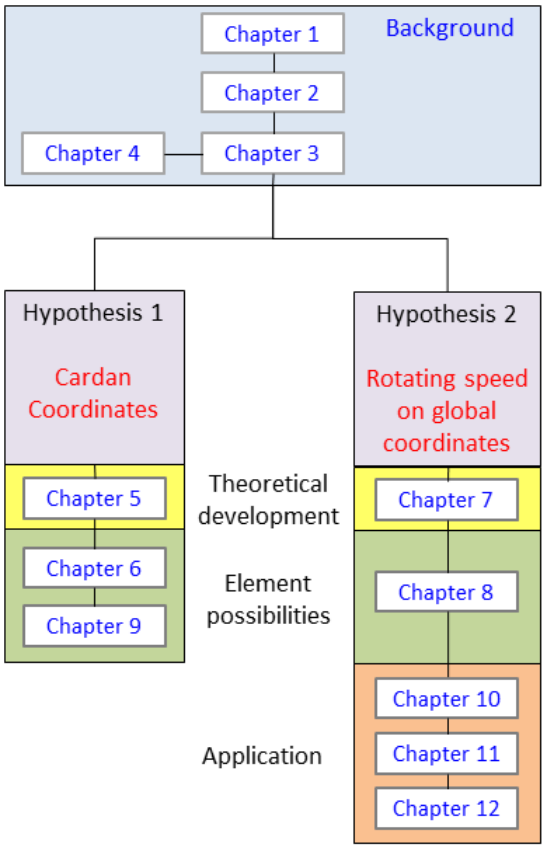

Figure 1.4: Thesis organization.

- *Hypothesis 1*: Model using Cardan coordinates (Chapters 5, 6, and 9).
- *Hypothesis 2*: Model adopting the rotating speed on global coordinates (Chapters 7, 8 10, 11, and 12).

Chapter 4 presents results from the modal analysis of a real clutch system in order to understand the structural behaviour of the system. It supports the assumption of a rigid pressure plate during a squealing event (Fig. 1.1) on Chapters 5 and 7.

1.4.2 Theoretical development

Real clutch discs contain imperfections due to usage, manufacturing tolerances, etc. To take these facts into consideration, a rotating stiffness/viscous damper element with friction (Fig. 1.5) was created to represent the cushion springs and support arbitrary distributions along the perimeter of the disc, allowing each element to have its own characteristics. Chapters 5 (Hypothesis 1) and

7 (Hypothesis 2) contain the formulation steps taken to obtain the contact element compatible with hypotheses 1 and 2. They were calculated under the assumption of constant contact radius, with parameters that enable the creation of different configurations for the cushion. Viscous damping was considered, differently from the approach from the literature, that took into account structural damping without a deep physical bound to the system (Fidlin (2006) and Fidlin *et al.* (2011)).

Each element is represented on Sections 5.5 (Hypothesis 1) and 7.4 (Hypothesis 2) in a linearized form by a combination of matrices, relating the stiffness, damping, and friction efforts. This assumption is helpful for their numerical implementation. With a more general form, this element is able to include errors and variations on the parameters in a very practical way on the models. The studies will focus on the element on Cardan coordinates, once that it resulted on constant modal properties in a situation of fixed elements (Section 9.1.2). The assumption of movement on the viscous damper element brought a new set of efforts to the model, that are discussed separately on Sections 5.3, 5.4 (Hypothesis 1), and 7.3 (Hypothesis 2). They are responsible for the introduction of terms on the global stiffness matrix related to damping and the rotating speed of the element on Sections 5.5.2 (Hypothesis 1) and 7.4.2 (Hypothesis 2).

1.4.3 Element possibilities

The element matrices from Sections 5.5 (Hypothesis 1) and 7.4 (Hypothesis 2) are gradually included on a symmetric distributed model on Chapters 6 (Hypothesis 1) and 8 (Hypothesis 2), providing results for the comparison of the model obtained on Cardan coordinates and the one derived with the rotating speed on global coordinates. Section 6.1 has a physical interpretation to the wobbling modes associated with squeal in a didactic manner. The models considering the effect of movement on the viscous damper element are provided on Sections 6.4 (Hypothesis 1) and 8.4 (Hypothesis 2).

All the previous effort leads to Chapter 9, were the full potential of the element is discussed. Simulations will be performed to study the effect of a small error on the position of one element on the global behaviour of the system. The cushion variability or heterogeneity, emerge from the natural manufacturing tolerances or usage. Those errors are responsible for the modification of the mode shapes, specially coupling the pressure plate wobbling angles with the axial movement of the plate.

1.4.4 Application and mitigation

The formulation developed on Chapters 5,6,7, 7, 10, 9, 11, and 12 serve for the purpose of combination and analysis of different elements as presented in Fig. 1.5. They are "building blocks" for the computational implementation of clutch squeal models.

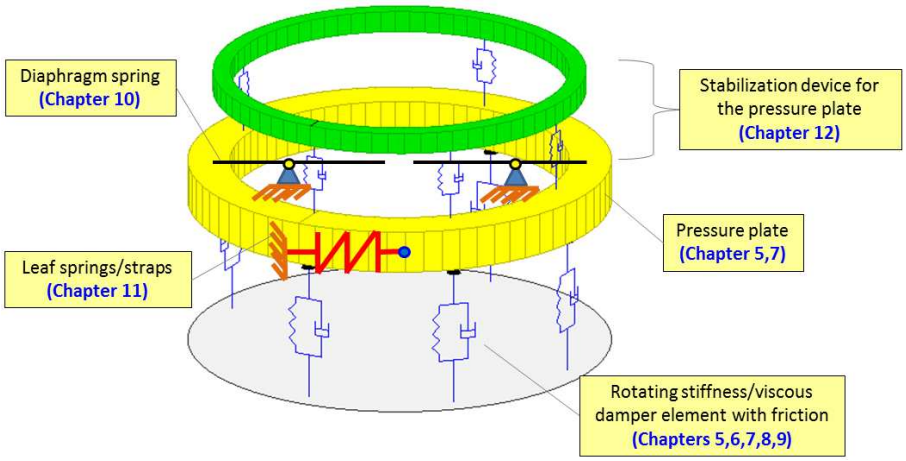

Figure 1.5: Elements representation.

With the theoretical development and the possibilities of the element established, the works start a phase of application, bringing technical aspects in order to give more realistic features to the model. The formulation chosen was the one assuming the rotating speed on global coordinates due to the reduced influence of the rotating speed (Chapter 8).

Chapter 10 (Fig. 1.5) introduces a lever model for the diaphragm spring, assuming that it is operating after the point of deformation of the clutch cover. The real clutch system involves the interaction of the diaphragm spring with the cushion curve. More realistic models will only be obtaining matching the operating points of both elements. Real measurements of the characteristic function of those elements are included on the model.

Chapter 11 (Fig. 1.5) presents a formulation for the leaf springs or straps. Those elements are not included on the models from literature and they represent an important characteristic: a real possibility of reduction on influence of the frictional skew symmetric terms from the system. Simulations will be performed in order to find the best configurations for instability mitigation.

Another attempt for the stabilization of the pressure plate is provided on Chapter 12 (Fig. 1.5) by the use of device. It is an alternative idea for the inclusion of damping on the cushion springs. It will mitigate instability under the occurrence of *veering* on the mode shapes (Liu (2002) and Perkins and Mote Jr (1986)).

2 Clutch system introduction

This chapter will give a very short introduction on the clutch. As any other automotive component, there are several technical aspects and constructive types to discuss. It will attain to its most basic principles and characteristic curves to give basic technical knowledge necessary to understand the terminology on the literature review (Chapter 3) and to provide the physical association for the models on this thesis. References for a deeper research are Micknass (1993), Drexl (1999), and Shaver and Shaver (1997).

2.1 Working principles

The whole system is presented in Fig. 2.1 in a condition of torque transmission. The flywheel is bolted to the crankshaft and it moves due to the moments from the crank mechanism of each cylinder of the engine. The clutch cover is attached to the flywheel, rotating together with it.

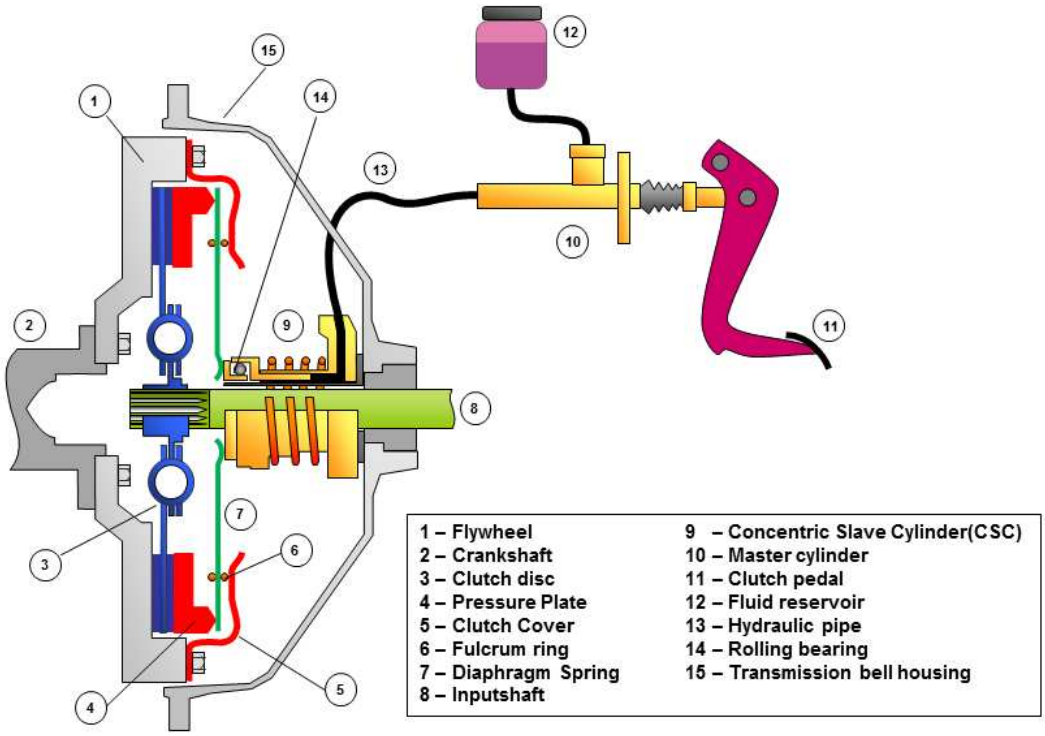

Figure 2.1: Clutch system during torque transmission (Fig. 2.1) (Adapted from Lerestrelo (2013)).

A very important element named diaphragm spring is responsible to apply the compression effort necessary to guarantee torque transmission in terms of friction. It acts like a lever where its outer radius is in contact with the pressure plate. At the other end, there are the spring fingers that slide against a ball bearing.

Figure 2.2(a) depicts the fulcrum ring that is attached to the cover by rivets. Those elements are used as an articulation point for the diaphragm spring when load is applied on its fingers (Fig. 2.2(b)).

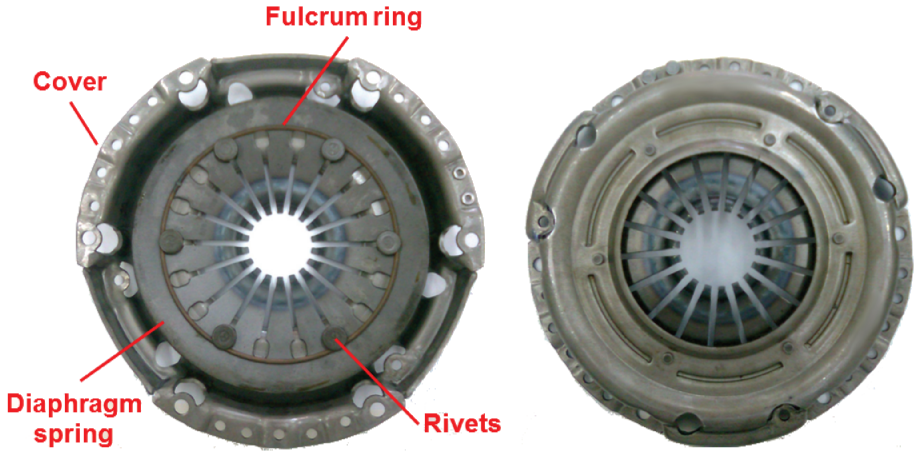

(a) (b)

Figure 2.2: Internal (Fig. 2.2(a)) and external (Fig. 2.2(b)) views of the clutch cover.

Basically, torque is transmitted from the clutch to the gearbox inputshaft by a splined connection. Access to this system is very difficult once that all these components are enclosed by the bell housing. Experimental investigations are made even difficult due to the fact that most of the elements are rotating, creating real big problems for the usage of wired sensors, like accelerometers.

If the driver needs to interrupt torque transmission, effort is applied on the clutch pedal (Fig. 2.3). For this vehicle, the master cylinder is responsible for its conversion to hydraulic pressure that reaches the Concentric Slave Cylinder (CSC) that increase the releasing forces on the bearing, that acts on the diaphragm spring, ceasing the normal load. Then, the leaf springs or straps (not displayed on Fig. 2.3) are responsible to separate the pressure plate from the clutch.

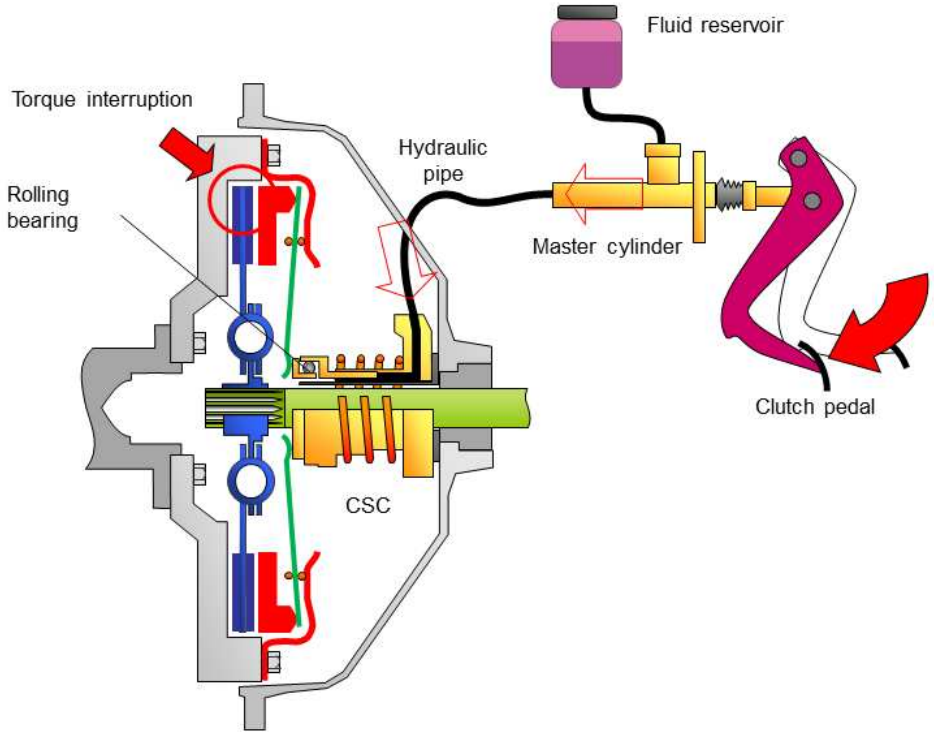

Figure 2.3: Clutch system during torque interruption (Adapted from Lerestrelo (2013)).

2.2 Cushion curve characteristics

The cushion springs are positioned between the friction facings (flywheel and pressure plate side), as presented in Fig 2.4(a). The total curve of cushion (Fig. 2.4(b)) results basically from the combined characteristics of facings, rivets and cushion springs. Looking for the new disc function, an initial stage combines low values of normal load with low stiffness condition, being favourable for torque modulation. The slope increases more significantly near the nominal load, achieved when there is full torque transmission from the flywheel to the inputshaft without slip.

After several couplings, the cushion curve is degraded. On the same picture, the point of maximum load is now shifted to a lower value of displacement. Besides the material removal due to wear on the facings, Sfarni *et al.* (2011) provided a complementary comment by explaining the *embedding phenomenon*. The cushion springs gradually deforms the facings, resulting in an "aged profile" Fig. 2.4(b). The most important point here is that it is not related to wear. The cushion spring is the physical entity related to the friction element modelled on Sections 5.2 and 7.2.

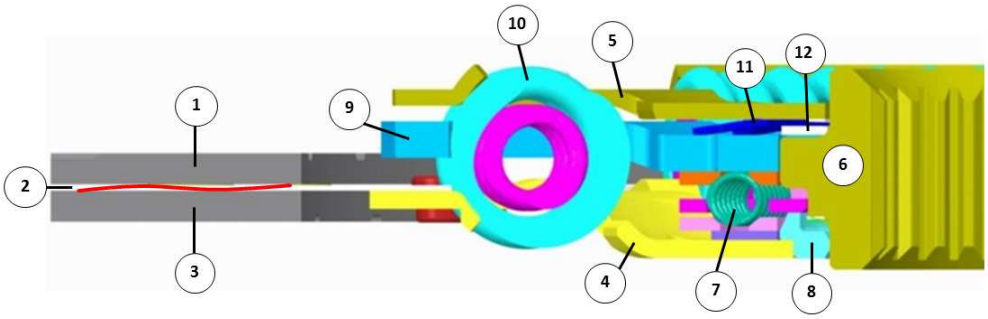

1 – Facing on pressure plate side	7 – Predamper spring
2 – Cushion spring	8 – Bushing
3 – Facing on flywheel side	9 – Hub disc
4 – Driving plate	10 – Main damper spring
5 – Retainer plate	11 – Belleville spring
6 – Hub	12 – Annular spring

(a)

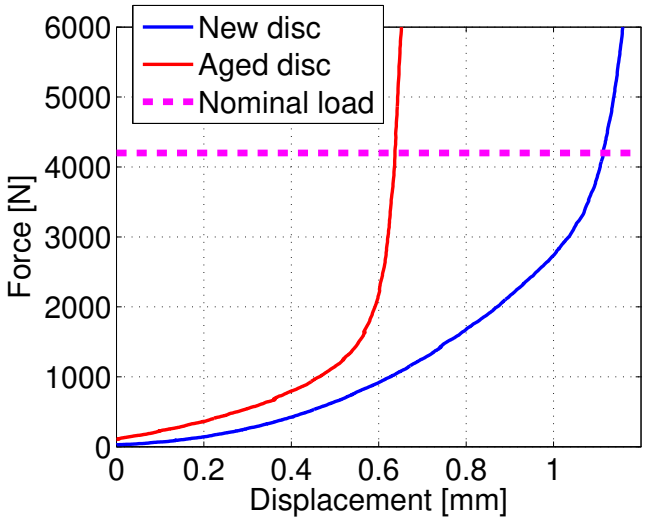

(b)

Figure 2.4: Clutch disc main elements (Fig. 2.4(a)) and cushion curve (Fig. 2.4(b)) for a passenger car.

3 Review on the minimal models for clutch squeal/Eek

Brake noise/vibration has been widely studied since the early decades of the twentieth century and has produced many literature reviews (Crolla and Lang (1991), Papinniemi *et al.* (2002), Kinkaid *et al.* (2003)). Authors have gone into the analysis of more specific aspects of the theme, such as numerical analysis (Ouyang *et al.*, 2005), minimal models (von Wagner *et al.*, 2007) and comfort (Cantoni *et al.*, 2009). For other systems, the interaction between railway wheel and noise also produced several studies, reviewed by Thompson and Jones (2000).

In the past 10 years a significant number of publications about clutch squeal/eek have appeared (Section 1.1). Section 3.2 shows that the literature on the matter covers at least six different lumped models directly dedicated for clutch squeal/eek up to the date of publication of this thesis(Wickramarachi *et al.* (2005), Fidlin (2006), Hervé *et al.* (2008b), Hervé *et al.* (2009), Fidlin *et al.* (2011) and Senatore *et al.* (2013)).

There are drastic simplifications on in comparison to the real system. From the technical point of view, there is still a lot of work to determine exactly what the phenomenon is. Maybe, on the future, with more cases and investigation, clutch squeal can be more certainly categorized just like brake squeal (Kinkaid *et al.*, 2003). By now, there are four distinct research directions for squeal/eek:

1. Pressure plate bending modes (Wickramarachi *et al.*, 2005)
2. Rigid body motion (Fidlin (2006), Hervé *et al.* (2008b) and Hervé *et al.* (2009))
3. Inputshaft influence (Fidlin *et al.* (2011) and Freitag *et al.* (2010))
4. Powertrain mode shapes (Senatore *et al.*, 2013)

von Wagner *et al.* (2007) is included on this review, besides that it was conceived for brake squeal, once that some of its features had a great impact on the following clutch squeal works. Fidlin *et al.* (2011) reported a friction related damping phenomenon that was credited to Hochlenert (2006). Similar terms involving this characteristic occur in several publications (von Wagner *et al.* (2007), Hervé *et al.* (2009) and Fidlin *et al.* (2011)).

The discussion on Section 3.2 will be focused on both theoretical and technical aspects. Related reports are described in Section 3.3. Section 3.4 will organize the models in terms of similarities points. This chapter ends with a discussion over the pending questions or some possibilities of innovation based on this literature.

3.1 A comment on the limitations for the usage of a Finite Element with friction

Ouyang *et al.* (2005) on his review about numerical study of brake squeal have traced the usage of a linear frictional spring element back to Liles (1989). Equation 3.1 contains the formulation provided by Soom *et al.* (2003). The element gives the normal forces (N_1 and N_2) and the tangential efforts (T_1 and T_2) between nodes 1 and 2 on directions x and y.

$$\begin{Bmatrix} N_1 \\ T_1 \\ N_2 \\ T_2 \end{Bmatrix} = \begin{bmatrix} k_n & 0 & -k_n & 0 \\ \mu k_n & 0 & -\mu k_n & 0 \\ -k_n & 0 & k_n & 0 \\ -\mu k_n & 0 & \mu k_n & 0 \end{bmatrix} \begin{Bmatrix} y_1 \\ x_1 \\ y_2 \\ x_2 \end{Bmatrix} \tag{3.1}$$

Massi *et al.* (2007) introduced Eq. 3.1 on Ansys using an element named MATRIX27. Soom *et al.* (2003) explains that the linearized contact stiffness k_n is often calculated based on the ratio between the pressure and the roughness of the surfaces (average asperity heights). It is, in general, a very high value, found above $10^6 N/m$ on Massi *et al.* (2007) and Soom *et al.* (2003). Section 3.2 shows many examples of a friction damping effect that cannot be reproduced by this approach (von Wagner *et al.* (2007), Hervé *et al.* (2009) and Fidlin *et al.* (2011)).

3.2 Clutch squeal/eek theoretical models chronology

In this section, the literature is organized based on the date of publication and each paper is described in detail.

3.2.1 Wickramarachi *et al.* (2005)

Wickramarachi *et al.* (2005) published the first academic paper mentioning "eek noise". Near the engagement of a dry friction clutch the sound spectrum , measurements indicated a frequency nearby 500 Hz related to the wobbling modes of the disc, where it vibrated as a rigid component. A multiple of this frequency coincided with the first bending modes of the plate, contributing to the noise. For this purpose, the authors have created a mixed representation taking into account both wobbling and bending. The pressure plate structure was distributed within four lumped mass elements, connected by the plate stiffness. The equations of motion on Wickramarachi *et al.* (2005) did not include the gyroscopic effect on the formulation. Wickramarachi *et al.* (2005) based his analysis on the eigenvalues of this system. Conclusions were obtained by the verification of the

effect of some parameter on their real part. The results from the simulations indicated that a thinner pressure plate could reduce instability and a reduction on the friction coefficient could stabilize the system. The structural stiffness was the most influential parameter to avoid coupling on the mode shapes.

3.2.2 Fidlin (2006)

Fidlin (2006) created a wobbling model for a clutch disc on his book on nonlinear dynamics. There was a consideration of a disc over an elastic support. The gyroscopic effects are not included on the model. Unlike many works from the literature review, contact occurred on the very thin friction ring distributed along the outer radius of the disc. Damping coefficients are included on the system matrix after the formulation is finished, without a physical assumption. Fidlin (2006) concluded that the system without damping on the elastic layer would always be unstable.

3.2.3 von Wagner *et al.* (2007)

Following a comment from Cantoni *et al.* (2009), the work from von Wagner *et al.* (2007) resulted in a model very close to a real brake system , where two contact elements represents the braking pads, maintaining fixed positions in relation to the rotating disc. The authors included Cardan coordinates on the formulation. The new feature that makes this model part of this review is the existence of friction damping terms that depend on the inverse of the rotating speed of the disc. This friction induced damping ((Hochlenert, 2006) as reported on Fidlin *et al.* (2011)) causes a threshold on the stability. von Wagner *et al.* (2007) made a simulation where the real part of an unstable eigenvalue crossed the imaginary plane from a positive value (indicating instability or brake squeal, in this case) to negative one (stable behaviour).

3.2.4 Hervé *et al.* (2008b) and Hervé *et al.* (2009)

The same model was used as basis for Hervé *et al.* (2008b) and Hervé *et al.* (2009). The authors clearly explain on the beginning of one of the works that this is a "*phenomenological model*" (Hervé *et al.*, 2008b). Hervé *et al.* (2008b) did not present the necessary steps to obtain the equations of motion, but it presented a model using a different coordinate system in comparison to von Wagner *et al.* (2007), once that there are different combinations of the inertial moments inside the matrices of mass, damping and stiffness. This thesis obtained the same inertial terms adopting

the rotating speed on global coordinates. Such procedure will be shown on Section 7.1 and the matrices will be presented in Section 7.1.3, with additional terms that depend on the acceleration, that where certainly cancelled due to the consideration of a constant rotating speed. Hervé *et al.* (2008b) included the signal of the relative speed between the flywheel and the disc on the skew symmetric terms of the stiffness matrix.

The authors worked with the structure of the system matrices using non dimensional terms, concluding that an increase on the total amount of damping could enhance the stability region for this system. If it is not equally distributed between the degrees of freedom, the stability region may present abrupt transitions.

Those damping distributions are obtained only by changes on external elements. Hervé *et al.* (2008b) and Hervé *et al.* (2009) deals with equally distributed parameters on the contact, because the skew symmetric terms of those matrices are equal.

Hervé *et al.* (2008a) created a mathematical tool for the identification of limit cycles that was used on Hervé *et al.* (2009), that expanded the findings from Hervé *et al.* (2008b) to include nonlinear effects. They concluded that an increase on the circulatory action (related to friction moments based on the stiffness forces) resulted in both increase of amplitude and frequency in relation to the linear case. The "*iso-damping distribution*" was not the best configuration for amplitude reduction in situations of nonlinear vibration.

3.2.5 Freitag *et al.* (2010) and Fidlin *et al.* (2011)

A new factor was introduced by Freitag *et al.* (2010), who explained that eek happened due to a mode shape of the system inputshaft+clutch disc (Fig. 3.1(a)). This picture resembles the configuration of clutch set of a passenger car (Fig. 2.1). Previous works directly refer to or could be associated to modification on the cushion spring(Wickramarachi *et al.* (2005), Fidlin (2006), Hervé *et al.* (2008b) and Hervé *et al.* (2009)).

Freitag *et al.* (2010) pointed on the influence of the tilting stiffness of the disc (Fig. 3.1(a)). In terms of product development, the radial stiffness of the disc had been modified to decouple it from the inputshaft motion. The radial motion of a friction disc was studied on Fidlin and Stamm (2009), where the authors identified a self-centering phenomenon at lower speeds and coupling between torsional and radial mode shapes on a phenomenological model.

It is essential to settle a major difference between the clutch systems on heavy duty vehicles to the one on passenger cars. On the first case, there is an extra bearing to allow an extended inputshaft, presented in Fig. 3.1(b). This shaft is sustained in two points inside the clutch bell

housing: one that sustains the shaft inside the transmission and other positioned on the flywheel. Even so, these vehicles may also present clutch squeal.

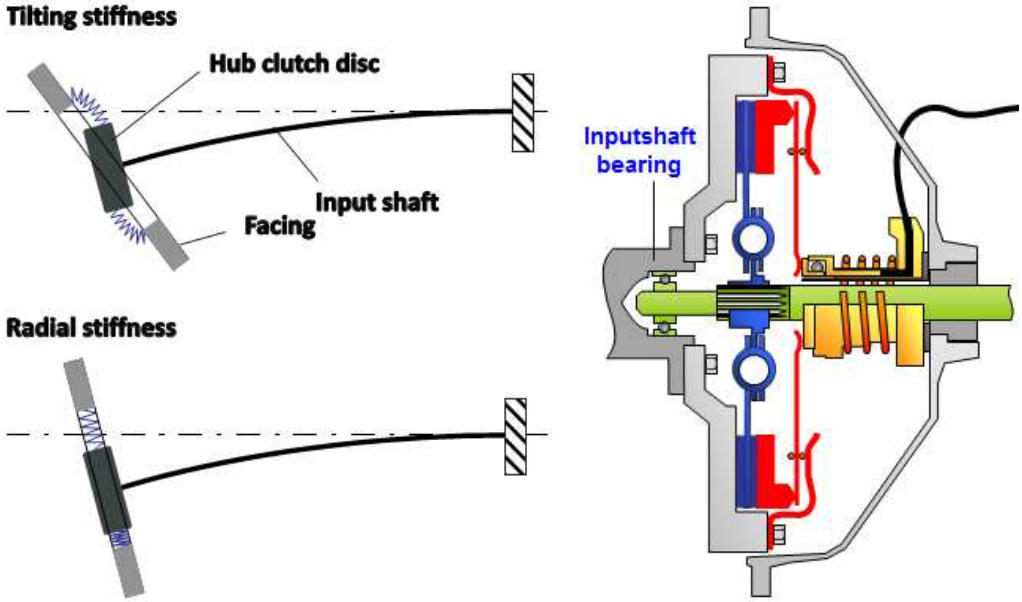

(a) Tilting and radial stiffness according to Freitag *et al.* (2010).

(b) Clutch system with a guided inputshaft (Adapted from Lerestrelo (2013)).

Figure 3.1: Ekk relation with the inputshaft from Freitag *et al.* (2010) (Fig. 3.1(a)) and a inputshaft with an extra bearing (Fig. 3.1(b))

Fidlin *et al.* (2011) concluded that the friction coefficient did not change the stability of an undamped system and a longer rod stabilized the disc. Without structural damping, the system stabilizes only through friction damping (Hochlenert, 2006). On the phenomenological model, they concluded that for each friction value there was a certain damping threshold that stabilizes the system. The authors found a linear relation between both parameters.

3.2.6 Senatore *et al.* (2013)

Senatore *et al.* (2013) expanded the representation including a pressure plate on a 5 degree-of-freedom driveline model with a dual mass flywheel (Albers (1994)). Unlike the previous works that separated part of the system and created a minimum phenomenological model, this paper brings a systemic approach for the study. Drozdetskaya *et al.* (2011) reported measurements of torsional vibrations on the transmission speed during an eek event. The pressure plate was modelled in order to investigate the coupling between torsional movements and the wobbling motions of the plate. Axial vibration of this element was also taken into account, but with the assumption of a equally

distributed cushion spring, this movement was not coupled with other movements of the plate. The pure axial motion was found within "169 Hz-750 Hz" (Senatore *et al.*, 2013). Senatore *et al.* (2013) concluded after linearization, the pressure plate motion was decoupled from the torsional degrees of freedom. Even so, torsional vibrating modes could happen on the eek/clutch squeal frequency range.

3.3 Related reports

Powertrain literature provide other occurrences of vibrating/noise phenomena that are not directly related to clutch squeal/eek. They are important to widen the practical knowledge or to create distinctions with other situations. By now, the works from Sections 3.3.1 and 3.3.2 are treated as having no relation with the ones from Section 3.2.

3.3.1 Kushwaha *et al.* (2002)

Kushwaha *et al.* (2002) published a paper about a phenomenon named "*whoop*". According to the authors, movements of the engine flywheel happen due to the explosions on the cylinders. As consequence of that, combined with the flexibility on the crankshaft, a natural frequency of the clutch system is excited during the operation of the clutch pedal. As a result, there is a combination of vibration and noise near the engaging phase of the clutch. None of the works from Section 3.2 reported an engine influence on the phenomenon.

3.3.2 Bearing squeal: Kirchner *et al.* (2005)

Kirchner *et al.* (2005) reported another condition named as "*cold start squeal*". According to them, such phenomenon happened on very low temperatures (below 5° C) and just in a situation where the clutch was not engaged during the engine start. The spectrum of this phenomenon involved at least 18 frequencies ranging from 2800-3200 Hz. The authors discovered that the phenomena excited mode shapes of the diaphragm spring (Fig. 2.2(b)). Due to manufacturing tolerances each local finger mode happens in a slightly different frequency from each other, resulting in very distinct but close modes.

3.4 Model comparisons and the most urgent pending questions

By thinking on the description of Chapter 2 it is possible to verify that the works from Section 3.2 are based on huge simplifications on the clutch system elements. For example, the diaphragm spring is not detailed or mentioned in some cases, the leaf springs, the engine, etc. Clutch squeal is on a very early developing stage, with each model representing a new characteristic that is found to be relevant on the matter.

Table 3.1 presents the organization and a new denomination of each work, referred to as W_i. Then, all the works are compared on Table 3.2. A common characteristic in this section is the assumption of a constant friction coefficient. Apart from Wickramarachi *et al.* (2005), all other works took into account rigid body movement, even in situations with the inclusion of the inputshaft dynamics Fidlin *et al.* (2011).

Table 3.1: Authors of clutch squeal related works.

Work	**Authors**
W1	Wickramarachi *et al.* (2005)
W2	Fidlin (2006)
W3	von Wagner *et al.* (2007)
W4	Hervé *et al.* (2008b)
W5	Hervé *et al.* (2009)
W6	Fidlin *et al.* (2011)
W7	Senatore *et al.* (2013)

Table 3.2: Comparison between clutch squeal works. Authorship is given by Table 3.1.

	W1	W2	W3	W4	W5	W6	W7
Flexible pressure plate	✓						
Rigid body wobbling		✓	✓	✓	✓	✓	✓
Gyroscopic effect			✓	✓	✓	✓	✓
Rotating speed on Cardan coordinates			✓			✓	✓
Rotating speed on global coordinates				✓	✓		
Constant friction coefficient	✓	✓	✓	✓	✓	✓	✓
Inputshaft influence						✓	
Friction damping terms					✓	✓	✓
Nonlinear effects					✓	✓	
Powertrain modelling							✓

Chapter 4 presents the results of modal analysis of a clutch system to show that the frequency detected on Fig. 1.1(b) is not related to bending modes of the pressure plate, that could be a source for the problem according to Wickramarachi *et al.* (2005).

From Table 3.2 it is possible to see that two distinct coordinates have been used to model the pressure plate. The true meaning of this occurrence is that *there are two different representations for the same real system* (Hervé *et al.* (2008b) and Hervé *et al.* (2009) vs. Fidlin *et al.* (2011) and Senatore *et al.* (2013)). This thesis will bring these two representations to a common set of parameters (rotating speeds, geometric relations, etc.) and physical disposition (assuming the friction contact between the clutch disc and pressure plate). Each conditions will be considered as a specific *hypothesis* for the generation of the model. The element on Cardan coordinates ("*Hypothesis 1*") is developed on Chapter 5, while the one considering the rotating speed on global coordinates ("*Hypothesis 2*") is presented on Chapter 7.

All works report a strong influence of the elastic/friction contact on the phenomenon. In other words, the cushion spring is crucial to the phenomenon and a detailed description of this region must be made. Besides Hervé *et al.* (2008b), Hervé *et al.* (2009) and Fidlin *et al.* (2011) there is no assumption on the relative displacement between the elements. Here this characteristic is explicitly included by a relative position angle. Such formulations are presented on both hypothesis on Sections 5.2.4 and 7.2.2. A comparison on their behaviour can be traced looking at the models with symmetric distribution of elements on Chapters 6 and 8.

The friction damping terms, which depend on the inverse of the relative angular speeds, will be discussed since its principle, the unitary tangential relative speed (Sections 5.2.5 and 7.2.3). A better understating of such behaviour is provided through the real configuration of the tangential speeds near coupling are found on Appendix A.1 and A.2. The limitations from the error on the unitary norm and direction can be consulted Appendix B.1 and B.2. Such discussions are not provided in detail on the literature.

Fidlin (2006) and Fidlin *et al.* (2011) included energy dissipation on the model using *structural damping*, after the equations of motion were obtained. Hervé *et al.* (2008b) also uses this term to refer to damping. This thesis explicitly includes a *rotating viscous damping element* on the formulation, allowing *relative movement* between the pressure plate and the clutch disc. The physical interpretation for the efforts and moments produced by the moving viscous damper is given on Sections 5.4 and 7.3.

A consequence from the element matrices (Sections 5.5 and 7.4) is the possibility for the creation of different element dispositions in relation to the pressure plate. Non symmetrical distribution involving position error on one element or unbalanced stiffness according to the coordinates are presented on Chapter 9.

From this whole literature there are still room for two possible technical approaches for attenuation:

- Chapter 11: thinking on other elements of the clutch system, the leaf springs may be used to stabilize this system.
- Chapter 12: a device for pressure plate stabilization is proposed to apply an external damping to the system.

4 Experimental modal analysis of the clutch system

The clutch system is composed by structural components, like the pressure plate and the cover (Chapter 2). The determination of the frequencies of the first non-rigid mode shape is important to rule out or not flexibility of the elements on the clutch squeal frequency range (Fig. 1.2). The analysis from this chapter is also created to emphasize that there is no relation between the squealing frequency and the excitation of mode shapes of components assumed as separate bodies. Iterations between the elements define the modal properties of the system.

4.1 Configurations tested

In this work, combinations between the components were gradually done, from the simplest (pressure plate only) to the more complex one (flywheel + cover + clutch disc). The conditions tested are shown in Fig. 4.1 and described as follows:

- Configuration **P** (Fig. 4.1(a)) resulted on the analysis of the pressure plate alone;
- Configuration **C** (clutch cover)(Fig. 4.1(b)) is used to study the interaction between the pressure plate , straps and the diaphragm spring;
- Configuration **FCP+** (Fig. 4.1(d)) was obtained when the clutch cover is bolted to the flywheel;
- Configuration **FCP-** (Fig. 4.1(c)) was created removing the pressure plate from the previous case;
- Configuration **FCPD** (flywheel + clutch cover + cutch disc) (Fig. 4.1(e)) is a condition closer to the original system. It is important to point out that the inputshaft, release system and the connection between the flywheel and the crankshaft were not taken into account;

Figure 4.2 contains the Frequency Response Function (FRF) sums for the experiments. Focusing only on the first amplitude peak, it is possible to see that configuration P presented greater levels of vibration around 900 Hz. Such results indicate that *the pressure plate is a rigid body on the squealing frequency range for this specific vehicle*, found nearby 280 Hz on Fig. 1.2.

Configuration **C** results on a visualization of peaks nearby 500 Hz. If the pressure plate is removed and the cover is bolted to the flywheel (**FCP-**), the first peak occurs between 550 and 600

Hz. The system without clutch disc (**FCP+**) present increased amplitudes for frequencies close to 400 Hz. Finally, the inclusion of the clutch disc (**FCPD**) causes the appearance of a reduced peak nearby 200 Hz.

These experiments were not able to introduce the effect of rotation on the system and the influence of different positions of the cushion curve (Fig. 2.4(b)). It serves as an introduction for the rigid body modelling of the pressure plate throughout this work.

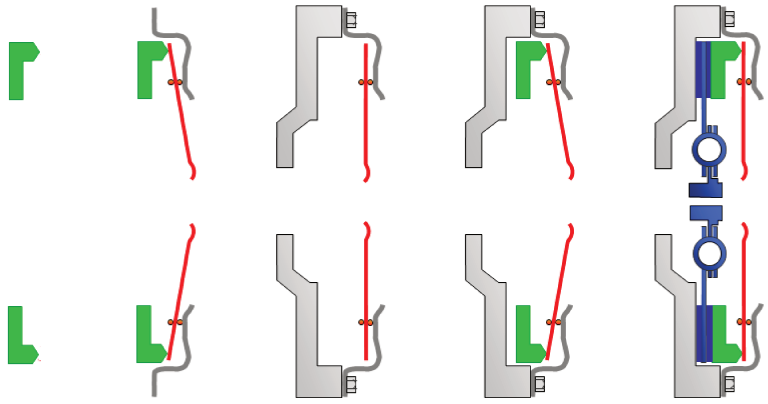

(a) P (b) C (c) FCP- (d) FCP+ (e) FCPD

Figure 4.1: Configurations tested for modal analysis (Adapted from Lerestrelo (2013)).

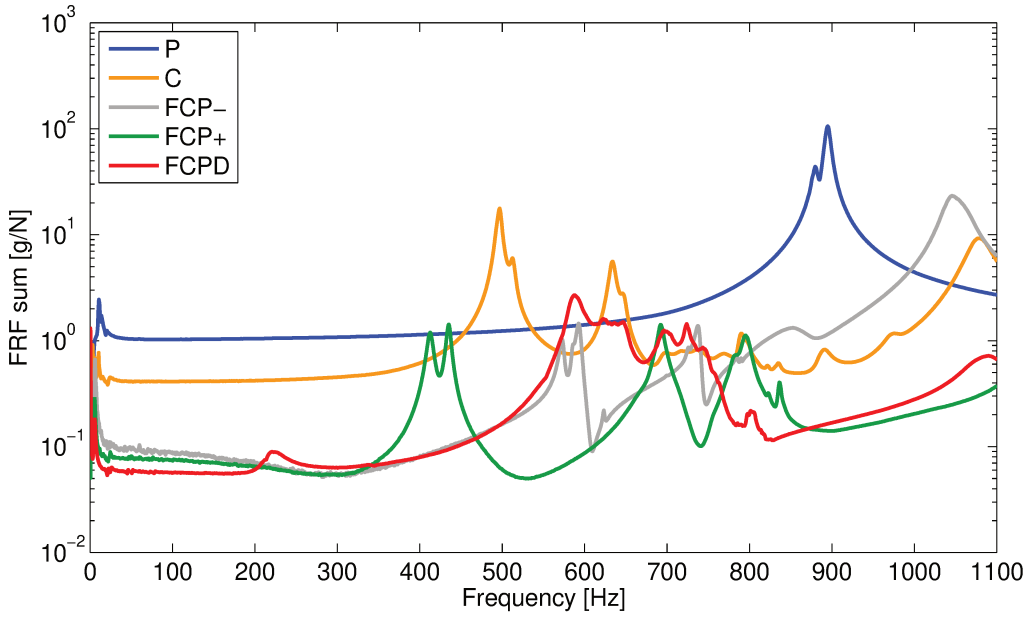

Figure 4.2: Frequency Fesponse Function (FRF) sum for different experiments from Fig. 4.1.

5 Hipothesis 1: Model using Cardan coordinates

As it was discussed in Chapter 3, the models from von Wagner *et al.* (2007), Fidlin *et al.* (2011), and Senatore *et al.* (2013) used Cardan coordinates to model the interaction disc/friction element. The model based on this hypothesis present results based on the *influence of the spin speed* during operation. This system is commonly seen in rotordynamic models (Childs (1993) and Muszynska (2010)).

A rotating spring/ damper element is derived in Section 5.2 to interact with a disc modelled in Section 5.1, making it possible to create different configurations. This possibility will be explored on Chapter 9. The physical interpretation of the moving damper element is shown in Sections 5.3 and 5.4. The moments and forces developed in this chapter will give origin to the stiffness and damping element matrices that will be discussed in Sections 5.5.1 and 5.5.3. The user can adopt them to create different designs by choosing the desired properties. The element matrices will be presented on Section 5.5.

5.1 Pressure plate model

Section 5.1.1 present the rotation matrices for Cardan coordinates. The angular speeds and accelerations are found on Section 5.1.2. The inertia matrices from Section 5.1.3 are studied in terms their eigenvalues characteristics.

5.1.1 Rotation matrices

The transformation matrices, speeds and accelerations for these coordinates are provided on Schiehlen and Eberhard (1986). Angle α (Fig. 5.1(b)) originates a rotation matrix for x axis $[R_\alpha]^T$ to transform a vector ${}_0\vec{r}$ from the coordinate system xyz (Fig. 5.1(a)) to $x_1y_1z_1$, represented as ${}_1\vec{r}$ (Eq. 5.1). The inverse transformation is calculated by Eq. 5.2.

$$ {}_1\vec{r} = [R_\alpha]^T \, {}_0\vec{r} = \begin{bmatrix} 1 & 0 & 0 \\ 0 & \cos\alpha & \sin\alpha \\ 0 & -\sin\alpha & \cos\alpha \end{bmatrix} {}_0\vec{r} \tag{5.1} $$

$$ {}_0\vec{r} = [R_\alpha] \, {}_1\vec{r} \tag{5.2} $$

A rotation given by β (Fig. 5.1(c)) moves the representation from $x_1y_1z_1$ to $x_2y_2z_2$ (Eq. 5.3) for y axis, while the inverse transformation is given by Eq. 5.4.

$$ {}_2\vec{r} = [R_\beta]^T \, {}_1\vec{r} = \begin{bmatrix} \cos\beta & 0 & -\sin\beta \\ 0 & 1 & 0 \\ sin\beta & 0 & \cos\beta \end{bmatrix} {}_1\vec{r} \tag{5.3} $$

$$ {}_1\vec{r} = [R_\beta] \, {}_2\vec{r} \tag{5.4} $$

Finally, the angle γ (Fig. 5.1(d)) is used to provide a rotation around the z axis from $x_2y_2z_2$ to $x_3y_3z_3$ according to Eq. 5.5. The inverse relation is shown in Eq. 5.6.

$$ {}_3\vec{r} = [R_\gamma]^T \, {}_2\vec{r} = \begin{bmatrix} \cos\gamma & \sin\gamma & 0 \\ -\sin\gamma & \cos\gamma & 0 \\ 0 & 0 & 1 \end{bmatrix} {}_2\vec{r} \tag{5.5} $$

$$ {}_2\vec{r} = [R_\gamma] \, {}_3\vec{r} \tag{5.6} $$

As a result, the transformation matrix $[R_{\alpha\beta\gamma}]$ is used to transfer a vector ${}_3\vec{r}$ from the coordinate system $x_3y_3z_3$ to a representation on xyz (Eq. 5.7). It results from the successive rotations combining the Eqs. 5.1, 5.3 and 5.5.

$$ [R_{\alpha\beta\gamma}] = \begin{bmatrix} \cos\beta\cos\gamma & -\cos\beta\sin\gamma & \sin\beta \\ \sin\alpha\sin\beta\cos\gamma + \cos\alpha\sin\gamma & -\sin\alpha\sin\beta\sin\gamma + \cos\alpha\cos\gamma & -\sin\alpha\cos\beta \\ -\cos\alpha\sin\beta\cos\gamma + \sin\alpha\sin\gamma & \cos\alpha\sin\beta\sin\gamma + \sin\alpha\cos\gamma & \cos\alpha\cos\beta \end{bmatrix} \tag{5.7} $$

$$ {}_0\vec{r} = [R_\alpha][R_\beta][R_\gamma] \, {}_3\vec{r} = [R_{\alpha\beta\gamma}] \, {}_3\vec{r} \tag{5.8} $$

5.1.2 Angular speeds and accelerations

The full expression of the angular speeds (Eq. 5.9) and accelerations (Eq. 5.10) are necessary for the equations of motion describing the wobbling movement of the disc.

$$ {}_3\vec{\omega} = \begin{bmatrix} \cos\beta\cos\gamma & \sin\gamma & 0 \\ -\cos\beta\sin\gamma & \cos\gamma & 0 \\ \sin\beta & 0 & 1 \end{bmatrix} \begin{Bmatrix} \dot{\alpha} \\ \dot{\beta} \\ \dot{\gamma} \end{Bmatrix} = \begin{Bmatrix} {}_3\omega_x \\ {}_3\omega_y \\ {}_3\omega_z \end{Bmatrix} \tag{5.9} $$

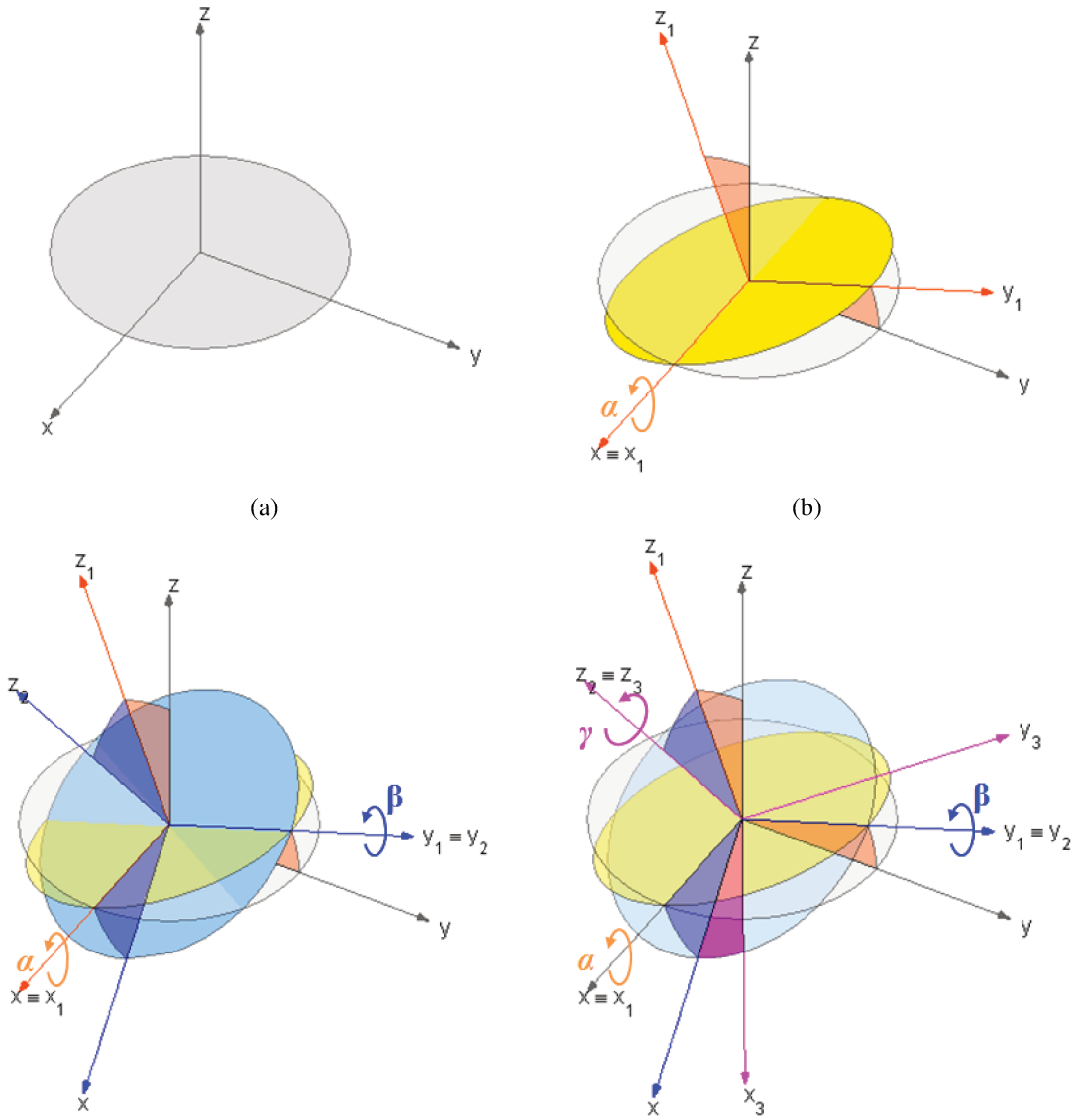

Figure 5.1: Rotations assumed on the model.

$$
{}_3\dot{\vec{\omega}} = \begin{bmatrix} \cos\beta\cos\gamma & \sin\gamma & 0 \\ -\cos\beta\sin\gamma & \cos\gamma & 0 \\ \sin\beta & 0 & 1 \end{bmatrix} \begin{Bmatrix} \ddot{\alpha} \\ \ddot{\beta} \\ \ddot{\gamma} \end{Bmatrix} + \dot{\alpha} \begin{bmatrix} -\sin\beta\cos\gamma & -\cos\beta\sin\gamma \\ \sin\beta\sin\gamma & -\cos\beta\cos\gamma \\ \cos\beta & 0 \end{bmatrix} \begin{Bmatrix} \dot{\beta} \\ \dot{\gamma} \end{Bmatrix} + \\
+ \dot{\beta}\dot{\gamma} \begin{Bmatrix} \cos\gamma \\ -\sin\gamma \\ 0 \end{Bmatrix} = \begin{Bmatrix} {}_3\dot{\omega}_x \\ {}_3\dot{\omega}_y \\ {}_3\dot{\omega}_z \end{Bmatrix} \tag{5.10}
$$

5.1.3 Inertia components and modal properties

The linearization of Eq. 5.11 (based on Ginsberg (1998)) results on Eq. 5.12, considering $\{p\}^T = \begin{Bmatrix} \alpha & \beta \end{Bmatrix}^T$. The mass $[M]$ and the gyroscopic $[G]$ matrices (represented on Eqs. 5.13 and 5.14) still depend on γ, generating non-diagonal terms of inertia.

$$\begin{cases} I_{xx}\,{}_3\dot{\omega}_x - (I_{yy} - I_{zz})\,{}_3\omega_y\,{}_3\omega_z = 0 \\ I_{yy}\,{}_3\dot{\omega}_y - (I_{zz} - I_{xx})\,{}_3\omega_z\,{}_3\omega_x = 0 \end{cases} \tag{5.11}$$

$$[M]\{\ddot{p}\} + [G]\{\dot{p}\} = \{0\} \tag{5.12}$$

$$[M] = \begin{bmatrix} I_{xx}\cos\gamma & I_{xx}\sin\gamma \\ -I_{yy}\sin\gamma & I_{yy}\cos\gamma \end{bmatrix} \tag{5.13}$$

$$[G] = \dot{\gamma}\begin{bmatrix} -\sin\gamma\,(I_{xx} - I_{yy} + I_{zz}) & \cos\gamma\,(I_{xx} - I_{yy} + I_{zz}) \\ -\cos\gamma\,(-I_{xx} + I_{yy} + I_{zz}) & -\sin\gamma\,(-I_{xx} + I_{yy} + I_{zz}) \end{bmatrix} \tag{5.14}$$

Assuming $I_{xx} = I_{yy} = I$ it is possible to remove the influence of γ by multiplying Eq. 5.12 by a matrix $[T]$ (Eqs. 5.15 and 5.16).

$$[T][M] = I\begin{bmatrix} \cos\gamma & -\sin\gamma \\ \sin\gamma & \cos\gamma \end{bmatrix}\begin{bmatrix} \cos\gamma & \sin\gamma \\ -\sin\gamma & \cos\gamma \end{bmatrix} = I\begin{bmatrix} 1 & 0 \\ 0 & 1 \end{bmatrix} \tag{5.15}$$

$$[T][G] = \dot{\gamma}I_{zz}\begin{bmatrix} \cos\gamma & -\sin\gamma \\ \sin\gamma & \cos\gamma \end{bmatrix}\begin{bmatrix} -\sin\gamma & \cos\gamma \\ -\cos\gamma & -\sin\gamma \end{bmatrix} = \dot{\gamma}I_{zz}\begin{bmatrix} 0 & 1 \\ -1 & 0 \end{bmatrix} \tag{5.16}$$

Looking in Eq. 5.17 it is possible to conclude that the modal properties on the system are not influenced by the angular rotation γ. The characteristic polynomial of this system is given by Eq. 5.18:

$$I\begin{bmatrix} 1 & 0 \\ 0 & 1 \end{bmatrix}\begin{Bmatrix} \ddot{\alpha} \\ \ddot{\beta} \end{Bmatrix} + \dot{\gamma}I_{zz}\begin{bmatrix} 0 & 1 \\ -1 & 0 \end{bmatrix}\begin{Bmatrix} \dot{\alpha} \\ \dot{\beta} \end{Bmatrix} = \begin{Bmatrix} 0 \\ 0 \end{Bmatrix} \tag{5.17}$$

$$\lambda^2\left[I^2\lambda^2 + (\dot{\gamma}I_{zz})^2\right] = 0 \tag{5.18}$$

A pair of null eigenvalues $\lambda_1, \lambda_1^* = 0$ are calculated, meaning that this system is semi definite. Another pair is $\lambda_2, \lambda_2^* = \pm j\left(\dfrac{|\dot{\gamma}|I_{zz}}{I}\right)$, characterizing a stable oscillating response. In the

case of a disc shown in Fig. 5.2(a), which will be used for many models in this whole work, the inertia moments are given by Eq 5.19 and 5.20, where R_{in} and R_{out} are its inner and outer radius, respectively. The mass is represented by m while its thickness is given by $2h$.

$$I_{xx} = I_{yy} = I = \frac{m}{12}\left[3\left(R_{in}^2 + R_{out}^2\right) + 4h^2\right] \tag{5.19}$$

$$I_{zz} = m\left(\frac{R_{in}^2 + R_{out}^2}{2}\right) \tag{5.20}$$

For $m = 2$ kg, $h = 0.01$ m, $R_{in} = 0.075$ m and $R_{out} = 0.1$ m, values close to a real pressure plate. Unless it is not clearly stated on the text, these properties will remain as standard throughout this work. Figure 5.2(b) contains a Campbell diagram showing the natural frequency close to the second order, whose approximation is presented in Eq. 5.21.

$$\omega_n = |\dot{\gamma}|\frac{I_{zz}}{I} = |\dot{\gamma}|\frac{6}{\left(3 + \dfrac{4h^2}{R_{in}^2 + R_{out}^2}\right)} \approx |\dot{\gamma}|2 \tag{5.21}$$

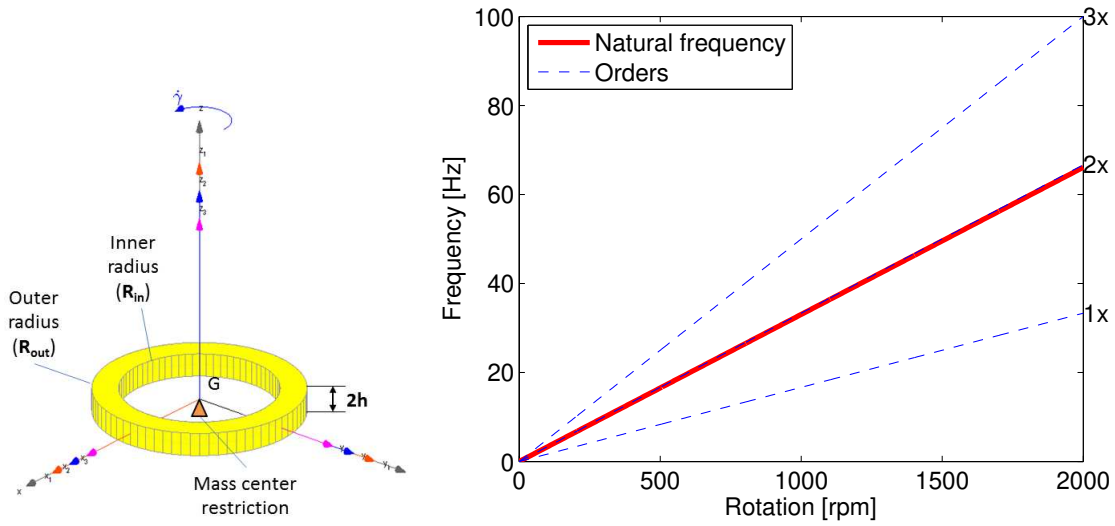

(a) (b)

Figure 5.2: Annular disc (Fig. 5.2(a)) and Campbell diagram of the system from Eq. 5.17 (Fig. 5.2(b)).

5.2 Modelling a rotating spring/viscous damper element with friction

It is important to state that such elements are found on the clutch squeal related literature (von Wagner *et al.* (2007), Hervé *et al.* (2008b), Hervé *et al.* (2009)) but they are derived for constant positions and properties, with restricted possibilities for the creation of different designs.

The most important contribution of this chapter for clutch squeal simulation is a formulation that allows *relative movement between disc and contact element* (Section 5.2.4). The angular relative position and speed is explicit on the equations and will have special impact on the damping matrices shown in Section 5.5. Modifications on stiffness can be implemented as well as the changes of geometry (angular distribution, radius distance, etc.). The formulation assumes a viscous damping element working in parallel with the elastic spring on the contact. It will allow the dynamic model an energy dissipation theory other than structural damping (Fidlin (2006), Fidlin *et al.* (2011)).

The normal force will be calculated on Section 5.2.7 with a procedure presented by von Wagner *et al.* (2007). The distribution of the friction forces according to the plate movement happens in Section 5.2.8. Limitations of this formulation will be provided on Appendix B.1.

The discussion on Section 5.2.8 over the friction force will be very useful to understand the skew symmetric terms on the system matrices (Section 6.1) and to explain the stable or unstable motion on Sections 6.1.1 and 6.1.2.

5.2.1 Basic relations

Figure 5.3(a) shows a simplified clutch system without the CSC (Fig. 2.1). The engine and the flywheel rotate at a constant speed $\dot{\gamma}$, while the clutch disc has the same speed as the inputshaft ($\dot{\theta}$). Based on this representation, the model from Fig. 5.3(b) is created.

On Fig.5.3(b) the point O describes the origin of the global coordinate system, while G stands for the mass center of the disc. The spring is attached to the surface rotating at speed ω_d, while frictional contact exists at point Q. P is located above the contact point Q, which is separated by a distance h. A force F_z is applied on the mass centre of the pressure plate to guarantee a static displacement z_e.

The rotating spring element (Fig. 5.3(b)) depends on the following parameters:

- k_i: element stiffness
- c_i: element damping

- R_i: radius distance
- ψ_i: relative angle used to describe the position of the ith element
- z_e: static displacement
- h: distance between the mass center and the contact point Q
- ${}_0\vec{\omega}_d = \left\{0 \quad 0 \quad \dot{\theta}\right\}^T$: rotating speed of the inputshaft and clutch disc (Fig. 5.3(a))
- μ_i: local friction coefficient, representing a punctual facing interaction with the pressure plate

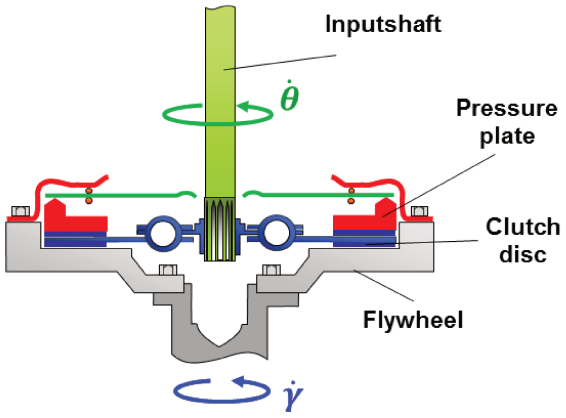

(a) Simplified clutch system adapted from Lerestrelo (2013).

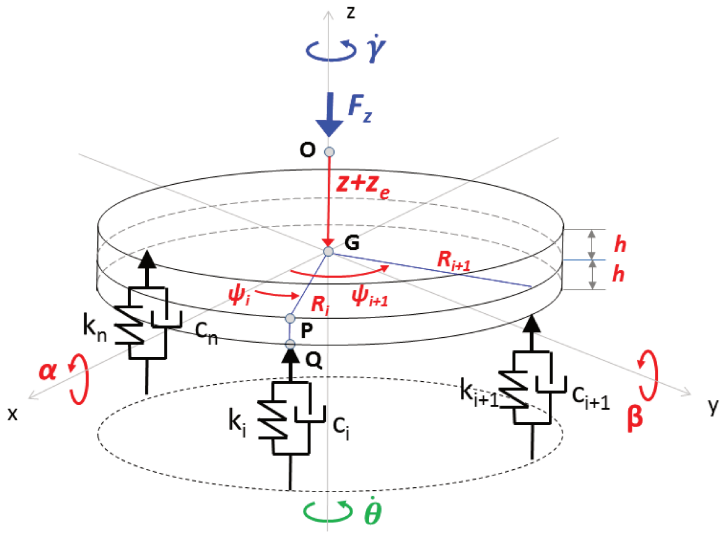

(b) Rotating element parameters.

Figure 5.3: Real clutch system and model.

5.2.2 Element effort and the constant contact position assumption

This element can be physically related to an elastic curve such as the cushion measurement, described on Sec. 2.2. Figure 5.4 shows that, for the nonlinear curve, the load N_0 occurs for the displacement z_e. In this situation, k_i represents a linearized stiffness around point z_e in a first order approximation. This approach allows studying load and stiffness separately from each other. For the linear case, there is $N_0 = k_i z_e$. The notation for static load on the works from the literature on Section 3.2 was maintained. On the following chapters, it will be possible to change the formulation from the linear case to the linearized version, by a substitution of the term $k_i z_e$ by the load N_0. This observation remains valid for the element matrices of Sections 5.5 and 7.4 and up to the end of this work.

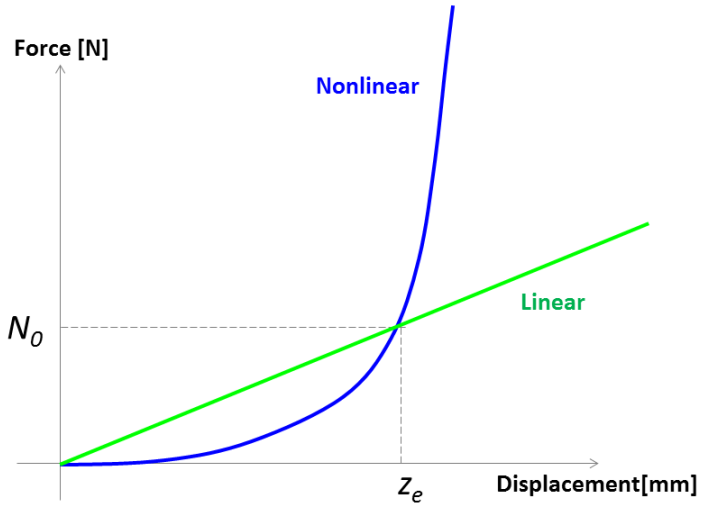

Figure 5.4: Comparison between a linear a nonlinear stiffness curves.

Figure 5.5(a) shows a representation of a cushion spring. It may look like the letter "Z" or "S", depending on the design (Micknass, 1993). It is important to note that it results from a curved metal plate. Its upper part is riveted to the facing on the pressure plate side, while the lower part is connected to the flywheel facing by the same procedure. The cushion spring for the contact on the pressure plate is assumed as a composition of two stiffness elements (Fig. 5.5(b)). The vertical load discussed on the previous section is given by the parameter k_i. The spatially oriented horizontal stiffness k_s supports the other element, acting both coordinate x and y. As consequence of this configuration, the same constant position vector ${}_3\vec{r}_{GQ}$ (Section 5.2.3) in relation to the centre of gravity G can be obtained when there is pressure plate motion (Fig. 5.5(c)). This assumption will have a strong impact on the normal force calculation on Section 5.2.7.

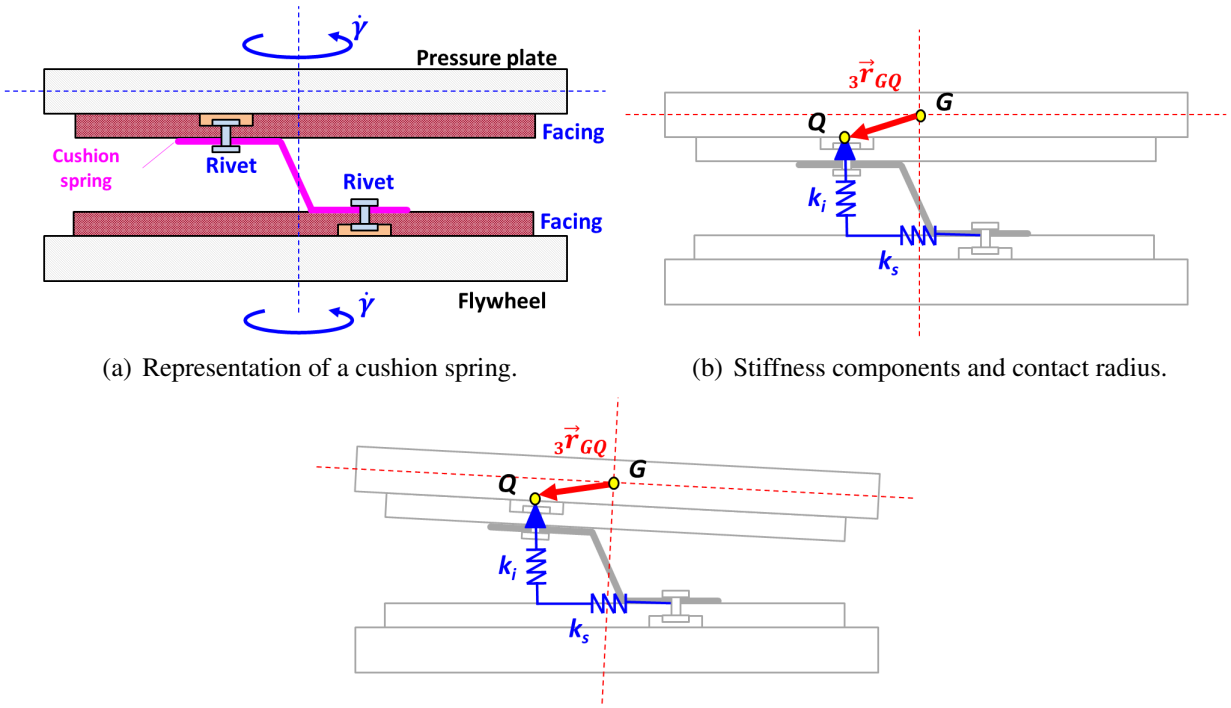

(a) Representation of a cushion spring.

(b) Stiffness components and contact radius.

(c) Element position after motion of the plate.

Figure 5.5: Considerations on the position of the friction element.

5.2.3 Elastic and damping forces

As a direct consequence of the coordinate system, Section 5.2.3 will show that the friction/damping efforts will be related to the displacements of the pressure plate γ and the relative displacement ψ. There is the position vector ${}_3\vec{r}_{GQ}$ (Eq. 5.22). The spring and damper only provide effort on the vertical direction. The displacement ${}_0r_{GQ_z}$ (Eq. 5.23) of the contact point Q in relation to the mass centre of the pressure plate is given by the following expression:

$$ {}_3\vec{r}_{GQ} = \begin{Bmatrix} R_i \cos\psi_i & R_i \sin\psi_i & -h \end{Bmatrix}^T \tag{5.22} $$

$$ \begin{aligned} {}_0r_{GQ_z} = &\left(-\cos\alpha \sin\beta \cos\gamma + \sin\alpha \sin\gamma\right) R_i \cos\psi_i + \\ &+ \left(\cos\alpha \sin\beta \sin\gamma + \sin\alpha \cos\gamma\right) R_i \sin\psi_i - h \cos\alpha \cos\beta \end{aligned} \tag{5.23} $$

The total displacement on contact (Eq. 5.24) is obtained by adding a negative displacement ${}_0r_{OG_z}$ of point G in relation to the system origin. A static equilibrium point is defined by z_e, which

is used to introduce a compression pre load to the spring. This parameter is important to make sure that the contact is never lost between pressure plate and friction element.

$$
\begin{aligned}
{}_0r_{OQ_z} = {}_0r_{OG_z} + {}_0r_{GQ_z} = &-(z+z_e) + (-\cos\alpha\sin\beta\cos\gamma + \sin\alpha\sin\gamma)\,R_i\cos\psi_i + \\
&+ (\cos\alpha\sin\beta\sin\gamma + \sin\alpha\cos\gamma)\,R_i\sin\psi_i - h\cos\alpha\cos\beta
\end{aligned}
\tag{5.24}
$$

The displacement on z axis is used to calculate the spring (${}_0\vec{F}_{k_i}$):

$$
{}_0\vec{F}_{k_i} = k_i\left[-h - {}_0r_{OQ_z}\right]\vec{k} = {}_0F_{k_i}\vec{k} \tag{5.25}
$$

The damping effort is calculated by Eq. 5.26 by the differentiation of Eq. 5.24:

$$
{}_0\vec{F}_{c_i} = c_i\left[-{}_0\dot{r}_{OQ_z}\right]\vec{k} = {}_0F_{c_i}\vec{k} \tag{5.26}
$$

5.2.4 Relative motion between the element and pressure plate

The relative motion will define the position the rotating element in relation to the coordinate system attached to the pressure plate. The friction element/clutch disc rotating speed ${}_3\vec{\omega}_d$ (Eq. 5.27) is calculated on the coordinate system $x_3y_3z_3$:

$$
{}_3\vec{\omega}_d = [R_{\alpha\beta\gamma}]^T\begin{Bmatrix}0\\0\\\dot{\theta}\end{Bmatrix} = \dot{\theta}\begin{Bmatrix}-\cos\alpha\sin\beta\cos\gamma + \sin\alpha\sin\gamma\\ \cos\alpha\sin\beta\sin\gamma + \sin\alpha\cos\gamma\\ \cos\alpha\cos\beta\end{Bmatrix} \tag{5.27}
$$

The angle ψ_i describes the relative position between element and plate. Looking from the coordinate system $x_3y_3z_3$ it is possible to see that when the pressure plate speed is greater than the friction disc speed ($\dot{\gamma} > \dot{\theta}$ on Fig. 5.6(a)), ψ_i increase clockwise from its initial location ($\psi_0 = 0°$). In this case, tangential relative speed (${}_3\vec{V}_{t_{rel}}$) follows the pressure plate rotation, while the friction force ${}_3\vec{F}_{r_i}$ points on the opposite direction. On the other hand, if $\dot{\gamma} < \dot{\theta}$ (Fig. 5.6(b)) the derivative $\dot{\psi}_i$ follows the counterclockwise direction, being calculated as Eq. 5.28:

$$
\dot{\psi}_i = -(\dot{\gamma} - {}_3\omega_{dz}) = -\left(\dot{\gamma} - \dot{\theta}\cos\alpha\cos\beta\right) \tag{5.28}
$$

Integrating Eq. 5.28 it is possible to calculate $\psi_i(t)$ (Eq. 5.29). The initial position angle ψ_{i_0} is very important to define the location of the i-th element in relation to the others. If the surfaces are slipping, all elements are displaced by $-\gamma(t) + \theta_d(t)$.

$$\psi_i(t) = -\int_0^t \dot{\gamma}\,\mathrm{d}t + \int_0^t \dot{\theta}\cos\alpha\cos\beta\,\mathrm{d}t = \psi_{i_0} - \gamma(t) + \theta_d(t) \tag{5.29}$$

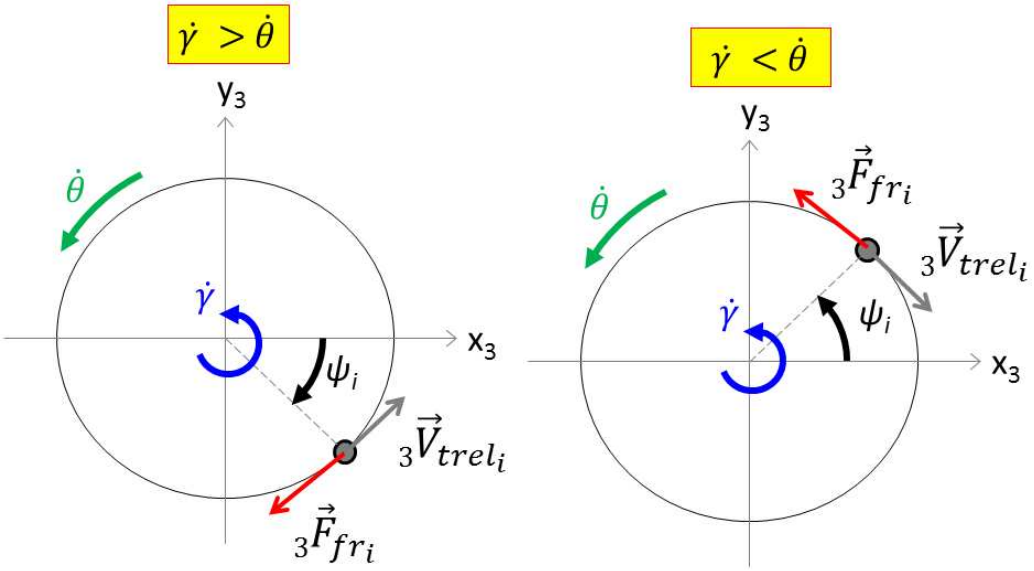

(a) Relative displacement for $\dot{\gamma} > \dot{\theta}$ (b) Relative displacement for $\dot{\gamma} < \dot{\theta}$

Figure 5.6: Relative motion between the disc and element.

5.2.5 Approximation of the tangential speed at contact point

The speed of the pressure plate at the contact point ${}_3\vec{V}_Q$ (Fig. 5.7) is calculated as Eq. 5.30:

$${}_3\vec{V}_Q = {}_3\vec{V}_G + {}_3\vec{V}_{GQ} \tag{5.30}$$

The vertical speed of its center of gravity ${}_3\vec{V}_G$ (Fig. 5.7) is calculated on the system $x_3y_3z_3$:

$${}_3\vec{V}_G = [R_{\alpha\beta\gamma}]^T \begin{Bmatrix} 0 \\ 0 \\ {}_0\dot{r}_{OG_z} \end{Bmatrix} = (-\dot{z}) \begin{Bmatrix} -\cos\alpha\sin\beta\cos\gamma + \sin\alpha\sin\gamma \\ \cos\alpha\sin\beta\sin\gamma + \sin\alpha\cos\gamma \\ \cos\alpha\cos\beta \end{Bmatrix} \tag{5.31}$$

The relative speed between points G and Q is calculated in Eq. 5.32. The angular speed of the pressure plate (${}_3\vec{\omega}$) was previously calculated on Eq. 5.9:

$$
\begin{aligned}
{}_3\vec{V}_{GQ} &= {}_3\vec{\omega} \times {}_3\vec{r}_{GQ} \\
&= \begin{Bmatrix} \dot{\alpha}\left(h\cos\beta\sin\gamma - \sin\beta R_i \sin\psi_i\right) - h\cos\gamma\dot{\beta} - \dot{\gamma}R_i\sin\psi_i \\ \dot{\alpha}\left(h\cos\beta\cos\gamma + \sin\beta R_i\cos\psi_i\right) + h\sin\gamma\dot{\beta} + \dot{\gamma}R_i\cos\psi_i \\ R_i\left[\dot{\alpha}\cos\beta\left(\cos\gamma\sin\psi_i + \sin\gamma\cos\psi_i\right) + \dot{\beta}\left(\sin\gamma\sin\psi_i - \cos\gamma\cos\psi_i\right)\right] \end{Bmatrix}
\end{aligned} \tag{5.32}
$$

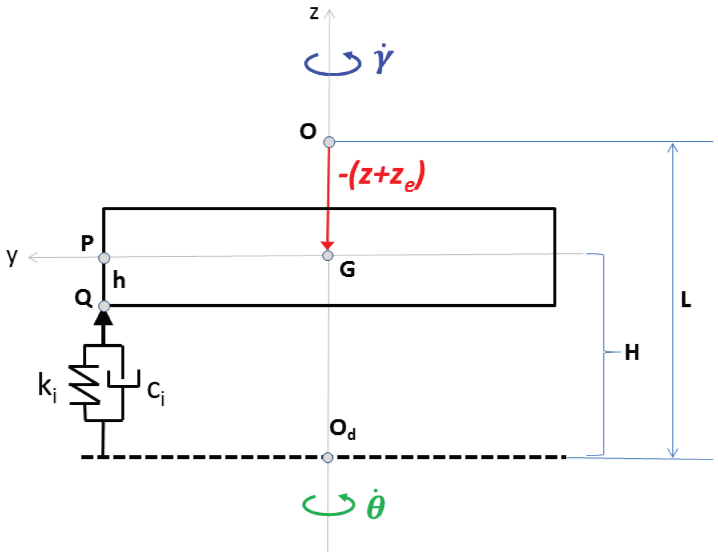

Figure 5.7: Distance between rotating basis and disc.

The tangential speed of the pressure plate ${}_3\vec{V}_{t_{sup}}$ takes into account components on the plane x_3y_3:

$$
{}_3\vec{V}_{t_{sup}} = \begin{Bmatrix} {}_3V_{Q_x} \\ {}_3V_{Q_y} \\ 0 \end{Bmatrix} = \begin{Bmatrix} {}_3V_{G_x} \\ {}_3V_{G_y} \\ 0 \end{Bmatrix} + \begin{Bmatrix} {}_3V_{GQ_x} \\ {}_3V_{GQ_y} \\ 0 \end{Bmatrix} \tag{5.33}
$$

Looking at Fig. 5.7 the distance between the disc and the rotating basis without axial movement is shown as L. This distance is dynamically defined as $H = L - (z - z_e)$ and the vector between the point O_d and the contact point Q is given by Eq. 5.34.

$$
{}_3\vec{r}_{O_dQ} = {}_3\vec{r}_{O_dG} + {}_3\vec{r}_{GQ} = \begin{Bmatrix} R_i\cos\psi_i \\ R_i\sin\psi_i \\ -h \end{Bmatrix} + H \begin{Bmatrix} -\cos\alpha\sin\beta\cos\gamma + \sin\alpha\sin\gamma \\ \cos\alpha\sin\beta\sin\gamma + \sin\alpha\cos\gamma \\ \cos\alpha\cos\beta \end{Bmatrix} \tag{5.34}
$$

The speed of the inferior disc on the contact point is calculated as Eq. 5.35. The tangential speed of the friction element (Eq. 5.36) takes into account only components on the x_3y_3 plane. It is important to note that this speed does not depend on H.

$$ {}_3\vec{V}_{inf} = {}_3\vec{\omega}_d \times {}_3\vec{r}_{O_dQ} \tag{5.35} $$

$$ {}_3\vec{V}_{t_{inf}} = \begin{Bmatrix} {}_3V_{inf_x} \\ {}_3V_{inf_y} \\ 0 \end{Bmatrix} = \dot{\theta} \begin{Bmatrix} -\left[h\left(\cos\alpha\sin\beta\sin\gamma + \sin\alpha\cos\gamma\right) + R_i\sin\psi_i\cos\alpha\cos\beta\right] \\ h\left(-\cos\alpha\sin\beta\cos\gamma + \sin\alpha\sin\gamma\right) + R_i\cos\psi_i\cos\alpha\cos\beta \\ 0 \end{Bmatrix} \tag{5.36} $$

The tangential relative speed ${}_3\vec{V}_{t_{rel}}$ between the contact element/pressure plate is given by Eq. 5.37. Its position in relation to the disc is shown in Figs. 5.9(a) and 5.9(b).

$$ \begin{aligned} {}_3\vec{V}_{t_{rel}} &= {}_3\vec{V}_{t_{sup}} - {}_3\vec{V}_{t_{inf}} \\ &= (-\dot{z}) \begin{Bmatrix} -\cos\alpha\sin\beta\cos\gamma + \sin\alpha\sin\gamma \\ \cos\alpha\sin\beta\sin\gamma + \sin\alpha\cos\gamma \\ 0 \end{Bmatrix} + \dot{\alpha} \begin{Bmatrix} h\cos\beta\sin\gamma - \sin\beta R_i\sin\psi_i \\ h\cos\beta\cos\gamma + \sin\beta R_i\cos\psi_i \\ 0 \end{Bmatrix} + \\ &+ \dot{\beta} \begin{Bmatrix} -h\cos\gamma \\ h\sin\gamma \\ 0 \end{Bmatrix} + \left(\dot{\gamma} - \dot{\theta}\cos\alpha\cos\beta\right) \begin{Bmatrix} -\sin\psi_i \\ \cos\psi_i \\ 0 \end{Bmatrix} + \\ &- \dot{\theta}h \begin{Bmatrix} -\left(\cos\alpha\sin\beta\sin\gamma + \sin\alpha\cos\gamma\right) \\ -\cos\alpha\sin\beta\cos\gamma + \sin\alpha\sin\gamma \\ 0 \end{Bmatrix} \end{aligned} \tag{5.37} $$

The expression of ${}_3\vec{V}_{t_{rel}}$ depends on the variable array $\vec{\varepsilon} = \begin{Bmatrix} \alpha & \dot{\alpha} & \beta & \dot{\beta} & \dot{z} \end{Bmatrix}^T$. It can be linearized using the Jacobian matrix $[J(\vec{\varepsilon}_0)]$ evaluated at an specific point $\vec{\varepsilon}_0$ (Eq. 5.38). Imposing $\vec{\varepsilon}_0 = \begin{Bmatrix} 0 & 0 & 0 & 0 & 0 \end{Bmatrix}^T$, the Jacobian no longer depends on $\dot{z}$ (Eq. 5.39). It will be important for the approximation of the unitary vector on the direction of ${}_3\vec{V}_{t_{rel}}$.

$$ {}_3\vec{V}_{t_{rel}} = \begin{Bmatrix} f_x(\alpha,\dot{\alpha},\beta,\dot{\beta},\dot{z}) \\ f_y(\alpha,\dot{\alpha},\beta,\dot{\beta},\dot{z}) \\ f_z(\alpha,\dot{\alpha},\beta,\dot{\beta},\dot{z}) \end{Bmatrix} = \vec{f}(\vec{\varepsilon}) \approx \vec{f}(\vec{\varepsilon}_0) + [J(\vec{\varepsilon}_0)]\left(\vec{\varepsilon} - \vec{\varepsilon}_0\right) \tag{5.38} $$

$$
\begin{aligned}
[J(\vec{\varepsilon}_0)] &= \left[\begin{array}{ccccc}
\dfrac{\partial f_x}{\partial \alpha} & \dfrac{\partial f_x}{\partial \dot{\alpha}} & \dfrac{\partial f_x}{\partial \beta} & \dfrac{\partial f_x}{\partial \dot{\beta}} & \dfrac{\partial f_x}{\partial \dot{z}} \\
\dfrac{\partial f_y}{\partial \alpha} & \dfrac{\partial f_y}{\partial \dot{\alpha}} & \dfrac{\partial f_y}{\partial \beta} & \dfrac{\partial f_y}{\partial \dot{\beta}} & \dfrac{\partial f_y}{\partial \dot{z}} \\
\dfrac{\partial f_z}{\partial \alpha} & \dfrac{\partial f_z}{\partial \dot{\alpha}} & \dfrac{\partial f_z}{\partial \beta} & \dfrac{\partial f_z}{\partial \dot{\beta}} & \dfrac{\partial f_z}{\partial \dot{z}}
\end{array}\right]\Bigg|_{\vec{\varepsilon}=\vec{\varepsilon}_0} \\
&= \begin{bmatrix}
\dot{\theta}h\cos\gamma & h\sin\gamma & \dot{\theta}h\sin\gamma & -h\cos\gamma & 0 \\
-\dot{\theta}h\sin\gamma & h\cos\gamma & \dot{\theta}h\cos\gamma & h\sin\gamma & 0 \\
0 & 0 & 0 & 0 & 0
\end{bmatrix}
\end{aligned}
\tag{5.39}
$$

The linearization of the tangential speed is given by Eq. 5.40 and it is influenced by the disc angles α and β and by its derivatives ($\dot{\alpha}$ and $\dot{\beta}$):

$$
{}_3\vec{V}_{t_{rel}} = \left\{\begin{array}{c}
-\left(\dot{\gamma}-\dot{\theta}\right)\sin\psi_i + h\left(\dot{\alpha}\sin\gamma - \dot{\beta}\cos\gamma\right) + \dot{\theta h}\left(\beta\sin\gamma + \alpha\cos\gamma\right) \\
\left(\dot{\gamma}-\dot{\theta}\right)\cos\psi_i + h\left(\dot{\alpha}\cos\gamma + \dot{\beta}\sin\gamma\right) + \dot{\theta h}\left(\beta\cos\gamma - \alpha\sin\gamma\right) \\
0
\end{array}\right\}
\tag{5.40}
$$

In a next step, an approximation on the norm of Eq. 5.40 is made considering that the terms which depend on h and h^2 are negligible:

$$
\left|{}_3\vec{V}_{t_{rel}}\right| \approx \left\{R_i^2(\dot{\gamma}-\dot{\theta})^2\right\}^{1/2} = R_i\left|\dot{\gamma}-\dot{\theta}\right|
\tag{5.41}
$$

With these simplification step, the normal vector on the direction of the relative tangential speed (${}_3\vec{\nu}$) is obtained in Eq. 5.42. Terms that depend on the inverse of $\left|\dot{\gamma}-\dot{\theta}\right|$ on Cardan coordinates appear on Fidlin *et al.* (2011), von Wagner *et al.* (2007) and Senatore *et al.* (2013). There are limitations of this approach, and they will be discussed on Appendices A.1 and B.1. The components ${}_3\nu_x$ and ${}_3\nu_y$ are described in Eqs. 5.43 and 5.44. Section 5.5 will present stiffness and damping terms related to them.

$$
{}_3\vec{\nu} = \frac{{}_3\vec{V}_{t_{rel}}}{\left|{}_3\vec{V}_{t_{rel}}\right|} = \left\{\begin{array}{c}
{}_3\nu_x \\
{}_3\nu_y \\
0
\end{array}\right\}
\tag{5.42}
$$

$$ {}_3\nu_x = -sign\left(\dot{\gamma} - \dot{\theta}\right)\sin\psi_i + \frac{h}{\left|\dot{\gamma} - \dot{\theta}\right|}\left(\dot{\alpha}\sin\gamma - \dot{\beta}\cos\gamma\right) + \frac{\dot{\theta}h}{\left|\dot{\gamma} - \dot{\theta}\right|}\left(\beta\sin\gamma + \alpha\cos\gamma\right) \quad (5.43) $$

$$ {}_3\nu_y = sign\left(\dot{\gamma} - \dot{\theta}\right)\cos\psi_i + \frac{h}{\left|\dot{\gamma} - \dot{\theta}\right|}\left(\dot{\alpha}\cos\gamma + \dot{\beta}\sin\gamma\right) + \frac{\dot{\theta}h}{\left|\dot{\gamma} - \dot{\theta}\right|}\left(\beta\cos\gamma - \alpha\sin\gamma\right) \quad (5.44) $$

5.2.6 Friction force

The friction force on Cardan coordinates ${}_3\vec{F}_{fr_i}$ (Eq. 5.45) is obtained with direction opposed to the tangential relative speed (Fig. 5.6). Its moments are calculated on Eq. 5.46. The results on the other system are the same.

$$ {}_3\vec{F}_{fr_i} = -\mu\,{}_3N\,{}_3\vec{\nu} = -\mu\,{}_3N\begin{Bmatrix} {}_3\nu_x \\ {}_3\nu_x \\ 0 \end{Bmatrix} = -\mu\,{}_3N\begin{Bmatrix} {}_3\nu_x \\ {}_3\nu_x \\ 0 \end{Bmatrix} = \begin{Bmatrix} {}_3F_{fr_{i_x}} \\ {}_3F_{fr_{i_y}} \\ 0 \end{Bmatrix} \quad (5.45) $$

$$ {}_3\vec{M}_{fr_i} = {}_3\vec{r}_{GQ} \times {}_3\vec{F}_{fr_i} = \begin{Bmatrix} -\mu h\,{}_3N\,{}_3\nu_y \\ \mu h\,{}_3N\,{}_3\nu_x \\ \mu\,{}_3NR_i\left({}_3\nu_x\sin\psi_i - {}_3\nu_y\cos\psi_i\right) \end{Bmatrix} \quad (5.46) $$

5.2.7 Normal force calculation

The normal contact force on the disc is given as Eq. 5.47 and it is represented on Fig. 5.8. The force ${}_0\vec{F}_s$ represent a static force that holds the element on a specific position.

$$ {}_3\vec{N}_i = \begin{Bmatrix} 0 \\ 0 \\ {}_3N_i \end{Bmatrix} \quad (5.47) $$

von Wagner *et al.* (2007) took into consideration that it is necessary to solve a system of equations to obtain the normal force of this system. All efforts involved on the contact, friction, damping and stiffness forces must be moved to the global system. The force ${}_0\vec{F}_s$ comes from the supporting stiffness presented in Section 5.2.2 (Fig. 5.5). Then equilibrium on the vertical direction

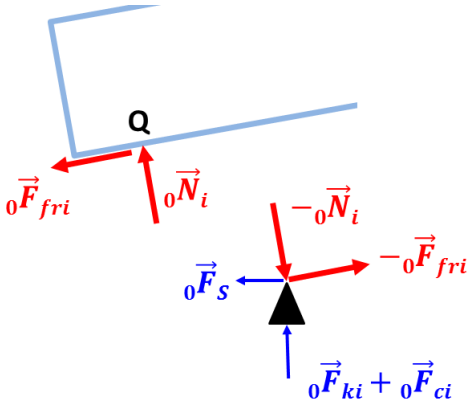

Figure 5.8: Diagram for normal force calculation.

on the element must be taken into account (Eq. 5.48):

$$-\,{}_0N_{i_z} - {}_0F_{fr_{i_z}} + {}_0F_{k_{i_z}} + {}_0F_{c_{i_z}} = 0 \tag{5.48}$$

Equation 5.48 lead to Eq. 5.49 presenting the actual amplitude of the normal force. The nonlinear expression depends on function f_1 (Eq. 5.50), that can be approximated by Eq. 5.51.

$$ {}_3N_i = f_1 \left({}_0F_{k_{i_z}} + {}_0F_{c_{i_z}} \right) \tag{5.49}$$

$$\begin{aligned} f_1 = \{ & \cos\alpha\cos\beta - \mu\left[(-\cos\alpha\sin\beta\cos\gamma + \sin\alpha\sin\gamma)\,{}_3\nu_x + \right. \\ & + \left. (\cos\alpha\sin\beta\sin\gamma + \sin\alpha\cos\gamma)\,{}_3\nu_y\right]\}^{-1} \end{aligned} \tag{5.50}$$

$$\begin{aligned} f_1 \approx 1 & + \mu sign(\dot{\gamma} - \dot{\theta})\left[-\sin\gamma\sin\psi_i + \cos\gamma\cos\psi_i\right]\alpha \\ & + \mu sign(\dot{\gamma} - \dot{\theta})\left[\cos\gamma\sin\psi_i + \sin\gamma\cos\psi_i\right]\beta \end{aligned} \tag{5.51}$$

The normal force on Eq. 5.52 contains the original stiffness and damping forces, but new parameters are the *friction related terms*:

$$\begin{aligned} {}_3N_i \approx {} & {}_0F_{k_{i_z}} + {}_0F_{c_{i_z}} + \mu k_i z_e sign(\dot{\gamma} - \dot{\theta})\left[-\sin\gamma\sin\psi_i + \cos\gamma\cos\psi_i\right]\alpha + \\ & + \mu k_i z_e sign(\dot{\gamma} - \dot{\theta})\left[\cos\gamma\sin\psi_i + \sin\gamma\cos\psi_i\right]\beta \end{aligned} \tag{5.52}$$

Equation 5.45 imposes that the friction force always remains on the plane x_3y_3. But it can be

represented on global coordinates as ${}_0F_{fr_{ix}}$, ${}_0F_{fr_{iy}}$ and ${}_0F_{fr_{iz}}$ on Figs. 5.9(a) and 5.9(b). In both pictures, ${}_0F_{fr_{iz}}$ occurs on a vertical direction and an equilibrium assumption allows the resolution of this problem, making necessary the step on Eq. 5.48.

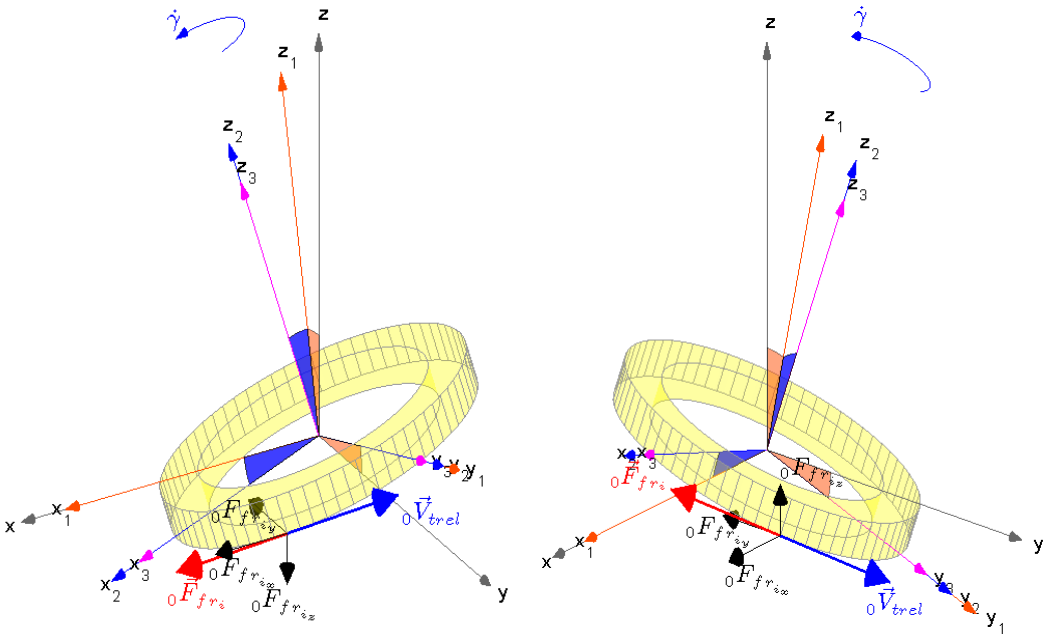

(a) Angles imposed as $\alpha > 0$ and $\beta > 0$.

(b) Angles imposed as $\alpha < 0$ and $\beta < 0$.

Figure 5.9: Friction force components in an element positioned at $\psi_i = 45°$

The element linearized matrices on Section 5.5 are obtained from the normal contact force (Eq. 5.53):

$$ {}_3\vec{M}_{N_i} = {}_3\vec{r}_{GQ} \times {}_3\vec{N}_i \tag{5.53} $$

5.2.8 Friction distribution and its relation with plate movement

To assure contact, it is necessary that ${}_3N_i > 0$ (positive normal force) for all situations (Eq. 5.54). The preload is constant as ${}_3N_{cons_i} = k_i z_e$ which is always positive. A variable normal force can be either positive or negative (${}_3N_{var_i} > 0$ or ${}_3N_{var} < 0$) resulting from the motion of the surface above an elastic/damped support.

$$ {}_3N_i = {}_3N_{cons_i} + {}_3N_{var_i} \tag{5.54} $$

If the pressure plate does not vibrate, the normal force is uniform as it can be seen in Fig. 5.10 ($z_e = 0.001$ m in this example). Hence, the friction force has the same magnitude in every position. To understand the effect of motion on the distribution of friction forces, a series of examples were created assuming rotation on the pressure plate only, while the element remained still ($\dot{\gamma} > 0$ and $\dot{\theta} = 0$). In this representation, only the constant friction vector ($_3\vec{F}_{fr_{cons_i}}$) is opposed to the relative speed, while the variable portion ($_3\vec{F}_{fr_{var_i}}$) can be interpreted as a vector which possesses the same line of action as the relative speed, but it changes direction according to $_3N_{var_i}$. Figure 5.10 presents $_3N_{var_i} = 0$.

$$_3\vec{F}_{fr_i} = -\mu\,{}_3N\,{}_3\vec{\nu} = -\mu\,(_3N_{cons_i} + {}_3N_{var_i})\,{}_3\vec{\nu} = {}_3\vec{F}_{fr_{cons_i}} + {}_3\vec{F}_{fr_{var_i}} \tag{5.55}$$

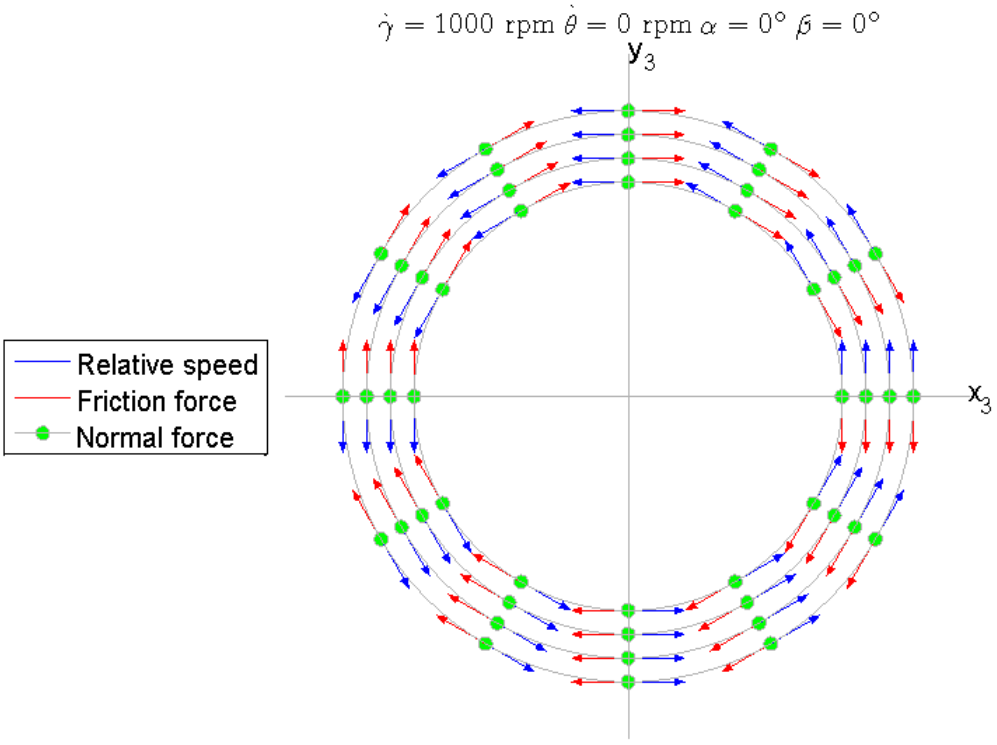

Figure 5.10: Friction forces under uniform normal load distribution.

Figure 5.11(a) illustrates the case when the variable normal force is positive, and there is compression of the element around the static position. The variable friction force has the same direction as $_3\vec{F}_{fr_{cons_i}}$, resulting in an increased total friction force $_3\vec{F}_{fr_i}$. In the other hand, if the variable normal force is negative (Figure 5.11(b)), it means that the total normal force is reduced from its mean value. As consequence of that, the total friction force decreases in terms of magnitude and this condition can be represented by a variable friction force opposed to the constant vector.

It is important to emphasize here that ${}_3\vec{F}_{fr_i}$ *never changes its direction due to the preload on the spring* but it can vary along the disc due to the wobbling movement. The variable friction forces (${}_3\vec{F}_{fr_{var_i}}$ and ${}_3N_{var_i}$) are *purely theoretical*, but they will be very helpful on the comprehension of the physical effects caused by effort fluctuations.

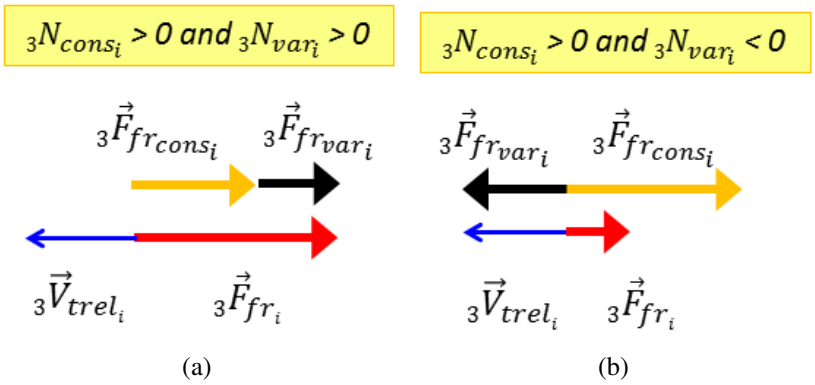

Figure 5.11: Friction forces for two different conditions of ${}_3N_{var}$.

Figure 5.12(a) contains an scheme for the distribution of the variable friction force when $\alpha > 0°$ and $\beta = 0°$. All elements positioned with coordinates $y_3 > 0$ are found with ${}_3N_{var_i} < 0$ (decreased normal force). The variable friction vectors point in opposition to ${}_3\vec{F}_{fr_{cons_i}}$ (Fig. 5.12(b)), which result in a lower friction ${}_3\vec{F}_{fr_i}$. For $x_3 = 0$, there is no variable force once that no displacements occur around the static position.

If $\alpha < 0°$ and $\beta = 0°$, an inversion on the variable force distribution takes place compared to the previous case (Figure 5.12(c)). Here, elements located at $y_3 > 0$ are found with an increased normal force (${}_3N_{var_i} > 0$) and the variable friction follows the direction of ${}_3\vec{F}_{fr_{cons_i}}$ (Figure 5.12(d)). Elements positioned assuming $y_3 < 0$ present ${}_3\vec{F}_{fr_{var_i}}$ opposed to the total friction force, which is lower than ${}_3\vec{F}_{fr_{cons_i}}$ (Figure 5.12(d)).

Angular displacements on β affect the force distribution along the x axis. For $\beta > 0°$ and $\alpha = 0°$ the compression force is increased from its static value (${}_3N_{var_i} > 0$) for $x_3 > 0$ (Figure 5.13(a)). As consequence of that, the disc sector for $x_3 > 0$ presents an increase on the total friction force (Figure 5.13(b)). If $x_3 < 0$, it occurs a decrease on ${}_3\vec{F}_{fr_i}$ once that the variable friction force is opposed to the constant portion. Figures 5.13(c) and 5.13(d) display the variable and total friction forces in a situation where $\beta < 0°$ and $\alpha = 0°$.

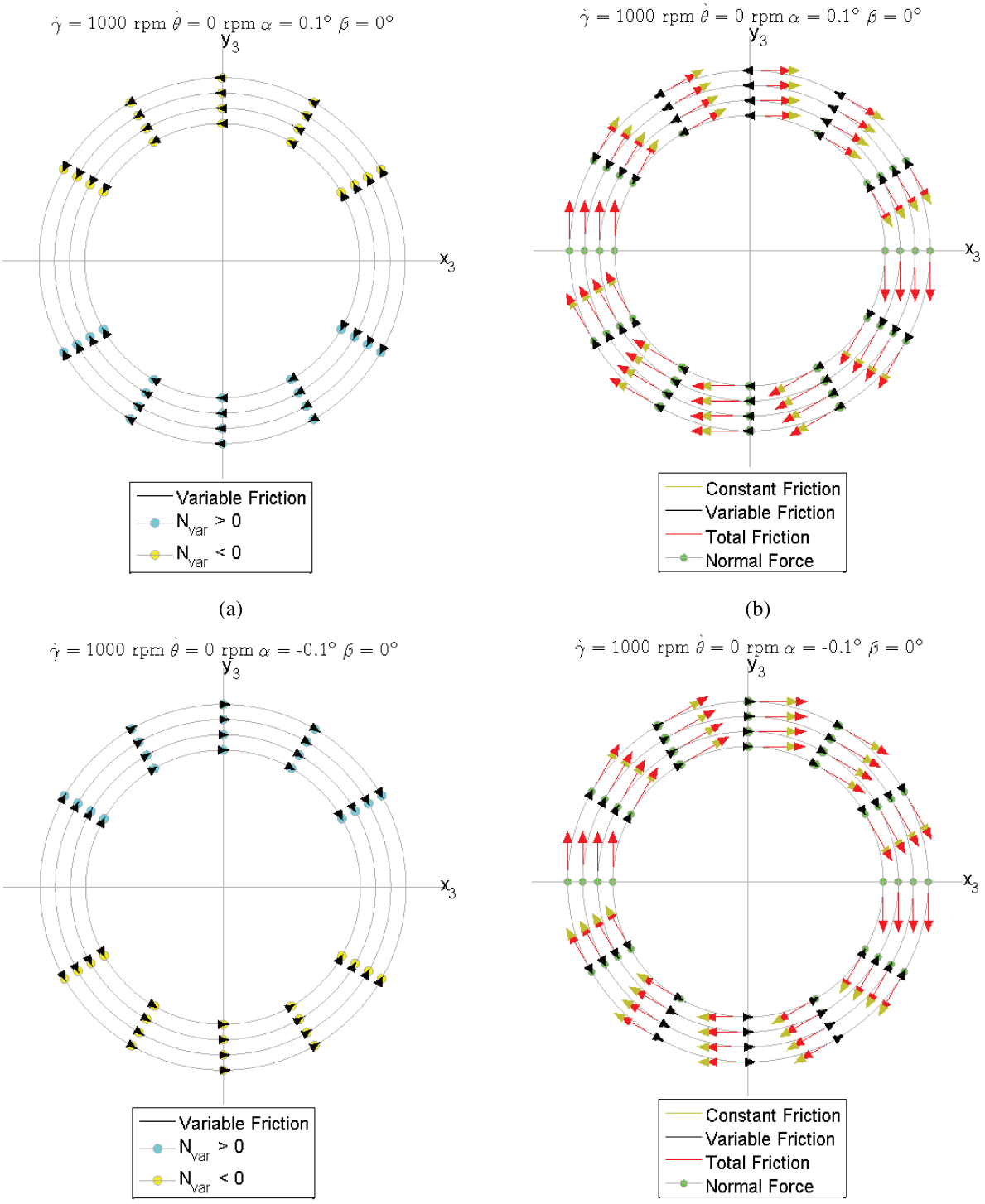

Figure 5.12: Friction forces on the disc for changes on α

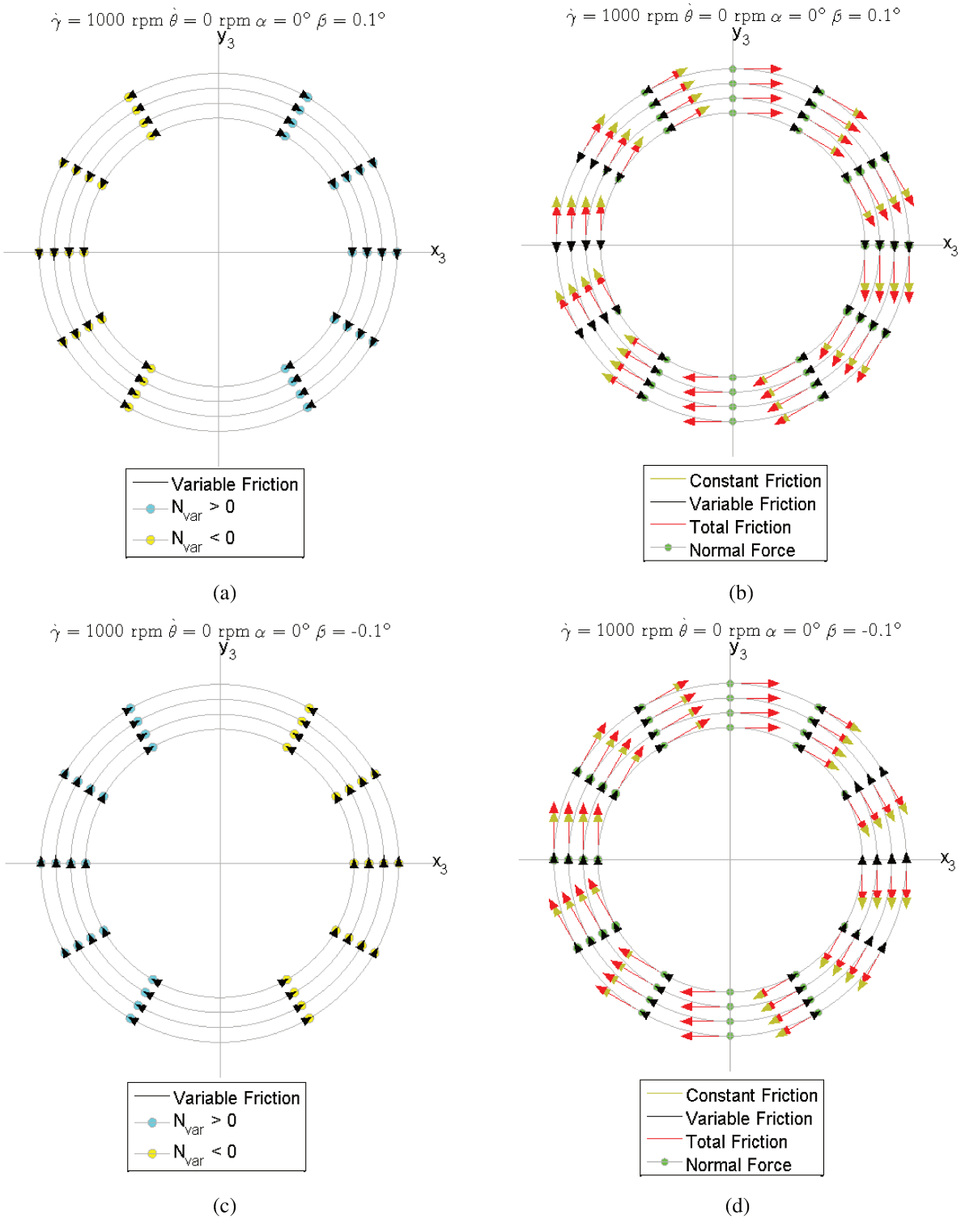

Figure 5.13: Friction forces on the disc for changes on β

5.3 A phenomenological example for a moving viscous damper

This section presents damping efforts that only happen if a *viscous damper element* moves in relation to a surface that changes its profile. Figure 5.14 shows a viscous damper element moving with a constant speed v. One of its extremities, marked as Q, follows a hypothetical infinite track that can be inclined according to the angle δ. The positions q_x and q_y define the position of this element according to the inertial frame positioned at O.

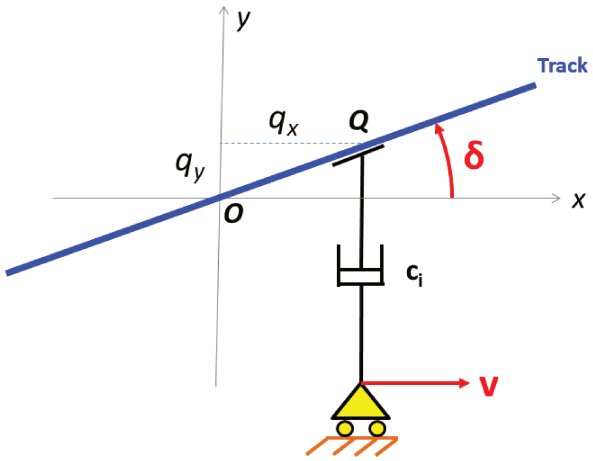

Figure 5.14: Moving viscous element.

The vertical and horizontal position are related by Eq. 5.56:

$$\tan\delta = \frac{q_y}{q_x} \rightarrow q_y = q_x \tan\delta \tag{5.56}$$

Taking the derivative of the vertical position (Eq. 5.56) in relation to time:

$$\begin{aligned} \frac{dq_y}{dt} &= \frac{dq_x}{dt}\tan\delta + q_x\frac{d(\tan\delta)}{dt} \\ &= \frac{dq_x}{dt}\tan\delta + q_x\dot{\delta}\sec^2\delta \\ &= \frac{dq_x}{dt}\tan\delta + q_x\dot{\delta}(1+\tan^2\delta) = v\tan\delta + q_x\dot{\delta}(1+\tan^2\delta) \end{aligned} \tag{5.57}$$

For any instant of time, the damping effort at the point Q is given by Eq. 5.58:

$$\vec{F}_Q = -c_i\left(\frac{dq_y}{dt}\right)\vec{j} \tag{5.58}$$

At $q_x = q_y = 0$ the previous equation can be approximated by Eq. 5.59.

$$\vec{F_Q} = -c_i v \tan\delta\vec{j} \approx -c_i v \delta\vec{j} \tag{5.59}$$

The situation from Eq. 5.59 is represented on Fig. 5.15(a). In this case, *a viscous damper element may produce a vertical effort that depends on the slope of the track (δ) and its moving speed (v)*. The previous example illustrate the case where $q_y = 0$ and $\dot{q}_y \neq 0$.

Figure 5.15(a) also shows that the element apply a negative effort on the track and works *under traction*. If the movement happens on the opposite direction ($v < 0$) (Fig. 5.15(b)), there will be a positive effort on the track, but it would operate *under compression*.

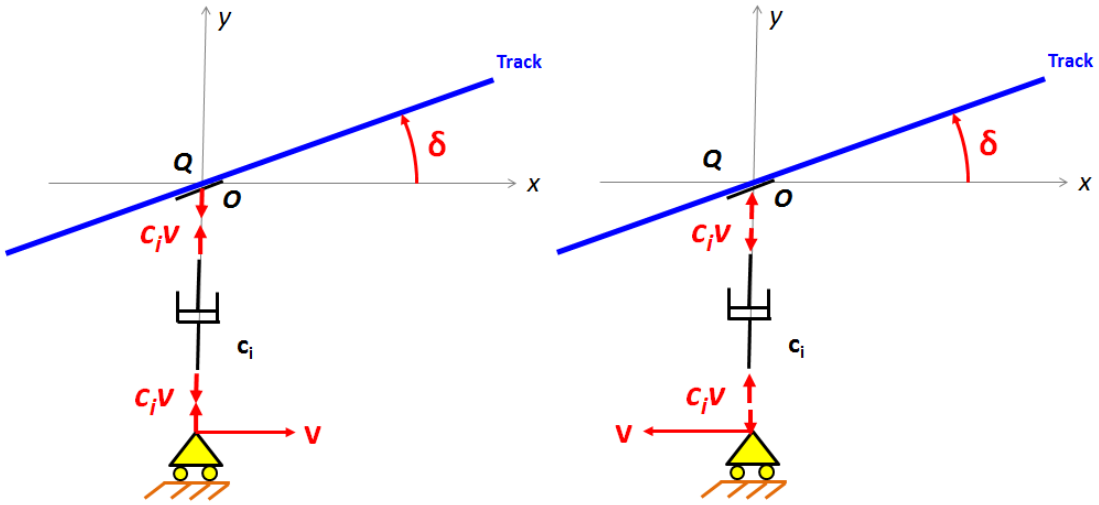

(a) (b)

Figure 5.15: Moving viscous element for $v > 0$ (Fig. 5.15(a)) and $v < 0$ (Fig. 5.15(b)).

5.4 Efforts for a moving viscous damper and their relation with the element matrices

The previous example can be the initial spark for the comprehension of the behaviour of the rotating damper element. But on this case, the track will be substituted by a constant radius track on a wobbling disc. For illustrative purposes, pressure plate is fixed ($\dot{\gamma} = 0$ and $\gamma = 0$) and only the clutch rotates ($\dot{\theta} \neq 0$). Friction is not included on this example ($\mu = 0$).

5.4.1 Damper efforts for $\alpha \neq 0°$ and $\beta = 0°$

Based on the equation for vertical displacement on the contact point Q (Eq. 5.24), the expressions can be simplified for a constant angle α ($\dot{\alpha} = 0$, $\beta = 0°$ and $\dot{\beta} = 0$), resulting in Eqs. 5.60 and 5.61. The damping force is calculated by Eq. 5.62.

$$ {}_0r_{OQ_z} = \sin\alpha R_i \sin\psi_i - h \tag{5.60} $$

$$ {}_0\dot{r}_{OQ_z} = \sin\alpha \left(\dot{\gamma} + \dot{\psi}_i\right) R_i \cos\psi_i = \sin\alpha \left(\dot{\gamma} - \dot{\gamma} + \dot{\theta}\right) R_i \cos\psi_i = \dot{\theta}\sin\alpha R_i \cos\psi_i \tag{5.61} $$

$$ {}_0\vec{F}_{c_i} = -c_i \left[{}_0\dot{r}_{OQ_z}\right] \vec{k} = -c_i\dot{\theta}\sin\alpha R_i \cos\psi_i \vec{k} \tag{5.62} $$

A crucial fact is that, even in case of $\dot{\gamma} \neq 0$, the expression of Eq. 5.61 depends only on the rotating speed of the clutch disc $\dot{\theta}$. It will happen again on Eq. 5.64. It indicates a physical behaviour that will be detailed on Section 5.4.3.

The vertical displacement (Eq. 5.60) and speed (Eq. 5.61) are presented in Fig. 5.16(a). By looking at the shape of ${}_0r_{OQ_z}$, it is possible to stablish analogous behaviour with Figs. 5.15(a) and 5.15(b) remembering that on this case movement occurs in relation to a sinusoidal track. The explanation involves positions named as Q_1, Q_2, Q_3 and Q_4 indicated in Figs. 5.16(a), 5.16(b) and on the realistic system on Fig. 5.17(a).

If the element moves on a region with $x_1 > 0$ ($-270° < \psi_i < 90°$), the situation is analogous to Fig. 5.15(a), and the viscous damper moves on a track with *increasing height*. During this condition there is a negative damping effort (Fig. 5.16(b)) that reaches a peak at point Q_1 ($\psi_i = 0°$), located on the middle of this path.

A transition the previous behaviour occur on Q_2 ($\psi_i = 90°$ on Fig. 5.17(a)) with a *maximum vertical position* (Fig. 5.16(a)), but with *no force* (Fig. 5.16(b)). Then, ${}_0\vec{F}_{c_i}$ changes its direction for positions where $x_1 < 0$ ($90° < \psi_i < -270°$), on a case analogous to Fig. 5.15(b), due to a *decreasing height* in relation to the rotating direction. A maximum damping force happens on Q_3 ($\psi_i = 0°$), but on a different direction compared to Q_2. Another transition happens at Q_4($\psi_i = 270°$), where the track profile changes to an increasing behaviour.

The damping force for the rotating element in different positions is shown in Fig. 5.17(a), adopting $h = 0$ and $\alpha > 0°$. A positive total torque ${}_0\vec{M}_{c_y}$ could happen considering that there was a single damper element in every position of Fig. 5.17(a) . For a situation with $\alpha < 0$ (Fig. 5.17(b)),

this hypothetical torque would be on the opposite direction.

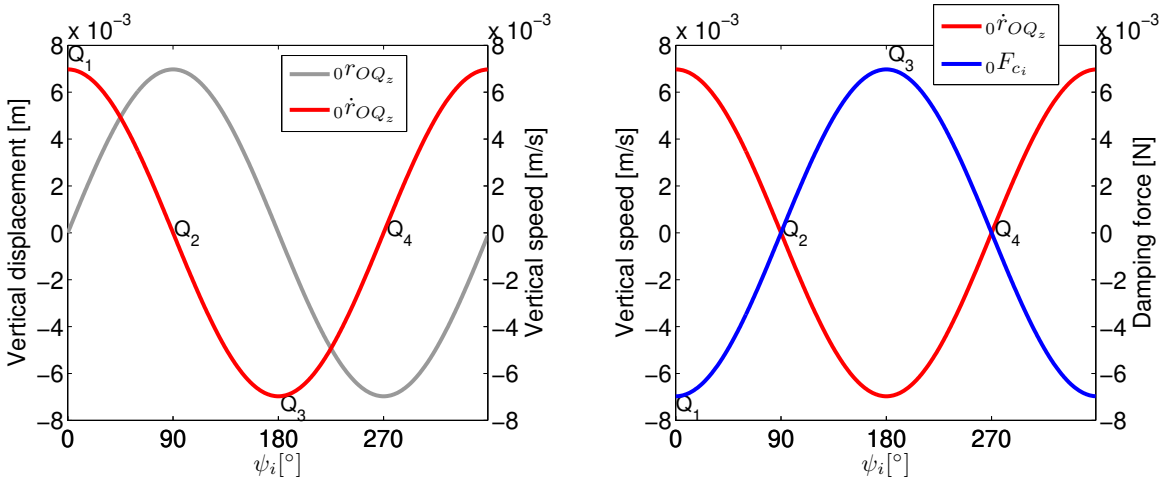

(a) (b)

Figure 5.16: Vertical displacement and speed on Fig. 5.18(a) for $\alpha > 0°$. The damping force appears on Fig. 5.18(b). Data: $R_i = 0.08m$, $c = 1Ns/m$, $\dot{\psi}_i = 1rad/s$ and $\alpha = 5°$.

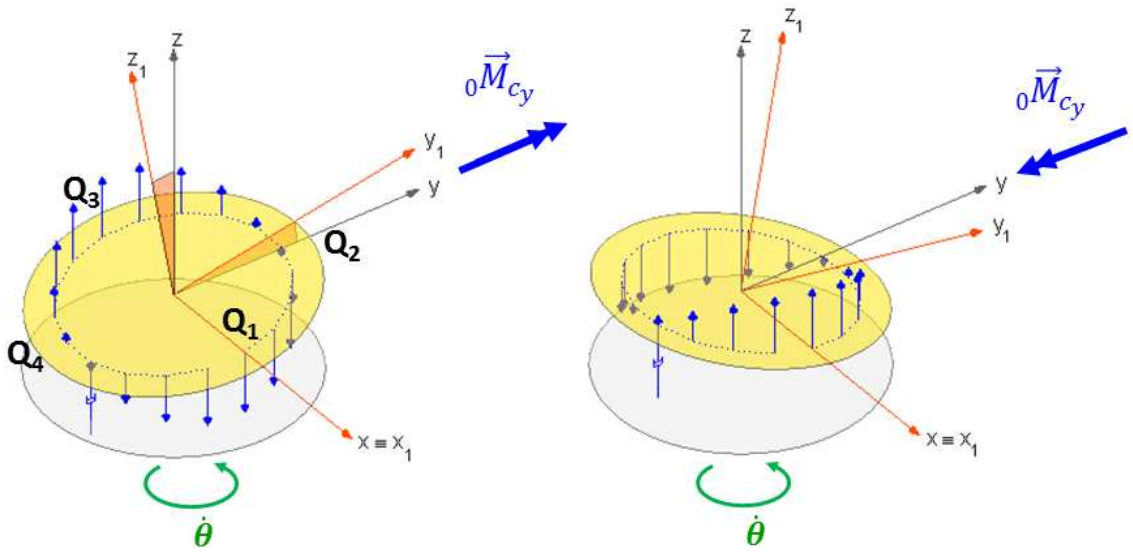

(a) (b)

Figure 5.17: Damping forces in different positions for $\alpha > 0°$ (Fig. 5.17(a)) and $\alpha < 0°$ (Fig. 5.17(b)).

5.4.2 Damper efforts for $\alpha = 0°$ and $\beta \neq 0°$

The following examples will be made under similar assumptions from the previous case but considering on $\alpha = 0°$ on Eqs. 5.24 , resulting on Eq. 5.63 and 5.64. The damping force in this case is calculated by Eq. 5.65.

$$ {}_0r_{OQ_z} = -\sin\beta R_i \cos\psi_i - h \tag{5.63} $$

$$ {}_0\dot{r}_{OQ_z} = \sin\beta\left(\dot{\gamma} + \dot{\psi}_i\right) R_i \sin\psi_i = \sin\beta\left(\dot{\gamma} - \dot{\gamma} + \dot{\theta}\right) R_i \sin\psi_i = \dot{\theta}\sin\beta R_i \sin\psi_i \tag{5.64} $$

$$ {}_0\vec{F}_{c_i} = -c_i\left[{}_0\dot{r}_{OQ_z}\right]\vec{k} = -c_i\dot{\theta}\sin\beta R_i \sin\psi_i\vec{k} \tag{5.65} $$

The approach done for the previous case (Section 5.4.1) was repeated here. Displacements, speeds and damping forces with $\beta = 5°$ are shown in Figs. 5.18(a) and 5.18(b), respectively. In this situation, the region comprehending the points Q_1, Q_2 and Q_3 ($0° < \psi_i < 180°$) presents negative damping forces (Fig. 5.18(b)), with increasing amplitudes. This region is similar to the example from Fig. 5.15(a).

For ($180° < \psi_i < 360°$) the forces are positive, with a maximum value at Q_4. The vertical position is gradually decreased in a similar way to Fig. 5.15(b). Combining the forces on both sides of the plate, paying attention to the directions of forces on points Q_2 and Q_4, it is possible to observe that the hypothetical torque ${}_0\vec{M}_{c_x}$ is *negative* for $\beta > 0°$. Figure 5.19(b) shows that ${}_0\vec{M}_{c_x}$ is *positive* if $\beta < 0°$.

5.4.3 Related element matrices and the damping force for $\dot{\gamma} \neq 0$

Moments due to rotation of the damper element were related to *angular displacements*, so they resulted on the stiffness matrix contribution $[K_{IV}]_i$ on Eq. 5.73. Just like the friction moments, this effect may result on *skew symmetric terms* on the equations of motion. Matrix $[K_V]_i$ (Eq. 5.74) represents friction forces related to the influence of the moving damper on the normal force.

The damping moments for static displacements for α or β were displayed on Figs. 5.17 and 5.19. The conditions can be organized on Table 5.1. The point to discuss here is that displacements on α resulted on moments on y axis with the same signal. Besides that, angular changes on β resulted on ${}_0\vec{M}_{c_x}$ with opposed signal on x axis. Such results remind the Figs. 6.2 and 6.3, where

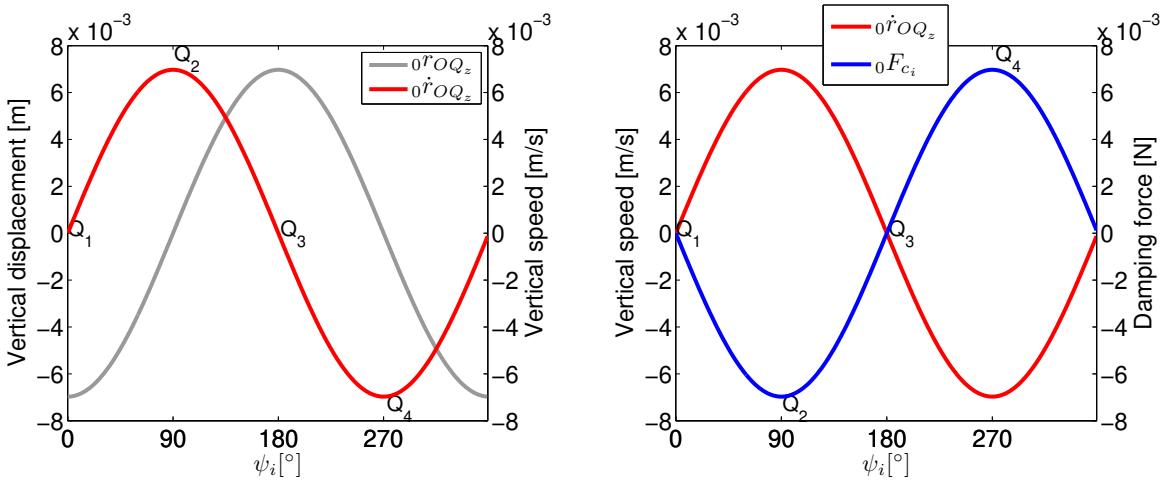

(a) (b)

Figure 5.18: Vertical displacement and speed on Fig. 5.18(a) for $\beta > 0°$. The damping force appears on Fig. 5.18(b). Data: $R_i = 0.08m$, $c = 1Ns/m$, $\dot{\psi}_i = 1rad/s$ and $\beta = 5°$.

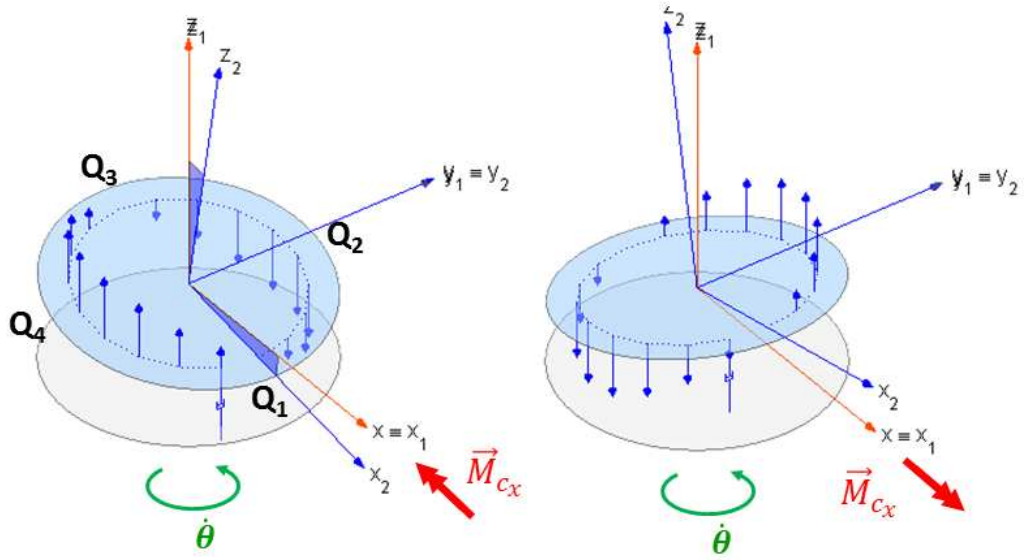

(a) (b)

Figure 5.19: Damping forces in different positions for $\beta > 0°$ (Fig. 5.19(a)) and $\beta < 0°$ (Fig. 5.19(b)).

the friction moments also presented similar characteristics in relation to the angles.

Figure 5.20 illustrates the case of a grounded element, where the height h between the contact point Q and the centre of gravity G remains constant no matter the inclination angle α or rotating speed of the disc ($\dot{\gamma}$). It means that, damping moments similar to the ones presented on Sections

Table 5.1: Damping moments for $\dot{\gamma} = 0$ and $\dot{\theta} \neq 0$ on Cardan coordinates.

Fixed angles	$\alpha = 0°$		$\beta = 0°$	
Static angular displacements	$\beta > 0°$	$\beta < 0°$	$\alpha > 0°$	$\alpha < 0°$
${}_0\vec{M}_{c_x}$	-	+	0	0
${}_0\vec{M}_{c_y}$	0	0	+	-

5.4.1 and 5.4.2 *are not affected* by the *spin speed* of the disc on Cardan coordinates. This is the main reason behind the fact that matrices $[K_{IV}]_i$ (Eq. 5.73) and $[K_V]_i$ (Eq. 5.74) from Section 5.5 depend only on $\dot{\theta}$. The impact of this effect on the system equations and behaviour will be presented at Sections 6.3 and 6.4.

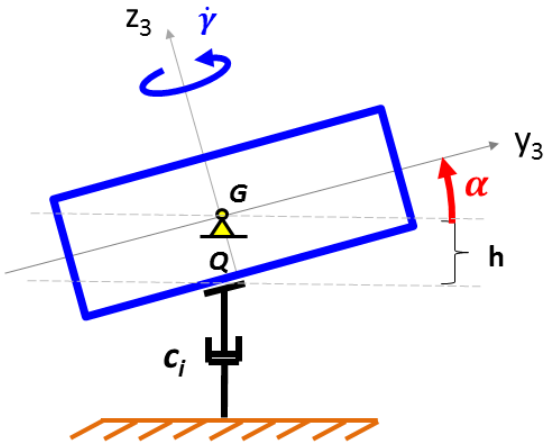

Figure 5.20: Viscous damper fixed on the ground (Fig. 5.20) with the rotating speed on Cardan coordinates.

5.5 Element matrices

The element on Fig. 5.3(b) will influence the system in terms of stiffness , damping and friction terms from the combination of moments from the normal (Eqs. 5.53) and friction (Eq. 5.46) forces in Eq. 5.66:

$$\begin{cases} {}_3M_{x_i} = {}_3M_{N_{i_x}} + {}_3M_{fri_x} \\ {}_3M_{y_i} = {}_3M_{N_{i_x}} + {}_3M_{fri_x} \end{cases} \tag{5.66}$$

The full expression of the angular speeds (Eq. 5.9) and accelerations (Eq. 5.10) are necessary for the equations of motion describing the wobbling movement of the pressure plate (Eq. 5.67),

calculated using the torque contribution of the *ith* element. The expression on the vertical direction is written on the global reference frame. Auxiliary angles derivatives, such as the relative angle ($\dot{\psi}_i$) need to be included.

$$\begin{cases} I_{xx}\,{}_3\dot{\omega}_x - (I_{yy} - I_{zz})\,{}_3\omega_y\,{}_3\omega_z = \sum_{i=1}^{n} {}_3M_{x_i} \\ I_{yy}\,{}_3\dot{\omega}_y - (I_{zz} - I_{xx})\,{}_3\omega_z\,{}_3\omega_x = \sum_{i=1}^{n} {}_3M_{y_i} \\ m\,{}_0\ddot{r}_{OG_z} = \sum_{i=1}^{n} \left({}_0N_{i_z} + {}_0F_{fr_{i_z}}\right) - F_z \\ \dot{\psi}_i = -\left(\dot{\gamma} - \dot{\theta}\cos\alpha\cos\beta\right) \end{cases} \tag{5.67}$$

Linearizing the Eqs. 5.67, a new representation of the system is obtained for $\{p\} = \begin{Bmatrix} \alpha & \beta & z \end{Bmatrix}^T$ (Eq. 5.68). It presents a mass ($[M]$) and gyroscopic ($[G]$) matrices shown in Eqs. 5.11. The contribution of the *ith* element is inserted as an stiffness $[K_i]$ and damping $[C_i]$ matrix. The constant friction forces and moments originate a excitation vector $\{f_i\}$ (Eq. 5.80). The constant axial force for the static displacement is represented by $\{F\} = \begin{Bmatrix} 0 & 0 & -F_z \end{Bmatrix}^T$. This approach is very helpful once that a complex eigenvalue analysis can lead to a verification of the stability of this system.

$$[M]\{\ddot{p}\} + \left([G] + \sum_{i=1}^{n}[C_i]\right)\{\dot{p}\} + \sum_{i=1}^{n}[K_i]\{p\} = \sum_{i=1}^{n}\{f_i\} + \{F\} \tag{5.68}$$

5.5.1 Element stiffness components

The matrices for the rotating speed on Cardan coordinates depend on γ and ψ_i. The relative movement between the pressure plate and spring/damper element generate a stiffness matrix that can be formed from the combination of 6 different matrices (Eq. 5.69), each one having an characteristic feature. In order to simulate a linearized version, it is possible to substitute $N_0 = k_i z_e$ (Section 5.2.2). For all following matrices (Eqs. 5.70, 5.71, 5.72, 5.73, 5.75, 5.77, 5.78, and 5.79) the trigonometric functions are represented by $sg = \sin\gamma$, $cg = \cos\gamma$, $sp = \sin\psi_i$, $cp = \cos\psi_i$ and $s2p = \sin(2\psi_i)$.

$$[K_i] = [K_I]_i + [K_{II}]_i + [K_{III}]_i + [K_{IV}]_i + [K_V]_i + [K_{VI}]_i \tag{5.69}$$

Matrix $[K_I]_i$ (Eq. 5.70) represents the effect of the contact stiffness itself, existing even on

the frictionless case. The normal force containing friction related terms (Eq. 5.48) results *friction stiffness terms* depending on μ^2 in $[K_{II}]_i$ (Eq. 5.71). The difference from von Wagner *et al.* (2007) and Senatore *et al.* (2013) is the absence of the stiffness due to the normal load $N_0 = k_i z_e$, due to the constant radius assumption made on Section 5.2.2.

$$[K_I]_i = k_i \begin{bmatrix} sg.(R_i^2/2).s2p + cg.R_i^2.sp^2 & -cg.(R_i^2/2).s2p + sg.R_i^2.sp^2 & -R_i.sp \\ -sg.R_i^2.cp^2 - cg.(R_i^2/2).s2p & cg.R_i^2.cp^2 - sg.(R_i^2/2).s2p & R_i.cp \\ -sg.R_i.cp - cg.R_i.sp & cg.R_i.cp - sg.R_i.sp & 1 \end{bmatrix} \tag{5.70}$$

$$[K_{II}]_i = \mu^2 h k_i z_e \begin{bmatrix} -sg.(1/2).s2p + cg.cp^2 & cg.(1/2).s2p + sg.cp^2 & 0 \\ -sg.sp^2 + (1/2).cg.s2p & cg.sp^2 + (1/2).sg.s2p & 0 \\ 0 & 0 & 0 \end{bmatrix} \tag{5.71}$$

In undamped systems, friction force is included by matrix $[K_{III}]_i$ (Eq. 5.72). It is influenced by the relative speed between the element and the pressure plate and by the term h, which is half of the height of the plate.

$$[K_{III}]_i = \mu k_i sign(\dot{\gamma} - \dot{\theta}) \begin{bmatrix} h.(-sg.R_i.cp^2 - cg.(R_i/2).s2p) & h.(cg.R_i.cp^2 - sg.(R_i/2).s2p) & h.cp \\ h.(-sg.(R_i/2).s2p - cg.R_i.sp^2) & h.(cg.(R_i/2).s2p - sg.R_i.sp^2) & h.sp \\ 0 & 0 & 0 \end{bmatrix} \tag{5.72}$$

5.5.2 Characteristics for Cardan coordinates

The relative movement assumption (Section 5.2.1) results in frictionless damped systems an influence of $c_i\dot{\theta}$ on a stiffness matrix $[K_{IV}]_i$ (Eq. 5.73). Here is a major difference in relation to the literature (Chapter 3). Damped systems will change their stiffness according to the clutch disc rotating speed $\dot{\theta}$. This additional influence is included in case of friction on $[K_V]_i$ (Eq. 5.74). This is part of the innovation of this work, once that it does not appear on the formulations from von Wagner *et al.* (2007), Fidlin *et al.* (2011) or Senatore *et al.* (2013).

$$[K_{IV}]_i = c_i\dot{\theta} \begin{bmatrix} cg.(R_i^2/2).s2p - sg.R_i^2.sp^2 & sg.(R_i^2/2).s2p + cg.R_i^2.sp^2 & 0 \\ -cg.R_i^2.cp^2 + sg.(R_i^2/2).s2p & -sg.R_i^2.cp^2 - cg.(R_i^2/2).s2p & 0 \\ -cg.R_i.cp + sg.R_i.sp & -sg.R_i.cp - cg.R_i.sp & 0 \end{bmatrix} \tag{5.73}$$

$$[K_V]_i = \mu h c_i \dot{\theta} sign(\dot{\gamma} - \dot{\theta}) \begin{bmatrix} sg.(R_i/2).s2p - cg.R_i.cp^2 & -cg.(R_i/2).s2p - sg.R_i.cp^2 & 0 \\ sg.R_i.sp^2 - cg.(R_i/2).s2p & -cg.R_i.sp^2 - sg.(R_i/2).s2p & 0 \\ 0 & 0 & 0 \end{bmatrix} \tag{5.74}$$

Matrix $[K_{VI}]_i$ contains the effect of the static equilibrium (Eq. 5.75). If the clutch disc is rotating ($\dot{\theta} \neq 0$) this matrix contains circulatory terms that are influenced by the inverse of the relative speed. It is a direct consequence of the approximation on the unitary vector of the tangent relative speed (Eq. 5.42). Similar terms occur on the work from Fidlin *et al.* (2011).

$$[K_{VI}]_i = \frac{\mu h^2 k_i z_e \dot{\theta}}{|\dot{\gamma} - \dot{\theta}|} \begin{bmatrix} -sg & cg & 0 \\ -cg & -sg & 0 \\ 0 & 0 & 0 \end{bmatrix} \tag{5.75}$$

5.5.3 Element damping components

The element damping matrix $[C_i]$ (5.76) is composed by a pure damping matrix $[C_I]_i$ (Eq. 5.77) and a friction related one $[C_{II}]_i$ (Eq. 5.78). The matrix $[C_{III}]_i$ (Eq. 5.79) depends on the inverse o the relative speed $\dot{\gamma} - \dot{\theta}$ and represents the friction damping effect. Similar terms occur on von Wagner *et al.* (2007), Senatore *et al.* (2013) and Fidlin *et al.* (2011).

$$[C_i] = [C_I]_i + [C_{II}]_i + [C_{III}]_i \tag{5.76}$$

$$[C_I]_i = c_i \begin{bmatrix} sg.(R_i^2/2).s2p + cg.R_i^2.sp^2 & -cg.(R_i^2/2).s2p + sg.R_i^2.sp^2 & -R_i.sp \\ -sg.R_i^2.cp^2 - cg.(R_i^2/2).s2p & cg.R_i^2.cp^2 - sg.(R_i^2/2).s2p & R_i.cp \\ -sg.R_i.cp - cg.R_i.sp & cg.R_i.cp - sg.R_i.sp & 1 \end{bmatrix} \tag{5.77}$$

$$[C_{II}]_i = \mu c_i sign(\dot{\gamma} - \dot{\theta}) \begin{bmatrix} h.(-sg.R_i.cp^2 - cg.(R_i/2).s2p) & h.(cg.R_i.cp^2 - sg.(R_i/2).s2p) & h.cp \\ h.(-sg.(R_i/2).s2p - cg.R_i.sp^2) & h.(cg.(R_i/2).s2p - sg.R_i.sp^2) & h.sp \\ 0 & 0 & 0 \end{bmatrix} \tag{5.78}$$

$$[C_{III}]_i = \frac{\mu h^2 k_i z_e}{R_i |\dot{\gamma} - \dot{\theta}|} \begin{bmatrix} cg & sg & 0 \\ -sg & cg & 0 \\ 0 & 0 & 0 \end{bmatrix} \tag{5.79}$$

5.5.4 Excitation vector

The excitation vector $\{f_i\}$ (Eq. 5.80) takes into account terms that depend on $k_i z_e$:

$$\{f_i\} = \begin{Bmatrix} k_i z_e R_i \sin\psi_i - \mu h k_i z_e \cos\psi_i sign(\dot{\gamma} - \dot{\theta}) \\ -k_i z_e R_i \cos\psi_i - \mu h k_i z_e \sin\psi_i sign(\dot{\gamma} - \dot{\theta}) \\ -k_i z_e \end{Bmatrix} \tag{5.80}$$

5.5.5 Very important remarks on the stability study of this system

It is important to stablish here that the system presented on Eq. 5.68 which uses the element matrices is a linear time-varying system. The relative position angle ψ_i and the pressure plate rotation γ will result on changes on the inner structure of every element matrix. Future works will involve the application of the Floquet Theory (Nayfeh and Balachandran (2008), Bittanti and Colaneri (2008)) to fully determine its stability regions. By now, this thesis will analyse the eigenvalues of the linear system, assuming ψ_i and γ as instantaneous angles.

6 Hipothesis 1: Wobbling modes and characteristics of systems with equal and symmetrically distributed elements

This chapter is intended to be the point of introduction for the wobbling movements of the pressure plate under the assumption of Cardan coordinates. Fidlin (2006) provided an explanation for the excitation of the phenomena in terms of frictional moments. Here, the distinction made on Section 5.2.8 between constant/variable friction will be used to show how their moments may excite the pressure plate on Sections 6.1.1 and 6.1.2.

The influence of the rotating speed, cushion stiffness, relative speed and viscous damping will be gradually added to the system. It will provide the comprehension of the importance of each matrix deduced in Section 5.5. The properties of systems with equal and symmetrically distributed elements will serve as basis for the differences found with more complex cushion configurations describe on Chapter 9 in case of positioning errors.

6.1 Rotating speed influence

Figure 6.1 shows a model of a pressure plate supported by four spring elements. If the element are equal,the frictional moments, indicated by the pairs $\vec{M}_{fr_{cons_{x1}}}$,$\vec{M}_{fr_{cons_{x2}}}$, $\vec{M}_{fr_{cons_{y1}}}$ and $\vec{M}_{fr_{cons_{y2}}}$ cancel each other.

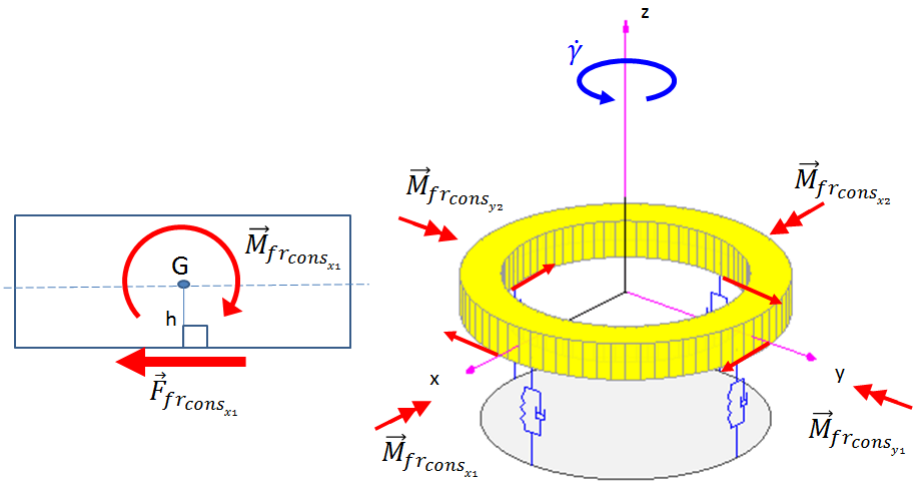

Figure 6.1: Constant moments under uniform normal load distribution.

For equally spaced elements ($\psi_{i0} = 0°$, $90°$, $180°$ and $270°$) and imposing $\gamma = 0$, wobbling can be studied apart from the axial motion, as expressed in Eq. 6.1. It results from the contribution of matrices $[K_I]_i$ (Eq. 5.70), $[K_{II}]_i$ (Eq. 5.71) and $[K_{III}]_i$ (Eq. 5.72). Here, each component have the same stiffness (k), radial position R and friction coefficient μ . The friction damping terms from Eq. 5.79 will be neglected at this point, with the consideration that the relative speed field remains always tangent to the disc, in permanent slip and far from the coupling condition (Appendix A.1). The gyroscopic matrix in this situation depends only on I_{zz}.

$$\begin{bmatrix} I_{xx} & 0 & 0 \\ 0 & I_{yy} & 0 \\ 0 & 0 & m \end{bmatrix} \begin{Bmatrix} \ddot{\alpha} \\ \ddot{\beta} \\ \ddot{z} \end{Bmatrix} + \dot{\gamma} \begin{bmatrix} 0 & I_{zz} & 0 \\ -I_{zz} & 0 & 0 \\ 0 & 0 & 0 \end{bmatrix} \begin{Bmatrix} \dot{\alpha} \\ \dot{\beta} \\ \dot{z} \end{Bmatrix} + \\ + k \begin{bmatrix} 2R^2 + 2\mu^2 z_e h & 2\mu R h sign(\dot{\gamma}) & 0 \\ -2\mu R h sign(\dot{\gamma}) & 2R^2 + 2\mu^2 z_e h & 0 \\ 0 & 0 & 4 \end{bmatrix} \begin{Bmatrix} \alpha \\ \beta \\ z \end{Bmatrix} = \begin{Bmatrix} 0 \\ 0 \\ 0 \end{Bmatrix} \tag{6.1}$$

The variable friction forces (explained on Section 5.2.8) are introduced inside the equations of motion as skew symmetric terms. They express its interaction with the wobbling angles. The comprehension of how they are interact with the pressure plate to result in Eq. 6.1 is given by the analysis of the displacement on each angle separately. On the following examples, the disc rotating speed is assumed as $\dot{\gamma} > 0$.

Positive α causes an inversion of $\vec{F}_{fr_{var}}$ on the element positioned at $\psi_0 = 90°$ due to the decrease on the normal force (Fig. 6.2(a)). As a result, both forces induce a positive friction moment on the disc on y_3 (Eq. 6.2).

$$\left. \begin{Bmatrix} M_{fr_{varx}} \\ M_{fr_{vary}} \end{Bmatrix} \right|_{\alpha \neq 0, \beta = 0} = \begin{Bmatrix} 0 \\ 2\mu R h sign(\dot{\gamma}) \alpha \end{Bmatrix} \tag{6.2}$$

In a similar way of thinking, Figure 6.2(b) shows that a negative rotation in α results in friction forces producing negative moment on y_3 axis.

For $\beta > 0$ there is an inversion on the variable friction force on $\psi_0 = 180°$ (Fig. 6.3(a)). Consequently, *negative friction torque* is applied on x_3 axis (Eq. 6.3).

$$\left. \begin{Bmatrix} M_{fr_{varx}} \\ M_{fr_{vary}} \end{Bmatrix} \right|_{\alpha = 0, \beta \neq 0} = \begin{Bmatrix} -2\mu R h sign(\dot{\gamma}) \beta \\ 0 \end{Bmatrix} \tag{6.3}$$

Figure 6.3(b) represents that $\beta < 0$ results in friction forces producing *positive torque* on x_3 axis.

It is important to emphasize here that, in al cases (Figs. 6.2(a), 6.2(b), 6.3(a) and 6.3(b)) the constant friction moments cancel each other just like the case described in Fig. 6.1.

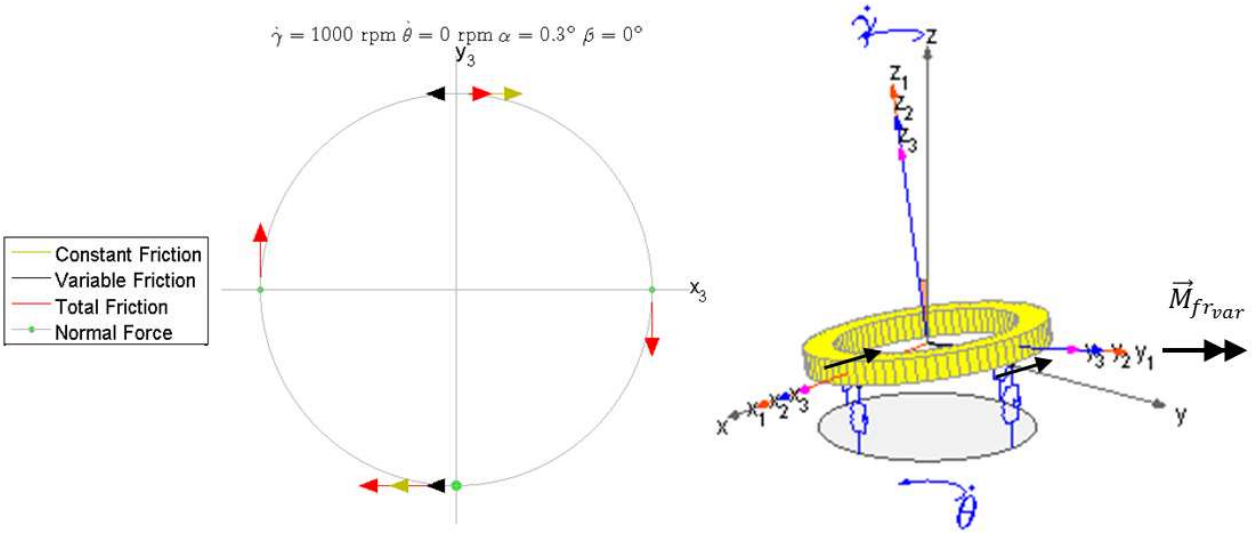

(a)

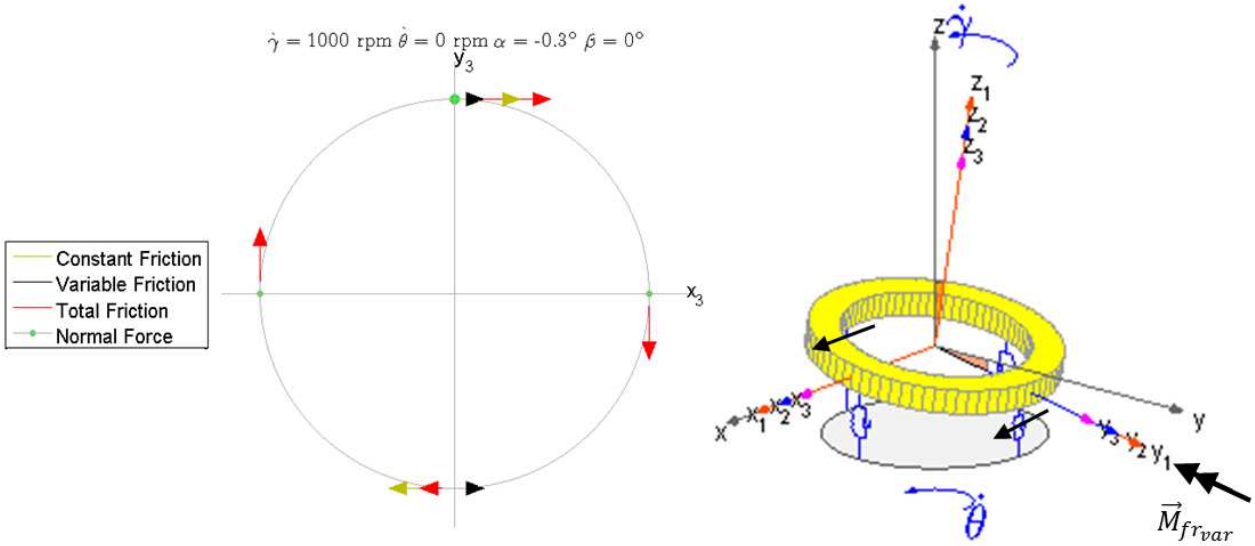

(b)

Figure 6.2: Variable friction force distribution for $\alpha > 0$ and $\alpha < 0$ ($\dot{\gamma} > 0$ and $\dot{\theta} = 0$).

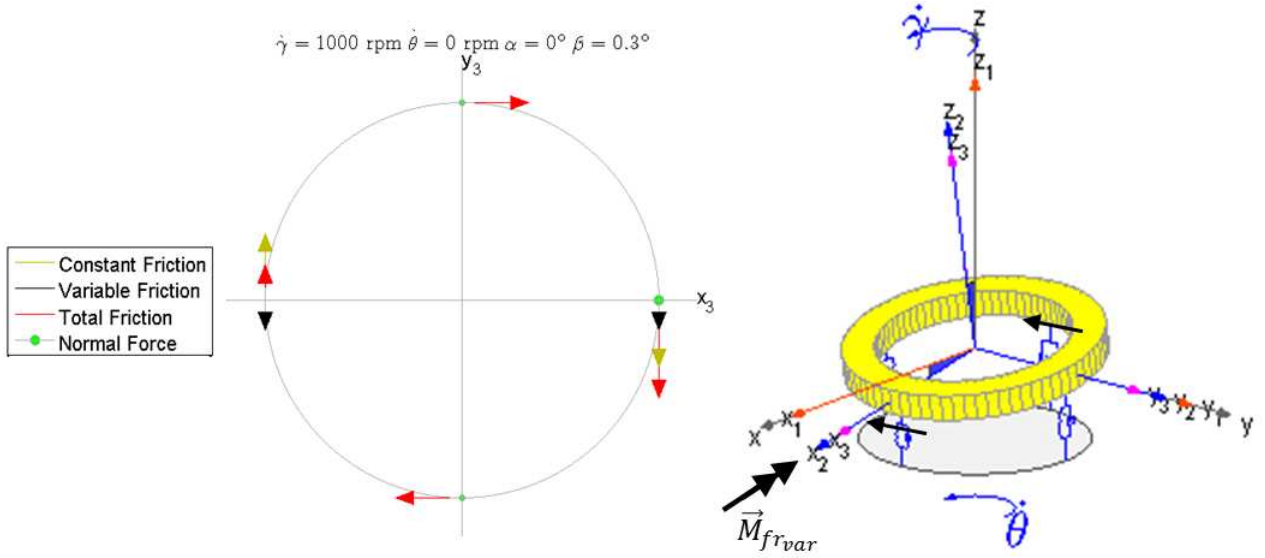

(a)

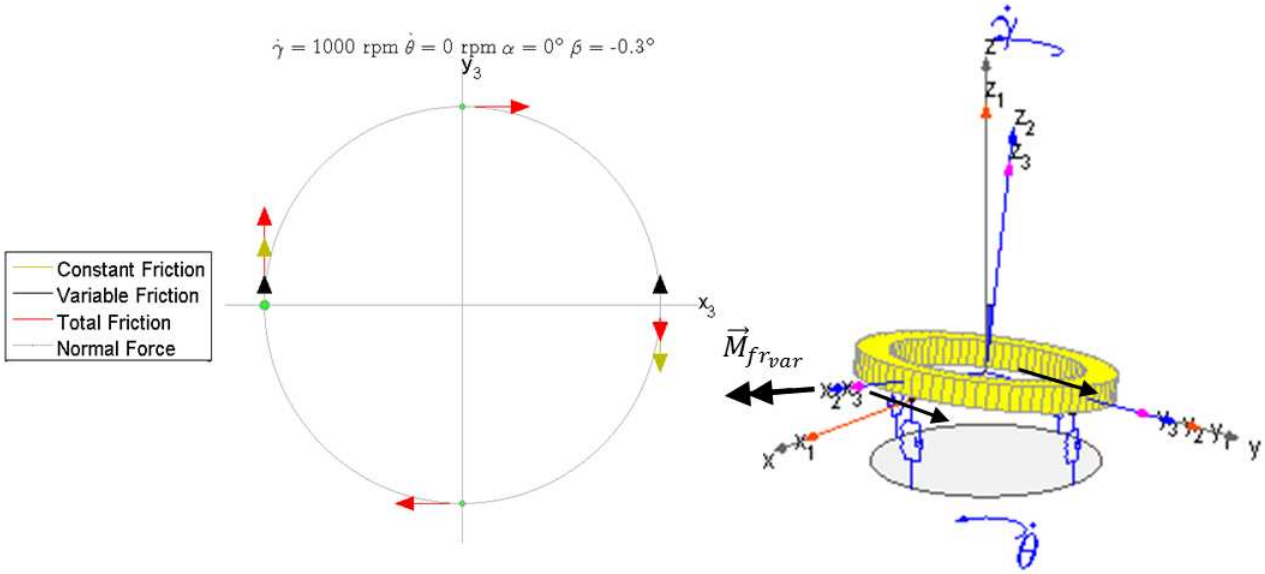

(b)

Figure 6.3: Variable friction force distribution for $\beta > 0$ and $\beta < 0$ ($\dot{\gamma} > 0$ and $\dot{\theta} = 0$).

Figure 6.4(a) contains the variation of the modal properties for different rotating speeds adopting m = 2 kg, R = 0.0875 m, z_e = 0.001m, μ = 0.3 and h = 0.01 m. A total stiffness of 3×10^6 N/m is distributed on the 4 spring elements. Both frequencies present similar values for very low rotating speed (185 Hz for a $|\dot{\gamma}| = 1$ rpm). As speed is augmented, the natural frequency related to the unstable mode increases up to 220.9 Hz at $|\dot{\gamma}| = 2000$ rpm. On the other hand, the stable mode presents a natural frequency of 154.8 Hz at $|\dot{\gamma}| = 2000$ rpm.

The increasing rate of the natural frequency of the unstable mode was found to be 0.019 Hz/rpm at 2000 rpm (Fig. 6.4(b)). For the stable mode, this derivative was calculated as -0.013 Hz/rpm at 2000 rpm. These results will be important later on Section 8.1. Figure 6.4(c) shows the real part of the eigenvalues, emphasizing that instability occurs due to a positive real part found near 20.

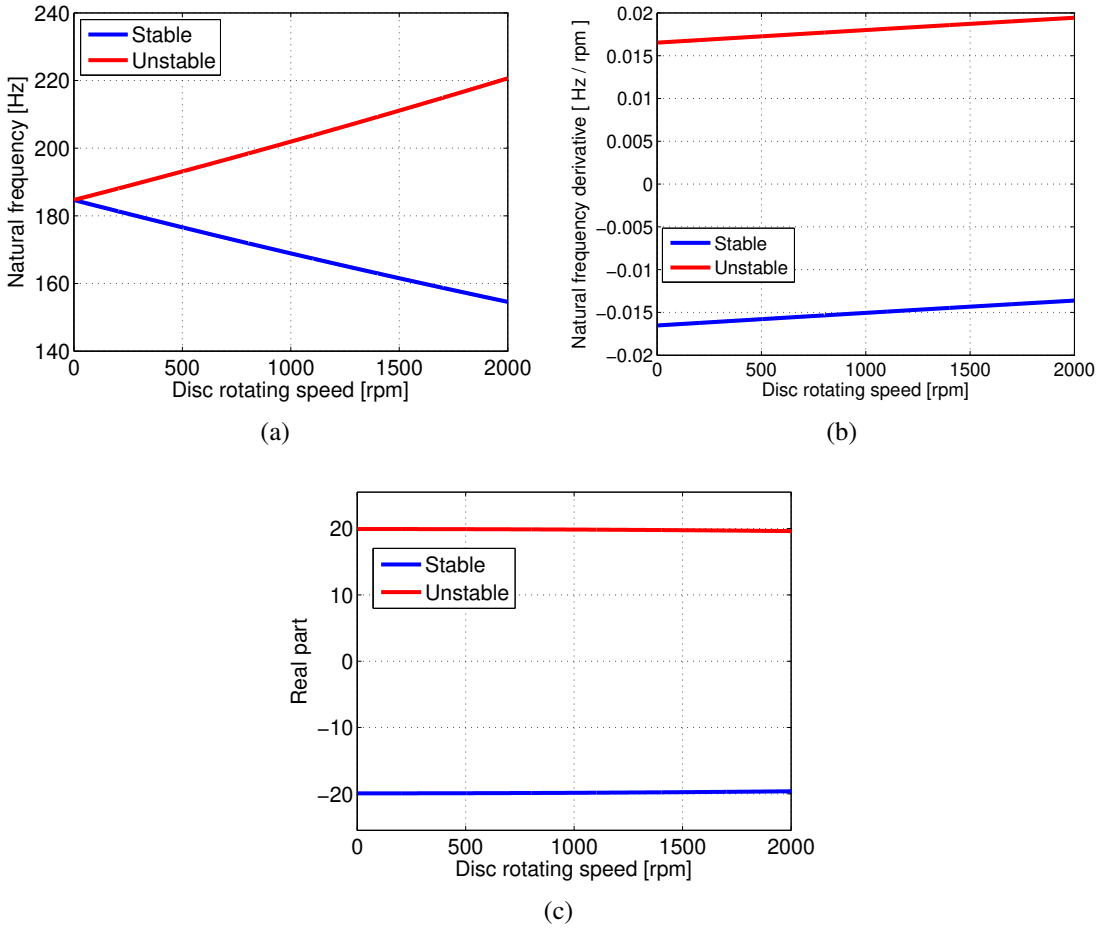

Figure 6.4: Natural frequencies of the system in Eq. 6.1.

The free response of the system is calculated by the combination of its modes as shown in Eq. 6.4. Variables d_i and d_i^* form complex conjugate pairs of numbers that account for the contribution of each vibration mode.

$$\begin{Bmatrix} \alpha(t) \\ \beta(t) \end{Bmatrix} = d_1 \begin{Bmatrix} X_{11} \\ X_{21} \end{Bmatrix} e^{\lambda_1 t} + d_1^* \begin{Bmatrix} X_{11} \\ X_{21} \end{Bmatrix}^* e^{\lambda_1^* t} + d_2 \begin{Bmatrix} X_{21} \\ X_{22} \end{Bmatrix} e^{\lambda_2 t} + d_2^* \begin{Bmatrix} X_{21} \\ X_{22} \end{Bmatrix}^* e^{\lambda_2^* t} \tag{6.4}$$

A specific mode response is shown in Eq. 6.5, by setting to zero the contributions $d_i\ d_i^*$ of other modes. It is necessary to manipulate the real ($\mathrm{Re}(\{X_i\})$) and imaginary part ($\mathrm{Im}(\{X_i\})$) of the eigenvector as well as the complex components of d_i. The eigenvalue is written as $\lambda_i = \sigma_i + j\varpi_i$:

$$\begin{aligned}\{x(t)\} &= d_i\,\{X_i\}\,e^{\lambda_i t} + d_i^*\,\{X_i^*\}\,e^{\lambda_i^* t} \\ &= [\mathrm{Re}(d_i) + j\,\mathrm{Im}(d_i)]\,[\mathrm{Re}(\{X_i\}) + j\,\mathrm{Im}(\{X_i\})]\,e^{(\sigma_i + j\varpi_i)t} + \\ &+ [\mathrm{Re}(d_i) - j\,\mathrm{Im}(d_i)]\,[\mathrm{Re}(\{X_i\}) - j\,\mathrm{Im}(\{X_i\})]\,e^{(\sigma_i - j\varpi_i)t} \\ &= 2e^{\sigma_i t}\,\{[\mathrm{Re}(d_i)\,\mathrm{Re}(\{X_i\}) - \mathrm{Im}(d_i)\,\mathrm{Im}(\{X_i\})]\cos\varpi_i t + \\ &- [\mathrm{Re}(d_i)\,\mathrm{Im}(\{X_i\}) + \mathrm{Im}(d_i)\,\mathrm{Re}(\{X_i\})]\sin\varpi_i t\}\end{aligned} \tag{6.5}$$

6.1.1 Stable motion - Backward wobbling for $\dot{\gamma} > 0$ and $\dot{\theta} = 0$

Complex eigenvectors where obtained for different rotating speeds. The results were represented based on the eigenvector associated to eigenvalues with positive imaginary part ($\lambda_i = \sigma_i + j\varpi_i$).

With $\dot{\gamma} > 0$, there is $X_{21} = j$ (Fig. 6.5(b)), while $X_{11} = 1$ in all situations (Figs. 6.5(a)). It means that on the stable mode shape β presents a phase shift of 90° in relation to α (Eq. 6.6).

$$\begin{Bmatrix} X_{11} \\ X_{21} \end{Bmatrix} = \begin{Bmatrix} 1 \\ j \end{Bmatrix} = \begin{Bmatrix} 1 \\ \exp\left(j\dfrac{\pi}{2}\right) \end{Bmatrix}, \text{ for } \dot{\gamma} > 0 \tag{6.6}$$

Substituting Eq. 6.6 on Eq. 6.5 it is possible to obtain the free response of the stable mode in Eq. 6.7. By choosing $\mathrm{Re}(d_i) = 0$ the expression is simplified to Eq. 6.8. Equation 6.9 represents the angular wobbling speeds calculated from the differentiation of Eq. 6.8.

$$\begin{aligned}\begin{Bmatrix} \alpha(t) \\ \beta(t) \end{Bmatrix} = 2e^{\sigma_i t} \Bigg\{ &\left[\mathrm{Re}(d_1) \begin{Bmatrix} 1 \\ 0 \end{Bmatrix} - \mathrm{Im}(d_1) \begin{Bmatrix} 0 \\ 1 \end{Bmatrix}\right] \cos\varpi_i t + \\ &- \left[\mathrm{Re}(d_1) \begin{Bmatrix} 0 \\ 1 \end{Bmatrix} + \mathrm{Im}(d_1) \begin{Bmatrix} 1 \\ 0 \end{Bmatrix}\right] \sin\varpi_i t \Bigg\}\end{aligned} \tag{6.7}$$

$$\begin{Bmatrix} \alpha(t) \\ \beta(t) \end{Bmatrix} = -2e^{\sigma_i t}\,\mathrm{Im}(d_1) \begin{Bmatrix} \sin\varpi_i t \\ \sin(\varpi_i t + 90°) \end{Bmatrix} \tag{6.8}$$

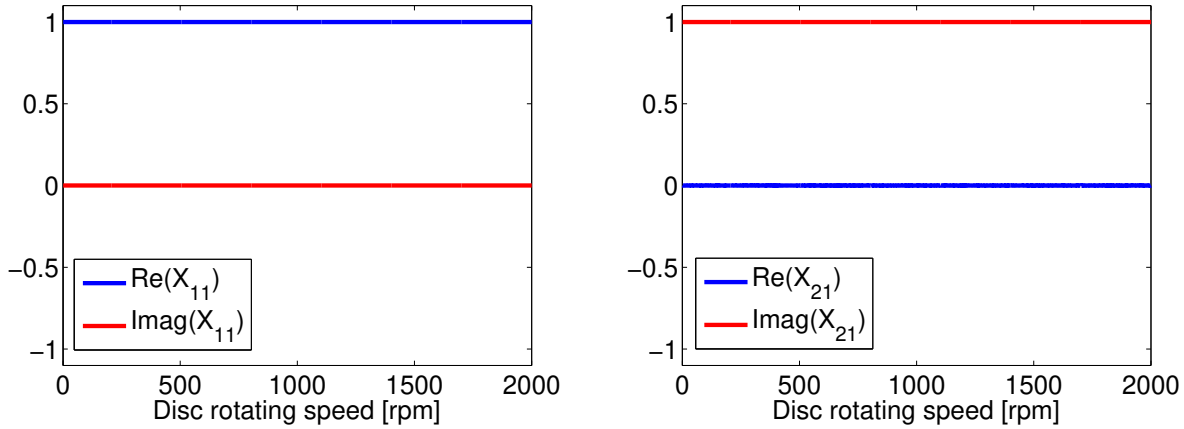

(a) Mode element X_{11} (b) Mode element X_{21}

Figure 6.5: Complex stable mode shape for $\dot{\gamma} > 0$ and $\dot{\theta} = 0$. Eigenvalue with positive imaginary part ($\lambda_i = \sigma_i + j\varpi_i$).

$$\begin{Bmatrix} \dot{\alpha}(t) \\ \dot{\beta}(t) \end{Bmatrix} = 2e^{\sigma_i t}\,\mathrm{Im}(d_1)\left[-\sigma_i \begin{Bmatrix} \sin\varpi_i t \\ \cos\varpi_i t \end{Bmatrix} + \varpi_i \begin{Bmatrix} -\cos\varpi_i t \\ \sin\varpi_i t \end{Bmatrix}\right] \tag{6.9}$$

Decaying responses of the system in terms of displacement and speed are shown in Figs. 6.6(a) and 6.6(b), respectively, for a natural frequency of 169.2 Hz.

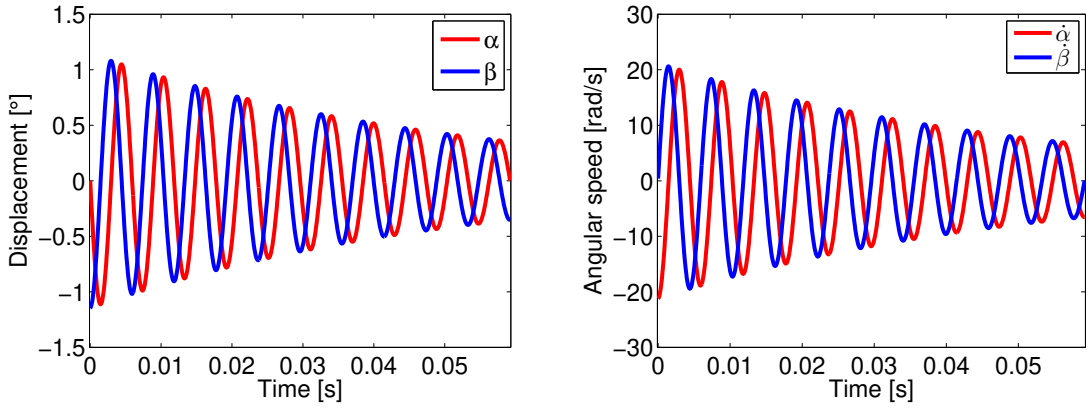

(a) (b)

Figure 6.6: Displacement free response after 10 complete periods (Fig. 6.6(a)) and angular speeds (Fig. 6.6(b)) for $d_i = 0.01j$, $\dot{\gamma} = 1000$ rpm and $\dot{\theta} = 0$.

Besides the mathematical notation previously presented in Eq. 6.6, it is necessary to give a

physical explanation for the stability of this mode shape. Combining the variable friction established in Eqs. 6.2 and 6.3 the system is excited by the friction related torque provided by Eq. 6.10. This moment can be normalized if it is divided by $2\mu Rh$. The result can be explicitly written in Eq. 6.11 by substituting the expression of displacements (Eq. 6.8).

$$\begin{Bmatrix} M_{fr_{varx}} \\ M_{fr_{vary}} \end{Bmatrix} = 2\mu Rh sign(\dot{\gamma}) \begin{Bmatrix} -\beta(t) \\ \alpha(t) \end{Bmatrix} \tag{6.10}$$

$$\begin{Bmatrix} M_{fr_{varx}} \\ M_{fr_{vary}} \end{Bmatrix}_{normalized} = \begin{Bmatrix} -\beta(t) \\ \alpha(t) \end{Bmatrix} = 2e^{\sigma_i t}\,\mathrm{Im}(d_1) \begin{Bmatrix} \cos\varpi_i t \\ -\sin\varpi_i t \end{Bmatrix} \tag{6.11}$$

Figure 6.7(a) presents the angular speed $\dot{\alpha}$ with $M_{fr_{varx}}$, while Fig. 6.7(b) shows the relation in time between $\dot{\beta}$ and $M_{fr_{vary}}$. It is possible to see that the friction moments are always opposed to the motion of the disc. The variable component of the friction force introduced in Section 5.2.8 expresses the role of friction on this system. It is the reason why amplitudes decrease with time.

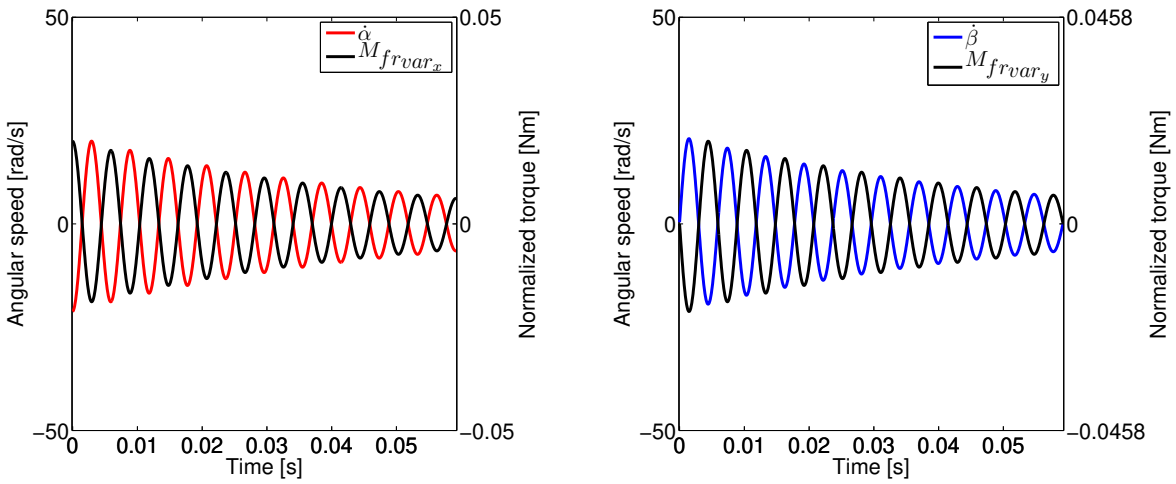

(a) (b)

Figure 6.7: Angular speeds and variable friction in x and y directions (Figs. 6.7(a) and 6.7(b)) for $d_i = 0.01j$, $\dot{\gamma} = 1000$ rpm and $\dot{\theta} = 0$.

One period of motion is depicted in terms of angular displacements and friction forces in Figs. 6.8(a) and 6.8(b), respectively. They are totally related once that every instant labelled as *a, b, c,... i* is represented as wobbling condition of the pressure plate in Fig. 6.9. For a observer situated on the global reference frame xyz, the axis z_3 *seem to move against* the direction given by the rotating speed $\dot{\gamma}$ as presented in Figs. 6.9(a), 6.9(c), 6.9(e) , 6.9(g) and 6.9(i). In analogy to the

field of rotordyamics (Muszynska (2010), Childs (1993) and Genta (2007)), this pattern could be interpreted as a *backward wobbling*. The friction force distribution in these cases was presented in detail in Figs. 6.2 and 6.3 once that only one friction moment component is acting on the system.

Intermediary states are presented by Figs. 6.9(b), 6.9(d), 6.9(f) and 6.9(h) where the friction forces configurations are represented right bellow each one of them. As it is possible to visualize in Figs. 6.8(a) and 6.8(b), these are conditions where both $M_{fr_{varx}}$ and $M_{fr_{vary}}$ are acting on the disc simultaneously.

From Fig. 6.9(a) to 6.9(c) the disc moves from $\alpha = 0°$ to $\alpha < 0$ and from $\beta < 0$ to $\beta = 0$. Meanwhile, Fig. 6.9(b) shows that the variable friction forces generate moments such that $M_{fr_{var_x}} > 0$ and $M_{fr_{var_y}} < 0$. In sequence, the disc changes its position from Fig. 6.9(c) to another state where $\alpha = 0$ and $\beta > 0$. During this process, Figure 6.9(d) presents $M_{fr_{var_x}} < 0$ and $M_{fr_{var_y}} < 0$.

Between Fig. 6.9(e) to 6.9(g) the disc moves from $\alpha = 0$ to $\alpha > 0$ and from $\beta > 0$ to $\beta = 0$, while the friction moments are oriented as $M_{fr_{var_x}} < 0$ and $M_{fr_{var_y}} > 0$. Finally, the disc returns to its initial position from Fig. 6.9(e) to 6.9(i). The coordinate α decreases from $\alpha > 0$ to $\alpha = 0$ while $M_{fr_{var_x}}$ is positive (Fig. 6.9(d)). Angle β becomes negative while $M_{fr_{var_y}}$ is positive. During the whole period, the variable friction forces always produced torque in opposition to the movement.

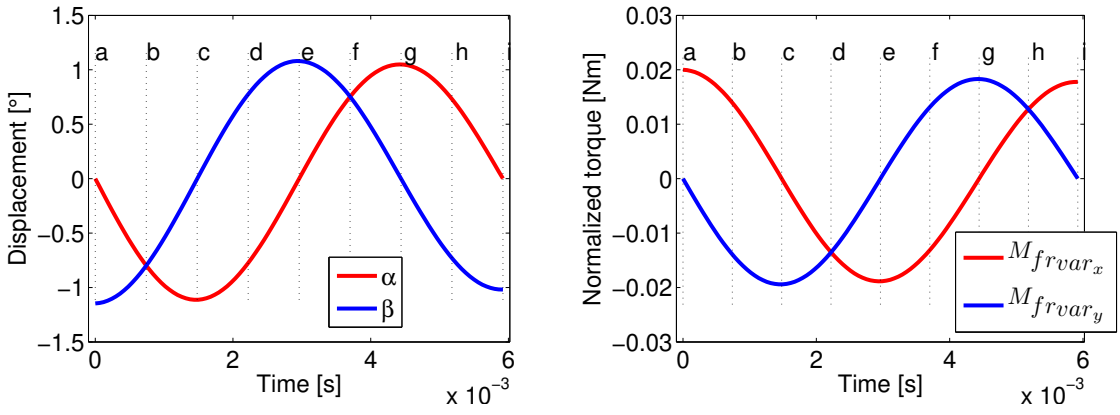

(a) (b)

Figure 6.8: Stable free response viewed in detail in Fig. 6.8(a) and normalized moments (Fig. 6.8(b)) ($d_i = 0.01j$, $\dot{\gamma} = 1000$ rpm and $\dot{\theta} = 0$).

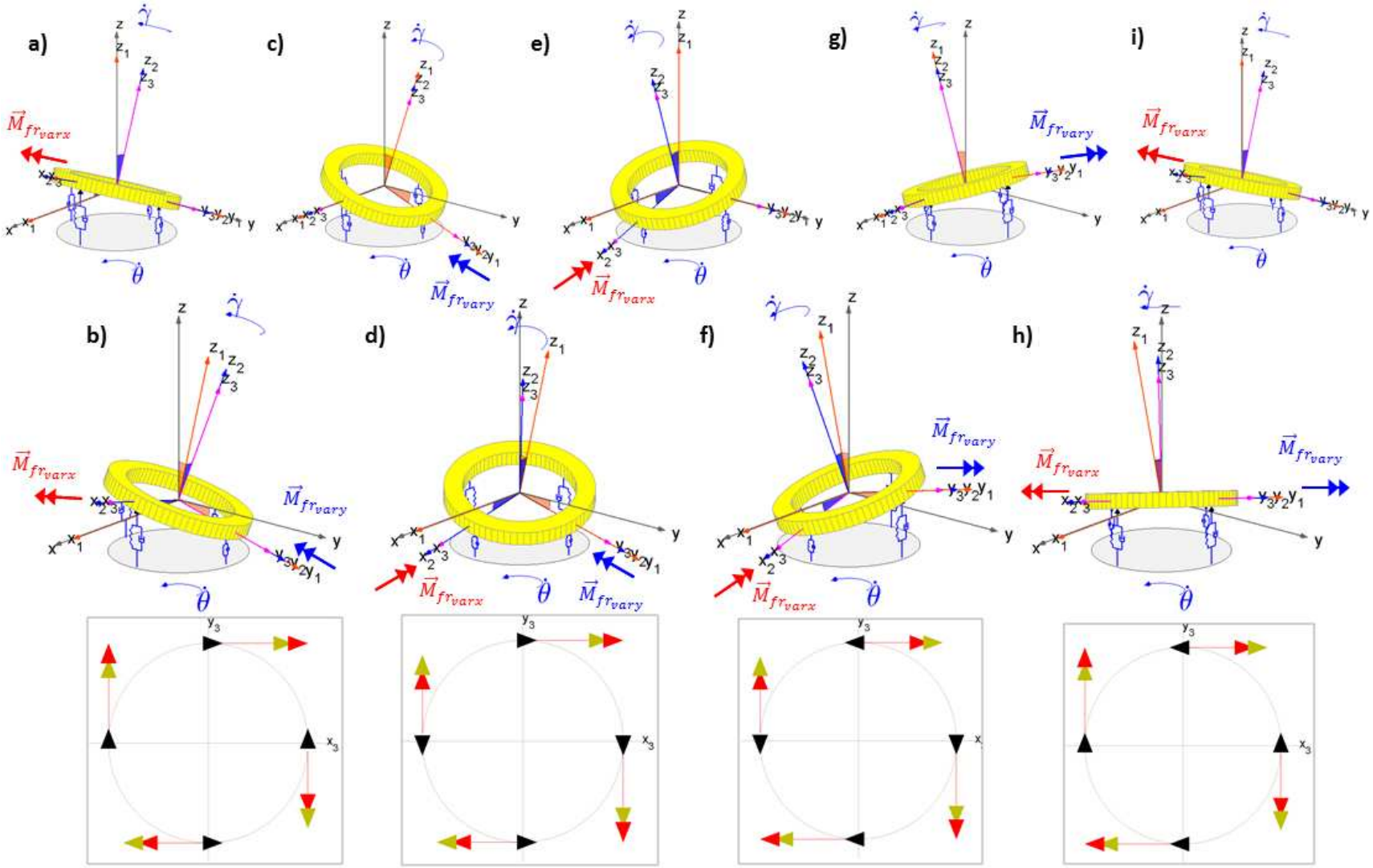

Figure 6.9: Stable mode for $\dot{\gamma} > 0$ and $\dot{\theta} = 0$ (Backward wobbling).

6.1.2 Unstable motion - Forward wobbling with $\dot{\gamma} > 0$ and $\dot{\theta} = 0$

Looking on Figs. 6.10(a) and 6.10(b) it is possible to see that the unstable mode is expressed by Eq. 6.12, where β presents a phase shift of -90° in relation to α.

$$\begin{Bmatrix} X_{12} \\ X_{22} \end{Bmatrix} = \begin{Bmatrix} 1 \\ -j \end{Bmatrix} = \begin{Bmatrix} 1 \\ \exp\left(-j\frac{\pi}{2}\right) \end{Bmatrix}, \text{ for } \dot{\gamma} > 0 \tag{6.12}$$

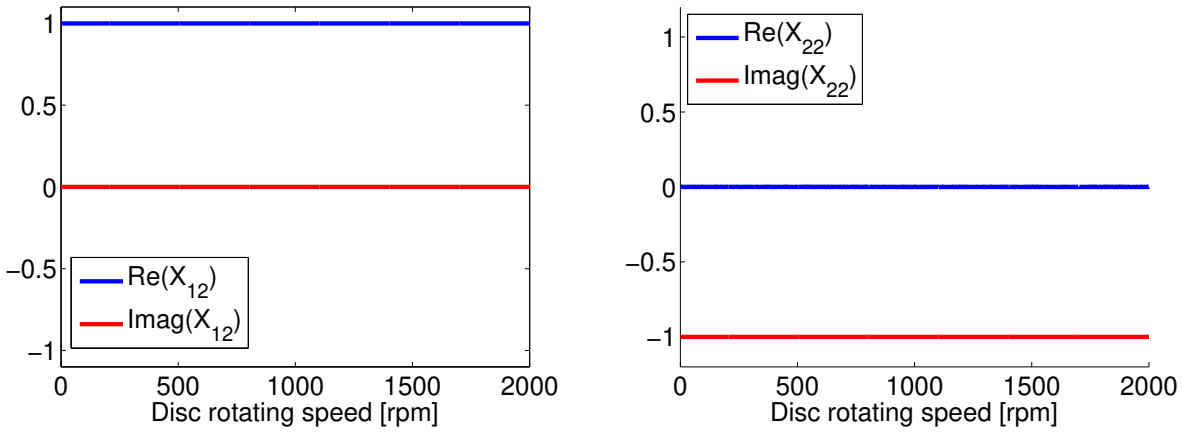

(a) Mode element X_{12} (b) Mode element X_{22}

Figure 6.10: Complex unstable mode shape for $\dot{\gamma} > 0$ and $\dot{\theta} = 0$. Eigenvalue with positive imaginary part ($\lambda_i = \sigma_i + j\varpi_i$).

Substituting Eq. 6.12 on 6.5 the free response of the unstable mode is calculated (Eq. 6.13). This expression is simplified to Eq. 6.14 using $\mathrm{Re}(d_i) = 0$.

$$\begin{aligned} \begin{Bmatrix} \alpha(t) \\ \beta(t) \end{Bmatrix} = 2e^{\sigma_i t} \Bigg\{ \left[\mathrm{Re}(d_2) \begin{Bmatrix} 1 \\ 0 \end{Bmatrix} + \mathrm{Im}(d_2) \begin{Bmatrix} 0 \\ 1 \end{Bmatrix} \right] \cos \varpi_i t + \\ + \left[\mathrm{Re}(d_2) \begin{Bmatrix} 0 \\ 1 \end{Bmatrix} - \mathrm{Im}(d_2) \begin{Bmatrix} 1 \\ 0 \end{Bmatrix} \right] \sin \varpi_i t \Bigg\} \end{aligned} \tag{6.13}$$

$$\begin{Bmatrix} \alpha(t) \\ \beta(t) \end{Bmatrix} = -2e^{\sigma_i t} \, \mathrm{Im}(d_2) \begin{Bmatrix} \sin \varpi_i t \\ \sin\left(\varpi_i t - 90°\right) \end{Bmatrix} \tag{6.14}$$

Figure 6.11(a) presents the increasing displacement response of the system while Fig. 6.11(b)

shows its angular speeds according to Eq. 6.15:

$$\begin{Bmatrix} \dot{\alpha}(t) \\ \dot{\beta}(t) \end{Bmatrix} = 2e^{\sigma_i t}\,\mathrm{Im}(d_1)\left[\sigma_i \begin{Bmatrix} -\sin\varpi_i t \\ \cos\varpi_i t \end{Bmatrix} - \varpi_i \begin{Bmatrix} \cos\varpi_i t \\ \sin\varpi_i t \end{Bmatrix}\right] \tag{6.15}$$

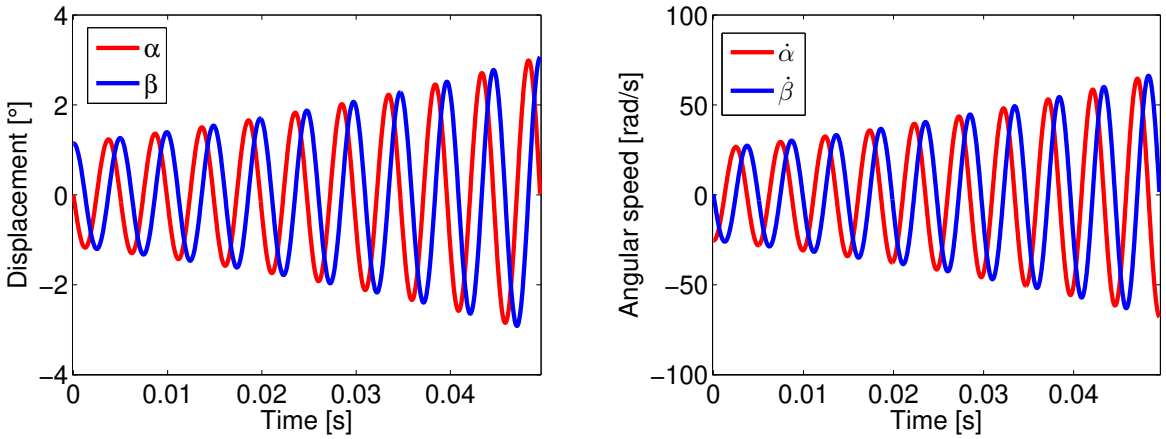

(a) (b)

Figure 6.11: Displacement free response after 10 complete periods (Fig. 6.11(a)) and angular speeds (Fig. 6.11(b)) for $d_i = 0.01j$, $\dot{\gamma} = 1000$ rpm and $\dot{\theta} = 0$.

The normalized friction force is shown in Eq. 6.16 following the same procedure done in the previous section. The results from Figs. 6.12(a) and 6.12(b) reveals that the *friction moments act in favour of motion*, once that $M_{fr_{varx}}$ acts in phase with $\dot{\alpha}$ as well as the torque $M_{fr_{vary}}$ according to $\dot{\beta}$. This is the physical explanation behind the instability indicated by the positive real part of the eigenvalue.

$$\begin{Bmatrix} M_{fr_{varx}} \\ M_{fr_{vary}} \end{Bmatrix}_{normalized} = \begin{Bmatrix} -\beta(t) \\ \alpha(t) \end{Bmatrix} = 2e^{\sigma_i t}\,\mathrm{Im}(d_1) \begin{Bmatrix} -\cos\varpi_i t \\ -\sin\varpi_i t \end{Bmatrix} \tag{6.16}$$

Like the previous case, the points indicated as *a,b,... i* on Fig. 6.13(a) are represented physically in Fig. 6.9. The complete time period is lower than the one presented in Fig. 6.8(a) once that the unstable mode has a greater natural frequency of 201.9 Hz.

The sequence shown in Figs. 6.14a, 6.14c, 6.14e, 6.14g and 6.14i represent that the axis z_3 *seems to move according to the sense of the angular speed* $\dot{\gamma}$. Details of the friction distribution in these cases are found on Figs. 6.2 and 6.3.

In Fig. 6.14a the disc is a position where $\alpha = 0$ and $\beta > 0$. During the motion to Fig. 6.14b

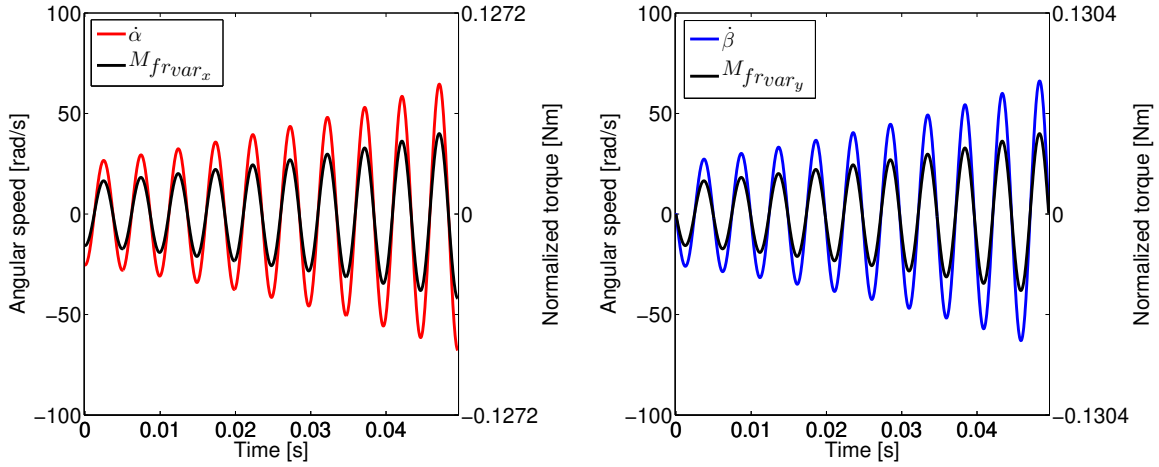

(a) (b)

Figure 6.12: Angular speeds and variable friction in x and y directions (Figs. 6.12(a) and 6.12(b)) for $d_i = 0.01j$, $\dot{\gamma} = 1000$ rpm and $\dot{\theta} = 0$.

($\alpha = 0$ and $\beta = 0$) the variable friction forces generate $M_{fr_{var_x}} < 0$ and $M_{fr_{var_y}} < 0$, that act in favour of the movement. The same occurs when the disc moves from Fig. 6.14c to 6.14e ($\alpha = 0$ and $\beta < 0$). Figure 6.14d presents $M_{fr_{var_x}} > 0$ and $M_{fr_{var_y}} < 0$. The body performs a positive rotation around axis x_3 simultaneously with a negative rotation on axis y_3.

From Fig. 6.14e to Fig. 6.14g ($\alpha < 0$ and $\beta = 0$) the disc presents positive rotations on both axis with $M_{fr_{var_x}} > 0$ and $M_{fr_{var_y}} > 0$ (Fig. 6.14f). It is returning to the original position when it goes from Fig. 6.14g to Fig. 6.14i ($\beta > 0$ and $\alpha = 0$). The friction forces are arranged such that$M_{fr_{var_x}} < 0$ and $M_{fr_{var_y}} > 0$.

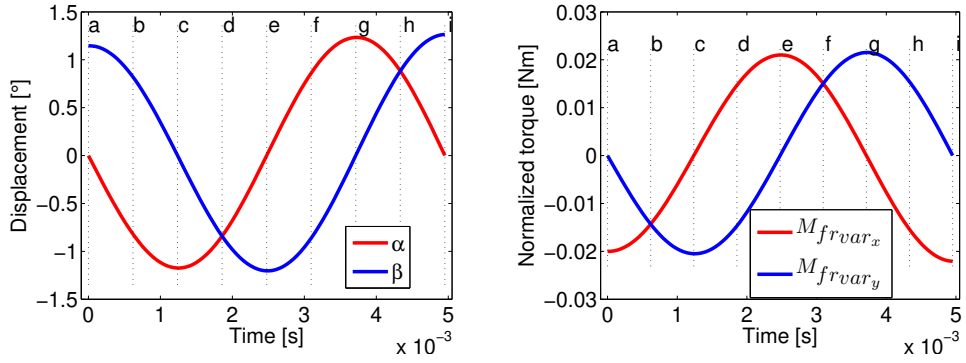

(a) (b)

Figure 6.13: Unstable free response viewed in detail in Fig. 6.13(a) and normalized moments (Fig. 6.13(b)) ($d_i = 0.01j$, $\dot{\gamma} = 1000$ rpm and $\dot{\theta} = 0$).

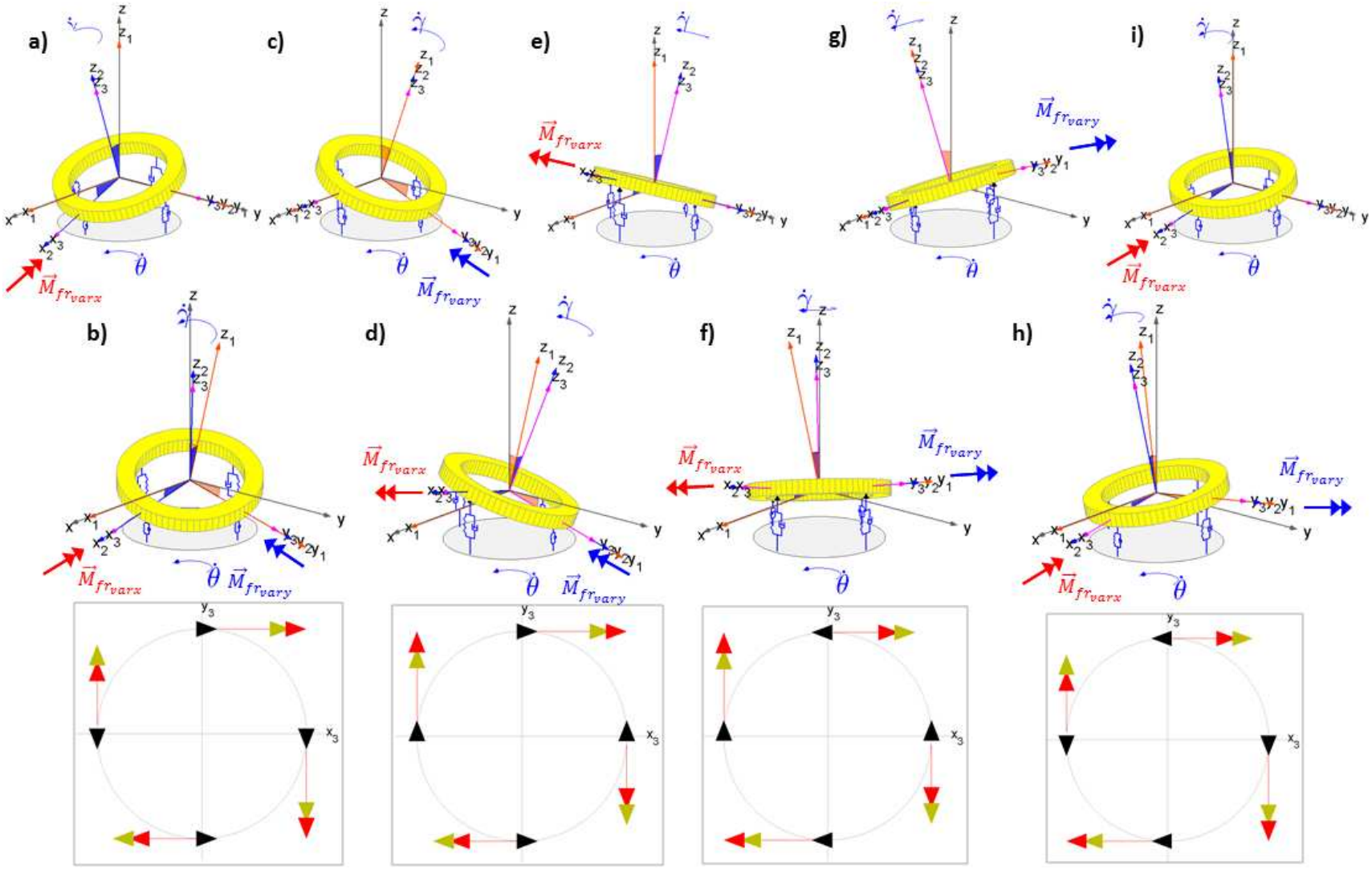

Figure 6.14: Unstable mode for $\dot{\gamma} > 0$ and $\dot{\theta} = 0$ (Forward wobbling).

6.2 Stiffness and relative speed influence

The friction damping effect was included in Eq. 6.1 using $[C_{III}]_i$ (Eq. 5.79). The equations of motion are presented in Eq. 6.17. The friction damping terms are included as the matrix terms $c_{11} = c_{22}$ (Eq. 6.18). The matrix $[K_{VI}]_i$ (Eq. 5.75) introduces new skew symmetric terms that depend on the inverse of $|\dot{\gamma} - \dot{\theta}|$ on (Eq. 6.19).

$$\begin{bmatrix} I_{xx} & 0 & 0 \\ 0 & I_{yy} & 0 \\ 0 & 0 & m \end{bmatrix} \begin{Bmatrix} \ddot{\alpha} \\ \ddot{\beta} \\ \ddot{z} \end{Bmatrix} + \left(\dot{\gamma} \begin{bmatrix} 0 & I_{zz} & 0 \\ -I_{zz} & 0 & 0 \\ 0 & 0 & 0 \end{bmatrix} + \begin{bmatrix} c_{11} & 0 & 0 \\ 0 & c_{22} & 0 \\ 0 & 0 & 0 \end{bmatrix} \right) \begin{Bmatrix} \dot{\alpha} \\ \dot{\beta} \\ \dot{z} \end{Bmatrix} + \\ + k \begin{bmatrix} 2R^2 + 2\mu^2 z_e h & k_{12} & 0 \\ -k_{21} & 2R^2 + 2\mu^2 z_e h & 0 \\ 0 & 0 & 4 \end{bmatrix} \begin{Bmatrix} \alpha \\ \beta \\ z \end{Bmatrix} = \begin{Bmatrix} 0 \\ 0 \\ 0 \end{Bmatrix} \tag{6.17}$$

$$c_{11} = c_{22} = 4\frac{\mu h^2 k z_e}{R|\dot{\gamma} - \dot{\theta}|} \tag{6.18}$$

$$k_{12} = k_{21} = 2\mu k R h sign(\dot{\gamma} - \dot{\theta}) + 4\frac{\mu h^2 k z_e \dot{\theta}}{R|\dot{\gamma} - \dot{\theta}|} \tag{6.19}$$

Figure 6.15 contains the natural frequencies if the total cushion stiffness is increase from 1 to 10^7 N/m. The rotating speeds were adopted as $\dot{\gamma}$ = 2000 rpm and $\dot{\theta} = 0$ rpm. Such results are similar to the ones obtained by Senatore *et al.* (2013). The forward wobbling mode presents the greatest values even for low stiffness. Section 5.1.3 presented that this system is semi definite, with a zero frequency. As a result from that, the backward wobbling mode starts with extremely low frequencies (Fig. 6.15(b)) that grows up to figures from the forward mode. The axial mode is also strongly influenced by this parameter. The real part of the forward mode increases with this stiffness, specially after 10^4 N/m. The axial mode is stable and conservative, once that friction damping occurs only for angular degrees-of-freedom.

Figs. 6.15(d) and 6.15(e) contains the results keeping the pressure plate speed as $\dot{\gamma}$ = 2000 rpm and varying the clutch disc rotating speed between 0 rpm $< \dot{\theta} < 1990$ rpm and 2010 rpm $< \dot{\theta} < 4000$ rpm. Natural frequencies are not affected by the clutch disc speed, as presented in Fig. 6.15(d). In this case, the axial mode shape have an intermediate value between the backward and forward wobbling modes.

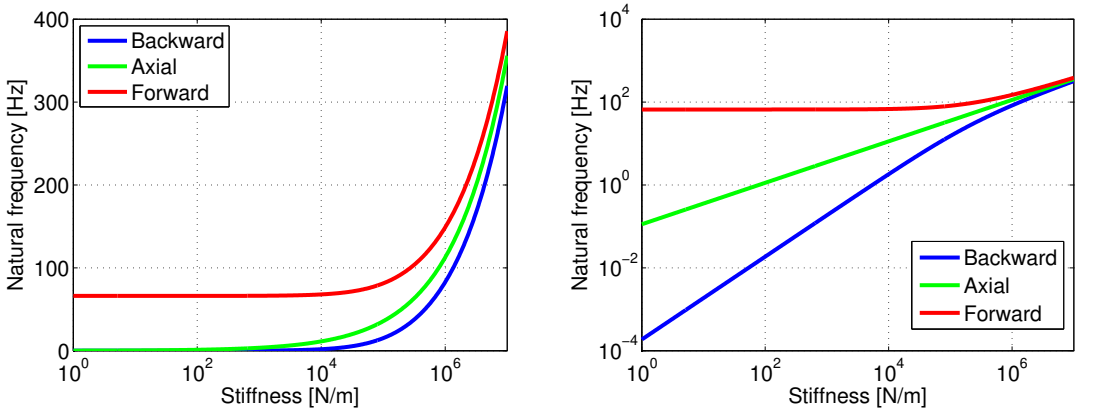

(a)

(b)

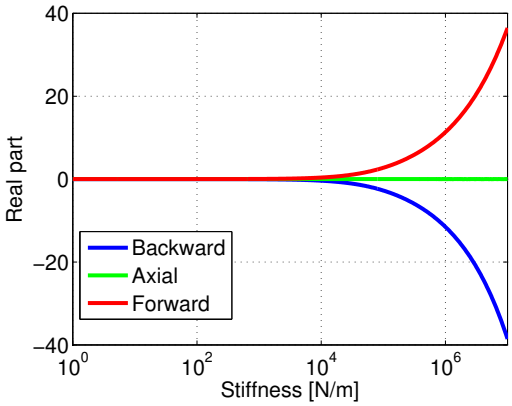

(c)

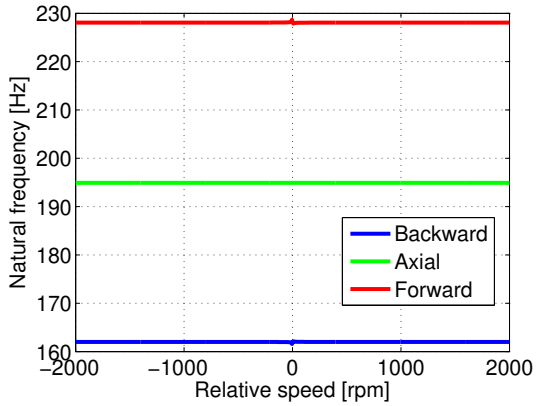

(d)

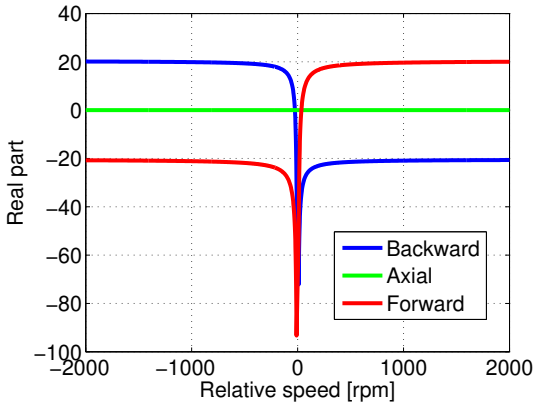

(e)

Figure 6.15: Natural frequencies according to cushion stiffness in linear (Fig. 6.15(a)) and logarithmic (Fig. 6.15(b)) scales. Figure 6.15(c) contains the real part of the eigenvalues. Natural frequencies (Fig. 6.15(d)) and real parts (Fig. 6.15(e)) in relation to the relative speed.

The relative speed ($\dot{\gamma} - \dot{\theta}$) affects the stability. On the verge of coupling, no matter the condition, both wobbling modes have negative real parts on its eigenvalues. This is the consequence from the friction damping effect (von Wagner *et al.*, 2007). The skew symmetric stiffness terms multiplied by $\dot{\theta}$ on Eq. 6.19 become greater when $|\dot{\gamma} - \dot{\theta}| \longrightarrow 0$ with $\dot{\theta} \neq 0$, which could increase the variable friction terms. In this case, the damping from Eq. 6.18 prevails. There are limitations on the range of usage of this element, that are found in Appendix B.1. For $\dot{\gamma} - \dot{\theta} > 0$, the forward mode is unstable, but if the relative displacement changes its signal, it is stabilized, while the backward mode presents positive real parts on its eigenvalues. Hervé *et al.* (2008b) produced such results by changing the signal of the circulatory action (Section 3.2.4). Once again, the axial mode is not affected by the relative speed.

6.3 System with viscous damping effects

To create the model from Eq. 6.20 damper and stiffness elements were equally distributed around the perimeter of the disc ($\psi_{i0} = 0°$, 90°, 180° and 270°). This condition is *theoretical*, with the assumption of $\mu = 0$ on Eq. 6.17. The skew symmetric terms $2\dot{\theta}cR^2$ on the stiffness matrix are contributions from $[K_{IV}]_i$ (Eq. 5.73), which are related to the moving viscous damper element (Section 5.4). Section 6.4 will present a combination with friction.

$$\begin{bmatrix} I & 0 & 0 \\ 0 & I & 0 \\ 0 & 0 & m \end{bmatrix} \begin{Bmatrix} \ddot{\alpha} \\ \ddot{\beta} \\ \ddot{z} \end{Bmatrix} + \left(\dot{\gamma} \begin{bmatrix} 0 & I_{zz} & 0 \\ -I_{zz} & 0 & 0 \\ 0 & 0 & 0 \end{bmatrix} + \begin{bmatrix} 2cR^2 & 0 & 0 \\ 0 & 2cR^2 & 0 \\ 0 & 0 & 4c \end{bmatrix} \right) \begin{Bmatrix} \dot{\alpha} \\ \dot{\beta} \\ \dot{z} \end{Bmatrix} + \\ + \begin{bmatrix} 2kR^2 & 2cR^2\dot{\theta} & 0 \\ -2cR^2\dot{\theta} & 2kR^2 & 0 \\ 0 & 0 & 4k \end{bmatrix} \begin{Bmatrix} \alpha \\ \beta \\ z \end{Bmatrix} = \begin{Bmatrix} 0 \\ 0 \\ 0 \end{Bmatrix} \tag{6.20}$$

Figure 6.16 presents the natural frequencies with c = 5 Ns/m and a total cushion stiffness of 3×10^2 N/m. The disc has a rotating speed of $\dot{\gamma} = 2000$ rpm. In this situation, the frequency of the forward wobbling mode occurs above 60 Hz, while the axial and backward modes presented very low frequencies.

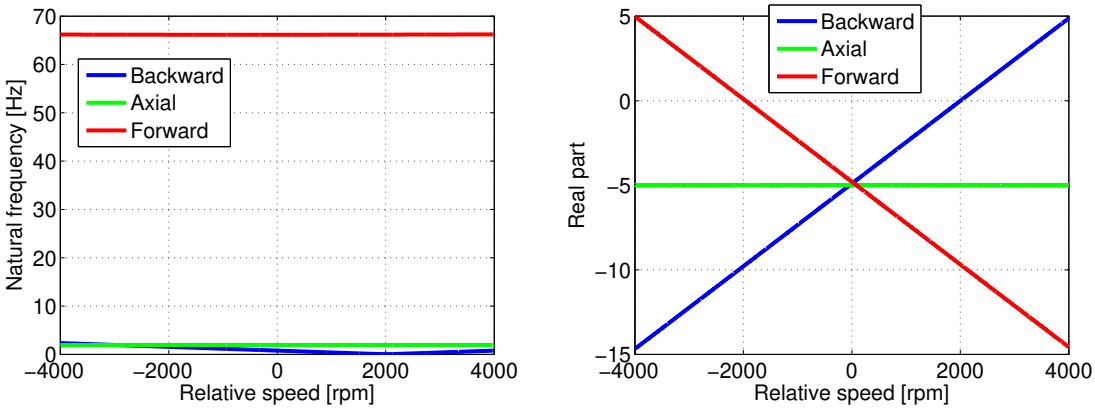

(a) (b)

Figure 6.16: Eigenvalue real parts (Fig. 6.16(b)) and natural frequencies (Fig. 6.16(a)) for a system with viscous damping without friction for c = 5 Ns/m and a total cushion stiffness of 3×10^2 N/m.

The observation of the real part of those eigenvalues (Fig. 6.16(b)) lead to the following observations:

- For $\dot{\gamma} - \dot{\theta} < 0$, the rotating speed of the elements ($\dot{\theta}$) is greater than the one on the pressure plate ($\dot{\gamma}$). With $\dot{\gamma} - \dot{\theta} < -2000$ rpm, the forward wobbling motion is unstable, while the backward and axial motions remain stable.
- With -2000 rpm $< \dot{\gamma} - \dot{\theta} < 2000$ rpm the system is stable.
- When $0 < \dot{\gamma} - \dot{\theta} < 2000$ rpm the rotating speed of the elements is lower than the one on the pressure plate but on the same direction.
- With $\dot{\gamma} - \dot{\theta} > 2000$ rpm the backward motion is unstable. This condition is *theoretical*, because it is necessary to *assume an inversion on the direction of rotation of the damper/stiffness elements* when $\dot{\gamma} = 2000$ rpm.

The damping factors ($\zeta_i = -Re(\lambda_i)/|\lambda_i|$) are presented in Fig. 6.3 in terms of percentage. It is possible to observe that modifications on $\dot{\theta}$ changes the damping factor for the backward mode when $\dot{\gamma} - \dot{\theta}$ becomes closer to 2000 rpm. The axial motion presents a constant characteristics. The forward wobbling have very low levels of $|\zeta_i|$, indicating that the unstable response will have a slow increase rate.

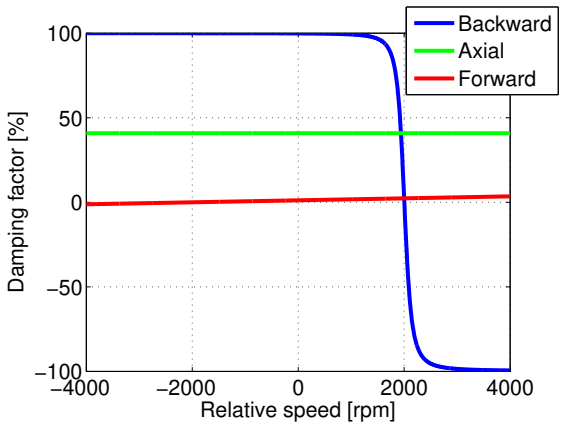

Figure 6.17: Eigenvalue damping factors for a system with viscous damping without friction for c = 5 Ns/m and a total cushion stiffness of 3×10^2 N/m.

The damping efforts due to the movement of the viscous damper elements on Eq. 6.20 are given by $\vec{M}_{mov}$ (Eq. 6.21):

$$\vec{M}_{mov} = \begin{Bmatrix} M_{mov_x} \\ M_{mov_y} \end{Bmatrix} = -2cR^2\dot{\theta} \begin{Bmatrix} \beta(t) \\ -\alpha(t) \end{Bmatrix} \tag{6.21}$$

The time response for the backward/forward motions can be obtained as Eq. 6.5. For $d_i = 0.001$, $\dot{\gamma} = 2000$ rpm and $\dot{\theta} = 6000$ rpm , the backward response is presented by Fig. 6.18. The torque components M_{mov_x} and M_{mov_y} are opposed to the wobbling speeds $\dot{\alpha}$ and $\dot{\beta}$ on Figs. 6.18(a) and 6.18(b), respectively. On the other hand, such torques act in favour of the forward motion on Figs. 6.19(a) and 6.19(b).

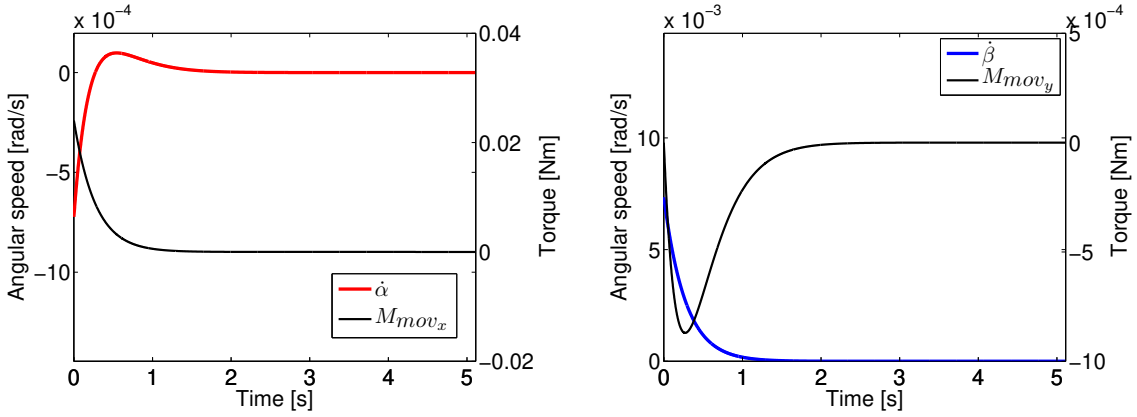

(a) (b)

Figure 6.18: Backward wobbling motion (Figs 6.18(a) and 6.18(b)) Parameters considered as $\dot{\gamma} = 2000$ rpm and $\dot{\theta} = 6000$ rpm (c = 5 Ns/m and a total cushion stiffness of 3×10^2 N/m).

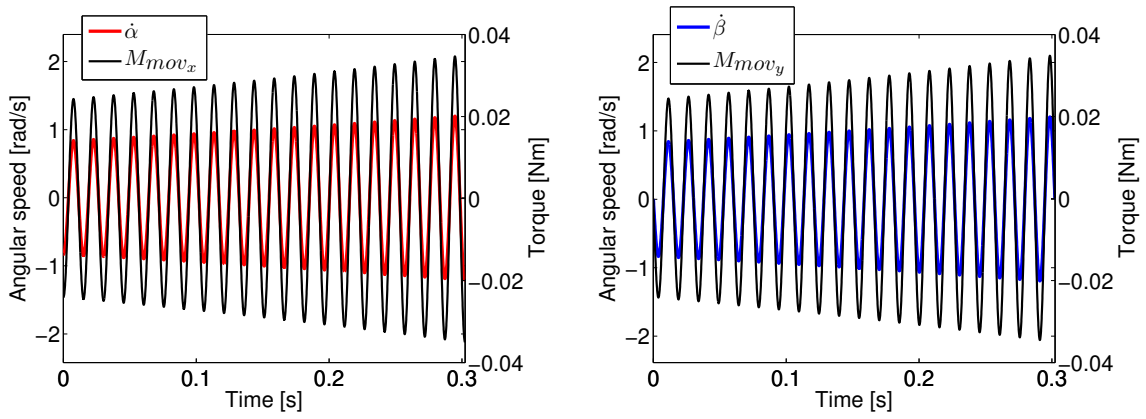

(a) (b)

Figure 6.19: Forward wobbling motion (Figs. 6.19(a) 6.19(b)). Parameters considered as $\dot{\gamma} = 2000$ rpm and $\dot{\theta} = 6000$ rpm (c = 5 Ns/m and a total cushion stiffness of 3×10^2 N/m).

The sequence on Fig. 6.20 results from the combination of configurations obtained on Section 5.4 (Figs. 5.17 and 5.19). The forward wobbling is excited by the vertical damping forces (indicated as F_{c_i}), that result on M_{mov_x} and M_{mov_y}. In every condition, such efforts act in favour for the next position.

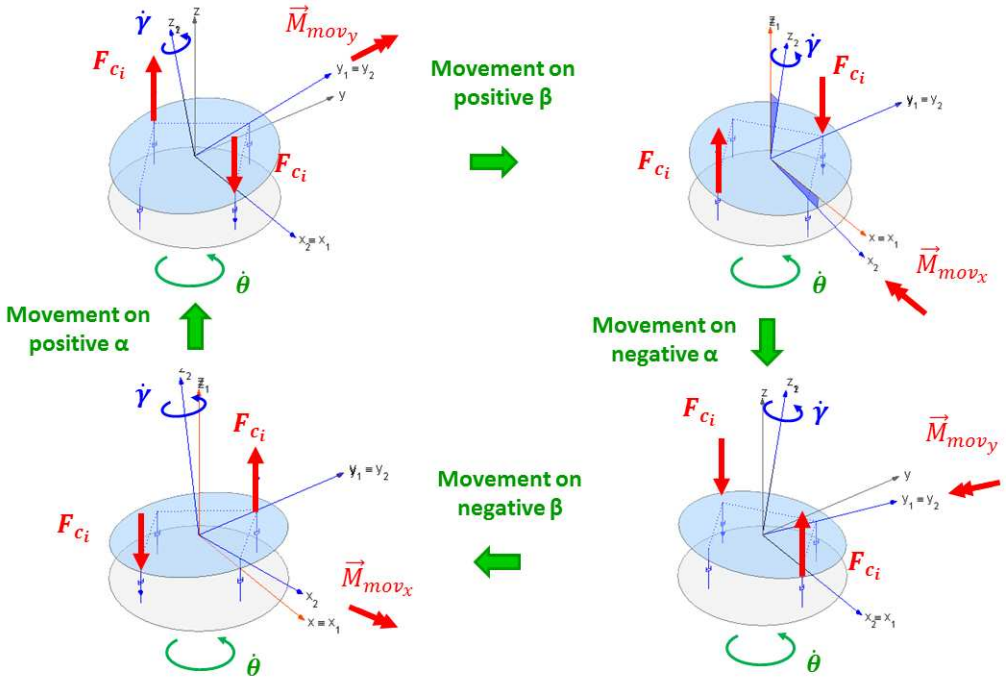

Figure 6.20: Damping efforts for unstable motion due to the moving viscous damper element on Cardan coordinates ($\dot{\gamma} \neq 0$ and $\dot{\theta} \neq 0$).

6.4 System with viscous damping and friction

Viscous damping was included in Eq. 6.17 resulting in Eq. 6.22. Matrices $[C_I]_i$ (Eq. 5.77) and $[C_{II}]_i$ (Eq. 5.78) are responsible for new terms on $c_{11} = c_{22}$ (Eq. 6.23) and $c_{12} = c_{21}$ (Eq. 6.24). Matrix $[K_V]_i$ (Eq. 5.74) result in a new term involving the clutch disc rotating speed $\dot{\theta}$, damping and friction on $k_{11} = k_{22}$ (Eq. 6.25). The terms from $[K_{IV}]_i$ (Eq. 5.73) appear on $k_{12} = k_{21}$ (Eq. 6.26), as presented on Eq. 6.20. Friction coefficient of $\mu = 0.3$ is considered.

$$\begin{bmatrix} I & 0 & 0 \\ 0 & I & 0 \\ 0 & 0 & m \end{bmatrix} \begin{Bmatrix} \ddot{\alpha} \\ \ddot{\beta} \\ \ddot{z} \end{Bmatrix} + \left(\dot{\gamma} \begin{bmatrix} 0 & I_{zz} & 0 \\ -I_{zz} & 0 & 0 \\ 0 & 0 & 0 \end{bmatrix} + \begin{bmatrix} c_{11} & c_{12} & 0 \\ -c_{21} & c_{22} & 0 \\ 0 & 0 & 4c \end{bmatrix} \right) \begin{Bmatrix} \dot{\alpha} \\ \dot{\beta} \\ \dot{z} \end{Bmatrix} + \\ + \begin{bmatrix} k_{11} & k_{12} & 0 \\ -k_{21} & k_{22} & 0 \\ 0 & 0 & 4k \end{bmatrix} \begin{Bmatrix} \alpha \\ \beta \\ z \end{Bmatrix} = \begin{Bmatrix} 0 \\ 0 \\ 0 \end{Bmatrix} \tag{6.22}$$

$$c_{11} = c_{22} = 4\frac{\mu h^2 k z_e}{R|\dot{\gamma} - \dot{\theta}|} + 2cR^2 \tag{6.23}$$

$$c_{12} = c_{21} = 2\mu cRh sign(\dot{\gamma} - \dot{\theta}) \tag{6.24}$$

$$k_{11} = k_{22} = 2kR^2 + 2\mu^2 k z_e h - 2\mu hc\dot{\theta} sign(\dot{\gamma} - \dot{\theta}) \tag{6.25}$$

$$k_{12} = k_{21} = 2\mu kRh sign(\dot{\gamma} - \dot{\theta}) + 4\frac{\mu h^2 k z_e \dot{\theta}}{R|\dot{\gamma} - \dot{\theta}|} + 2cR^2\dot{\theta} \tag{6.26}$$

Depending on the values involved on the friction contact the effect from the moving viscous damping can prevail on this system. For example, Figures 6.21(a) and 6.21(b) present the natural frequencies and eigenvalue real parts with c = 5 Ns/m and a total cushion stiffness of $k_{cushion} = 3 \times 10^2$ N/m. Those results are practically the same as the ones from Fig. 6.16.

If the cushion stiffness is increased to 3×10^6 N/m with c = 5 Ns/m, the natural frequencies and real parts (Figs. 6.21(c) and 6.21(d)) are very similar to the case on the previous section (Fig. 6.2).

Increasing the damping to $c = 30$ Ns/m, all eigenvalues are found with negative real parts (Fig. 6.21(f)), but unaltered in terms of frequency (Fig. 6.21(e)). The damping influence for

stabilization was tested by Hervé *et al.* (2008b). Figure 6.21(f) shows that, *greater values of viscous damping allow the influence of the clutch disc rotating speed ($\dot{\theta}$) on the real parts of the eigenvalues*. It is caused by the terms related to the moving viscous elements introduced on Eqs. 6.25 and 6.26.

The simulations on Figs. 6.21 indicate two different mechanisms for self excitation on this model:

1. a combination of viscous damping with very low levels of cushion stiffness or friction resulted on instability of the plate, due to the forces produced by the movement of the damper element. The physical explanation for the efforts were presented on Sections 5.4.1, 5.4.2 and 6.3. An important point is that this is not related to friction, but to the shape of the elements and the assumption of rotation on the element.

2. low damping in comparison to the stiffness resulted on wobbling motions, excited by friction related moments. This case was carefully detailed on Section 6.1 and documented in all the works from Chapter 3.

There are no traceable works on the physical model of energy dissipation on the interaction between the cushion springs and the facings. The assumption of viscous damping was arbitrary on this thesis, but it includes a representation energy dissipation on the model with physical meaning. With another arbitrary assumption of proportional damping, the dependence on the rotating speed of the disc $\dot{\theta}$ disappears. Even so, this is a theoretical advance on the subject, once that such phenomena was not documented on the clutch squeal literature and cannot be reproduced by any of the models from Chapter 3.

6.5 Chapter summary

The observations from this chapter are separated into different physical domains:

6.5.1 Rotating speeds

The system modelled on Cardan coordinates presented the following characteristics ($\dot{\gamma} \neq 0$ and $\dot{\theta} = 0$):

- The natural frequency of the unstable mode was greater and increased with the rotating speed. It was represented as a forward wobbling mode.

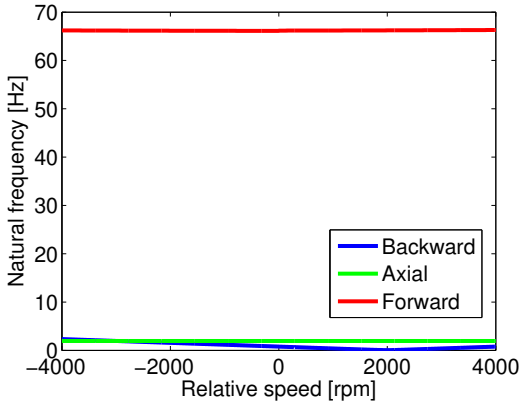

(a) $c = 5$ Ns/m and $k_{cushion} = 3 \times 10^2$ N/m

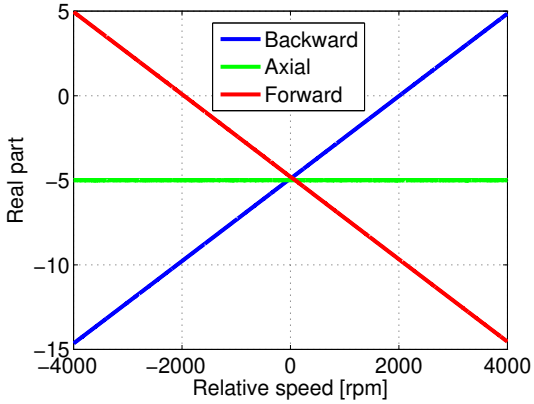

(b) $c = 5$ Ns/m and $k_{cushion} = 3 \times 10^2$ N/m

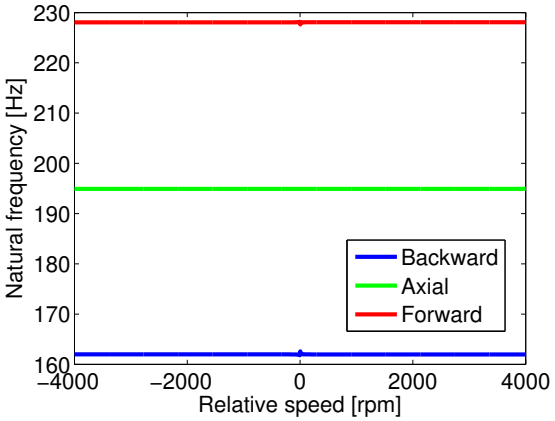

(c) $c = 5$ Ns/m and $k_{cushion} = 3 \times 10^2$ N/m

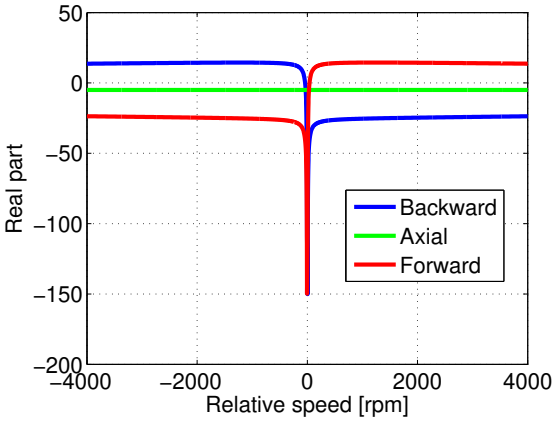

(d) $c = 5$ Ns/m and $k_{cushion} = 3 \times 10^6$ N/m

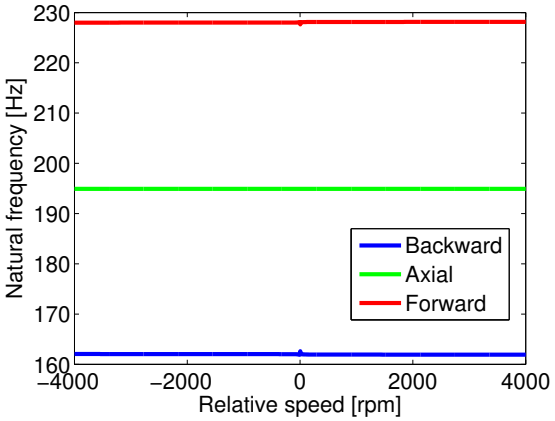

(e) $c = 30$ Ns/m and $k_{cushion} = 3 \times 10^6$ N/m

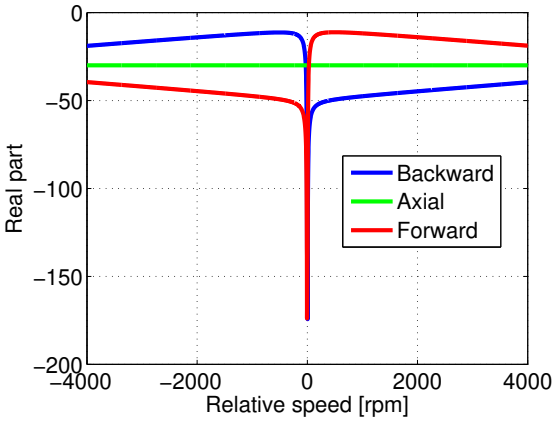

(f) $c = 30$ Ns/m and $k_{cushion} = 3 \times 10^6$ N/m

Figure 6.21: Natural frequencies (Fig. 6.21(a), 6.21(c) and 6.21(e)) and eigenvalue real parts (Fig. 6.21(b), 6.21(d) and 6.21(f)) according to the relative speed ($\dot{\gamma} - \dot{\theta}$) with $\mu = 0.3$ and $\dot{\gamma} = 2000$ rpm.

- The stable mode presented a backward motion, with a natural frequency that decreased with the rotating speed .

6.5.2 Relative speed

The relative speed resulted on the following conditions on the simulations:

- Friction damping stabilized both models near coupling conditions, according to the findings from von Wagner *et al.* (2007).
- The axial mode remained stable for all situations
- Due to the modification on the direction o friction moments, the forward mode was unstable for $\dot{\gamma} - \dot{\theta} > 0$. Such relations were first proposed by Hervé *et al.* (2008b). The backward mode became unstable for $\dot{\gamma} - \dot{\theta} < 0$.

6.5.3 Stiffness

From the previous simulations it was possible to verify that, for low stiffness:

- On Cardan coordinates, low values of cushion stiffness influenced the backward wobbling and the axial modes.

For high cushion stiffness, the following behaviour was observed:

- On Cardan coordinates, the forward/backward/axial mode frequencies increased but remained distant from each other.
- Greater values of stiffness increased the real part from the eigenvalue for the forward mode.

6.5.4 Viscous damping

- Viscous damping introduced instability for low levels of cushion stiffness. The rotating speed of the disc $\dot{\theta}$ altered the behaviour of the real parts of the eigenvalues.

7 Hipothesis 2: Model considering the rotating speed on global coordinates

By choosing this representation, the model present results based on the *influence of the precession speed* during operation. Although Hervé *et al.* (2008b) and Hervé *et al.* (2009) did not specify in detail the procedures to obtain the equations of motion, the author found similar inertia matrices adopting the rotating speed on global coordinates.

First, Section 7.1 presents the rigid body formulation of the pressure plate for Hypothesis 2. The necessary steps to obtain the stiffness/viscous damper element with friction are provided on Section 5.2, followed by the efforts due to the movement of the viscous damper element (Section 7.3). Finally, the element matrices are described on Section 7.4.

7.1 Pressure plate model

The proper sequence of rotations using the matrices presented on Section 7.1.1 result on the angular speed and accelerations on Section 7.1.2. Hervé *et al.* (2008b) and Hervé *et al.* (2009) used a similar formulation, but here it will be shown on Section 7.1.3 that this system is not only influenced by the rotating speed as presented on Section 5.1.3 (Hypothesis 1) but also by the angular acceleration.

7.1.1 Rotation matrices

Angle γ (Fig. 7.1(b)) originates a rotation matrix for z' axis $[R_\gamma]^T$ to transform a vector ${}_0\vec{r'}$ from the coordinate system $x'y'z'$ (Fig. 7.1(a)) to $x'_1y'_1z'_1$, represented as ${}_1\vec{r'}$ (Eq. 7.1). The inverse transformation is calculated by Eq. 7.2.

$$ {}_1\vec{r'} = [R_\gamma]^T \, {}_0\vec{r'} \tag{7.1} $$

$$ {}_0\vec{r'} = [R_\gamma] \, {}_1\vec{r'} \tag{7.2} $$

A rotation given by β (Fig. 7.1(c)) moves the representation from $x'_1y'_1z'_1$ to $x'_2y'_2z'_2$ (Eq. 7.3), while the inverse transformation is given by Eq. 7.4.

$$ {}_2\vec{r'} = [R_\beta]^T \, {}_1\vec{r'} \tag{7.3} $$

$$ {}_1\vec{r'} = [R_\beta] \, {}_2\vec{r'} \tag{7.4} $$

Finally, the angle α (Fig. 7.1(d)) is used to provide a rotation around the x' axis from $x'_2y'_2z'_2$ to $x'_3y'_3z'_3$ according to Eq. 7.5. The inverse relation is shown in Eq. 7.6.

$$ {}_3\vec{r'} = [R_\alpha]^T \, {}_2\vec{r'} \tag{7.5} $$

$$ {}_2\vec{r'} = [R_\alpha] \, {}_3\vec{r'} \tag{7.6} $$

As a result, a vector can be expressed on global coordinates using Eq. 7.7. The matrix $[R_{\gamma\beta\alpha}]$ is shown in Eq. 7.8.

$$ {}_0\vec{r'} = [R_\gamma][R_\beta][R_\alpha] \, {}_3\vec{r} = [R_{\gamma\beta\alpha}] \, {}_3\vec{r'} \tag{7.7} $$

$$ [R_{\gamma\beta\alpha}] = \begin{bmatrix} \cos\beta\cos\gamma & -\cos\alpha\sin\gamma + \sin\alpha\sin\beta\cos\gamma & \sin\alpha\sin\gamma + \cos\alpha\sin\beta\cos\gamma \\ \cos\beta\sin\gamma & \cos\alpha\cos\gamma + \sin\alpha\sin\beta\sin\gamma & -\sin\alpha\cos\beta + \cos\alpha\sin\beta\sin\gamma \\ -\sin\beta & \sin\alpha\cos\beta & \cos\alpha\cos\beta \end{bmatrix} \tag{7.8} $$

7.1.2 Angular speeds and accelerations

The full expression of the angular speeds (Eq. 7.9) and accelerations (Eq. 7.10) are necessary for the equations of motion describing the wobbling movement of the pressure plate.

$$ {}_3\vec{\omega}' = \begin{bmatrix} 1 & 0 & -\sin\beta \\ 0 & \cos\alpha & \sin\alpha\cos\beta \\ 0 & -\sin\alpha & \cos\alpha\cos\beta \end{bmatrix} \begin{Bmatrix} \dot{\alpha} \\ \dot{\beta} \\ \dot{\gamma} \end{Bmatrix} = \begin{Bmatrix} {}_3\omega_{x'} \\ {}_3\omega_{y'} \\ {}_3\omega_{z'} \end{Bmatrix} \tag{7.9} $$

$$
{}_3\dot{\vec{\omega}}' = \begin{bmatrix} 1 & 0 & -\sin\beta \\ 0 & \cos\alpha & \sin\alpha\cos\beta \\ 0 & -\sin\alpha & \cos\alpha\cos\beta \end{bmatrix} \begin{Bmatrix} \ddot{\alpha} \\ \ddot{\beta} \\ \ddot{\gamma} \end{Bmatrix} + \dot{\gamma} \begin{bmatrix} 0 & -\cos\beta \\ \cos\alpha\cos\beta & -\sin\alpha\cos\beta \\ -\sin\alpha\cos\beta & -\cos\alpha\sin\beta \end{bmatrix} \begin{Bmatrix} \dot{\alpha} \\ \dot{\beta} \end{Bmatrix} + \\
- \dot{\alpha}\dot{\beta} \begin{Bmatrix} 0 \\ \sin\alpha \\ \cos\alpha \end{Bmatrix} = \begin{Bmatrix} {}_3\dot{\omega}_{x'} \\ {}_3\dot{\omega}_{y'} \\ {}_3\dot{\omega}_{z'} \end{Bmatrix} \tag{7.10}
$$

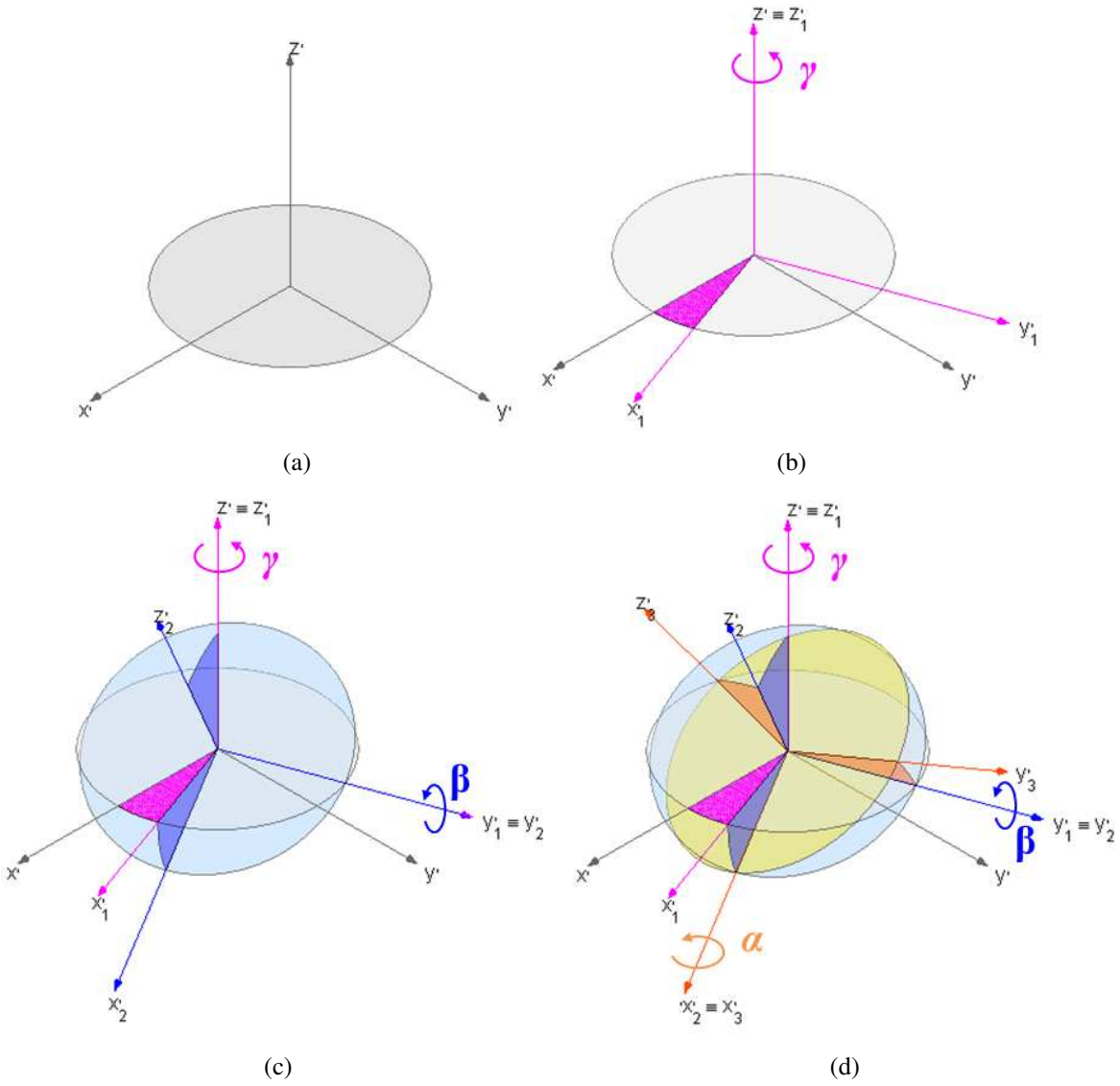

Figure 7.1: Rotations assumed on the model keeping the rotating speed on global coordinates.

7.1.3 Inertia components and modal properties

The body modelled in these coordinates presents more inertia effects than the previous one (Eq. 5.12). The coordinates are considered as $\{p\}^T = \begin{Bmatrix} \alpha & \beta \end{Bmatrix}^T$. Equation 7.11 shows a mass matrix $[M]$ (Eq. 7.12) and a gyroscopic one $[G]$ (Eq. 7.13), that depends on all inertia moments $I_{x'x'}$, $I_{y'y'}$ and $I_{z'z'}$. It also has the contribution of matrix $[H_1(\dot{\gamma})]$ (Eq. 7.14), which includes terms that depend on $\dot{\gamma}$ on the stiffness matrix. Even the disc acceleration have influence on its behaviour, expressed through the term $[H_2(\ddot{\gamma})]$ (Eq. 7.15). It occurs that $I_{x'x'} = I_{y'y'} < I_{z'z'}$ for the disc (Eq. 5.19 and 5.20) so matrix $[H_2(\ddot{\gamma})]$ is skew symmetric but its non diagonal terms have opposite signals compared to the ones found on $[G]$ (Eq. 7.13). The term $[H_2(\ddot{\gamma})]$ is not found on Hervé *et al.* (2008b) or Hervé *et al.* (2009).

$$[M]\{\ddot{p}\} + [G]\{\dot{p}\} + ([H_1(\dot{\gamma})] + [H_2(\ddot{\gamma})])\{p\} = \{0\} \tag{7.11}$$

$$[M] = \begin{bmatrix} I_{x'x'} & 0 \\ 0 & I_{y'y'} \end{bmatrix} \tag{7.12}$$

$$[G] = \dot{\gamma} \begin{bmatrix} 0 & -I_{x'x'} - I_{y'y'} + I_{z'z'} \\ I_{x'x'} + I_{y'y'} - I_{z'z'} & 0 \end{bmatrix} \tag{7.13}$$

$$[H_1(\dot{\gamma})] = \dot{\gamma}^2 \begin{bmatrix} I_{z'z'} - I_{y'y'} & 0 \\ 0 & (I_{z'z'} - I_{x'x'}) \end{bmatrix} \tag{7.14}$$

$$[H_2(\ddot{\gamma})] = \ddot{\gamma} \begin{bmatrix} 0 & -I_{x'x'} \\ I_{y'y'} & 0 \end{bmatrix} \tag{7.15}$$

The modal properties of the system are found by Eq. 7.16 assuming $I_{x'x'} = I_{y'y'} = I$ and an eigenvalue λ_i. The numerical examples will use the data from Section 5.1.3. Non trivial solutions are obtained imposing a determinant different from zero, which results on the characteristic polynomial shown in Eq. 7.17.

$$\begin{bmatrix} I\lambda_i^2 + \dot{\gamma}^2 (I_{z'z'} - I) & \dot{\gamma}\lambda_i (-2I + I_{z'z'}) - \ddot{\gamma} I \\ \dot{\gamma}\lambda_i (2I - I_{z'z'}) + \ddot{\gamma} I & I\lambda_i^2 + \dot{\gamma}^2 (I_{z'z'} - I) \end{bmatrix} \begin{Bmatrix} X_{1i} \\ X_{2i} \end{Bmatrix} = \begin{Bmatrix} 0 \\ 0 \end{Bmatrix} \tag{7.16}$$

$$\left[I\lambda_i^2 + \dot{\gamma}^2 (I_{z'z'} - I)\right]^2 + \left[\dot{\gamma}\lambda_i (2I - I_{z'z'}) + \ddot{\gamma} I\right]^2 = 0 \tag{7.17}$$

Equation 7.17 can be separated into Eqs. 7.18 and 7.19:

$$\lambda_i^2 + \lambda\dot{\gamma}\left(\frac{I_{z'z'}}{I} - 2\right)j + \left[\dot{\gamma}^2\left(\frac{I_{z'z'}}{I} - 1\right) - \ddot{\gamma}j\right] = 0 \tag{7.18}$$

$$\lambda_i^2 - \lambda\dot{\gamma}\left(\frac{I_{z'z'}}{I} - 2\right)j + \left[\dot{\gamma}^2\left(\frac{I_{z'z'}}{I} - 1\right) + \ddot{\gamma}j\right] = 0 \tag{7.19}$$

The solutions from Eq. 7.18 are given by Eq. 7.20. They depend on Δ (Eq. 7.21), a complex parameter where the rotating speed affects its real part and acceleration has influence on the imaginary portion.

$$\lambda_i = -\left(\frac{\dot{\gamma}}{2}\right)\left[\frac{I_{z'z'}}{I} - 2\right]j \pm \frac{\sqrt{\Delta}}{2} \tag{7.20}$$

$$\Delta = -\dot{\gamma}^2\left(\frac{I_{z'z'}}{I}\right)^2 + 4\ddot{\gamma}j = |\Delta|e^{j\phi} = \left[\sqrt{\dot{\gamma}^4\left(\frac{I_{z'z'}}{I}\right)^4 + 16\ddot{\gamma}^2}\right]e^{j\phi} \tag{7.21}$$

The phase angle from Eq. 7.21 may assume different values according to the rotating speed and acceleration:

- $\pi/2 < \phi < \pi$, if $\dot{\gamma} \neq 0$ and $\ddot{\gamma} \neq 0$ (Fig. 7.2(a)).
- $\phi = \pi/2$, if $\dot{\gamma} = 0$ and $\ddot{\gamma} \neq 0$ (Fig. 7.2(b)).
- $\phi = \pi$, if $\dot{\gamma} \neq 0$ and $\ddot{\gamma} = 0$ (Fig. 7.2(c)).

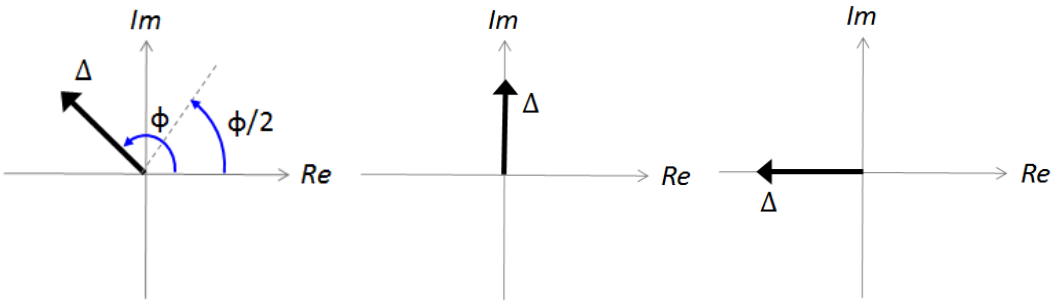

(a) $\dot{\gamma} \neq 0$ and $\ddot{\gamma} \neq 0$ (b) $\dot{\gamma} = 0$ and $\ddot{\gamma} \neq 0$ (c) $\dot{\gamma} \neq 0$ and $\ddot{\gamma} = 0$

Figure 7.2: Parameter Δ (Eq. 7.21) for different conditions of acceleration and rotating speeds.

Applying the same procedure done to Eq. 7.18 in Eq. 7.19 and combining the results, a pair of stable (Eq. 7.22) and unstable (Eq. 7.23) eigenvalues are obtained.

$$\lambda_1, \lambda_1^* = -\frac{\sqrt{|\Delta|}}{2}\cos\left(\frac{\phi}{2}\right) \pm j\left\{\frac{\dot{\gamma}}{2}\left[2 - \frac{I_{z'z'}}{I}\right] - \frac{\sqrt{|\Delta|}}{2}\sin\left(\frac{\phi}{2}\right)\right\} \tag{7.22}$$

$$\lambda_2, \lambda_2^* = \frac{\sqrt{|\Delta|}}{2}\cos\left(\frac{\phi}{2}\right) \pm j\left\{\frac{\dot{\gamma}}{2}\left[2 - \frac{I_{z'z'}}{I}\right] + \frac{\sqrt{|\Delta|}}{2}\sin\left(\frac{\phi}{2}\right)\right\} \tag{7.23}$$

7.1.4 Stability for $\ddot{\gamma} = 0$ and $\dot{\gamma} \neq 0$

If the disc is at constant rotating speed, Δ is a real number (Fig. 7.2(c)), resulting in two pairs of pure imaginary eigenvalues (Eqs. 7.24 and 7.25). *The non accelerated system presents an oscillatory behaviour*.

$$\lambda_1, \lambda_1^* = \pm j\left\{\frac{\dot{\gamma}}{2}\left[2 - \frac{I_{z'z'}}{I}\right] + \frac{\sqrt{|\Delta|}}{2}\right\} \tag{7.24}$$

$$\lambda_2, \lambda_2^* = \pm j\left\{\frac{\dot{\gamma}}{2}\left[2 - \frac{I_{z'z'}}{I}\right] - \frac{\sqrt{|\Delta|}}{2}\right\} \tag{7.25}$$

One of the natural frequencies match the first order (Eq. 7.27) while the other can be found quite close to this value (Eq. 7.26). They can be visualized in Fig. 7.1.4.

$$\omega_{n_1} = |\lambda_1| = |\lambda_1^*| = |\dot{\gamma}|\left(\frac{I_{z'z'}}{I} - 1\right) \tag{7.26}$$

$$\omega_{n_2} = |\lambda_2| = |\lambda_2^*| = |\dot{\gamma}| \tag{7.27}$$

7.1.5 Stability for $\dot{\gamma} = 0$ and $\ddot{\gamma} \neq 0$

In this case, the eigenvalues are presented at Eq. 7.29 and 7.28 for $0 \leqslant \ddot{\gamma} \leqslant 2000\ rad/s^2$. *The purely accelerated system is unstable*. An important event is that now they both have the same natural frequency, indicated by Eq. 7.30 and plotted in Fig. 7.4(a). In this situation, the eigenvalues keep their characteristics over the whole acceleration range (Fig. 7.4(b)).

$$\lambda_1, \lambda_1^* = \frac{\sqrt{2|\ddot{\gamma}|}}{2}(-1 \pm j) \tag{7.28}$$

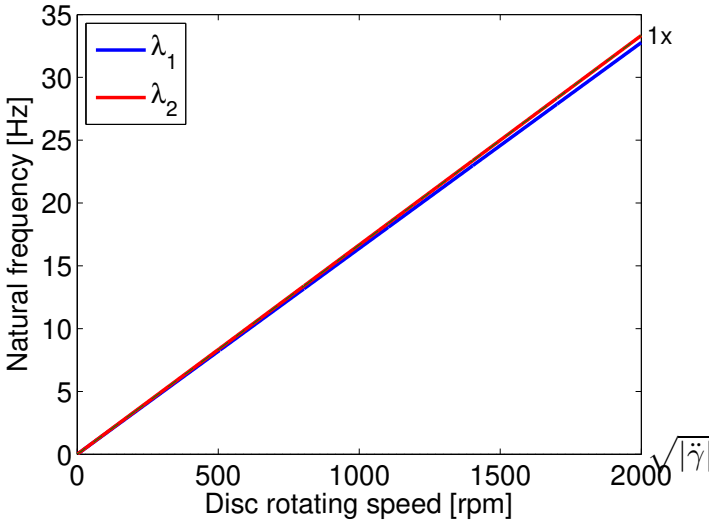

Figure 7.3: Natural frequencies for $\ddot{\gamma} = 0$.

$$\lambda_2, \lambda_2^* = \frac{\sqrt{2|\ddot{\gamma}|}}{2}(1 \pm j) \tag{7.29}$$

$$\omega_{n_1} = \omega_{n_2} = \sqrt{|\ddot{\gamma}|} \tag{7.30}$$

The condition with $\ddot{\gamma} \neq 0$ and $\dot{\gamma} = 0$ is very specific, happening on the verge of movement ($t = 0$ s) or when the disc is changing its rotating speed direction from $\dot{\gamma} > 0$ to $\dot{\gamma} < 0$ or the other way round. It is helpful to indicate asymptotic behavior when $\dot{\gamma} \to 0$ and $\ddot{\gamma} \neq 0$.

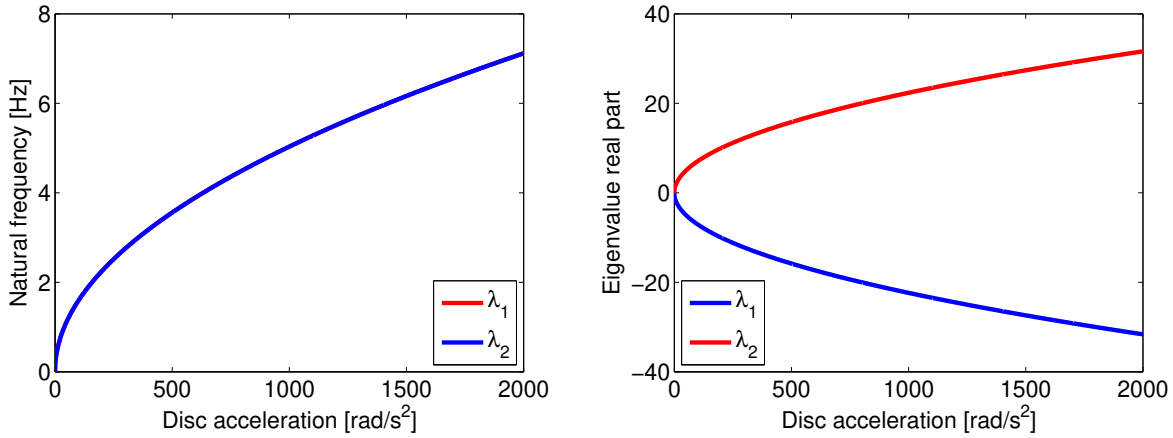

(a) (b)

Figure 7.4: Natural frequencies (Fig. 7.4(a)) and eigenvalue real part (Fig. 7.4(b)) for $\dot{\gamma} = 0$.

7.1.6 Stability for $\dot{\gamma} \neq 0$ and $\ddot{\gamma} \neq 0$

For this general case, Equation 7.31 shows that the unstable mode has a natural frequency greater than the stable one due to the negative signal that follows the term that is multiplied by $\dot{\gamma}$ in Eq. 7.32:

$$\omega_{n_2} = |\lambda_2| = |\lambda_2^*| = \frac{1}{2}\left\{|\Delta| + \dot{\gamma}^2\left[\frac{I_{z'z'}}{I} - 2\right]^2 + 2\dot{\gamma}\sqrt{|\Delta|}\left[2 - \frac{I_{z'z'}}{I}\right]\sin\left(\frac{\phi}{2}\right)\right\}^{1/2} \tag{7.31}$$

$$\omega_{n_1} = |\lambda_1| = |\lambda_1^*| = \frac{1}{2}\left\{|\Delta| + \dot{\gamma}^2\left[\frac{I_{z'z'}}{I} - 2\right]^2 - 2\dot{\gamma}\sqrt{|\Delta|}\left[2 - \frac{I_{z'z'}}{I}\right]\sin\left(\frac{\phi}{2}\right)\right\}^{1/2} \tag{7.32}$$

Fig. 7.5(a) presents the natural frequencies for an acceleration of 2000 rad/s^2. For lower speeds, the influence of acceleration prevails (Section 7.1.5) and the absolute value of the eigenvalues occur nearby $\sqrt{\ddot{\gamma}}$ (Eq. 7.30). As speed increases, the frequency ω_{n_2} (Eq. 7.31) occurs near the first order (Section 7.1.4). Figure 7.5(b) shows that the positive part of eigenvalue λ_2 is greater for lower rotating speeds. Increase $\dot{\gamma}$ reduces the instability level of this system.

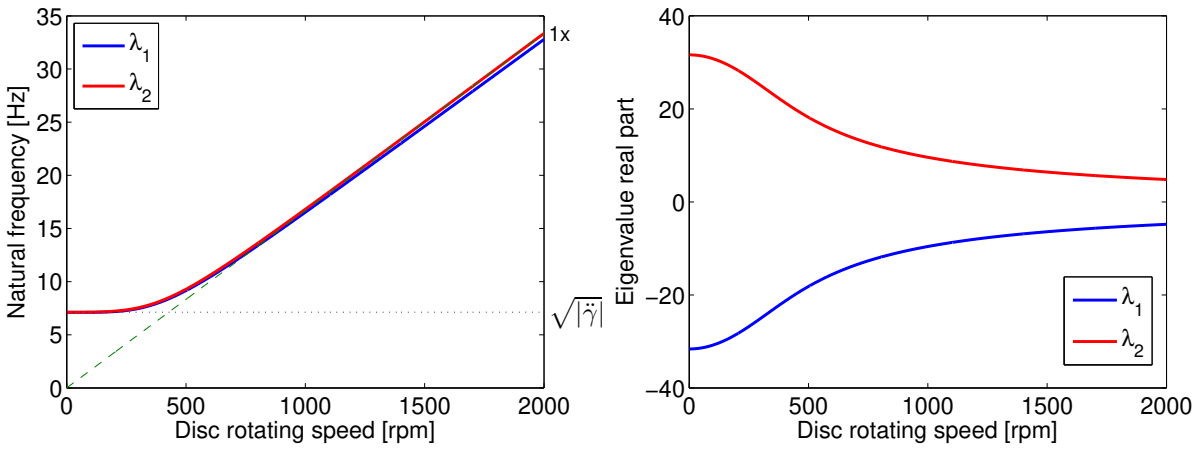

(a) (b)

Figure 7.5: Natural frequencies (Fig. 7.5(a)) and eigenvalue real parts (Fig. 7.5(b)) for $\ddot{\gamma} = 2000$ rad/s^2.

7.2 Modelling a rotating spring/viscous damper element with friction

The same sequence presented in Section 5.2 is followed to deduce the rotating element. Here the coordinate system shown in Section 7.1 will be used. First, the elastic and damping forces are defined on Section 7.2.1. Then, the relative motion between the element and the pressure plate is calculated on Section 7.2.2. The tangential relative speed and its approximated expression is deduced is on Section 7.2.3. Friction and normal forces are discussed on Section 7.2.4.

7.2.1 Elastic and damping forces

On coordinates $x'_3y'_3z'_3$, there is the position vector ${}_3\vec{r'}_{GQ} = \left\{ R_i\cos\psi_i \quad R_i\sin\psi_i \quad -h \right\}^T$, assuming the constant contact radius from Section 5.2.2. The procedure for the determination of contact forces is the same as the one as the case in Cardan coordinates. The total displacement ${}_0r'_{OQ_z}$ (Eq. 7.33) is obtained by adding a negative displacement ${}_0r'_{OG_z}$ of point G in relation to the system origin. The stiffness and damping efforts are given by Eqs. 7.33 and 7.34, respectively.

$$\begin{aligned} {}_0r'_{OQ_z} &= {}_0r'_{OG_z} + {}_0r'_{GQ_z} \\ &= -(z+z_e) - \sin\beta R_i\cos\psi_i + \sin\alpha\cos\beta R_i\sin\psi_i - h\cos\alpha\cos\beta \end{aligned} \tag{7.33}$$

$${}_0\vec{F'}_{k_i} = k_i\left[-h - {}_0r'_{OP'_z}\right]\vec{k} = {}_0F'_{k_i}\vec{k} \tag{7.34}$$

$${}_0\vec{F'}_{c_i} = c_i\left[-{}_0\dot{r'}_{OP'_z}\right]\vec{k} = {}_0F'_{c_i}\vec{k} \tag{7.35}$$

7.2.2 Relative motion between the element and pressure plate

The friction element/clutch disc rotating speed is calculated on the coordinate system $x'_3y'_3z'_3$ as Eq. 7.36:

$${}_3\vec{\omega'}_d = [R_{\gamma\beta\alpha}]^T \begin{Bmatrix} 0 \\ 0 \\ \dot{\theta} \end{Bmatrix} = \dot{\theta} \begin{Bmatrix} -\sin\beta \\ \sin\alpha\cos\beta \\ \cos\alpha\cos\beta \end{Bmatrix} \tag{7.36}$$

The rotating speed component of the disc (Eq. 7.37) comes from Eq. 7.9 presented on Section

7.1.2.

$$ {}_3\omega_{z'} = \dot{\gamma}\cos\gamma\cos\beta - \dot{\beta}\sin\alpha \tag{7.37} $$

Following the methodology from Section 5.2.4, Equation 7.38 shows that in this case the relative angular speed depends on the wobbling speed $\dot{\beta}$ as well as on $\dot{\gamma}$ and $\dot{\theta}$:

$$ \dot{\psi}_i = -\left({}_3\omega_{z'} - {}_3\omega'_{dz}\right) = -\left[\left(\dot{\gamma} - \dot{\theta}\right)\cos\gamma\cos\beta - \dot{\beta}\sin\alpha\right] \tag{7.38} $$

7.2.3 Approximation of the tangential speed at contact point

With the simplification step similar to the one found in Section 5.2.5, the relative tangential speed ${}_3\vec{V'}_{t_{rel}}$ is given by Eq. 7.39:

$$ {}_3\vec{V'}_{t_{rel}} = {}_3\vec{V'}_{t_{sup}} - {}_3\vec{V'}_{t_{inf}} \approx \begin{Bmatrix} -(\dot{\gamma}-\dot{\theta})\left(\alpha h + R_i\sin\psi_i\right) - h\dot{\beta} \\ (\dot{\gamma}-\dot{\theta})\left(R_i\cos\psi_i - \beta h\right) + \dot{\alpha}h \\ 0 \end{Bmatrix} \tag{7.39} $$

The normal vector on the direction of the relative tangential speed ($\vec{\nu}$) is approximated by Eq. 7.40. Similar terms are noted on the equations of motion on Hervé *et al.* (2009). It is important to note that terms that depend on the inverse of $|\dot{\gamma} - \dot{\theta}|$ multiply *only the wobbling angular speeds* $\dot{\alpha}$ and $\dot{\beta}$. The same unitary vector calculated for Cardan coordinates (Eq. 5.42) also presented such terms involving the wobbling angles α and β. These characteristics result in lower error in terms of wobbling angles near coupling on Appendices A.2 and B.2.

$$ {}_3\vec{\nu'} = \frac{{}_3\vec{V'}_{t_{rel}}}{\left|{}_3\vec{V'}_{t_{rel}}\right|} \approx \begin{Bmatrix} \left(-\sin\psi_i - \dfrac{h}{R_i}\alpha\right) sign(\dot{\gamma}-\dot{\theta}) - \dfrac{h\dot{\beta}}{|\dot{\gamma}-\dot{\theta}|R_i} \\ \left(\cos\psi_i - \dfrac{h}{R_i}\beta\right) sign(\dot{\gamma}-\dot{\theta}) + \dfrac{h\dot{\alpha}}{|\dot{\gamma}-\dot{\theta}|R_i} \\ 0 \end{Bmatrix} = \begin{Bmatrix} {}_3\nu'_x \\ {}_3\nu'_y \\ 0 \end{Bmatrix} \tag{7.40} $$

7.2.4 Normal and friction force calculation

The normal force of the element is given by Eq. 7.41 and its position in relation to the friction force ${}_3\vec{F'}_{fr_i}$ (Eq. 7.42) was presented in Fig. 5.8. With an equilibrium condition solved (Section 5.2.7 based on von Wagner *et al.* (2007)), an approximation of the amplitude of the normal force is given by Eq. 7.43.

$$ {}_3\vec{N'}_i = \left\{ \begin{array}{c} 0 \\ 0 \\ {}_3N'_i \end{array} \right\} \tag{7.41} $$

$$ {}_3\vec{F'}_{fr_i} = -\mu \, {}_3N'_i \, {}_3\vec{\nu'} \tag{7.42} $$

$$ {}_3N'_i \approx {}_0F'_{k_{i_z}} + {}_0F'_{c_{i_z}} + \mu k_i z_e sign(\dot{\gamma} - \dot{\theta}) \left(\cos\psi_i \alpha + \sin\psi_i \beta\right) \tag{7.43} $$

The moments of the friction and normal forces are given by Eqs. 7.44 and 7.45:

$$ {}_3\vec{M'}_{fr_i} = {}_3\vec{r'}_{GQ} \times {}_3\vec{F'}_{fr_i} \tag{7.44} $$

$$ {}_3\vec{M'}_{N_i} = {}_3\vec{r'}_{GQ} \times {}_3\vec{N'}_i \tag{7.45} $$

7.3 Efforts for a moving viscous damper and their relation with the element matrices

Beside the differences on the stability of the pure inertial system on Section 7.1.3, the assumption of the rotating speed on global coordinates will present another aspect for the moments assuming a rotating disc. As it will be presented in Sections 7.3.1 and 7.3.2, this approach results on damping forces with $\dot{\gamma} \neq 0$ or $\dot{\theta} \neq 0$.

7.3.1 Damping efforts for $\alpha \neq 0°$ and $\beta = 0°$

With $\alpha \neq 0°$ and $\beta = 0°$, Eqs. 7.33 and its derivative result on Eqs. 7.46 and 7.47. The vertical effort in this situation depends on $\dot{\gamma}$ and $\dot{\theta}$ (Eq. 7.48). For $\dot{\gamma} = 0$, they are exactly the same as Eqs. 5.60 and 5.61.

$$ {}_0r'_{OQ_z} = \sin\alpha R_i \sin\psi_i - h \tag{7.46} $$

$$ {}_0\dot{r}'_{OQ_z} = \sin\alpha R_i \cos\psi_i \dot{\psi}_i = (\dot{\theta} - \dot{\gamma}) \sin\alpha R_i \cos\psi_i \tag{7.47} $$

$$ {}_0\vec{F}'_{c_i} = -c_i \left[{}_0\dot{r}'_{OQ_z} \right] \vec{k} = c_i(\dot{\gamma} - \dot{\theta}) \sin\alpha R_i \cos\psi_i \vec{k} \tag{7.48} $$

The angle γ positioned on global coordinates represents the movement of *precession*. Fig. 7.6 have a sequence of conditions with $\gamma = 0°$, $45°$ and $90°$ for a static displacement $\alpha > 0$. Back on Fig. 5.20, the angular rotation did not change the height on the damper contact. On this case, *the precession movement allows the pressure plate to rotate with an constant inclination α for every rotating angle γ*. Point Q_1 present *positive damping forces* once that between Figs. 7.6(a),7.6(b) and 7.6(c) the distance l is *decreasing its height*. This situation is similar to Fig. 5.15(b).

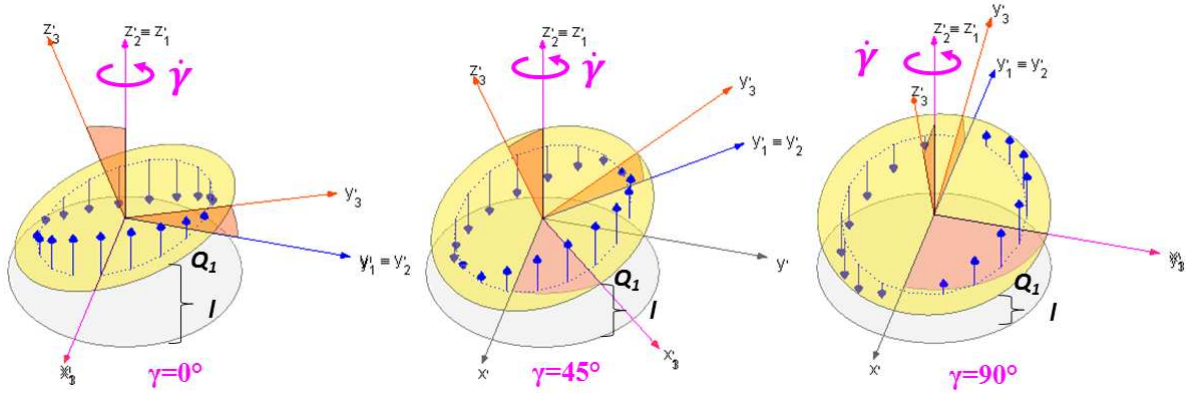

(a) (b) (c)

Figure 7.6: Damping forces for $\gamma = 0°$, $45°$ and $90°$ (Figs. 7.6(a), 7.6(b) and 7.6(c)) with $\alpha > 0$.

7.3.2 Damping efforts for $\beta \neq 0°$ and $\alpha = 0°$

The vertical displacement and speed on the contact becomes Eqs. 7.49 and 7.50 for $\beta \neq 0°$ and $\alpha = 0°$. With $\dot{\gamma} = 0$, Eqs. 5.63 and 7.50 are the same as Eqs. 5.63 and 5.64. The damping effort on this situation si represented by Eq. 7.51.

$$ {}_0r'_{OQ_z} = -\sin\beta R_i \cos\psi_i - h \tag{7.49} $$

$$ {}_0\dot{r'}_{OQ_z} = \sin\beta R_i \sin\psi_i \dot{\psi}_i = (\dot{\theta} - \dot{\gamma}) \sin\beta R_i \sin\psi_i \tag{7.50} $$

$$ {}_0\vec{F'}_{c_i} = -c_i \left[{}_0\dot{r'}_{OQ_z} \right] \vec{k} = c_i(\dot{\gamma} - \dot{\theta}) \sin\beta R_i \sin\psi_i \vec{k} \tag{7.51} $$

A precession movement with $\beta > 0$ is presented in Fig. 7.7 for $\gamma = 0°$, $45°$ and $90°$. Point Q_1 present *negative damping forces* once that between Figs. 7.7(a),7.7(b) and 7.7(c) the distance l is *increasing its height*. This situation is similar to Fig. 5.15(a).

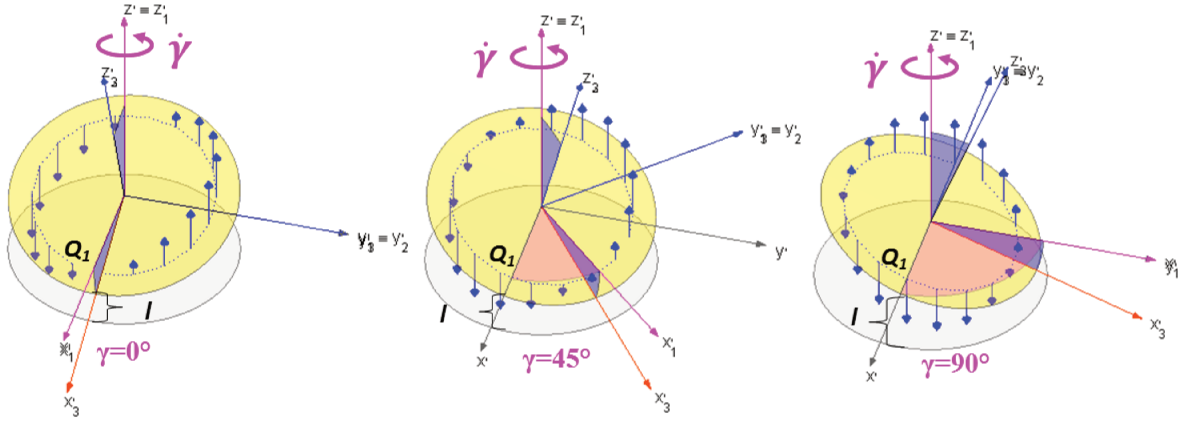

(a) (b) (c)

Figure 7.7: Damping forces for $\gamma = 0°$, $45°$ and $90°$ (Figs. 7.7(a), 7.7(b) and 7.7(c)) with $\beta > 0$.

7.3.3 Related element matrices

The matrix $[K'_{IV}]_i$ (Eq. 7.58) depends on the relative speed $\dot{\psi}_i$, once that this coordinate system allow the models to replicates the movement for $\dot{\theta} \neq 0$ (Sections 5.4.1 and 5.4.2) and $\dot{\gamma} \neq 0$ (Sections 7.3.1 and 7.3.2). In case of friction on the contact, $[K'_V]_i$ (Eq. 7.59) includes the effect from this additional normal force.

7.4 Element matrices

Just like the previous case (Section 5.5), the expressions of the angular speeds (Eq. 5.9) and accelerations (Eq. 5.10) are necessary for the equations of motion describing the wobbling movement of the pressure plate (Eq. 7.52), calculated using the torque contribution of the *ith* element. Auxiliary angles derivatives, are also included. Just l

$$\begin{cases} I_{x'x'}\,{}_3\dot{\omega}_{x'} - (I_{y'y'} - I_{z'z'})\,{}_3\omega_{y'}\,{}_3\omega_{z'} = \sum_{i=1}^{n} {}_3M_{x'_i} \\ I_{y'y'}\,{}_3\dot{\omega}_{y'} - (I_{z'z'} - I_{x'x'})\,{}_3\omega_{z'}\,{}_3\omega_{x'} = \sum_{i=1}^{n} {}_3M_{y'_i} \\ m\,{}_0\ddot{r}'_{OG_{z'}} = \sum_{i=1}^{n} \left({}_0N'_i + {}_3F'_{fr_{i_z}}\right) - F_{z'} \\ \dot{\psi}_i = -\left({}_3\omega'_z - {}_3\omega_{dz}\right) = -\left[\left(\dot{\gamma} - \dot{\theta}\right)\cos\gamma\cos\beta - \dot{\beta}\sin\alpha\right] \end{cases} \tag{7.52}$$

The equations of motion of this system are described by Eq. 7.53.The mass $[M]$ and gyroscopic matrices ($[G]$ and $[H_1(\dot{\gamma})]$) were developed on Section 7.1.3. With the assumption of constant rotating speed, the inertial term $[H_2(\ddot{\gamma})]$ (Eq. 7.15) is not included on the formulations. The element matrices ($[K'_i]$,$[C'_i]$) and effort arrays $\{f_i\}$ will be presented on Sections 7.4.1, 7.4.3, and 7.4.3.

$$[M]\{\ddot{p}\} + \left([G] + \sum_{i=1}^{n}[C'_i]\right)\{\dot{p}\} + \left([H_1(\dot{\gamma})] + \sum_{i=1}^{n}[K'_i]\right)\{p\} = \sum_{i=1}^{n}\{f'_i\} + \{F\} \tag{7.53}$$

7.4.1 Element stiffness components

The matrices for the rotating speed on global coordinates depend only on ψ_i. The relative movement between the pressure plate and spring/damper element generate a stiffness matrix that can be formed from the combination of 6 different matrices (Eq. 7.54), each one having an characteristic feature. In order to simulate a linearized version, it is possible to substitute $N_0 = k_i z_e$ (Section 5.2.2).

$$[K'_i] = [K'_I]_i + [K'_{II}]_i + [K'_{III}]_i + [K'_{IV}]_i + [K'_V]_i + [K'_{VI}]_i \tag{7.54}$$

Matrices $[K'_I]_i$ (Eq. 7.55), $[K'_{II}]_i$ (Eq. 7.56) and $[K'_{III}]_i$ (Eq. 7.57) can be obtained by imposing $\gamma = 0°$ on Eqs. 5.70, 5.71 and 5.72 from the case using Cardan coordinates.

$$[K'_I]_i = k_i \begin{bmatrix} R_i^2\sin^2\psi_i & -(R_i^2/2)\sin(2\psi_i) & -R_i\sin\psi_i \\ -(R_i^2/2)\sin(2\psi_i) & (R_i^2/2)\cos^2\psi_i & R_i\cos\psi_i \\ -R_i\sin\psi_i & R_i\cos\psi_i & 1 \end{bmatrix} \tag{7.55}$$

$$[K'_{II}]_i = \mu^2 h k_i z_e \begin{bmatrix} \cos^2\psi_i & (1/2)\sin(2\psi_i) & 0 \\ (1/2)\sin(2\psi_i) & \sin^2\psi_i & 0 \\ 0 & 0 & 0 \end{bmatrix} \tag{7.56}$$

$$[K'_{III}]_i = \mu sign(\dot{\gamma} - \dot{\theta}) \begin{bmatrix} -k_i h(R_i/2)\sin(2\psi_i) & k_i h R_i \cos^2\psi_i & k_i h \cos\psi_i \\ -k_i h R_i \sin^2\psi_i & k_i h(R_i/2)\sin(2\psi_i) & k_i h \sin\psi_i \\ 0 & 0 & 0 \end{bmatrix} \tag{7.57}$$

7.4.2 Characteristics for the rotating speed on the global reference system

In Section 5.5.2, the damping related contributions on the stiffness matrices (Eqs. 5.73 and 5.74) were related to the friction element rotating speed $\dot{\theta}$. One greater difference obtained for this case is presented on $[K'_{IV}]_i$ (Eq. 7.58) and $[K'_V]_i$ (Eq. 7.59) that depend on the relative speed $\dot{\psi}$ only. Such terms does not occur on the literature (Hervé *et al.* (2008b), Hervé *et al.* (2009)) and they are consequence on the initial assumption of relative movement between the friction element and the pressure plate.

$$[K'_{IV}]_i = c_i \dot{\psi}_i \begin{bmatrix} (R_i^2/2)\sin(2\psi_i) & R_i^2 \sin^2\psi_i & 0 \\ -R_i^2 \cos^2\psi_i & -(R_i^2/2)\sin(2\psi_i) & 0 \\ -R_i \cos\psi_i & -R_i \sin\psi_i & 0 \end{bmatrix} \tag{7.58}$$

$$[K'_V]_i = \mu h c_i \dot{\psi}_i sign(\dot{\gamma} - \dot{\theta}) \begin{bmatrix} -R_i \cos^2\psi_i & -(R_i/2)\sin(2\psi_i) & 0 \\ -(R_i/2)\sin(2\psi_i) & -R_i \sin^2\psi_i & 0 \\ 0 & 0 & 0 \end{bmatrix} \tag{7.59}$$

A specific term is represented by $[K'_{VI}]_i$ (Eq. 7.60), where the friction force cause a stiffness contribution that depends on the ratio h^2/R_i. For its equivalent counterpart on Cardan coordinates (Eq. 5.75), such terms would not influence the system if the clutch disc does not rotate $\dot{\theta} = 0$. Here, the skew symmetric terms provided by Eq. 7.60 are *unavoidable* if $\mu \neq 0$.

$$[K'_{VI}]_i = \mu \left(\frac{h^2}{R_i}\right) k_i z_e sign(\dot{\gamma} - \dot{\theta}) \begin{bmatrix} 0 & -1 & 0 \\ 1 & 0 & 0 \\ 0 & 0 & 0 \end{bmatrix} \tag{7.60}$$

7.4.3 Element damping components

The element damping matrix $[C_i']$ (7.61) is composed by a pure damping matrix $[C_I']_i$ (Eq. 7.62) and a friction related one $[C_{II}']_i$ (Eq. 7.63). The matrix $[C_{III}']_i$ (Eq. 7.64) depends on the inverse o the relative speed $\dot{\gamma} - \dot{\theta}$ and represents the friction damping effect. Similar terms occur on Hervé *et al.* (2009). These matrices can be obtained from Eqs. 5.77, 5.78 and 5.79 with the imposition of $\gamma = 0°$.

$$[C_i'] = [C_I']_i + [C_{II}']_i + [C_{III}']_i \tag{7.61}$$

$$[C_I']_i = c_i \begin{bmatrix} R_i^2 \sin^2 \psi_i & -(R_i^2/2)\sin(2\psi_i) & -R_i \sin \psi_i \\ -(R_i^2/2)\sin(2\psi_i) & (R_i^2/2)\cos^2 \psi_i & R_i \cos \psi_i \\ -R_i \sin \psi_i & R_i \cos \psi_i & 1 \end{bmatrix} \tag{7.62}$$

$$[C_{II}']_i = c_i \mu h sign(\dot{\gamma} - \dot{\theta}) \begin{bmatrix} -(R_i/2)\sin(2\psi_i) & R_i \cos^2 \psi_i & \cos \psi_i \\ -R_i \sin^2 \psi_i & (R_i/2)\sin(2\psi_i) & \sin \psi_i \\ 0 & 0 & 0 \end{bmatrix} \tag{7.63}$$

$$[C_{III}']_i = \frac{\mu h^2 k_i z_e}{R_i |\dot{\gamma} - \dot{\theta}|} \begin{bmatrix} 1 & 0 & 0 \\ 0 & 1 & 0 \\ 0 & 0 & 0 \end{bmatrix} \tag{7.64}$$

7.4.4 Excitation vector

The excitation vector $\{f_i\}$ takes into account terms that depend on $k_i z_e$ (Eq. 7.65). It is equal to the the results given on Eq. 5.80.

$$\{f_i'\} = \begin{Bmatrix} k_i z_e R_i \sin \psi_i - \mu h k_i z_e \cos \psi_i sign(\dot{\gamma} - \dot{\theta}) \\ -k_i z_e R_i \cos \psi_i - \mu h k_i z_e \sin \psi_i sign(\dot{\gamma} - \dot{\theta}) \\ -k_i z_e \end{Bmatrix} \tag{7.65}$$

7.4.5 Very important remarks on the stability study of this system

The element matrices from Section 7.4 depend on the relative position angle ψ_i. The comments from Section 5.5.5 are also valid for this case.

8 Hipothesis 2: Wobbling modes and characteristics of systems with equal and symmetrically distributed elements

The element matrices from Section 7.2 (Hypothesis 2) are gradually included on the model in order to verify the influence of rotating speed (Section 8.1), cushion stiffness and relative speed (Section 8.2). Finally, the viscous damping influence is provided by Sections 8.3 and 8.4.

8.1 Rotating speed influence

Initially, the element matrices $[K'_I]_i$ (Eq. 7.55) , $[K'_{II}]_i$ (Eq. 7.56) and $[K'_{III}]_i$ (Eq. 7.57) from Section 7.4.1 were applied , removing the influence of the friction damping terms. Combining elements for $\psi_{i0} = 0°$, $90°$, $180°$ and $270°$ results on the model from Eq. 8.1. The elements inside the stiffness matrix are given by k_{11} (Eq. 8.2) and k_{12} (Eq. 8.3), respectively. An important characteristic on this approach is the existence of inertia terms that depending on the rotating speed in k_{11} ($\dot{\gamma}^2(I_{z'z'} - I)$). These formulation is practically the one found on Hervé *et al.* (2008b) adding the terms with μ^2, changing the physical disposition of the elements.

$$\begin{bmatrix} I & 0 & 0 \\ 0 & I & 0 \\ 0 & 0 & m \end{bmatrix} \begin{Bmatrix} \ddot{\alpha} \\ \ddot{\beta} \\ \ddot{z} \end{Bmatrix} + \dot{\gamma} \begin{bmatrix} 0 & -2I + I_{z'z'} & 0 \\ 2I - I_{z'z'} & 0 & 0 \\ 0 & 0 & 0 \end{bmatrix} \begin{Bmatrix} \dot{\alpha} \\ \dot{\beta} \\ \dot{z} \end{Bmatrix} + \begin{bmatrix} k_{11} & k_{12} & 0 \\ -k_{12} & k_{22} & 0 \\ 0 & 0 & 4k \end{bmatrix} \begin{Bmatrix} \alpha \\ \beta \\ z \end{Bmatrix} = \begin{Bmatrix} 0 \\ 0 \\ 0 \end{Bmatrix} \quad (8.1)$$

$$k_{11} = (2R^2 + 2\mu^2 z_e h)k + \dot{\gamma}^2(I_{z'z'} - I) \quad (8.2)$$

$$k_{12} = \left[2\mu kRh - 4\mu(h^2/R)kz_e\right] sign(\dot{\gamma}) \quad (8.3)$$

An example is tested with the same data from the model in cardan coordinates (Section 6.1) (m = 2 kg, R = 0.0875 m, μ = 0.3, h = 0.01 m and k = $3 \times 10^6/4$ N/m) and $\dot{\gamma}$ ranges from 1 to 8000 rpm. Looking at Fig. 8.1(a) it is possible to see that the frequencies do not increase as a line like the model on cardan coordinates (Fig. 6.4(a)). The stable and unstable modes present natural frequencies really close to each other that change like a polynomial curve, reaching 234.4 and 232.2 Hz at 8000 rpm, respectively. At 1 rpm, both frequencies are closer to 192.2 Hz.

The numerical derivatives from the curves on Fig. 8.1(a) are presented on Fig. 8.1(b). It

is possible to see that, at 8000 rpm, both eigenvalues have a maximum positive increase rate that is lower than 0.02 Hz/rpm. The representation obtained on Cardan coordinates (Section 6.1) had similar increasing rates at 2000 rpm (Fig. 6.4(b)).

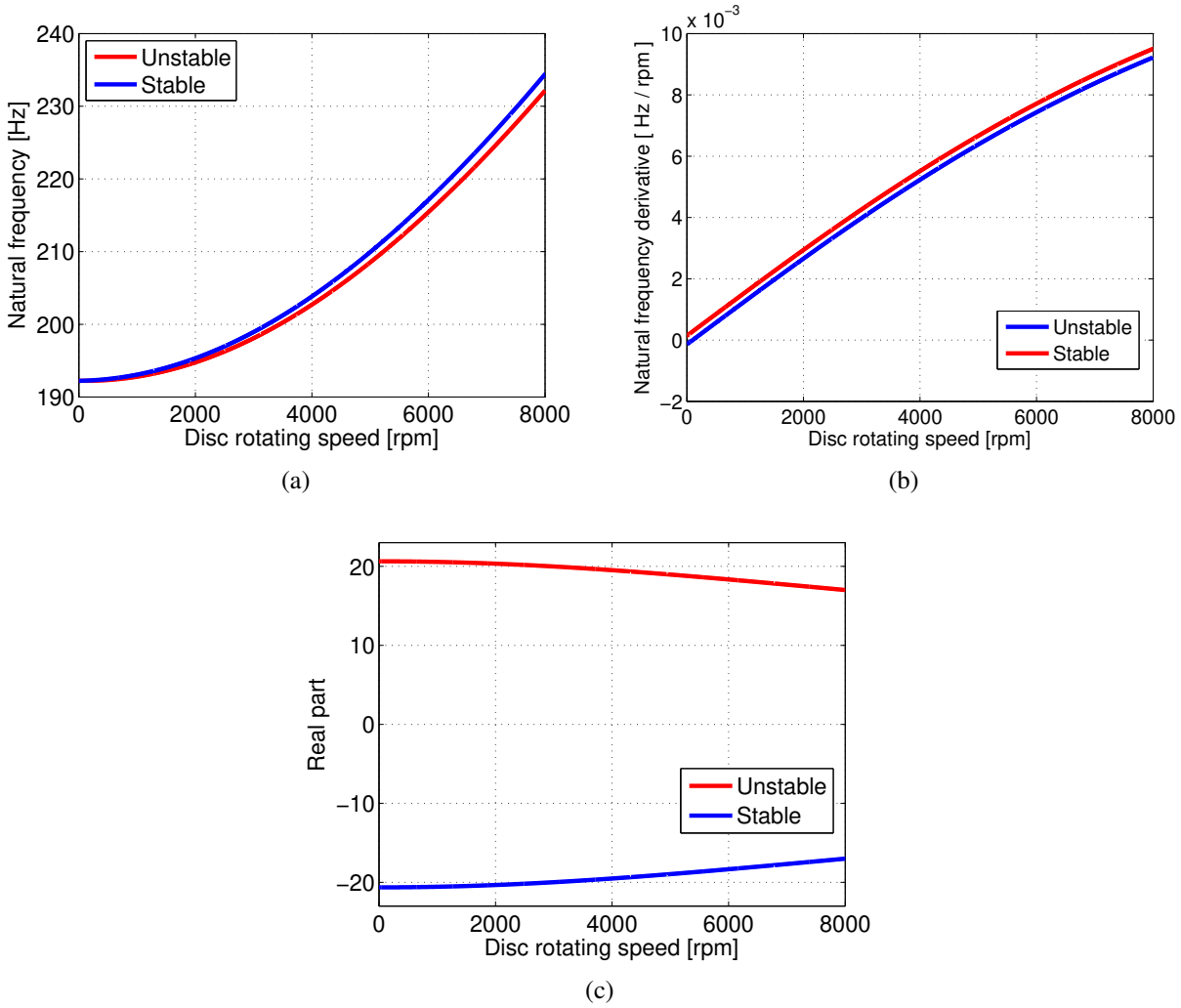

Figure 8.1: Natural frequencies according to the rotating speed ($\dot{\gamma} > 0$ and $\dot{\theta} = 0$).

An important conclusion that comes from the results from Fig. 8.1:

- *the model becomes less sensitive to modifications on the pressure plate rotating speed if it is assumed on the global reference system.* Thinking on the real measurements from Fig. 1.1, it is possible to note a constant frequency in relation to variations of the engine rotating speed. It is still very early in terms of research to take this step without taking into account all possible nonlinear effects and deep structural analysis, but the rotating speed on global coordinates seems to be more suited for this condition. It is not possible to locate any clear

comment on that in Hervé *et al.* (2008b), Hervé *et al.* (2008a) and Hervé *et al.* (2009). As consequence of these considerations, the formulation on Chapters 10, 11, and 12 will be done using it.

The real part of the eigenvalues changed with speed, as presented in Fig. 8.1(c). The unstable case had a real value close to 20 while the stable one presented values nearby -20 at 1 rpm. With higher rotating speeds, the absolute value from the real part of the eigenvalues reached 17 at 8000 rpm.

8.1.1 Unstable motion - Forward wobbling with $\dot{\gamma} > 0$ and $\dot{\theta} = 0$

The unstable motion is represented by Eq. 8.4, is the same as the one on Eq. 6.12. Likewise the previous case, unstable motion can be described by Fig. 6.14. The wobbling characteristics were not affected by the coordinate system.

$$\begin{Bmatrix} X_{11} \\ X_{21} \end{Bmatrix} = \begin{Bmatrix} 1 \\ -j \end{Bmatrix} = \begin{Bmatrix} 1 \\ \exp\left(-j\frac{\pi}{2}\right) \end{Bmatrix}, \text{ for } \dot{\gamma} > 0 \text{ and } \dot{\theta} = 0 \tag{8.4}$$

8.1.2 Stable motion - Backward wobbling for $\dot{\gamma} > 0$ and $\dot{\theta} = 0$

The stable mode shape found on this coordinate system is written as in Eq. 8.5. Looking at Section 6.1.1, it is the same as Eq. 6.6. The stable wobbling motion still apparently moves backwards in relation to the rotating speed. This motion is still physically described by 6.9.

$$\begin{Bmatrix} X_{12} \\ X_{22} \end{Bmatrix} = \begin{Bmatrix} 1 \\ j \end{Bmatrix} = \begin{Bmatrix} 1 \\ \exp\left(j\frac{\pi}{2}\right) \end{Bmatrix}, \text{ for } \dot{\gamma} > 0 \text{ and } \dot{\theta} = 0 \tag{8.5}$$

8.2 Stiffness and relative speed influence

The model from Eq. 8.6 is obtained from Eq. 8.1 with the inclusion of friction damping, given by matrix $[C'_{III}]_i$ (Eq. 7.64). The skew symmetric terms are a little bit different from the previous case (Eq. 8.7). The terms $c_{11} = c_{22}$ (Eq. 8.8) have the same dependence on the relative speed from Eq. 6.18.

$$\begin{bmatrix} I & 0 & 0 \\ 0 & I & 0 \\ 0 & 0 & m \end{bmatrix} \begin{Bmatrix} \ddot{\alpha} \\ \ddot{\beta} \\ \ddot{z} \end{Bmatrix} + \left(\dot{\gamma} \begin{bmatrix} 0 & -2I + I_{z'z'} & 0 \\ 2I - I_{z'z'} & 0 & 0 \\ 0 & 0 & 0 \end{bmatrix} + \begin{bmatrix} c_{11} & 0 & 0 \\ 0 & c_{22} & 0 \\ 0 & 0 & 0 \end{bmatrix} \right) \begin{Bmatrix} \dot{\alpha} \\ \dot{\beta} \\ \dot{z} \end{Bmatrix} +$$
$$+ \begin{bmatrix} (2R^2 + 2\mu^2 z_e h)k + \dot{\gamma}^2(I_{z'z'} - I) & k_{12} & 0 \\ -k_{12} & (2R^2 + 2\mu^2 z_e h)k + \dot{\gamma}^2(I_{z'z'} - I) & 0 \\ 0 & 0 & 4k \end{bmatrix} \begin{Bmatrix} \alpha \\ \beta \\ z \end{Bmatrix} = \begin{Bmatrix} 0 \\ 0 \\ 0 \end{Bmatrix} \tag{8.6}$$

$$k_{12} = \left[2\mu k R h - 4\mu (h^2/R) k z_e \right] sign(\dot{\gamma}) \tag{8.7}$$

$$c_{11} = c_{22} = 4 \frac{\mu h^2 k z_e}{R|\dot{\gamma} - \dot{\theta}|} \tag{8.8}$$

The foward/backward wobbling frequencies are close to each other (Fig. 8.2(a)). On this approach, only the axial mode is affected by low stiffness values (Fig. 8.2(b)). Higher cushion stiffness (approximately above 10^4 N/m) caused all natural frequencies to get closer to each other. The graphic on logarithmic scale indicates that the axial mode frequency follows the wobbling modes (Fig. 8.2(b)). Once again, greater values of stiffness resulted on increase of the real part of the forward eigenvalue on Fig. 8.3(a). The formulation on Eq. 8.6 is very similar to the one found on Hervé *et al.* (2009).

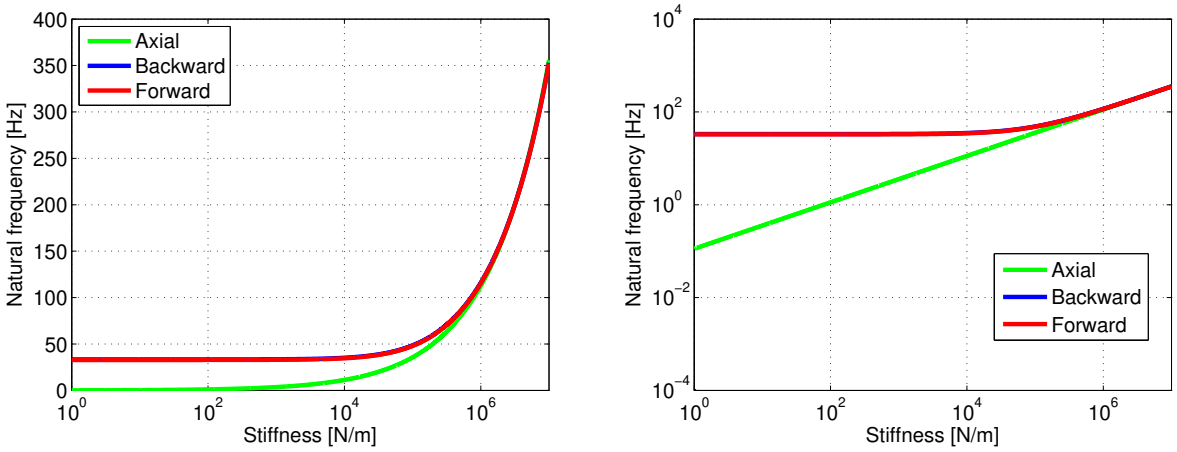

(a) (b)

Figure 8.2: Natural frequencies according to cushion stiffness in linear (Fig. 8.2(a)) and logarithmic (Fig. 8.2(b)) scales.

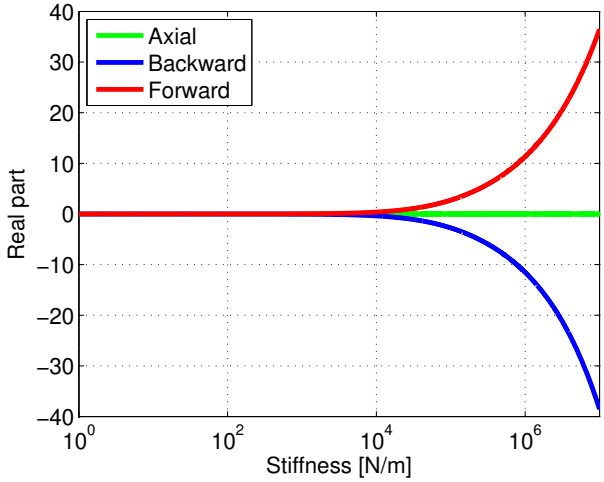

(a)

Figure 8.3: The real part of the eigenvalues.

Figure 8.4(a) shows that all eigenvalues are closer for $\dot{\gamma} = 2000$ rpm and they are not affected by the relative angular speed. The model with rotating speeds on global coordinates, is stabilized by friction damping (Fig. 8.4(b)). Modification on the stability also occurs due to the signal of relative speed (Hervé *et al.*, 2008b).

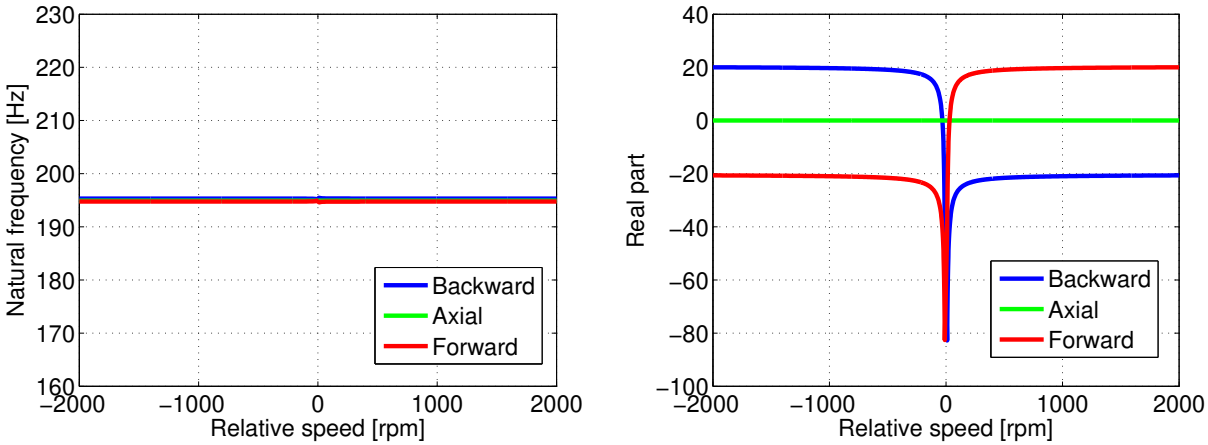

(a) (b)

Figure 8.4: Natural frequencies (Fig. 8.4(a)) and real parts (Fig. 8.4(b)) in relation to the relative speed considering a total cushion stiffness of 3×10^6 N/m.

8.3 System with viscous damping effects

The model from Eq. 8.9 is obtained considering $\mu = 0$ on Eq. 8.6 with additional terms related to equally distributed viscous damping elements, using matrices $[K'_{IV}]_i$ (Eq. 7.58) and $[C'_I]_i$ (Eq. 7.62).

$$\begin{bmatrix} I & 0 & 0 \\ 0 & I & 0 \\ 0 & 0 & m \end{bmatrix} \begin{Bmatrix} \ddot{\alpha} \\ \ddot{\beta} \\ \ddot{z} \end{Bmatrix} + \left(\begin{bmatrix} 0 & \dot{\gamma}\left(I_{zz} - 2I\right) & 0 \\ -\dot{\gamma}\left(I_{zz} - 2I\right) & 0 & 0 \\ 0 & 0 & 0 \end{bmatrix} + \begin{bmatrix} 2cR^2 & 0 & 0 \\ 0 & 2cR^2 & 0 \\ 0 & 0 & 4c \end{bmatrix} \right) \begin{Bmatrix} \dot{\alpha} \\ \dot{\beta} \\ \dot{z} \end{Bmatrix} +$$
$$+ \begin{bmatrix} 2kR^2 + \dot{\gamma}^2(I_{z'z'} - I) & 2cR^2\dot{\psi} & 0 \\ -2cR^2\dot{\psi} & 2kR^2 + \dot{\gamma}^2(I_{z'z'} - I) & 0 \\ 0 & 0 & 4k \end{bmatrix} \begin{Bmatrix} \alpha \\ \beta \\ z \end{Bmatrix} = \begin{Bmatrix} 0 \\ 0 \\ 0 \end{Bmatrix} \tag{8.9}$$

The moving damping effort on this case (Eq. 8.10) depends on $\dot{\psi} = -\dot{\gamma} + \dot{\theta}$. If $\dot{\psi} > 0$, the moment $\vec{M'}_{mov}$ have signals equal to Eq. 6.21. In a situation of instability, this effort excites the *forward wobbling mode*, as represented by Fig. 6.20.

$$\vec{M'}_{mov} = \begin{Bmatrix} M'_{mov_x} \\ M'_{mov_y} \end{Bmatrix} = -2cR^2|\dot{\psi}|sign(\dot{\psi}) \begin{Bmatrix} \beta(t) \\ -\alpha(t) \end{Bmatrix} = -2cR^2|\dot{\psi}| \begin{Bmatrix} \beta(t) \\ -\alpha(t) \end{Bmatrix} \tag{8.10}$$

On the other hand, if $\dot{\psi} < 0$ the orientation of those efforts is changed (Eq. 8.11). This is a specific characteristic for hypothesis 2, where the movement of the inclined plate creates the damping efforts (Section 7.3).

$$\vec{M'}_{mov} = \begin{Bmatrix} M'_{mov_x} \\ M'_{mov_y} \end{Bmatrix} = 2cR^2|\dot{\psi}| \begin{Bmatrix} \beta(t) \\ -\alpha(t) \end{Bmatrix} \tag{8.11}$$

8.4 System with viscous damping and friction

Equation 8.12 is obtained from the previous system (Eq. 8.6) using matrices $[C'_I]_i$ and $[C'_{II}]_i$ (Eqs. 7.62 and 7.63). The matrices $[K'_{IV}]_i$ and $[K'_V]_i$ (Eqs. 7.58 and 7.59) introduced terms related to $\dot{\psi} = -\dot{\gamma} + \dot{\theta}$ on Eqs. 8.13 and 8.14.

$$\begin{bmatrix} I & 0 & 0 \\ 0 & I & 0 \\ 0 & 0 & m \end{bmatrix} \begin{Bmatrix} \ddot{\alpha} \\ \ddot{\beta} \\ \ddot{z} \end{Bmatrix} + \left(\dot{\gamma} \begin{bmatrix} 0 & -2I + I_{z'z'} & 0 \\ 2I - I_{z'z'} & 0 & 0 \\ 0 & 0 & 0 \end{bmatrix} + \begin{bmatrix} c_{11} & c_{12} & 0 \\ -c_{21} & c_{22} & 0 \\ 0 & 0 & 4c \end{bmatrix} \right) \begin{Bmatrix} \dot{\alpha} \\ \dot{\beta} \\ \dot{z} \end{Bmatrix} + \\ + \begin{bmatrix} k_{11} & k_{12} & 0 \\ -k_{12} & k_{22} & 0 \\ 0 & 0 & 4k \end{bmatrix} \begin{Bmatrix} \alpha \\ \beta \\ z \end{Bmatrix} = \begin{Bmatrix} 0 \\ 0 \end{Bmatrix} \tag{8.12}$$

$$k_{11} = k_{22} = (2R^2 + 2\mu^2 z_e h)k + \dot{\gamma}^2(I_{z'z'} - I) - 2\mu hc\dot{\psi} sign(\dot{\gamma} - \dot{\theta}) \tag{8.13}$$

$$k_{12} = \mu \left[2kRh - 4(h^2/R)kz_e \right] sign(\dot{\gamma} - \dot{\theta}) + 2cR^2\dot{\psi} \tag{8.14}$$

$$c_{11} = c_{22} = 4\frac{\mu h^2 k z_e}{R|\dot{\gamma} - \dot{\theta}|} + 2cR^2 \tag{8.15}$$

$$c_{12} = c_{21} = 2\mu cRh sign(\dot{\gamma} - \dot{\theta}) \tag{8.16}$$

Figures 8.5(a) and 8.5(b) presents simulations varying -2000 rpm $< \dot{\theta} < 6000$ rpm with $\dot{\gamma} = 2000$ rpm with results similar to the case on Cardan coordinates (Section 6.3). For the total cushion stiffness off 3×10^2 N/m and $c = 5$ Ns/m, the natural frequencies remained close, as presented in Fig. 8.5(a). The forward mode is unstable for $\dot{\gamma} - \dot{\theta} < -2000$ rpm (Fig. 8.5(b)).

Under hypothesis 2, it is possible to induce instabilities by modifications on the rotating speed of the pressure plate (-2000 rpm $< \dot{\gamma} < 6000$ rpm), maintaining $\dot{\theta} = 2000$ rpm. With lower stiffness, the natural frequencies (Fig. 8.5(c)) were affected by rotation. There is a similar profile to the inertial system from Section 7.1.4 presented on Fig. 7.1.4. The rotating speed on global coordinates allowed the generation of moments related to the movement of the plate in relation to the element (Section 7.3). The real part of the eigenvalue related to the forward mode was greater for $\dot{\gamma} - \dot{\theta} < 0$ ($\dot{\psi} > 0$).

With a total cushion stiffness off 3×10^6 N/m and $c = 30$ Ns/m, Figure 8.5(e) shows that the natural frequencies are not significantly affected by the relative speed ($\dot{\gamma} - \dot{\theta}$). On the other hand, the real part of the eigenvalues indicate stability (Fig. 8.5(f)) and they are affected by the terms that depend on $\dot{\psi}$ on Eqs. 8.14 and 8.15. It depends on the relation between $\dot{\gamma}$ and $\dot{\theta}$.

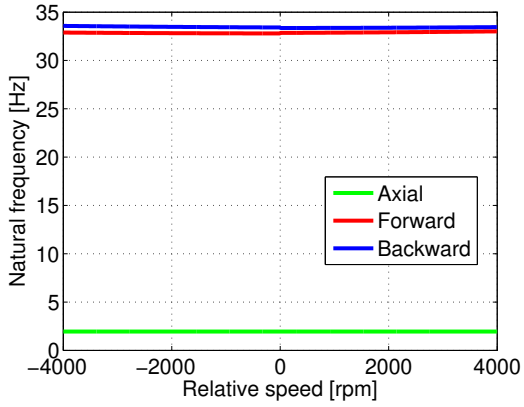

(a) $\dot{\gamma} = 2000$ rpm, $c = 5$ Ns/m, and $k_{cushion} = 3 \times 10^2$ N/m

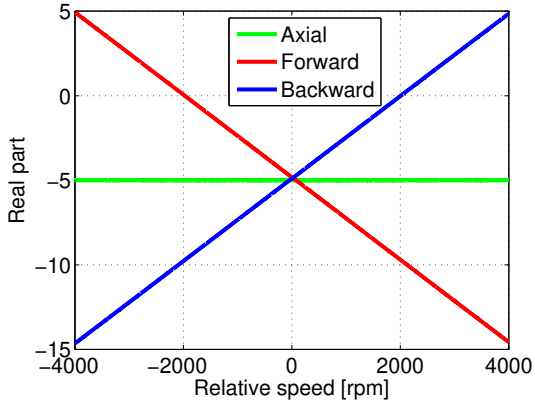

(b) $\dot{\gamma} = 2000$ rpm, $c = 5$ Ns/m, and $k_{cushion} = 3 \times 10^2$ N/m

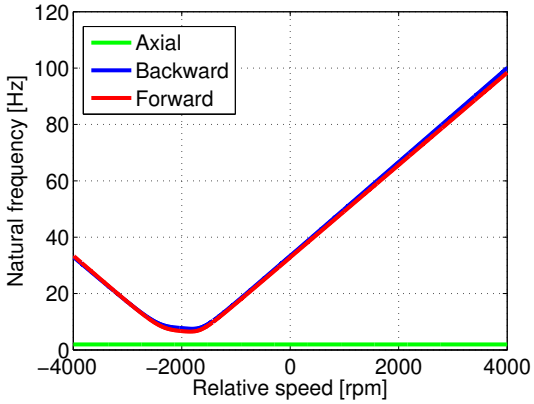

(c) $\dot{\theta} = 2000$ rpm, $c = 5$ Ns/m, and $k_{cushion} = 3 \times 10^2$ N/m

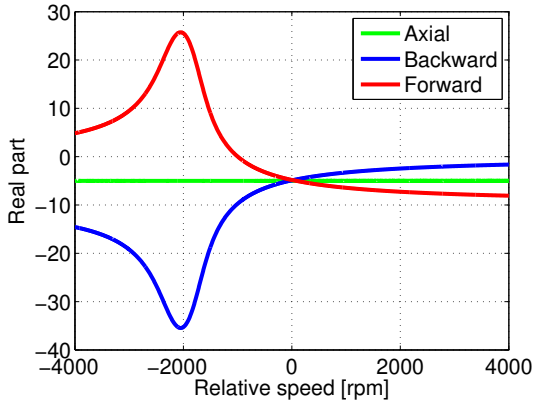

(d) $\dot{\theta} = 2000$ rpm,$c = 5$ Ns/m, and $k_{cushion} = 3 \times 10^2$ N/m

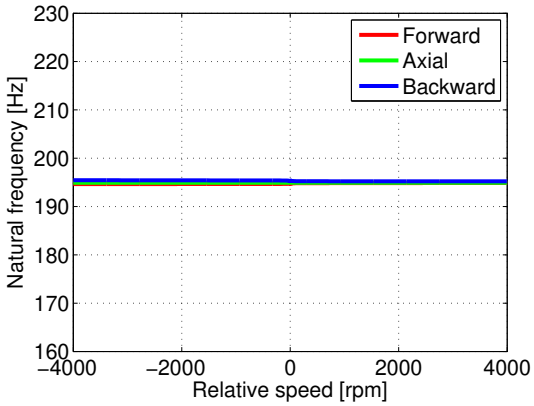

(e) $\dot{\gamma} = 2000$ rpm, $c = 30$ Ns/m, and $k_{cushion} = 3 \times 10^6$ N/m

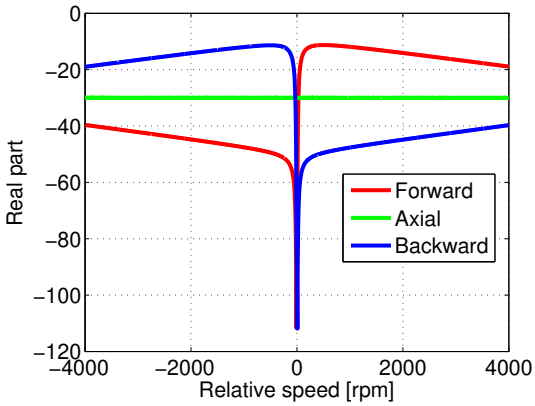

(f) $\dot{\gamma} = 2000$ rpm, $c = 30$ Ns/m, and $k_{cushion} = 3 \times 10^6$ N/m

Figure 8.5: Natural frequencies real parts in relation to the relative speed ($\dot{\gamma} - \dot{\theta}$).

8.5 Chapter summary

The observations from this chapter are separated into different physical domains:

8.5.1 Rotating speeds

In this chapter it was possible to observe for the model keeping the rotating speed on global coordinates ($\dot{\gamma} \neq 0$ and $\dot{\theta} = 0$):

- the natural frequencies are closer, but the one from the stable mode was greater than the value found for the unstable case.
- natural frequencies increase with the pressure plate rotating speed in a polynomial form.
- models obtained using these coordinates are less sensitive to the pressure plate rotating speed.
- the wobbling movements are the same as the ones obtained in Cardan coordinates.

8.5.2 Relative speed

The relative speed resulted on the following conditions on the simulations:

- Friction damping stabilized the model near coupling conditions, according to the findings from von Wagner *et al.* (2007).
- The axial mode remained stable for all situations.
- Due to the modification on the direction o friction moments, the forward mode was unstable for $\dot{\gamma} - \dot{\theta} > 0$. Such relations were first proposed by Hervé *et al.* (2008b).
- The backward mode became unstable for $\dot{\gamma} - \dot{\theta} < 0$.

8.5.3 Stiffness

From the previous simulations, it was possible to verify that, for low stiffness, only the axial mode frequency was modified.

For high cushion stiffness, the following behaviour was observed:

- All frequencies became very close to each other.
- Greater values of stiffness increased the real part from the eigenvalue for the forward mode.

8.5.4 Viscous damping

- Due to the consideration of viscous damping and relative movement between the pressure plate/element, the model with the rotating speed on global coordinates presented instability according to the relation between the engine and clutch disc rotating speeds in situation of low values of cushion stiffness.

9 Cushion heterogeneity

All the literature on clutch squeal takes into account symmetrically distributed friction elements, with equal physical properties for the contact (Chapter 3). The element matrices from Sections 5.5 and 7.4 were created with the intention of allowing more complex distributions in terms of position, stiffness, damping and friction coefficient. Those differences may emerge from:

- manufacturing problems or characteristics from production.
- uneven wear on the surfaces or more complex tribological interactions on the contact.
- intentional modifications made in order to generate prototypes.

Senatore *et al.* (2013) modelled the pressure plate with equally distributed elements, resulting on an axial movement decoupled from the wobbling motion. This chapter will show that even small changes on the position of the contact element may result in important modifications on the system behaviour. When the total stiffness is not balanced in relation to the axis, there is coupling between angular displacements and axial motion. Based on the conclusions from these simulations, Section 9.2 will be more specific focusing on the situations with proportional error on the total stiffness values without coupling with the vertical motions.

9.1 Position error simulations

Figure 9.1(a) represents a pressure plate with equally space elements ($\psi_{10} = 0°$,$\psi_{20} = 90°$,$\psi_{30} = 180°$ and $\psi_{40} = 270°$). A schematic of a deviation of $5°$ ($\psi_{20} = 95°$) on the position of element 2 is displayed on Fig. 9.1(b).

The element from Section 5.2 modelled on Cardan coordinates presents inertia matrices depending on γ (Eq. 5.12) and element matrices depending on γ and ψ (Section 5.5). It offers two possibilities for modifications on the displacement:

- **Fixed element** ($\dot{\theta} = 0$): Figure 9.2(a) shows that it is possible to change both angles, considering $\psi_i = \psi_{i0} - \gamma$, where ψ_{i0} is the initial position of the element, which stays on the same place in relation to the global reference frame.
- **Moving element** ($\dot{\theta} \neq 0$): Figure 9.2(b) presents the assumption of modification with $\psi_i = \psi_{i0} + \Delta\psi = \psi_{i0} - \gamma + \theta$. The position of the pressure plate (γ) as well as the one from the disc (θ) are necessary on this case.

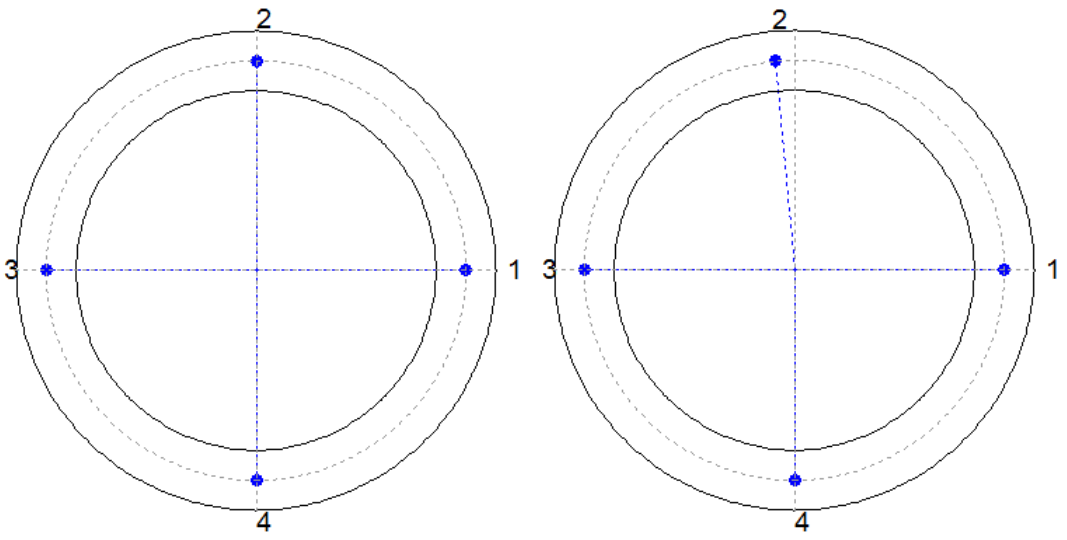

(a) (b)

Figure 9.1: Upper view for equally distributed elements (Fig. 9.1(a)). An error of 5° in element 2 (Fig. 9.1(b))

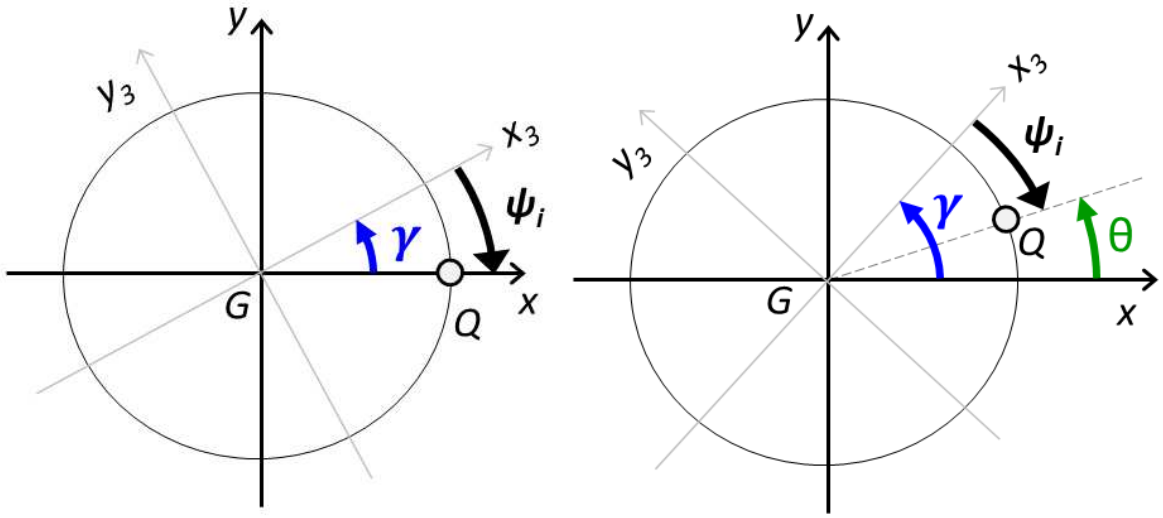

(a) (b)

Figure 9.2: Movement assuming a fixed (Fig. 9.2(a)), and moving element (Fig. 9.2(b)).

The element with the rotating speed on global coordinates (Section 7.2) only allows simulations assuming moving elements, once that its matrices are written in terms of the relative angle ψ_i (Section 7.4).

The simulations were done assuming a pressure plate with $m = 2$kg, $h = 0.01$m, $R_{in} = 0.075$ m and $R_{out} = 0.1$m. When not clearly explained, standard properties were assumed as $k = 3 \times 10^6/4$ N/m, $\dot{\gamma} = 2000$ rpm, $u = 0.3$, $R = 0.0875$m, and $z_e = 0.001$m..

9.1.1 Mode shapes for a symmetric distribution

The vector $\{X_i\} = \begin{Bmatrix} X_{1i} & X_{2i} & X_{3i} \end{Bmatrix}^T$ represents the i-th mode shape for coordinates $\{p\} = \begin{Bmatrix} \alpha & \beta & z \end{Bmatrix}^T$. All the results presents eigenvectors for eigenvalues with positive imaginary part ($\lambda_i = \sigma_i + j\varpi_i$).

For equally distributed elements (Fig. 9.2), the increase on the position ψ_{i0} did not produce changes on amplitude or phase on those mode shapes (Figs. 9.3). All models from Chapters 6 and 8 presented this characteristic.

Adopting a unitary norm and referencing the phase on the first degree of freedom, Equation 9.1 (Figs. 9.3(a) and 9.3(b)) represents a backward mode (Section 6.1.1):

$$\begin{Bmatrix} X_{11} \\ X_{21} \\ X_{31} \end{Bmatrix} = \begin{Bmatrix} 0.7071 \\ 0.7071j \\ 0 \end{Bmatrix} = \begin{Bmatrix} 0.7071\angle 0^\circ \\ 0.7071\angle 90^\circ \\ 0 \end{Bmatrix} \tag{9.1}$$

Equation 9.2 (Figs. 9.3(c) and 9.3(d)) is related to a pure axial movement with $|X_{32}| = 1$:

$$\begin{Bmatrix} X_{12} \\ X_{22} \\ X_{32} \end{Bmatrix} = \begin{Bmatrix} 0 \\ 0 \\ 1 \end{Bmatrix} \tag{9.2}$$

Equation 9.3 (Fig. 9.3(e) and 9.3(f)) can be interpreted as forward wobbling (Section 6.1.2):

$$\begin{Bmatrix} X_{13} \\ X_{23} \\ X_{33} \end{Bmatrix} = \begin{Bmatrix} 0.7071 \\ -0.7071j \\ 0 \end{Bmatrix} = \begin{Bmatrix} 0.7071\angle 0^\circ \\ 0.7071\angle -90^\circ \\ 0 \end{Bmatrix} \tag{9.3}$$

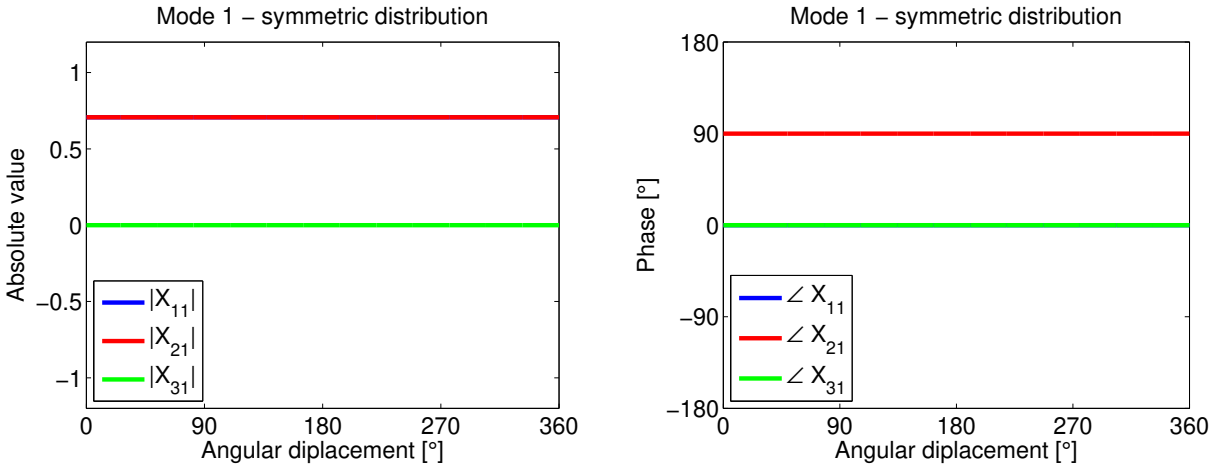

(a)

(b)

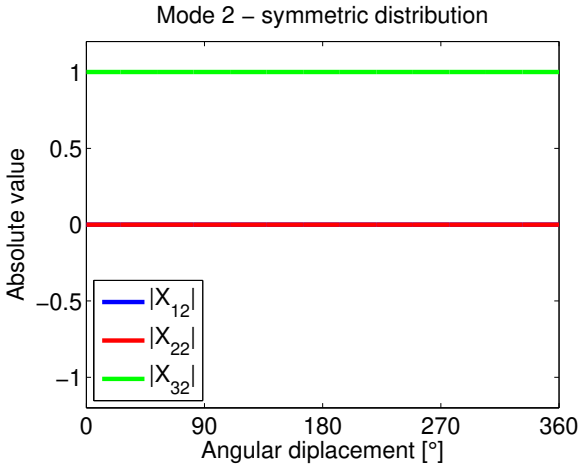

(c)

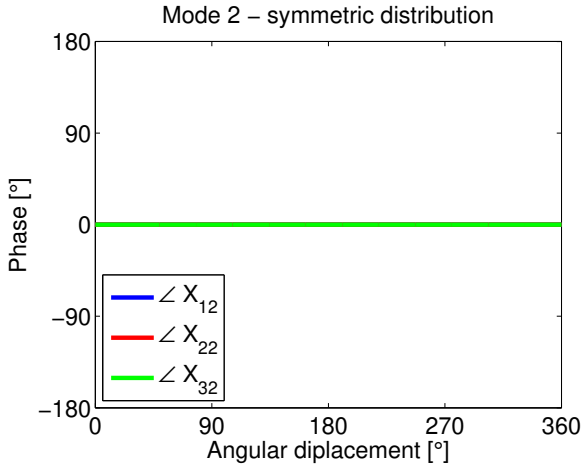

(d)

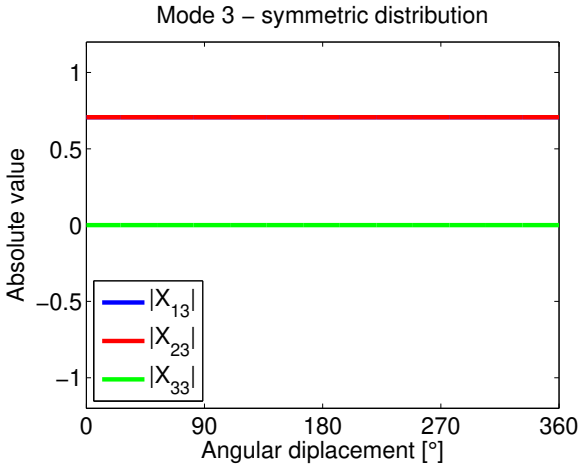

(e)

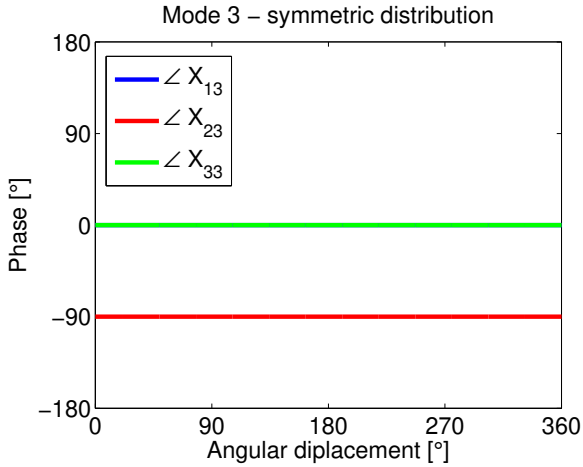

(f)

Figure 9.3: Absolute values (Figs. 9.3(a), 9.3(c) and 9.3(e)) and phase angles (Figs. 9.3(b), 9.3(d) and 9.3(f)) for the case from Fig. 9.1(a).

9.1.2 Mode shapes with a position error and fixed elements

For the fixed element (Fig. 9.1(a)), all properties remained constant with $\Delta\psi = -\gamma$ (Figs. 9.4,9.5, and 9.6). The main difference that emerged from the error of 5° was the *combination of the wobbling movements with axial vibrations*.

Mode 1 is written in Eq. 9.4 (Fig. 9.4(a) and 9.4(b)). On the previous simulation, this mode shape represented a pure backward wobbling mode (Eq. 9.1). The phase of X_{21} in relation to X_{11} is no longer $90°$, changing to $\angle X_{21} = 98.5083°$. The vertical coordinate X_{31} present a small amplitude.

$$\begin{Bmatrix} X_{11} \\ X_{21} \\ X_{31} \end{Bmatrix} = \begin{Bmatrix} 0.7131 \\ -0.1037 + 0.6933i \\ -0.0012 + 0.0041i \end{Bmatrix} = \begin{Bmatrix} 0.7131\angle 0° \\ 0.7010\angle 98.5083° \\ 0.0043\angle 105.8402° \end{Bmatrix} \tag{9.4}$$

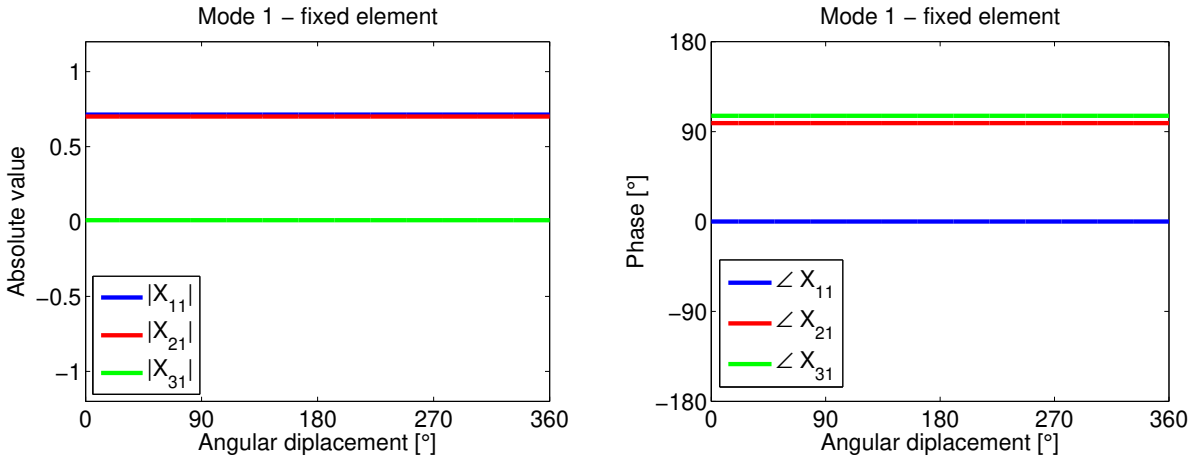

(a) (b)

Figure 9.4: Mode 1 assuming a fixed element (Figs. 9.4(a) and 9.4(b)).

Mode 2 is written in Eq. 9.5 (Fig. 9.5(a) and 9.5(b)). It still presents high values of vertical vibration $|X_{32}| = 0.5695$. I is the one with the most representative contribution of angular vibration, with $|X_{12}| = 0.8189$.

$$\begin{Bmatrix} X_{12} \\ X_{22} \\ X_{32} \end{Bmatrix} = \begin{Bmatrix} 0.8189 \\ 0.0216 - 0.0679i \\ 0.0141 - 0.5693i \end{Bmatrix} = \begin{Bmatrix} 0.8189\angle 0° \\ 0.0713\angle -72.3273° \\ 0.5695\angle -88.5793° \end{Bmatrix} \tag{9.5}$$

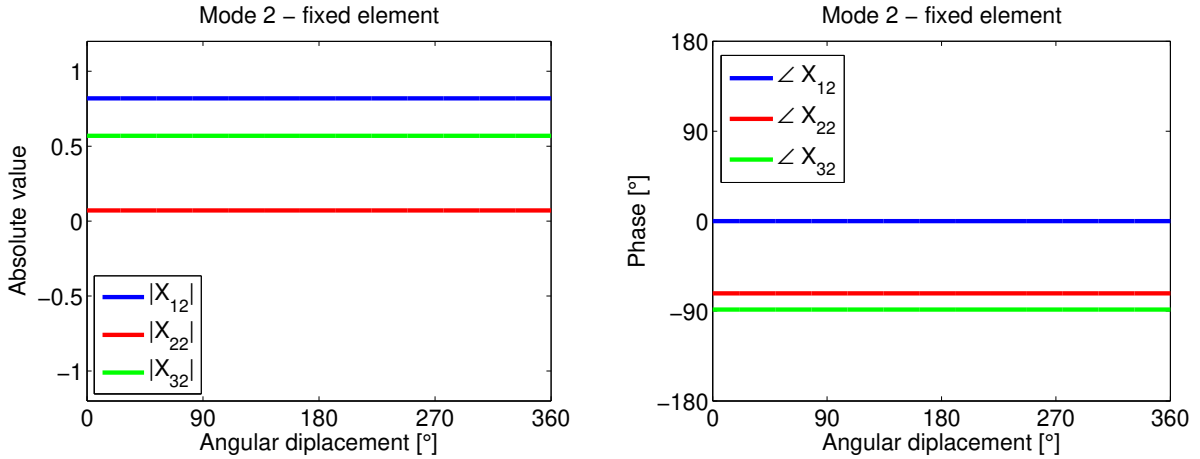

(a) (b)

Figure 9.5: Mode 2 assuming a fixed element (Figs. 9.5(a) and 9.5(b)).

Mode 3 is written in Eq. 9.6 (Fig. 9.6(a) and 9.6(b)). The angles X_{13} and X_{23} still contain similarities of amplitude and phase with the forward wobbling from Eq. 9.3. There is a small contribution of vertical motion, indicated by $|X_{33}| = 0.0036$.

$$\begin{Bmatrix} X_{13} \\ X_{23} \\ X_{33} \end{Bmatrix} = \begin{Bmatrix} 0.7077 \\ 0.0748 - 0.7026j \\ -0.0006 + 0.0035i \end{Bmatrix} = \begin{Bmatrix} 0.7077\angle 0° \\ 0.7065\angle -83.9223° \\ 0.0036\angle 99.5808° \end{Bmatrix} \tag{9.6}$$

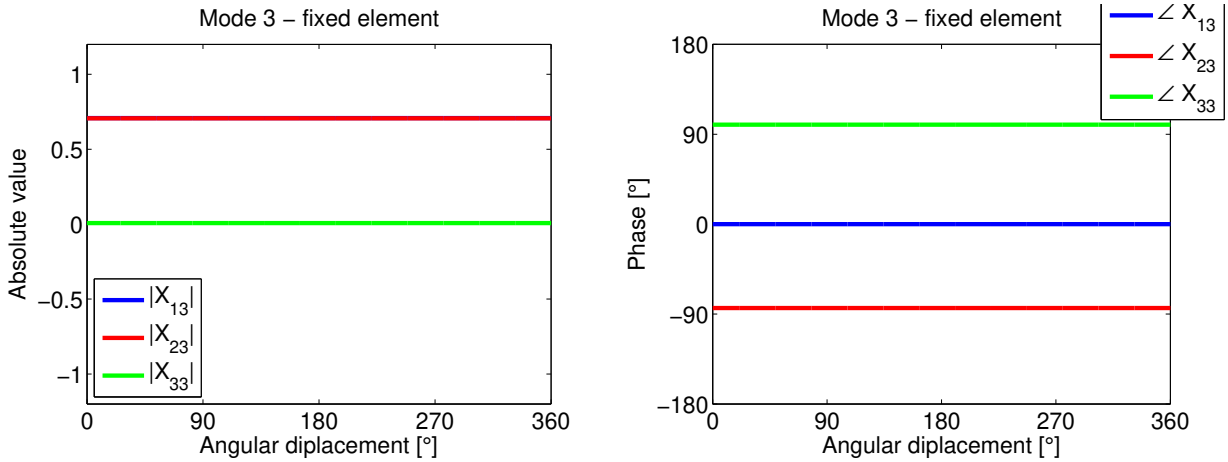

(a) (b)

Figure 9.6: Mode 3 assuming a fixed element (Figs. 9.6(a) and 9.6(b)).

In this case, the former pure vertical vibrating mode (Eq. 9.5) was modified with the inclusion of greater amount of angular displacements. The former pure wobbling modes (Eqs. 9.4 and 9.5) had smaller contribution of axial vibration. The most important verification is that, for position errors, the *properties for symmetrically distributed or fixed elements can be done for one position only*.

9.1.3 Mode shapes with a position error and moving elements

For these simulations, the rotating speeds were considered as $\dot{\gamma} = 2000$ rpm and $\dot{\theta} = 1000$ rpm. The eigenvalues were calculated for a complete turn of the pressure plate $0 < \gamma < 360°$ in Figs. 9.8, 9.9 and 9.11. Due to the fact that the rotating speed of the clutch disc is half the value found for the plate, for equal initial conditions, there is $\gamma = 2\theta$. In this case, all elements are equally moved according to $\psi_i = \psi_{i0} + \Delta\psi$, where $-180° < \Delta\psi < 0$. Physically, all elements are shifted from an initial disposition (Fig. 9.7(a)) to another distribution in relation to the plate x_3y_3 (Fig. 9.7(b)). The placement error on element 2 moves from positions with $y_3 > 0$ to $y_3 < 0$. From the theoretical perspective, there is $|\Delta\psi| \neq |\gamma|$.

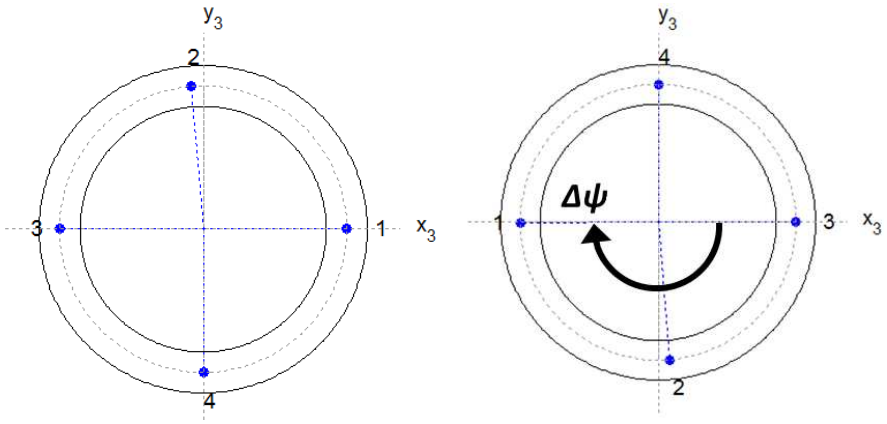

Figure 9.7: Initial (Fig. 9.7(a)) and final dispositions (Fig. 9.7(b)) .

The results from Figs. 9.8, 9.9, and 9.11 are all displayed according to the pressure plate angle γ. They all share a common behaviour of *mode shapes varying according to the relative position between the plate and the elements*.

Mode 1 preserves characteristics of a wobbling movement, once that $|X_{11}|$ and $|X_{21}|$ present the highest amplitudes (Fig. 9.8(a)) and the phase angle of the second degree-of-freedom ($\angle X_{21}$) remain close to 90°. If $\gamma < 180°$, α greater amplitudes than β ($|X_{11}| > |X_{21}|$). For $180° <$

$\gamma < 360°$, the previous relation is changed to $|X_{21}| < |X_{11}|$. The vertical contribution is low $|X_{31}| = 0.008544$, but there are strong variations on its phase nearby $\gamma = 165°$ (Fig. 9.8(b)).

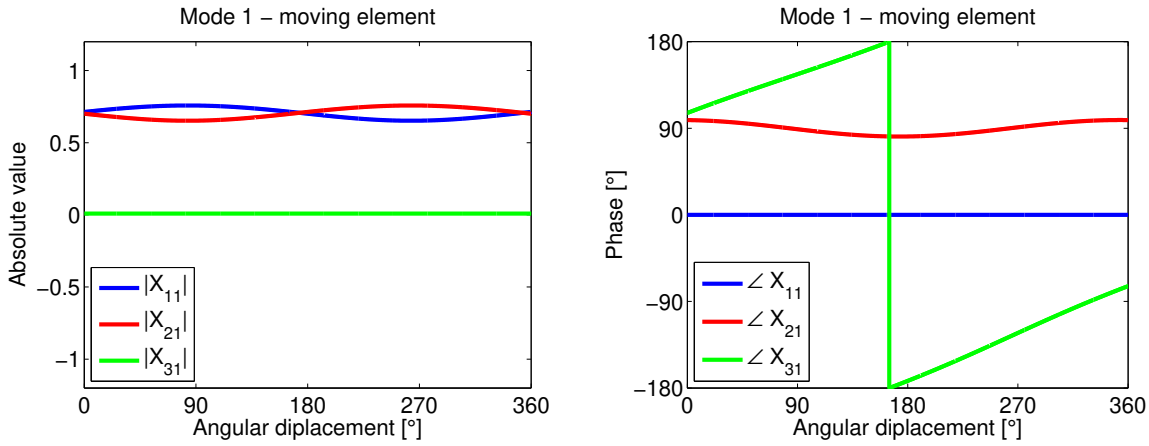

(a) (b)

Figure 9.8: Mode 1 assuming a moving element (Figs. 9.8(a) and 9.8(b)).

The second mode shape still have the greater values for axial vibration ($|X_{32}|$ on Fig. 9.9(a)). There is a peak value for $|X_{12}|$ with $|X_{22}| \approx 0$ at $\gamma = 0°$. This condition is changed to very high values of $|X_{22}|$ combined with $|X_{12}| \approx 0$ at $\gamma = 180°$. The phases from Fig. 9.9(b) *do not indicate wobbling motions*, once that $\angle X_{12}$ is closer to 0° for $0° < \gamma < 180°$. Figure 9.10 shows a sequence combining axial motion with angular movement in this situation. In phase or out of phase angles do not produce the aspect of wobbling, resulting in a pressure plate that seems to move up and down swinging its sides.

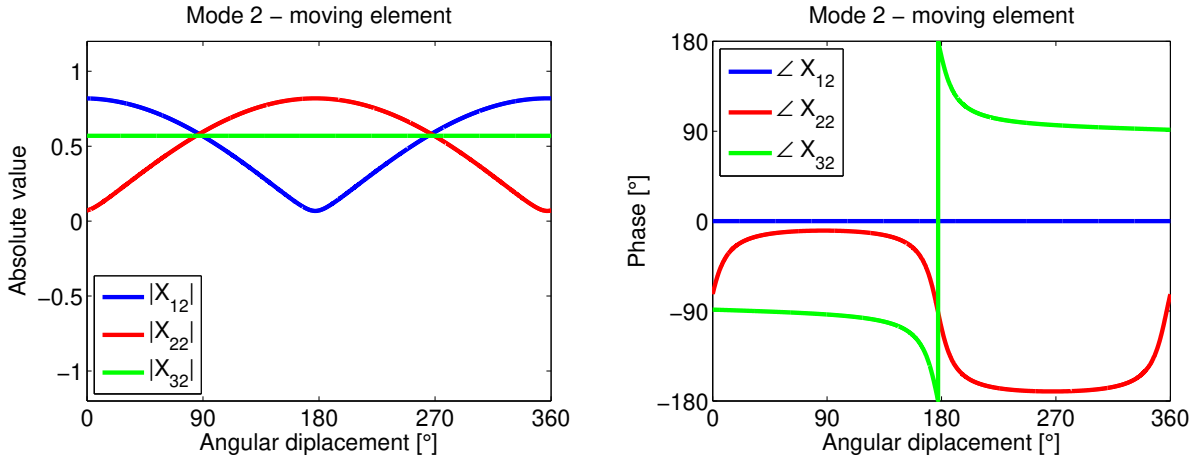

(a) (b)

Figure 9.9: Mode 2 assuming a moving element (Figs. 9.9(a) and 9.9(b)).

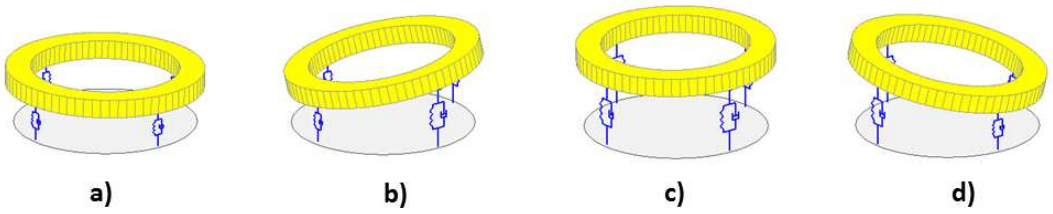

Figure 9.10: Combination of an axial vibration with an angular displacement that does not produce wobbling.

The amplitudes of the third mode from Fig. 9.11(a) are very similar to the case on Fig. 9.8(a). Both $|X_{13}|$ and $|X_{23}|$ are very high, but $|X_{13}| > |X_{23}|$ for $0 < \gamma < 180°$ and $|X_{13}| < |X_{23}|$ within $180 < \gamma < 360°$. The phase angle still indicates a forward wobbling movement ($\angle X_{23} \approx -90°$ on Fig. 9.11(b)). The vertical movement has an small contribution but, just link the case on Fig. 9.8(b), it presents abrupt changes on its phase.

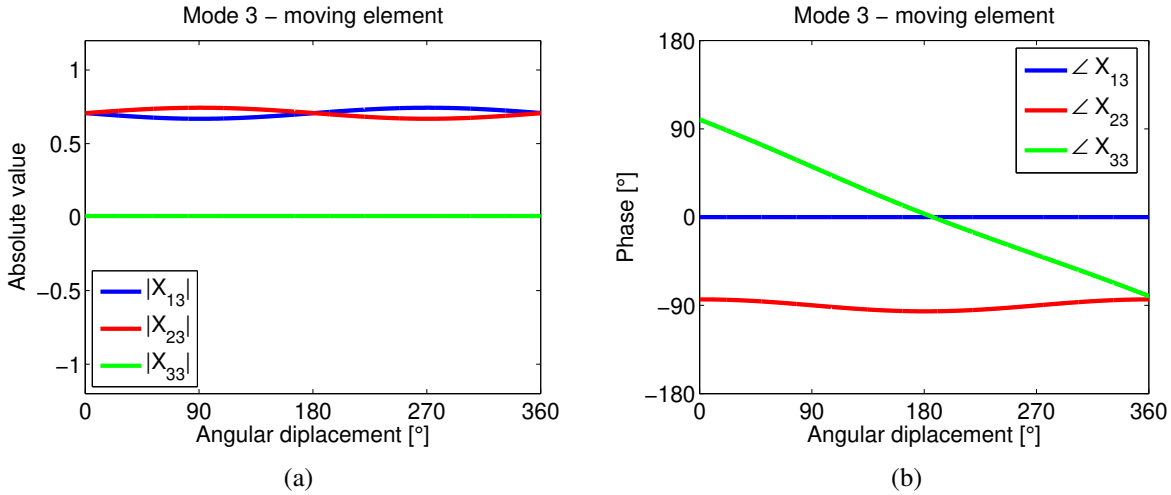

(a) (b)

Figure 9.11: Mode 3 assuming a moving element (Figs. 9.11(a) and 9.11(b)).

The element with the rotating speed on global coordinates produces only the aspect of Figs. 9.8, 9.9 and 9.11 on the mode shapes once that it allows only simulations based on moving elements. Due to the regularity on the modal properties with errors, the following studies will focus on the study of heterogeneity on the model on *Cardan coordinates with fixed elements*.

9.1.4 Eigenvalue characteristics for symmetric, fixed and moving elements

The eigenvalue characteristics for modes 1, 2, and 3 are represented in Figs. 9.12, and 9.13 for the conditions from Sections 9.1.1, 9.1.2, and 9.1.3. In all cases, the eigenvalues remained with *constant properties* along the simulations. Natural frequencies from modes 1 and 2 were lower in case of position error, with fixed or moving elements (Figs. 9.12(a) and 9.12(c)). The only situation were the errors increased the frequency occurred for mode 3 (Fig. 9.13(a)), with characteristics of a forward wobbling mode. The real parts of the eigenvalues were gently reduced in case of position error. The moving element produced the lowest values due to a reduction on the difference $\dot{\gamma} - \dot{\theta}$, which increases a little the effect of friction damping (Section 6.2) on this system.

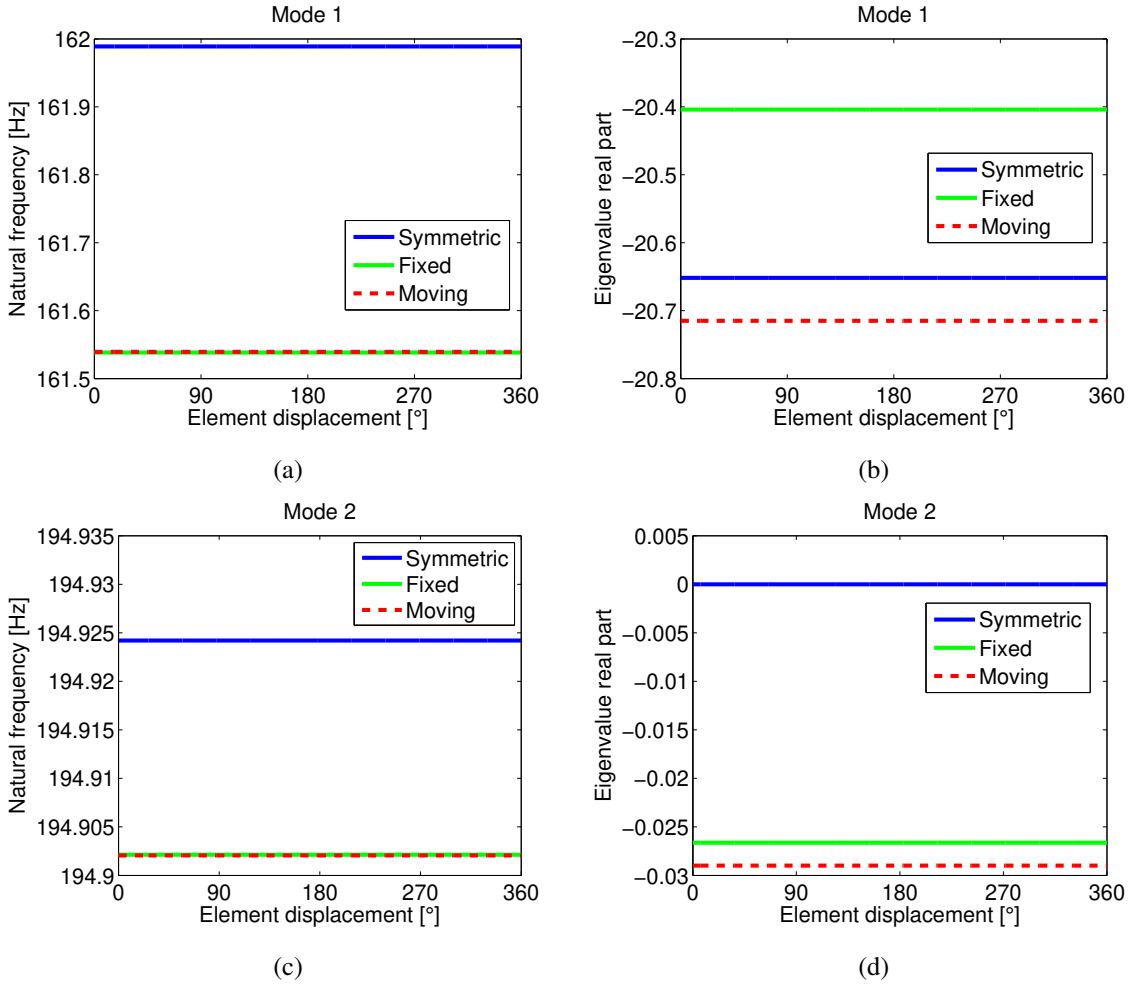

Figure 9.12: Natural frequencies (Fig. 9.12(a) and 9.12(c)) and eigenvalue real parts (Fig. 9.12(b) and 9.12(d)) for mode 1 and 2, adopting the conditions of symmetric distribution, fixed and moving elements.

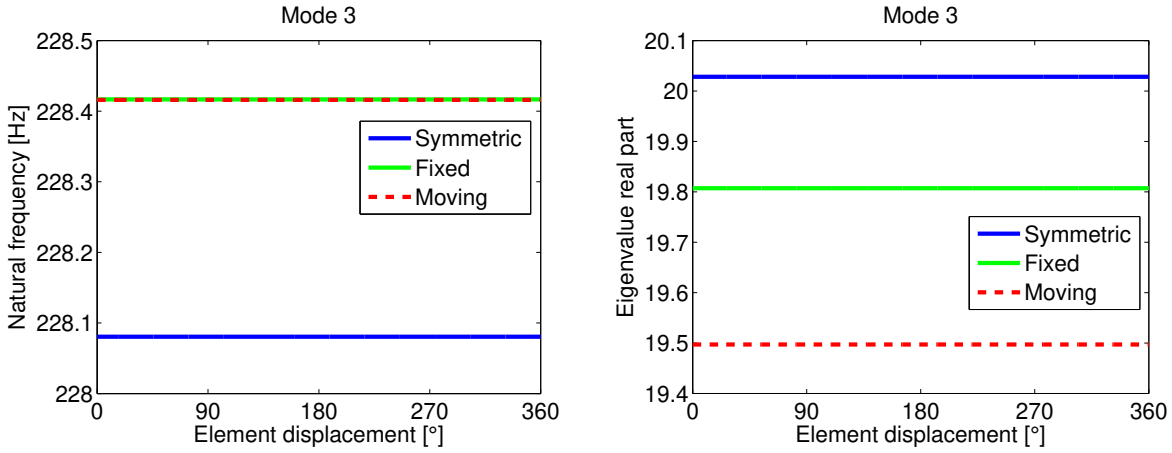

(a) (b)

Figure 9.13: Natural frequency (Fig. 9.13(a)) and eigenvalue real parts (Fig. 9.13(b)) for mode 3, adopting the conditions of symmetric distribution, fixed and moving elements.

9.1.5 Position error level and the coupling with vertical motions

This simulation takes into account position errors on the second element according to $\psi_2 = \psi_{20} + \Delta\psi$. The initial location is chosen as $\psi_{20} = 90°$ (Fig. 9.2(a)) and the error is varied within $-30° < \Delta\psi < 30°$. Figure 9.14(a) shows that the first natural frequency decreases for greater errors, while the third value increases with $\Delta\psi$. The eigenvalues real parts present more significant differences for greater $|\Delta\psi|$.

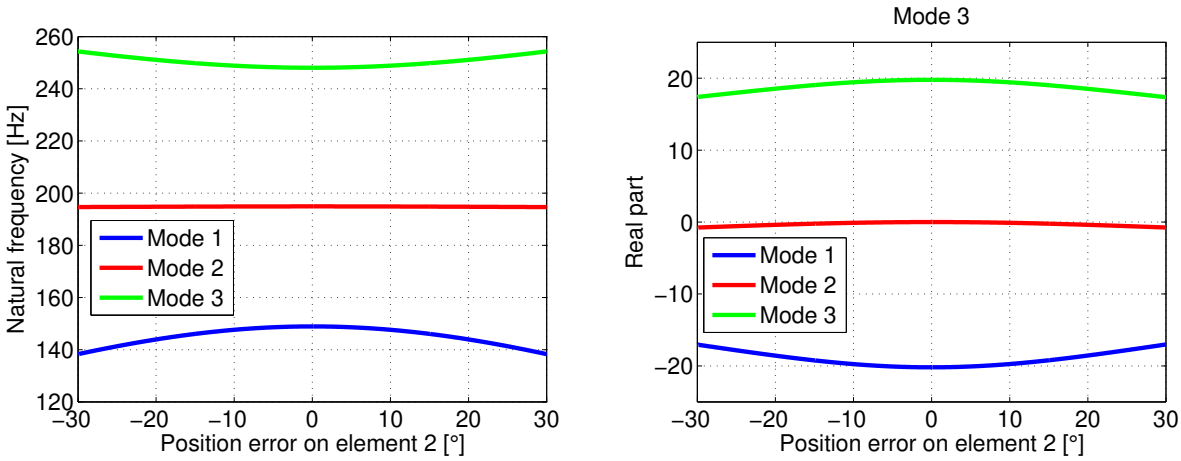

(a) (b)

Figure 9.14: Natural frequencies and eigenvalue real parts (Figs. 9.14(a) and 9.14(b)) for different levels of error on element 2.

If $\Delta\psi = 0°$, the second mode presents a purely axial vibration (Fig. 9.15). When $|\Delta\psi|$ is increased, the contribution from $|X_{32}|$ diminishes, followed by an enhanced contribution from α ($|X_{12}|$). There is a smaller contribution from β ($|X_{22}|$). During the simulation, conditions with $\Delta\psi \neq 0$ created an unbalanced distribution of stiffness on the system, coupling all coordinates.

The wobbling motions indicate higher amplitudes with greater errors (Fig. 9.16). Mode 1 (Fig. 9.16(a)) presented $|X_{11}| < |X_{21}|$, while mode 3 (Fig. 9.16(b)) had the opposite behaviour ($|X_{23}| > |X_{13}|$).

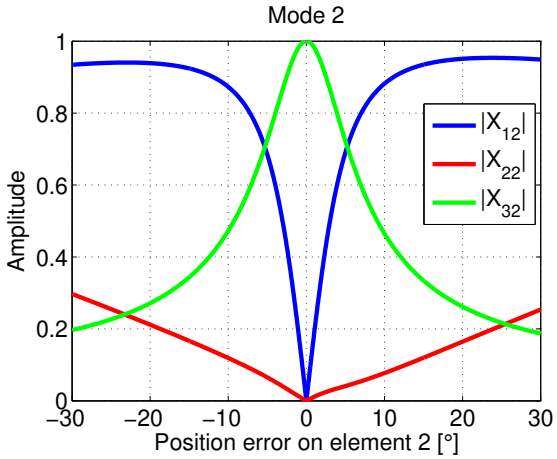

Figure 9.15: Second mode amplitude according to the position error on element 2.

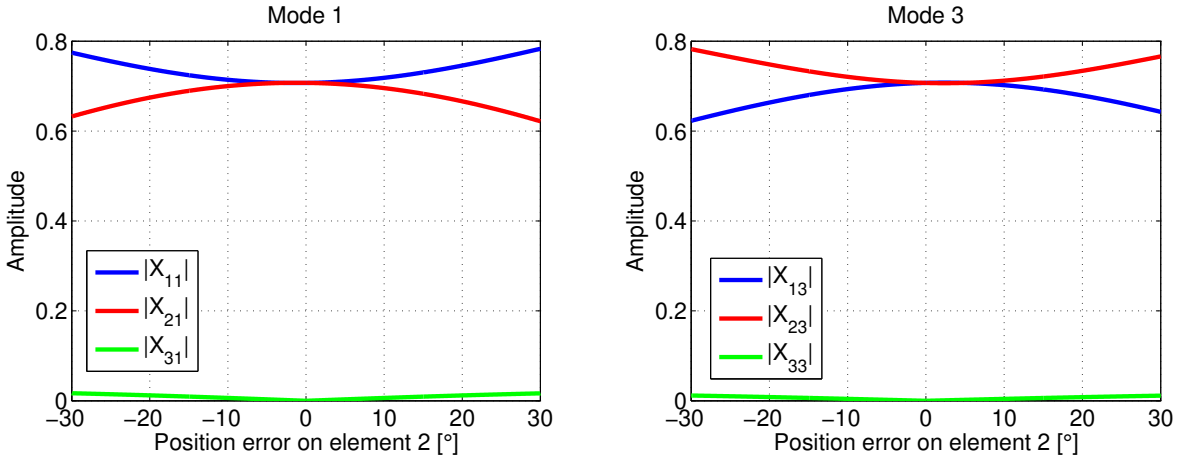

(a) (b)

Figure 9.16: Mode amplitudes (Figs. 9.16(a) and 9.16(b)) according to the position error on element 2.

9.2 Symmetric distributions according to axial motion with asymmetrical stiffness according to angular displacements

Figure 9.17 presents a spacial view of the element distribution from Fig. 9.1(a), that were assumed as fixed on Cardan coordinates, that produced constant properties with heterogeneity on Section 9.1.2. Elements 1 and 3 are positioned along the x axis, while the pair 2 and 4 remain on opposite sides along the y axis. Now, it is possible to distribute the total cushion stiffness $k_{cushion}$ between them assuming proportional changes. But on all modifications the relation $k_1 + k_2 + k_3 + k_4 = k_{cushion}$ is maintained. For any distributions considering $k_1 = k_3$ and $k_2 = k_4$ the mass of the plate is balanced on the vertical direction, without the coupling verified on Section 9.1.5. The only source of energy dissipation is friction damping. The rotating speed was chosen as $\dot{\gamma} = 2000rpm$.

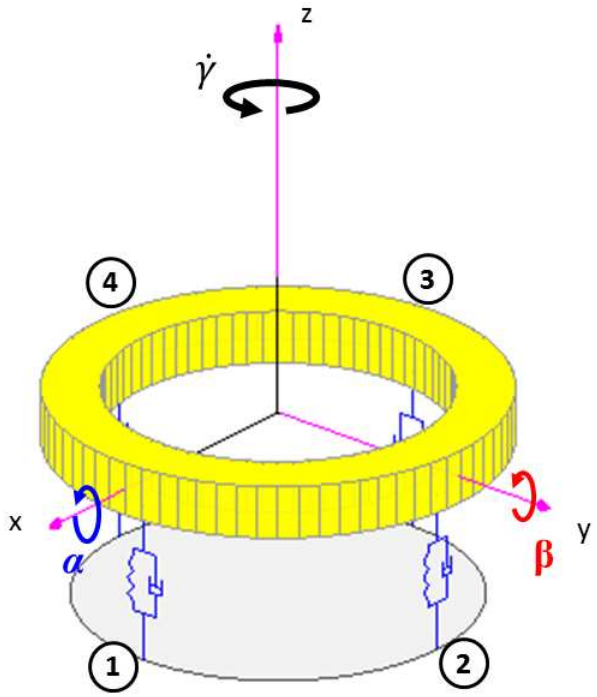

Figure 9.17: Element distribution in a situation for the simulation of unbalanced properties.

9.2.1 Unbalanced stiffness distribution without damping

Considering that $k_1 = k_3 = 0.275k_{cushion}$ and $k_2 = k_4 = 0.225k_{cushion}$, it is possible to achieve a proportion of $k_1 + k_3 = 0.55k_{cushion}$ and $k_2 + k_4 = 0.45k_{cushion}$. In other words, 55% of the total stiffness is concentrated for angular displacements on β and 45% for α.

The vector $\{X_i\} = \begin{Bmatrix} X_{1i} & X_{2i} & X_{3i} \end{Bmatrix}^T$ represents the i-th mode shape for coordinates $\{p\} = \begin{Bmatrix} \alpha & \beta & z \end{Bmatrix}^T$. All the results presents eigenvectors with unitary norm for eigenvalues with positive imaginary part ($\lambda_i = \sigma_i + j\varpi_i$).

In all cases, the natural frequencies increased with $k_{cushion}$ (Fig. 9.18(a)) with the mode 1 with higher frequencies and mode 2 with intermediate values. The real part of eigenvalue 3 augmented with greater stiffness values (Fig. 9.18(b)). This characteristic is similar to the one found on Section 6.2.

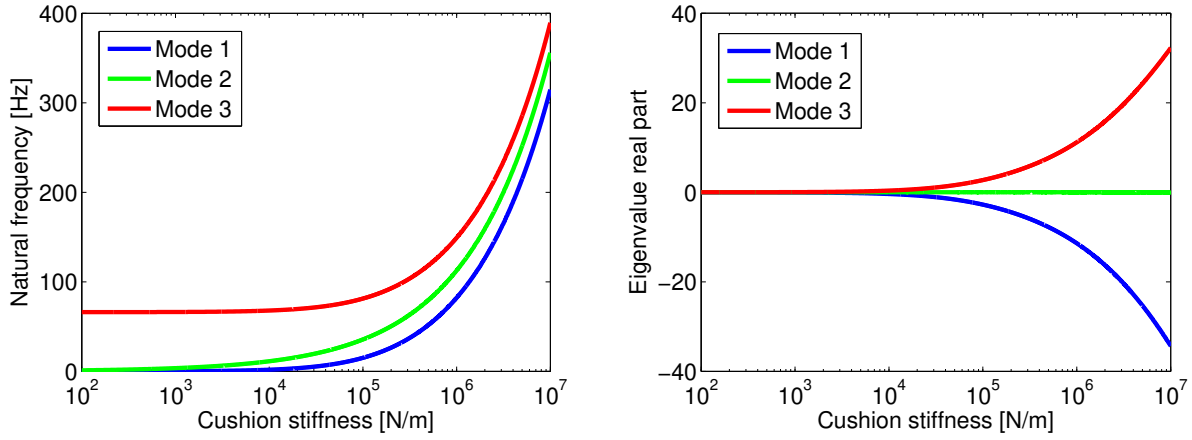

(a) (b)

Figure 9.18: Eigenvalues natural frequency (Fig. 9.18(a)) and real parts (Fig. 9.18(b)) for the unbalanced cushion case.

When the total cushion stiffness is varied within $100 < k_{cushion} < 10^7 N/m$, the first mode on Fig. 9.19(a) presents greater amplitudes on α ($|X_{11}|$) in relation to β ($|X_{21}|$). For stiffness values below $10^4 N/m$, these values are found as $|X_{11}| \approx 0.74$ and $|X_{21}| \approx 0.67$ (Eq. 9.7). For these cases, the phase $\angle X_{21} = 90.19°$ (Fig. 9.19(b)), indicating a backward wobbling.

$$\begin{Bmatrix} X_{11} \\ X_{21} \\ X_{31} \end{Bmatrix} = \begin{Bmatrix} 0.7416 \\ -0.0023 + 0.6709j \\ 0 \end{Bmatrix} = \begin{Bmatrix} 0.7416\angle 0° \\ 0.6709\angle 90.1974° \\ 0 \end{Bmatrix}, \text{ for } k_{cushion} < 10^4 N/m \qquad (9.7)$$

For higher values of stiffness, there is a situation where $|X_{11}|$ increases up to 0.86 and $|X_{21}|$ decreases to 0.5 for $10^7 N/m$ (Eq. 9.8). There is an almost imperceptible phase modification on this region.

$$\begin{Bmatrix} X_{11} \\ X_{21} \\ X_{31} \end{Bmatrix} = \begin{Bmatrix} 0.8661 \\ 0.0362 + 0.4985j \\ 0 \end{Bmatrix} = \begin{Bmatrix} 0.8661\angle 0° \\ 0.4998\angle 85.8517° \\ 0 \end{Bmatrix}, \text{for } k_{cushion} = 10^7 N/m \tag{9.8}$$

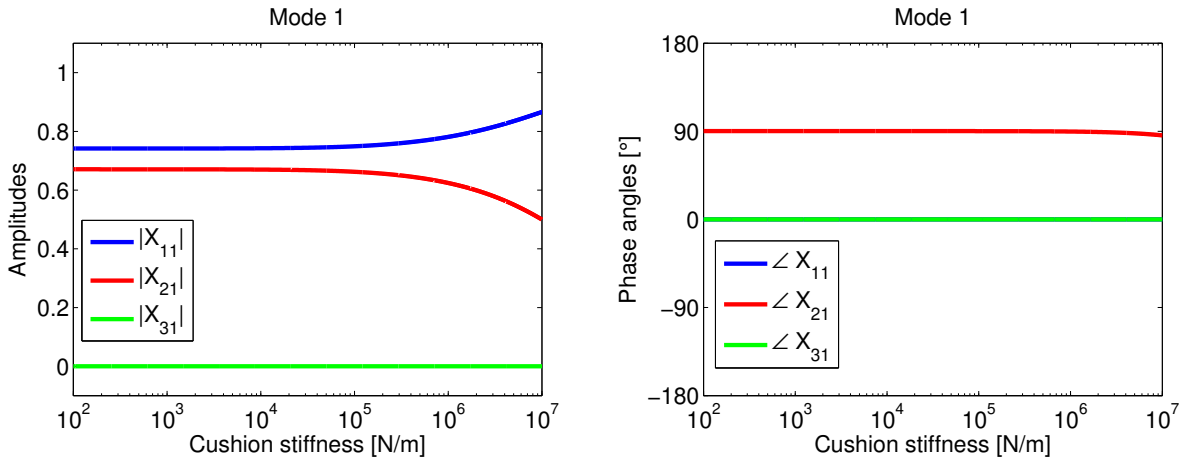

(a) (b)

Figure 9.19: Mode 1 for the unbalanced cushion case (Figs. 9.19(a) and 9.19(b)), assuming $k_1 + k_3 = 0.55k_{cushion}$ and $k_2 + k_4 = 0.45k_{cushion}$.

On mode 3 (Fig. 9.20(a)), the angular movement on both coordinates remained very similar in case of low stiffness values, as presented on Eq. 9.9 with $|X_{11}| = |X_{11}| = 0.707$. But, differently from the previous case (Fig. 9.19), there is an increase on the amplitudes of $|X_{21}|$ in relation to $|X_{11}|$ for very high values of cushion stiffness. Equation 9.10 presents $|X_{13}| = 0.539$ and $|X_{23}| = 0.8423$ for $k_{cushion} = 10^7 N/m$. This forward wobbling mode (Fig. 9.20(b)) presented higher vibration on β, which is the coordinate with greater stiffness ($k_1 + k_3 = 0.55k_{cushion}$).

$$\begin{Bmatrix} X_{13} \\ X_{23} \\ X_{33} \end{Bmatrix} = \begin{Bmatrix} 0.7071 \\ -0.7071j \\ 0 \end{Bmatrix} = \begin{Bmatrix} 0.7071\angle 0° \\ 0.7071\angle -89.9° \\ 0 \end{Bmatrix}, \text{for } k_{cushion} < 10^4 N/m \tag{9.9}$$

$$\begin{Bmatrix} X_{13} \\ X_{23} \\ X_{33} \end{Bmatrix} = \begin{Bmatrix} 0.5390 \\ 0.0760 - 0.8388j \\ 0 \end{Bmatrix} = \begin{Bmatrix} 0.539\angle 0° \\ 0.8423\angle -84.8234° \\ 0 \end{Bmatrix}, \text{for } k_{cushion} = 10^7 N/m \tag{9.10}$$

The axial mode remained unchanged for these tests (Fig. 9.21), meaning that these propor-

tional changes did not couple the angles with the vertical vibration.

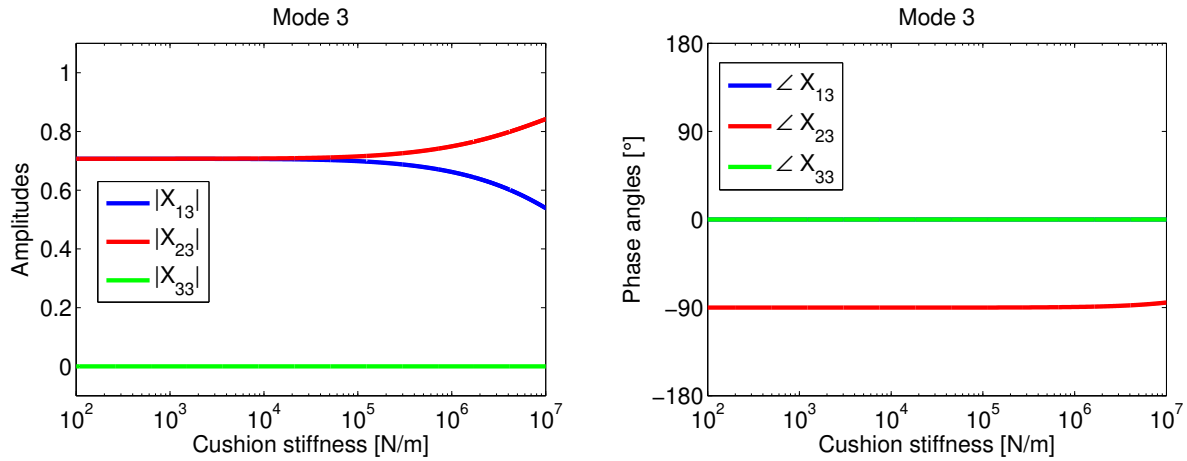

(a) (b)

Figure 9.20: Mode 3 for the unbalanced cushion case (Figs. 9.20(a) and 9.20(b)), assuming $k_1 + k_3 = 0.55k_{cushion}$ and $k_2 + k_4 = 0.45k_{cushion}$.

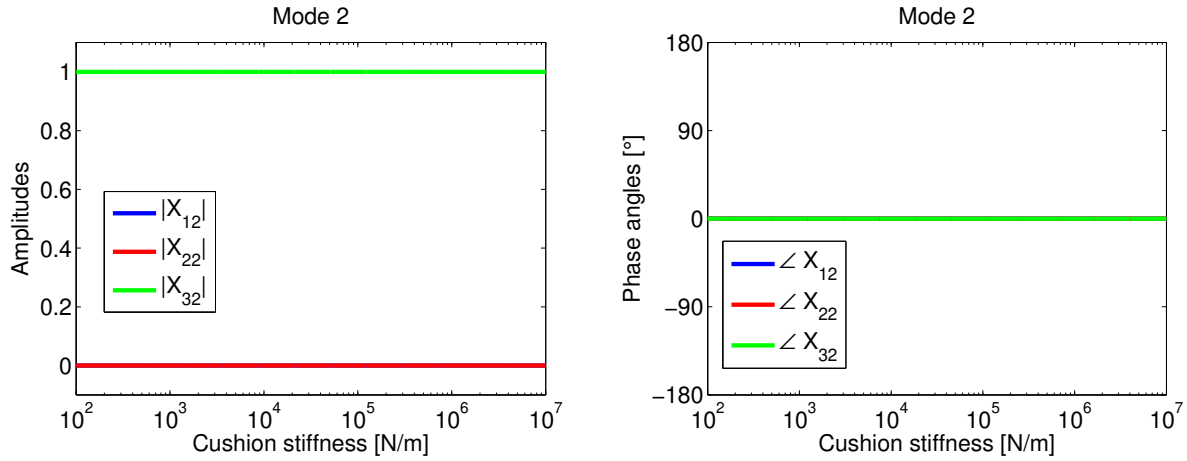

(a) (b)

Figure 9.21: Mode 2 for the unbalanced cushion case (Figs. 9.20(a) and 9.20(b)), assuming $k_1 + k_3 = 0.55k_{cushion}$ and $k_2 + k_4 = 0.45k_{cushion}$.

The previous case can be inverted with $k_2 = k_4 = 0.275k_{cushion}$ and $k_1 = k_3 = 0.225k_{cushion}$. Now there is more stiffness for movements on α than or β. The results on Fig. 9.22 are the opposite to the ones on Figs. 9.19 and 9.20. The backward wobbling on Fig. 9.22(a) have greater values of $|X_{21}|$ for high $k_{cushion}$. The forward movement have greater values on $|X_{11}|$ (Fig. 9.22(b)).

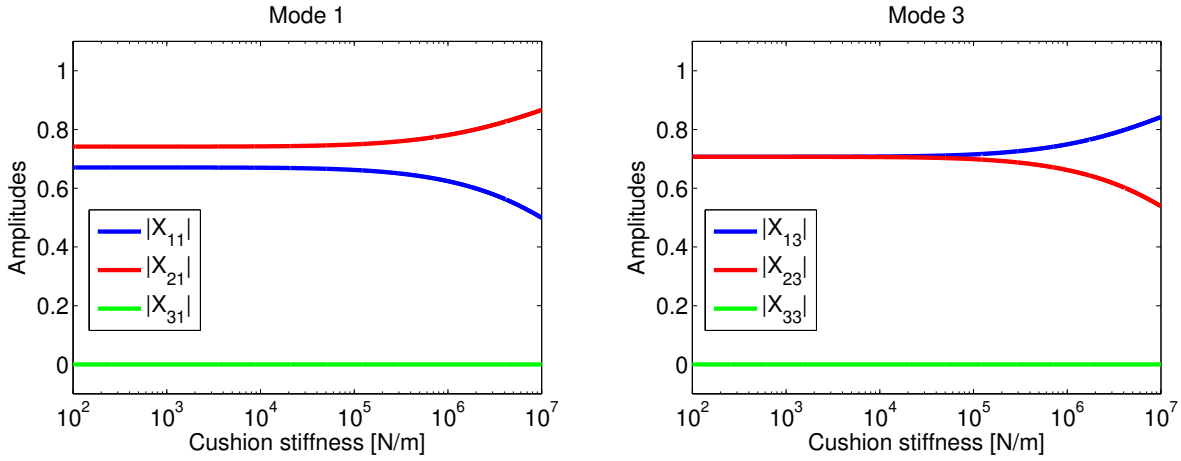

(a) (b)

Figure 9.22: Amplitude on mode 1 and 3 for $k_1 + k_3 = 0.45k_{cushion}$ and $k_2 + k_4 = 0.55k_{cushion}$ (Figs. 9.22(a) and 9.22(b)).

When the ratio $(k_1 + k_3)/k_{cushion}$ is increased, it means that the contribution of $k_2 + k_4$ are decreased for $k_1+k_2+k_3+k_4 = k_{cushion}$. Figure 9.23(a) shows that $(k_1+k_3)/k_{cushion} < 0.5$, there is more stiffness for angular displacements on α, reducing $|X_{11}|$ on Fig. 9.23(a) and an increment on $|X_{13}|$ on Fig. 9.23(b). Amplitudes on β ($|X_{22}|$ on Fig. 9.23(a) and $|X_{23}|$ on Fig. 9.23(b)) follow the opposite relations. For situations when the proportion is no longer equal between the element pairs ($(k_1 + k_3)/k_{cushion} \neq 0.5$), there is an increase on the natural frequency of mode 3 (Fig. 9.24(a)) that is followed by a decrease on its real part (Fig. 9.23(b)).

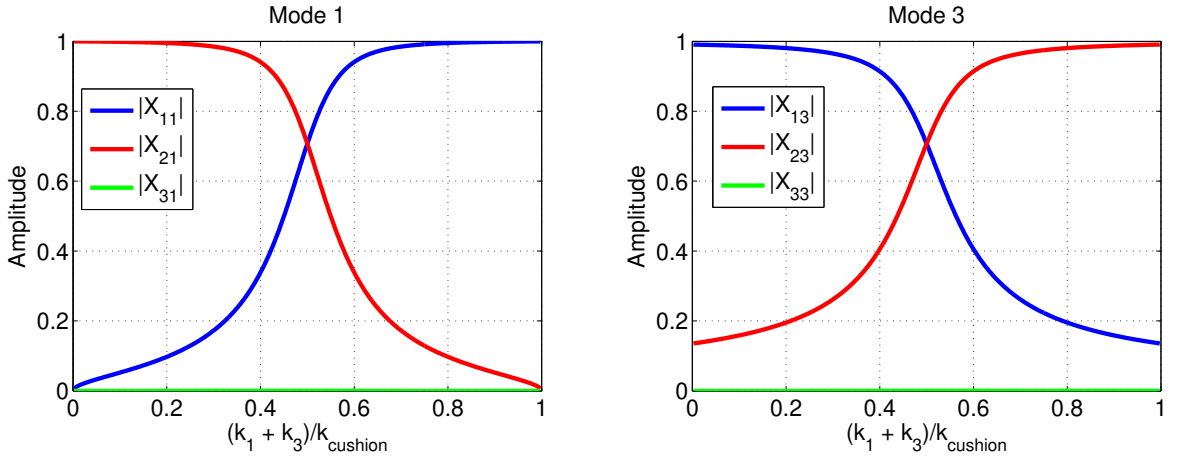

(a) (b)

Figure 9.23: Amplitudes for modes 1 and 2 (Figs. 9.23(a) and 9.23(b)) for $k_{cushion} = 10^7$N/m.

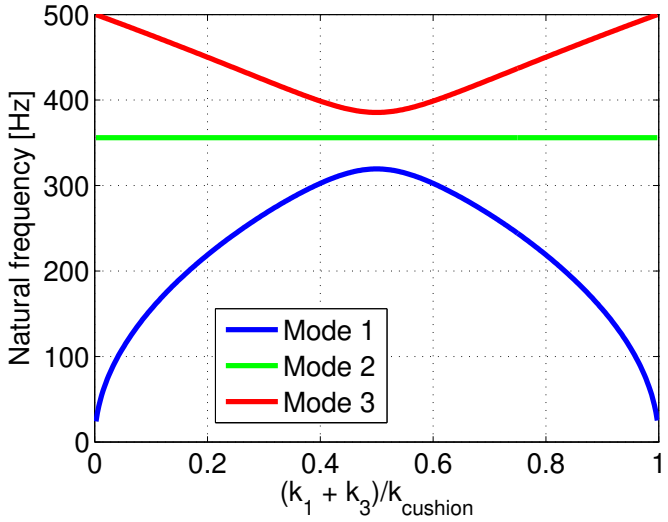

(a)

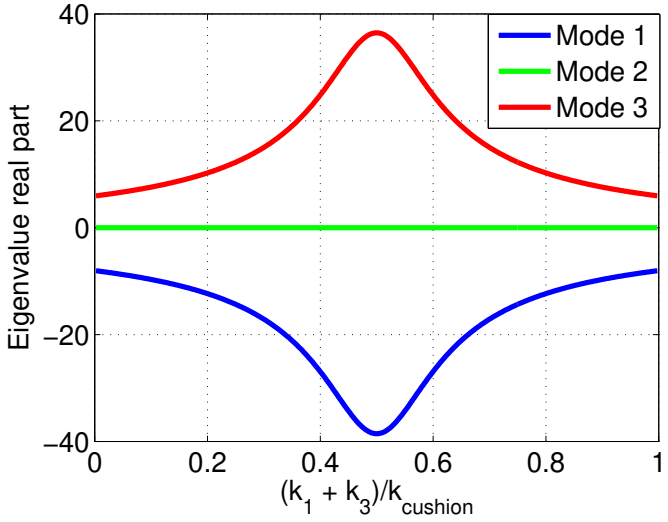

(b)

Figure 9.24: Amplitudes for modes 1,2,and 3 (Figs. 9.24(a) and 9.24(b)) for $k_{cushion} = 10^7$N/m.

9.3 Chapter summary

From Section 9.1, the model on Cardan coordinates allows modifications on γ and ψ_i, while the representation with the rotating speed on global coordinates worked on ψ_i. The following conditions were verified:

- The simulations with the position errors (for moving and fixed elements) created coupling

between the angular displacements with the axial vibration.

- Moving elements resulted on modifications o the mode shapes at each position of the plate.
- Symmetric distributions or irregularities considering fixed elements possessed constant properties during the simulations.
- In all cases, the eigenvalues of the system remained with constant properties according to the pressure plate angle.
- The relative amplitudes between the angular displacements were increased in situations of position error.

From Section 9.2.1, it was possible to observe that:

- With low values of cushion stiffness, the mode with characteristics of a backward wobbling mode presented greater differences of amplitude between coordinates α and β. The forward wobbling mode presented very close amplitudes on those coordinates.
- In both cases, the difference between amplitudes increased significantly for high stiffness values.
- The forward wobbling mode presented larger amplitudes for coordinates with a more significant stiffness amount.

10 Diaphragm spring: physical representation and the inclusion of real measurements in the model

The diaphragm spring applies normal load to the pressure plate and has specific nonlinear stiffness characteristics. A lever model for the diaphragm spring is made on Section 10.1. It assumes that there is no deflection on the elements on the clutch cover (Shaver and Shaver, 1997). The literature does not give support for a model that could assume arbitrary distributions of properties of the diaphragm spring (Chapter 3). Numerical simulations including real curves from a passenger car with manual transmission will be presented in Section 10.4 for new (Section 10.4.1) and worn (Section 10.4.1) clutch discs.

10.1 Diaphragm spring lever model

The diaphragm spring from Figs. 2.1 and 2.3 will be simplified to a lever pinned at point O_{m_i} Fig. 10.1, that represents the articulation point at the rivets in Fig. 10.1. The distances b_i and a_i will define the displacement/effort ratios. The constant moment M_{m_i} is included once that it applies a constant load to the pressure plate during torque transmission at a certain static position z_e. Such condition is presented by Kimmig (1998). The stiffness k_{m_i} and damping c_{m_i} will be linearized parameters related to the stiffness and damping of the diaphragm spring. The contact force representing the bearing effort on the fingers will be F_{r_i} (Figs. 10.1 and 10.1), that is considered as the release load.

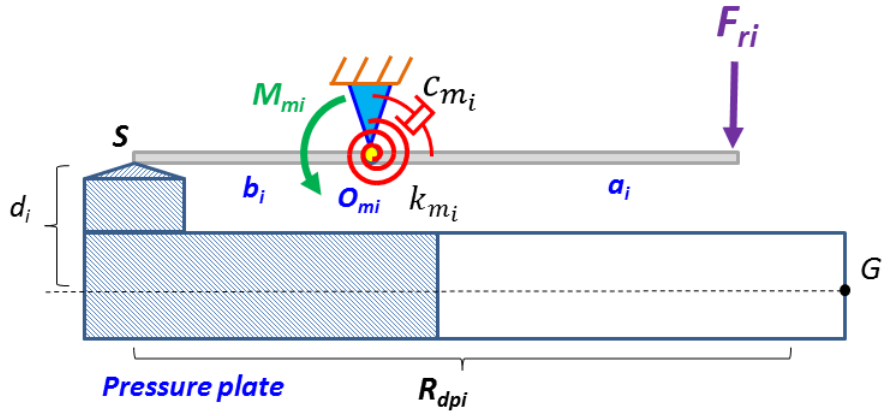

Figure 10.1: Side view of the diaphragm spring lever model (Fig. 10.1).

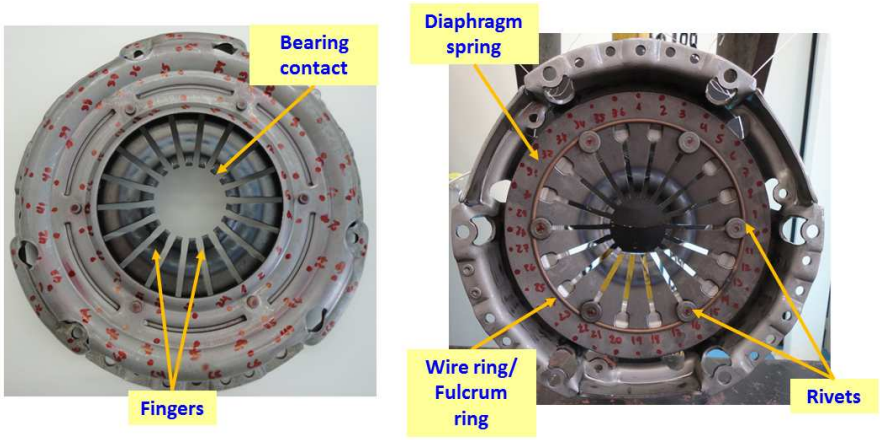

Figure 10.2: Diaphragm spring (Fig. 10.1).

The contact point S is located above the centre of gravity of the plate (G), by a distance d (Fig. 10.1). The position vector (Eq. 10.1) is obtained by the angle θ_{dp_i} and radius R_{dp_i} (Fig. 10.3).

$$ {}_3\vec{r'}_{GS} = \left\{ R_{dp_i} \cos\theta_{dp_i} \quad R_{dp_i} \sin\theta_{dp_i} \quad d_i \right\}^T \tag{10.1} $$

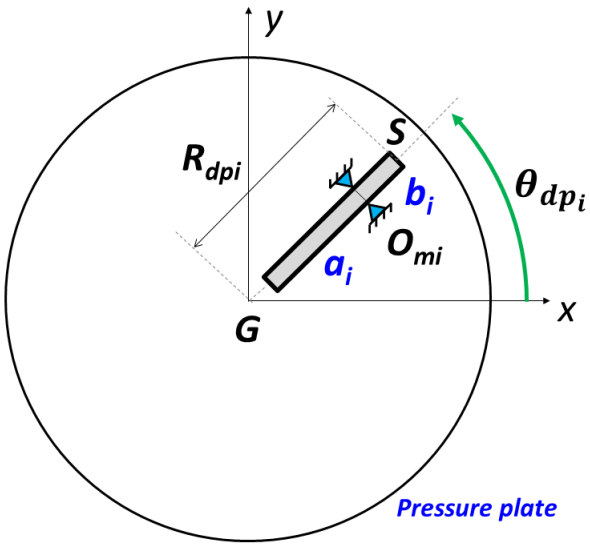

Figure 10.3: Upper view of the contact point S.

In global coordinates, this position is written as Eq. 10.2:

$$ {}_0\vec{r'}_{GS} = [R_{\gamma\beta\alpha}]\, {}_3\vec{r'}_{GS} \tag{10.2} $$

The total displacement in relation to the origin (Eq. 10.3) is obtained by assuming a variable

displacement z on the vertical direction. A static position is given by z_e.

$$ {}_0r'_{OS_z} = {}_0r'_{GS_z} - (z + z_e) = -R_{dp_i} \sin\beta \cos\theta_{dp_i} + R_{dp_i} \sin\alpha \cos\beta \sin\theta_{dp_i} + d_i \cos\alpha \cos\beta - z - z_e \tag{10.3} $$

The total displacement in relation to the initial position of S is calculated as in Eq. 10.4:

$$ \Delta\, {}_0r'_{OS_z} = d_i - {}_0r'_{OS_z} \tag{10.4} $$

The previous deformation resulted on a rotation θ_{m_i} around the point O_{m_i} a Fig. 10.4. This picture leads to the deduction of the deformation on the fingers of the spring $\Delta\, {}_0r_{f_z}$ on Eq. 10.5.

$$ \sin\theta_{m_i} = \frac{\Delta\, {}_0r'_{OS_z}}{b_i} = \frac{\Delta\, {}_0r'_{f_z}}{a_i} \tag{10.5} $$

It is necessary to perform a balance of moments around point O_{m_i} (Eq. 10.6) in order to obtain the force at the contact point F_s, that is presented in Eq. 10.7. The element moments are calculated by Eq. 10.8:

$$ -F_S b_i \cos\theta_{m_i} + M_{m_i} - F_{r_i} a \cos\theta_{dp_i} - c_{m_i}\dot{\theta}_{m_i} - k_{m_i}\theta_{m_i} = 0 \tag{10.6} $$

$$ {}_0\vec{F}'_S = -\left\{ \frac{M_{m_i}}{b_i} - F_{r_i}\left(\frac{a_i}{b_i}\right) - \Delta\, {}_0r'_{OS_z}\left[\frac{k_{m_i}}{b_i^2}\right] - \Delta\, {}_0\dot{r}'_{OS_z}\left[\frac{c_{m_i}}{b_i^2}\right] \right\} \vec{k} \tag{10.7} $$

$$ {}_3\vec{M}'_S = {}_3\vec{F}'_S \times {}_3\vec{r}'_{GS} \tag{10.8} $$

10.2 Element matrices

The element matrices result from Eq. 10.8. Equation 10.9 contains the influence of the stiffness k_{m_i}. The static efforts (contributions related to M_{m_i} and F_{r_i}) appear on Eq. 10.10. It is important to note that, in both case, an increase on the geometric parameter b results in a *reduction* on the total stiffness provided by the element.

$$ [K_{dp_I}] = \left[\frac{k_{m_i}}{b_i^2}\right] \begin{bmatrix} R_{dp_i}^2 \sin^2\theta_{dp_i} & -(R_{dp_i}^2/2)\sin(2\theta_{dp_i}) & -R_i \sin\theta_{dp_i} \\ -(R_{dp_i}^2/2)\sin(2\theta_{dp_i}) & -R_{dp_i}^2 \cos^2\theta_{dp_i} & R_{dp_i}\cos\theta_{dp_i} \\ -R_{dp_i}\sin\theta_{dp_i} & R_{dp_i}\cos\theta_{dp_i} & 1 \end{bmatrix} \tag{10.9} $$

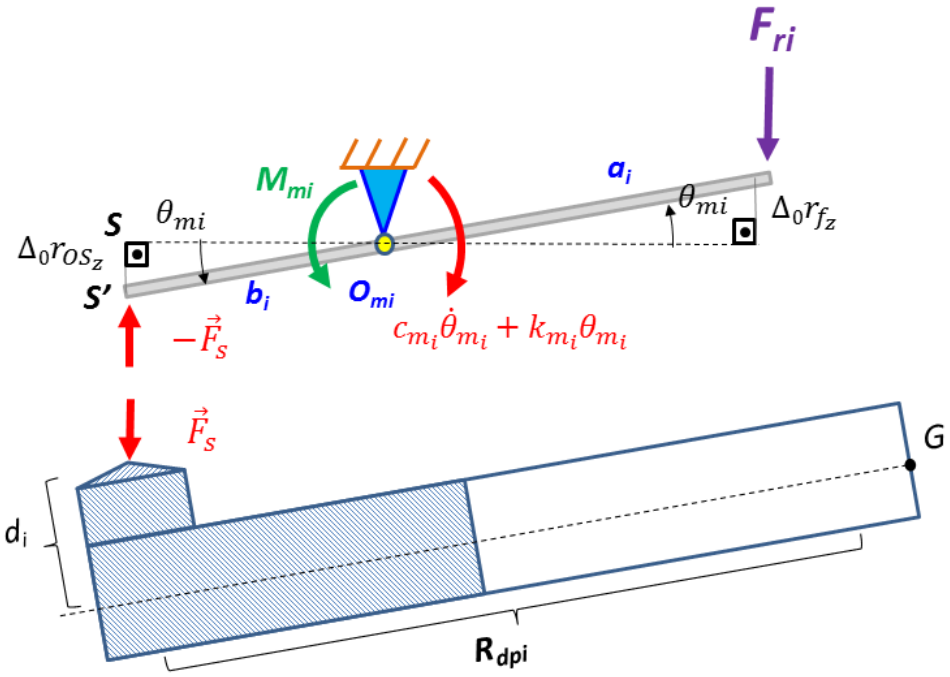

Figure 10.4: Lever model after a deformation θ_{m_i}.

$$[K_{dp_{II}}] = d_i \left[\frac{M_{m_i}}{b_i} - F_{r_i} \left(\frac{a_i}{b_i} \right) \right] \begin{bmatrix} -1 & 0 & 0 \\ 0 & -1 & 0 \\ 0 & 0 & 0 \end{bmatrix} \tag{10.10}$$

The damping matrix $[C_{dp_I}]$ (Eq. 10.11) contains a similar structure to $[K_{dp_I}]$ (Eq. 10.9). Greater values of b_i also resulted on reduction of damping. Equation 10.12 is an excitation vector.

$$[C_{dp_I}] = \left(\frac{c_{m_i}}{b_i^2} \right) \begin{bmatrix} R_{dp_i}^2 \sin^2 \theta_{dp_i} & -(R_{dp_i}^2/2) \sin(2\theta_{dp_i}) & -R_{dp_i} \sin \theta_{dp_i} \\ -(R_{dp_i}^2/2) \sin(2\theta_{dp_i}) & -R_{dp_i}^2 \cos^2 \theta_{dp_i} & R_{dp_i} \cos \theta_{dp_i} \\ -R_{dp_i} \sin \theta_{dp_i} & R_{dp_i} \cos \theta_{dp_i} & 1 \end{bmatrix} \tag{10.11}$$

$$\{F_{dp}\} = \begin{Bmatrix} -\left[\frac{M_{m_i} d_i}{b_i} - F_{r_i} \left(\frac{a_i}{b_i} \right) \right] R_i \sin \theta_{dp_i} \\ \left[\frac{M_{m_i} d_i}{b_i} - F_{r_i} \left(\frac{a_i}{b_i} \right) \right] R_i \cos \theta_{dp_i} \\ -\left[\frac{M_{m_i} d_i}{b_i} - F_{r_i} \left(\frac{a_i}{b_i} \right) \right] \end{Bmatrix} \tag{10.12}$$

An important point here is that the operation done on Eq. 10.7 creates *equivalent vertical stiffness/damping elements* at the connection point S (Figs. 10.4). Equivalent terms k_{dp_i}, c_{dp_i} and F_m from Eq. 10.13 could be replaced on Eqs. 10.9, 10.10, 10.11 and 10.12 .

$$\begin{cases} k_{dp_i} = \dfrac{k_{m_i}}{b_i^2} \\ c_{dp_i} = \dfrac{c_{m_i}}{b_i^2} \\ F_m = \dfrac{M_{m_i}}{b_i} - F_{r_i}\left(\dfrac{a_i}{b_i}\right) \end{cases} \tag{10.13}$$

The previous approach allows distinct ways to represent the diaphragm spring:

1. Create simulations using theoretical quantities for the physical parameters on Fig. 10.1.
2. *Introduce realistic measurements on the model*, handling with equivalent vertical quantities (Eq. 10.13). This approach will be presented in Section 10.4.
3. Create distributions of the lever element according to θ_{dp_i}.

10.3 Relations between the cushion, clamp load and release effort

Figure 10.5 contains the force balance on the system on a static condition. When the driver wants to separate the clutch from the flywheel, an effort F_{r_i} is applied on the diaphragm spring fingers. Two forces act in order to separate the pressure plate from the flywheel, one contribution from the cushion springs $F_{cushion}$ and another from the leaf springs F_{leaf} (studied in more detail in Chapter 11). They both result on the contact force F_S, which is in equilibrium with the diaphragm spring moment M_m and the release force.

Rigorously, there is $F_s = F_{cushion} + F_{leaf}$ (Kimmig, 1998). But considering that the leaf springs have a minor contribution in relation to the cushion, it is possible to approximate the previous expression as $F_s \approx F_{cushion}$. Such relation is indicated on Shaver and Shaver (1997). The normal force is defined by $F_{cushion}$ and was presented in Section 2.2. The clamp load curve (Fig. 10.7(a)) represents the *maximum load* that could be applied by the diaphragm spring. It is measured without the influence of $F_{release}$. But in any situation, the clamp load gives a measure of an approximation of the diaphragm stiffness (Fig. 10.7(b)).

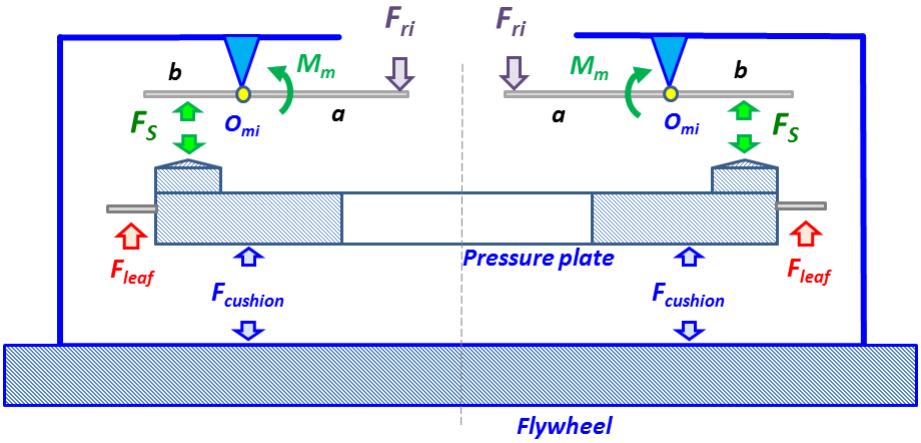

Figure 10.5: Force contributions on the system.

10.3.1 Clamp load

The clamp load curve is the total force that the diaphragm spring applies to the pressure plate. It is represented by the forces F_S when $F_{ri} = 0$ on Fig. 10.5. Figure 10.6 contains a schematic view of the instrumentation of the test bench used for the clutch cover. At the bottom, the total force on the pressure plate F_S is also monitored by clamp load sensor. The reference for a positive pressure plate position is indicated on Fig. 10.6.

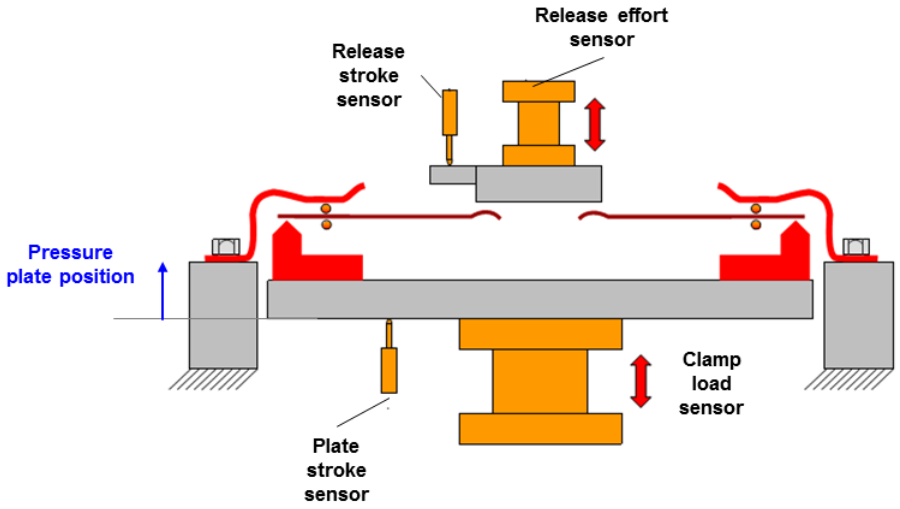

Figure 10.6: Clamp and release load experimental setup (Adapted from Lerestrelo (2013)).

Due to the hysteresis, the clamp load curve for a passenger car with manual transmission is represented on Fig. 10.7(a) with the following features:

- The upper curve is obtained for increasing pressure plate positions.
- The lower curve is measured if the position is reduced.
- The numerical mean value will be applied in Sections 10.4.1 and 10.4.2.

Figure 10.7(b) presents the derivative of Fig. 10.7(a) resulting on the necessary values for the stiffness k_{dp_i} (Eq. 10.13). Its contribution is not negligible to a model, once that the values found are greater than 10^6 N/m. Figure 10.7(a) provide a clear view of regions with *positive* and *negative* stiffness.

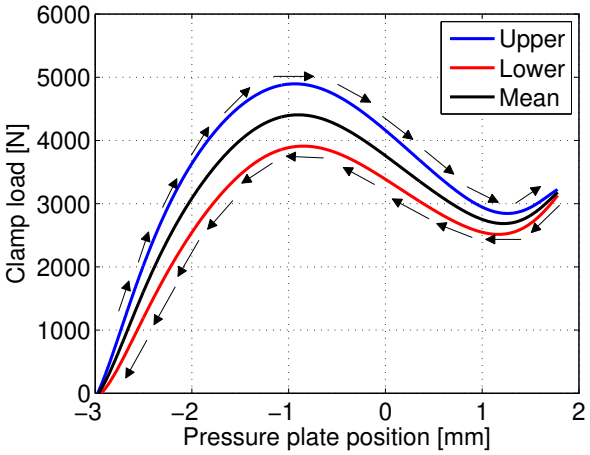

(a)

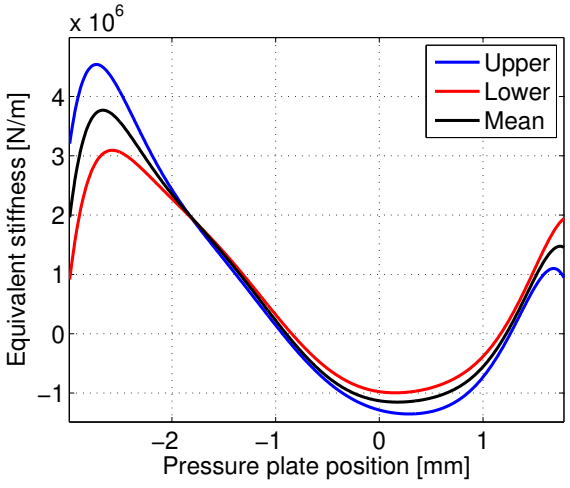

(b)

Figure 10.7: Clamp load curve with indication of the path for pressure plate position increase/decrease (Fig. 10.7(a)). Its derivative is represented on Fig. 10.7(b).

10.4 Numerical simulations

Having the previous explanations in mind, simulations were performed considering a new and a worn clutch disc (Sections 10.4.1 and 10.4.2), on the model from Section 8 with the cushion curves from Chapter 2. The pressure plate was assumed with a cylindrical shape ($m = 1.5kg$, $h = 0.01m$, $R_{in} = 0.075m$ and $R_{out} = 0.1m$). The contact radius was considered as $R_i = 0.0875m$.

10.4.1 New clutch disc

Figure 10.8(a) presents the clamp and cushion curves on the same graphic. The reference for displacement for the cushion curve was inverted in relation to Fig. 2.4(b). Point F_{new} indicates a fully coupled condition, where the cushion springs balance the effort of the plate. The pressure plate position according to the reference on Fig. 10.6 is shown on the abscissa. Point F_{new} is the reference for the clamp load measurement. When the driver needs to decouple the clutch, the displacement is moved to the right, as indicated on the picture. In this situation, the pressure plate can be separated from the clutch disc. The normal force on the plate is given by the value of the cushion function (F_m on Eq. 10.13). Considering the clutch cover ratio, the difference between those curves is related to the release effort F_{r_i}.

In this condition, the diaphragm spring works on a region of *negative stiffness* ranging between -1.2×10^6 and -0.8×10^6 N/m that gradually increases according to the position of the pressure plate (Fig. 10.8(b)). Between 0 and 0.2 mm , high values of cushion stiffness (above 5×10^6 N/m) are found.

It is possible to look at the natural frequencies on Fig. 10.8(c) and see that they follow the cushion profile. Near coupling condition, the natural frequencies of the stable and unstable wobbling modes as well as the axial movement of the plate start above 400 Hz. At approximately 0.1 mm, they reach values nearby 300 Hz, which is very close to the value found for real events (Fig. 1.1).

The real part of the unstable eigenvalue was augmented for greater levels of friction (Fig. 10.8(d)) as indicated by Wickramarachi *et al.* (2005). Its greatest values occurred closer to the position of F_{new}.

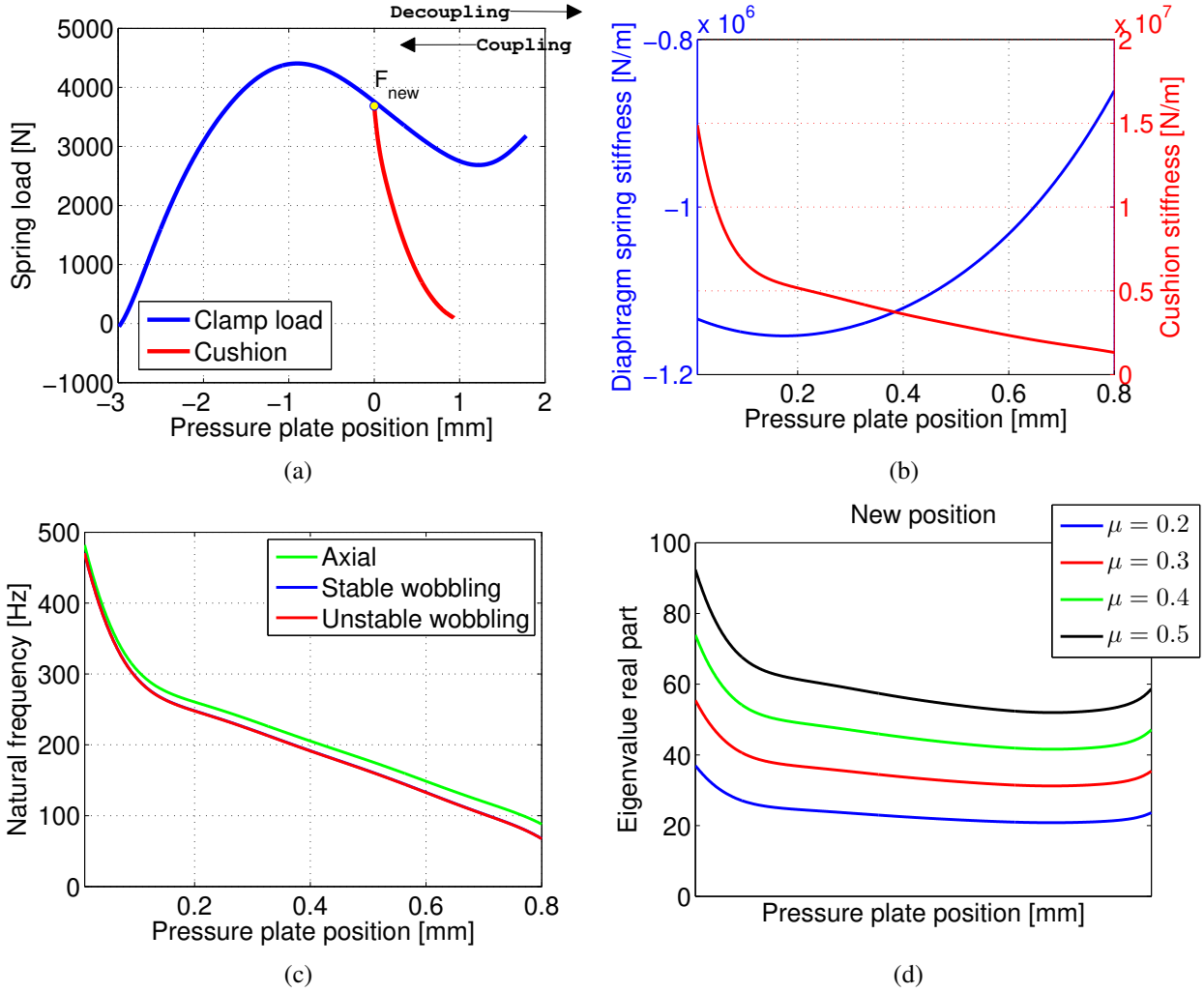

Figure 10.8: Clamp load and cushion curve on for a new clutch disc (Fig. 10.8(a)). Stiffness values (Fig. 10.8(b)), natural frequencies (Fig. 10.8(c)) and eigenvalue real parts (Fig. 10.8(d)) for a new clutch disc.

10.4.2 Worn clutch disc

When the clutch is worn, the thickness of the organic facings is reduced. The embedding phenomenon (Sfarni *et al.*, 2011) can change the cushion curve if the spring causes internal deformations on the facings. As a direct consequence from that, the equilibrium condition is shifted to the point F_{wear} in Fig. 10.9(a). The load value is practically the same as the one found for F_{new} (Fig. 10.8(a)). In this case, the cushion profile is modified to be the worn disc version from Fig. 2.4(b). For positive displacements from the equilibrium value, Fig. 10.9(a) presents that a positive slope on the clamp load, indicating positive stiffness for the diaphragm spring operating under these

conditions.

The derivative of the clamp and cushion curves is shown in Fig. 10.9(b). The diaphragm spring have a *positive stiffness* between 0.5 and 2×10^6 N/m that decreases for greater position from the equilibrium point. The cushion spring have stiffness above 0.5×10^7 N/m up to the position -1.5 mm. In comparison to the previous case (Fig. 10.8(c)), higher natural frequencies are computed under these circumstances. Values nearby 300 Hz occur only after at -1.4 mm, at least 0.3 mm far from the initial position. The unstable mode real part increased with the friction coefficient (Wickramarachi *et al.*, 2005), like the previous case, with peak on low displacement values.

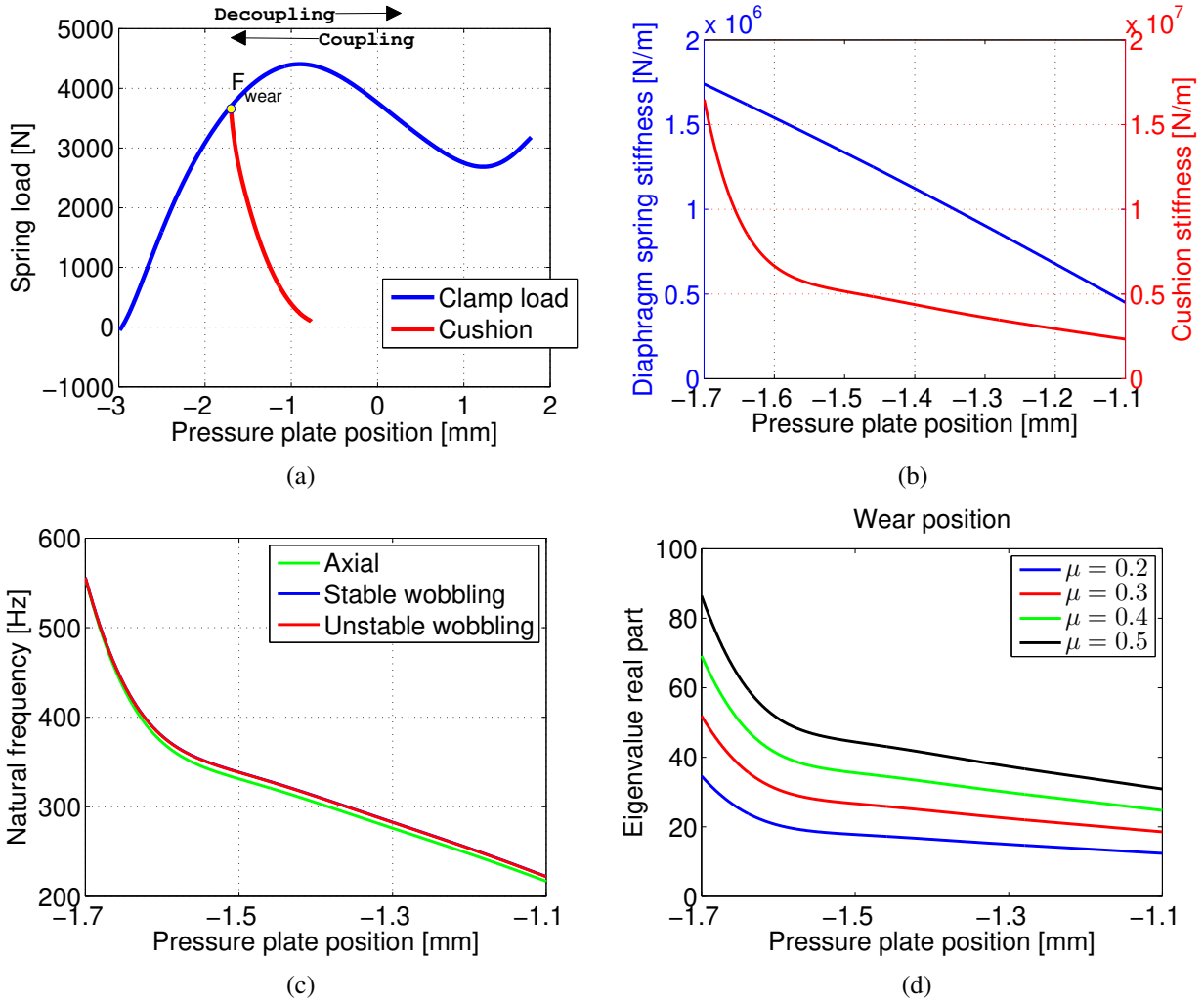

Figure 10.9: Clamp load and cushion curve on for a worn clutch disc (Fig. 10.9(a)). Stiffness values (Fig. 10.9(b)), natural frequencies (Fig. 10.9(c)) and eigenvalue real parts (Fig. 10.9(d)) for a worn clutch disc.

10.5 Chapter summary

A lever model for the diaphragm spring was presented in Section 10.1. Besides that, it was shown that clamp load and cushion measurements can be included to the simulations. This was intended to be helpful for designers, creating a bridge between the formulations on the previous chapters with the technical field. A realistic model needs to fulfil the points of the new and worn clutch disc.

By looking at the key conditions for the clutch its was possible to observe that the diaphragm spring may have regions with negative (new disc) or positive (worn disc) stiffness. Besides that, the greatest factor that determines the behaviour of the natural frequencies of this system was the cushion spring.

11 Considerations on the leaf spring representation

In this chapter, the leaf springs are modelled, taking into account its position in relation to the clutch cover/pressure plate system. It will be possible to observe that, due to its action on both wobbling coordinates, it can be effective to turn a skew symmetric stiffness matrix into an asymmetric form. This action will have a greater impact on the system stability.

This idea has not occurred on the clutch literature (Chapter 3) but Hoffmann *et al.* (2002) studied a minimal model for brake squeal where it was possible to modify its stability with the modification of the angles of inclined springs attached to a mass positioned over a moving belt with frictional contact. But here it will be explained that the inclined element representing the straps/leaf spring will allow modification on stiffness, distance from the centre of gravity, and preload. This approach tends to stabilize this system without the use of damping.

11.1 Leaf spring (strap) description

A leaf spring(s) or strap(s) from a passenger car clutch system are presented in Fig. 11.2. It does not have an know helical spring characterization, but it is responsible to separate the pressure plate from the clutch disc when the torque transmission is interrupted. In this work, it is assumed as a composition of an axial stiffness element (k_{z_i}) with a tangential one (k_{t_i}). Figure 11.2 depicts the points where the strap is connected to the clutch cover. The extremities of this element are fixed through rivets, one on the pressure plate (points E1, E2 and E3) and the other on the housing (points CV1, CV2 and CV3).

11.2 An inclined stiffness element subjected to wobbling

Figures 11.3(a) and 11.3(b) represent the movement of the pressure plate in relation to the clutch housing. During operation, both elements have the same rotating speed $\dot{\gamma}$. There is no relative angular motion between them. The tangential stiffness k_t is attached to the pressure plate at point E_i, while it is fixed on the housing at the point CV_i (Fig. 11.3(a)). This configuration is directly based on the real system (Fig. 11.2). The position of point E_i in relation to the centre of gravity of the plate G is given by angle θ_{r_i} and radius R_i (Fig. 11.3(a)) and the distance from the centre of gravity l (Fig. 11.3(b)). Due to the previous assumption of relative motion, the rotating angles γ do not cause deformation on the stiffness element, once that this angular motion happens

in both the pressure plate and housing simultaneously.

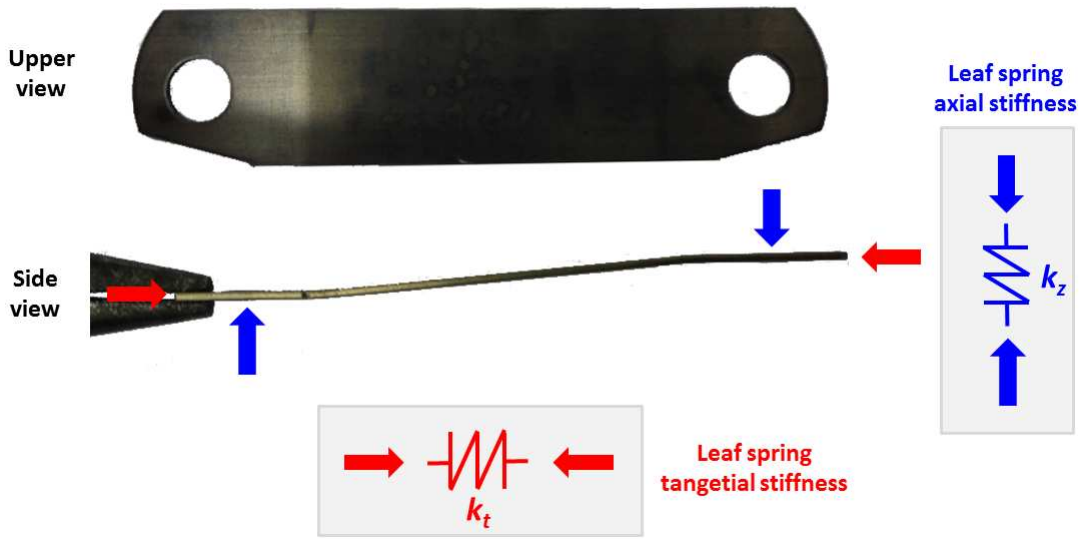

Figure 11.1: Leaf spring interpretation.

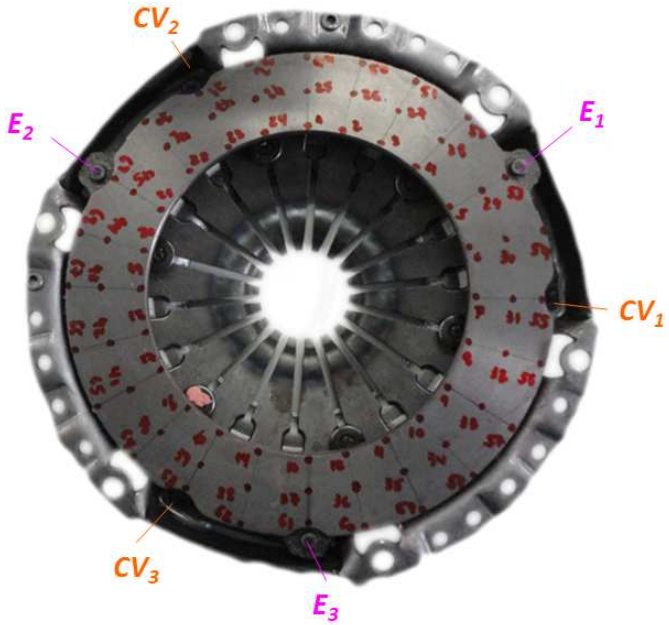

Figure 11.2: Position of the straps in relation to the pressure plate and clutch cover.

The position of attachment on the pressure plate is given by Eq. 11.1. This work considers the stiffness element in a position bellow the pressure plate (Fig. 11.3(b)). These model is suited for a pressure plate modelled on the coordinate system from Section 7.1.

$$ {}_3\vec{r'}_{GE_i} = \begin{Bmatrix} R_i \cos\theta_{r_i} & R_i \sin\theta_{r_i} & -l \end{Bmatrix}^T \tag{11.1} $$

The tangential efforts will be calculated on the coordinate system $x'_1 y'_1 z'_1$. Comparing Figs. 7.1(b) and 7.1(a), this approach will avoid unnecessary calculations involving the angle γ. In global coordinates, this position vector is given by:

$$ {}_1\vec{r'}_{GE_i} = [R_\beta][R_\alpha]\,{}_3\vec{r'}_{GE_i} \tag{11.2} $$

Adopting a vertical translation, the position of the point E_i in relation to the origin O is given by Eq. 11.3:

$$ {}_1\vec{r'}_{OE_i} = {}_1\vec{r'}_{OG} + {}_1\vec{r'}_{GE_i} = \begin{Bmatrix} 0 & 0 & -z - z_e \end{Bmatrix}^T + {}_1\vec{r'}_{GE_i} \tag{11.3} $$

The deformation on the element is calculated by Eq. 11.4:

$$ \Delta\,{}_1\vec{r'}_{OE_i} = \begin{Bmatrix} R_i \cos\theta_{r_i} & R_i \sin\theta_{r_i} & -l \end{Bmatrix}^T + {}_1\vec{r'}_{OE_i} \tag{11.4} $$

To move the representation from $x'_1 y'_1 z'_1$ to the system $x_4 y_4 z_4$ (Fig. 11.3(a)) it is necessary the use of a rotation matrix determined by angle ρ_i, and the transformations given by Eqs. 11.5 and 11.6.

$$ {}_4\vec{r'} = [R_{\varepsilon_i}]^T\,{}_1\vec{r'} = \begin{bmatrix} \cos\rho_i & \sin\rho_i & 0 \\ -\sin\rho_i & \cos\rho_i & 0 \\ 0 & 0 & 1 \end{bmatrix} {}_1\vec{r'} \tag{11.5} $$

$$ {}_1\vec{r'} = [R_{\varepsilon_i}]\,{}_4\vec{r'} = \begin{bmatrix} \cos\rho_i & -\sin\rho_i & 0 \\ \sin\rho_i & \cos\rho_i & 0 \\ 0 & 0 & 1 \end{bmatrix} {}_4\vec{r'} \tag{11.6} $$

The deformation $\Delta\,{}_1\vec{r'}_{OE_i}$ is transformed as presented on Eq. 11.7. The element effort is shown in Eq. 11.8 where k_{t_i} is the tangential stiffness and F_{te_i} is a preload of the spring opposed to the rotating speed $\dot{\gamma}$.

$$ \Delta\,{}_4\vec{r'}_{OE_i} = [R_{\varepsilon_i}]^T \Delta\,{}_1\vec{r'}_{OE_i} = \begin{Bmatrix} \Delta\,{}_4r'_{OE_{i_x}} \\ \Delta\,{}_4r'_{OE_{i_y}} \\ \Delta\,{}_4r'_{OE_{i_z}} \end{Bmatrix} \tag{11.7} $$

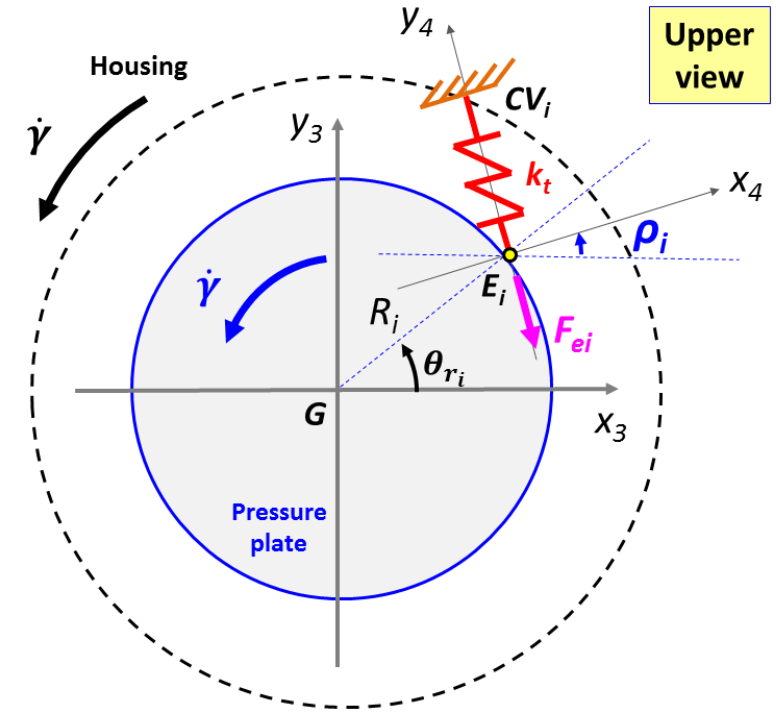

(a)

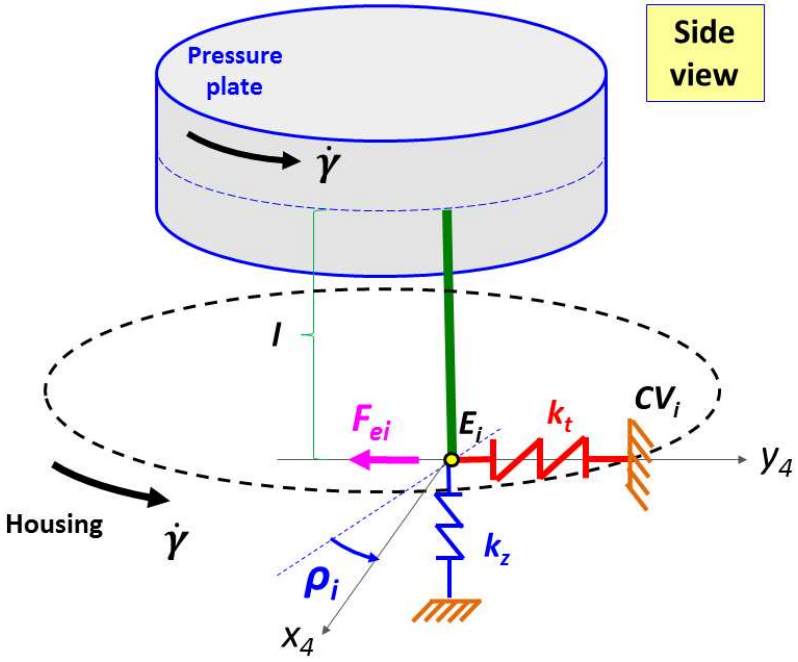

(b)

Figure 11.3: Leaf spring modelled on upper (Fig. 11.3(a)) and side (Fig. 11.3(b)) views.

$$ {}_4\vec{F'}_{t_i} = \begin{Bmatrix} 0 \\ -F_{e_i} + k_t \Delta\ {}_4 r'_{OE_{iy}} \\ 0 \end{Bmatrix} \tag{11.8} $$

The element effort is moved to the global coordinates (Eq. 11.9), which results on forces ${}_1F_{t_x}$ and ${}_1F_{t_y}$ on the plane xy. Then, they are written on the system attached to the body (Eq. 11.10):

$$ {}_1\vec{F'}_{t_i} = [R_{\varepsilon_i}]^T\ {}_4\vec{F'}_{t_i} = \begin{Bmatrix} {}_1F_{t_x} \\ {}_1F_{t_y} \\ 0 \end{Bmatrix} \tag{11.9} $$

$$ {}_3\vec{F'}_{t_i} = [R_\alpha]^T [R_\beta]^T\ {}_1\vec{F'}_{t_i} \tag{11.10} $$

The element matrices are calculated from moments around the centre off gravity on Eq. 11.11:

$$ {}_3\vec{M'}_{t_i} = {}_3\vec{r'}_{GE_i} \times {}_3\vec{F'}_{t_i} \tag{11.11} $$

11.3 Inclined stiffness matrices

The matrix $[K_{s_I}]_i$ from Eq. 11.12 has the effect of the spring static load that is defined by both position and orientation angles (θ_{r_i} and ρ_i).

$$ [K_{s_I}]_i = F_{e_i} R_i \begin{bmatrix} -\cos\rho_i \sin\theta_{r_i} & -\sin\rho_i \sin\theta_{r_i} & 0 \\ \cos\rho_i \cos\theta_{r_i} & \sin\rho_i \cos\theta_{r_i} & 0 \\ 0 & 0 & 0 \end{bmatrix} \tag{11.12} $$

Matrix $[K_{s_{II}}]_i$ (Eq. 11.13) has the effect of the tangential stiffness k_{t_i}. It is important to note here that it depends on the square of the distance l (Fig. 11.3(b)), meaning that the farther the element is positioned from the centre of gravity, the greater the inner elements off this matrix will be. If $\sin(2\rho_i) \neq 0$, the element is able to produce torque for movements on both α and β. This contribution of stiffness does not depend on the element position θ_{r_i}.

$$ [K_{s_{II}}]_i = k_{t_i} l^2 \begin{bmatrix} \cos^2\rho_i & (1/2)\sin(2\rho_i) & 0 \\ (1/2)\sin(2\rho_i) & \sin^2\rho_i & 0 \\ 0 & 0 & 0 \end{bmatrix} \tag{11.13} $$

11.4 Using the stiffness matrix ($[K_{s_{II}}]_i$)

Equation 11.14 presents the total contribution of a set of 3 inclined elements with same stiffness (k_t) and distance l. Function $f_{s_{11}}$, $f_{s_{22}}$ and $f_{s_{12}}$ are written in terms of trigonometric relations Eq. 11.15. Shift angles $\Delta\rho_{s_1}$ and $\Delta\rho_{s_2}$ allow the creation of elements in directions based on a common reference ρ.

$$[K_{s_{II}}] = \sum_{i=1}^{3} [K_{s_{II}}]_i = k_t l^2 \begin{bmatrix} f_{s_{11}}(\rho, \Delta\rho_s) & f_{s_{12}}(\rho, \Delta\rho_s) & 0 \\ f_{s_{12}}(\rho, \Delta\rho_s) & f_{s_{22}}(\rho, \Delta\rho_s) & 0 \\ 0 & 0 & 0 \end{bmatrix} \tag{11.14}$$

$$\begin{cases} f_{s_{11}} = \cos^2(\rho) + \cos^2(\rho + \Delta\rho_{s_1}) + \cos^2(\rho + \Delta_{s_2}) \\ f_{s_{22}} = \sin^2(\rho) + \sin^2(\rho + \Delta\rho_{s_1}) + \sin^2(\rho + \Delta\rho_{s_2}) \\ f_{s_{12}} = \left(\frac{1}{2}\right)\sin(2\rho) + \left(\frac{1}{2}\right)\sin\left[2(\rho + \Delta\rho_{s_1})\right] + \left(\frac{1}{2}\right)\sin\left[2(\rho + \Delta\rho_{s_2})\right] \end{cases} \tag{11.15}$$

11.4.1 Elements with the same direction ($\Delta\rho_{s_1} = \Delta\rho_{s_2} = 0$)

If all elements are arranged on with the same orientation angle, Equation 11.15 becomes Eq. 11.16. The elements on the main diagonal ($f_{s_{11}}$ and $f_{s_{22}}$) will be positive values, while the element $f_{s_{12}}$ is a sinusoidal function that can result on negative values. For $\rho = 45°$ the expression given by $f_{s_{12}}$ reaches a maximum value (Fig. 11.4(a)). In this case, $f_{s_{11}} = f_{s_{22}} = f_{s_{12}}$.

$$\begin{cases} f_{s_{11}} = 3\cos^2(\rho) \\ f_{s_{22}} = 3\sin^2(\rho) \\ f_{s_{12}} = \left(\frac{3}{2}\right)\sin(2\rho) \end{cases} \tag{11.16}$$

Combining the model from Chapter 8.1 with Eqs. 11.14 and 11.16 results on Eq. 11.17. The only source of damping in this case are the friction related terms ($c_{11} = c_{22}$ on Eq. 11.18).

$$\begin{bmatrix} I & 0 \\ 0 & I \end{bmatrix} \begin{Bmatrix} \ddot{\alpha} \\ \ddot{\beta} \end{Bmatrix} + \begin{bmatrix} c_{11} & \dot{\gamma}(-2I + I_{z'z'}) \\ \dot{\gamma}(2I - I_{z'z'}) & c_{22} \end{bmatrix} \begin{Bmatrix} \dot{\alpha} \\ \dot{\beta} \end{Bmatrix} + \begin{bmatrix} k_{11} & k_{12} \\ -k_{21} & k_{22} \end{bmatrix} \begin{Bmatrix} \alpha \\ \beta \end{Bmatrix} = \begin{Bmatrix} 0 \\ 0 \end{Bmatrix} \tag{11.17}$$

$$c_{11} = c_{22} = 4\frac{\mu h^2 k z_e}{R|\dot{\gamma} - \dot{\theta}|} \tag{11.18}$$

When all stiffness are have the same direction, the terms k_{12} and k_{21} out from the main diagonal (Eqs. 11.19 and 11.20) are different. The terms on the main diagonal (k_{11} and k_{22}) may be different if $\rho \neq 45°$ (Eqs. 11.21 and 11.22).

$$k_{12} = \left[2\mu k R h - 2\mu(h^2/R)kz_e\right] sign(\dot{\gamma}) + (k_t l)^2 \left(\frac{3}{2}\right) \sin(2\rho) \tag{11.19}$$

$$k_{21} = \left[2\mu k R h - 2\mu(h^2/R)kz_e\right] sign(\dot{\gamma}) - (k_t l)^2 \left(\frac{3}{2}\right) \sin(2\rho) \tag{11.20}$$

$$k_{11} = (2R^2 + 2\mu^2 z_e h)k + \dot{\gamma}^2(I_{z'z'} - I) + 3(k_t l)^2 \cos^2(\rho) \tag{11.21}$$

$$k_{22} = (2R^2 + 2\mu^2 z_e h)k + \dot{\gamma}^2(I_{z'z'} - I) + 3(k_t l)^2 \sin^2(\rho) \tag{11.22}$$

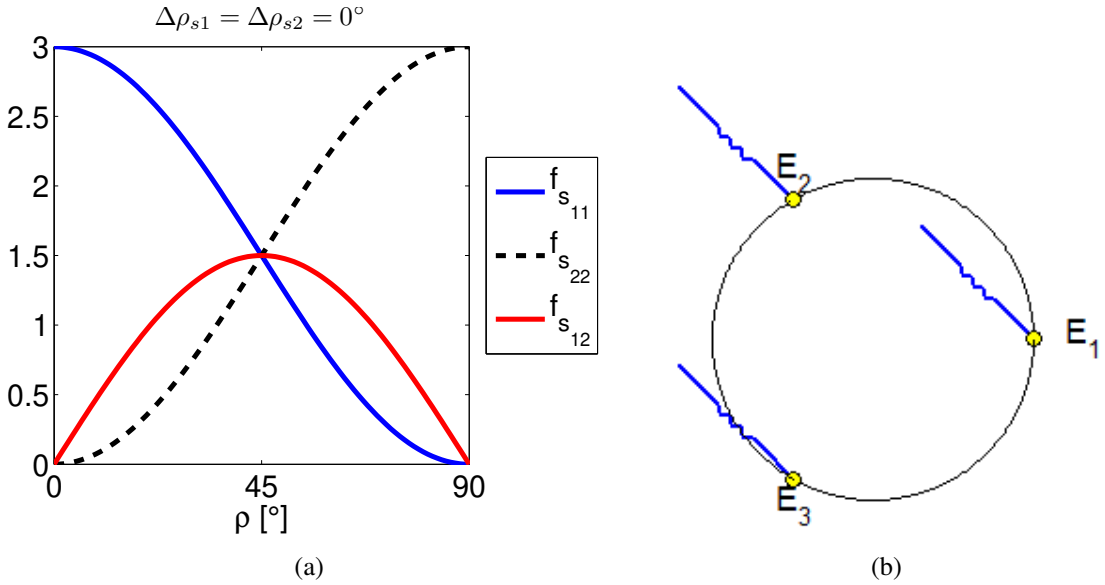

(a) (b)

Figure 11.4: Element functions for $\Delta\rho_{s_1} = \Delta\rho_{s_2} = 0°$ (Fig. 11.4(a)). Physical distribution with $\rho = 45°$ on Fig. 11.4(b).

The simulations were done assuming a pressure plate with $m = 2$kg, $h = 0.01$m, $R_{in} = 0.075$ m and $R_{out} = 0.1$m. The cushion parameters were assumed as $k = 3 \times 10^6/4$ N/m, $u = 0.3$, $R = 0.0875$m and $z_e = 0.001$m. A constant rotating speeds ($\dot{\gamma} = 2000$ rpm and $\dot{\theta} = 0$ rpm) were adopted on the model.

Figure 11.6(a) presents the unstable mode natural frequency that is found nearby 195-197 Hz. Due to the asymmetric stiffness terms, this characteristics for the stable mode may achieve very high values, up to 10^4 Hz with $k_t = 10^10 N/m$ (Fig. 11.6(b)). Figures 11.6(c) (eigenvalue real part) and 11.6(d) (real part signal) shows a transition on stability of this system. They present the following trend:

- if the element is positioned very close to the centre of gravity ($l \approx 0$), k_t must be greater than 10^{10} N/m.
- increase the absolute value of l requires a lower tangential stiffness for stability
- Equation 11.14 depends on l^2 and, as a direct consequence from that, all results in Fig. 11.6 are mirrored in relation to $l = 0$m. Physically, there is no difference if the tangential stiffness is positioned *bellow* or *above* the centre of gravity of the pressure plate.
- the real part of the stable eigenvalue is increased (Fig. 11.6(e)) but it is always negative (Fig. 11.6(f)).

11.4.2 Elements with symmetric orientation ($\Delta\rho_{s_1} = 120^\circ$ and $\Delta\rho_{s_2} = 240^\circ$)

A symmetric orientation of the elements is achieved with $\Delta\rho_{s_1} = 120^\circ$ and $\Delta\rho_{s_2} = 240^\circ$ (Fig. 11.5(a)). For this configuration, Equation 11.23 presents that the skew symmetric terms are zero $f_{s_{12}} = 0$. The elements on the main diagonal are constant ($f_{s_{11}} = f_{s_{11}} = 3/2$), independent from the reference angle ρ (Fig. 11.5(b)).

$$\begin{cases} f_{s_{11}} = \cos^2(\rho) + \cos^2(\rho + 120^\circ) + \cos^2(\rho + 240^\circ) = 3/2 \\ f_{s_{22}} = \sin^2(\rho) + \sin^2(\rho + 120^\circ) + \sin^2(\rho + 240^\circ) = 3/2 \\ f_{s_{12}} = \left(\frac{1}{2}\right)\sin(2\rho) + \left(\frac{1}{2}\right)\sin\left[2(\rho + 120^\circ)\right] + \left(\frac{1}{2}\right)\sin\left[2(\rho + 240^\circ)\right] = 0 \end{cases} \tag{11.23}$$

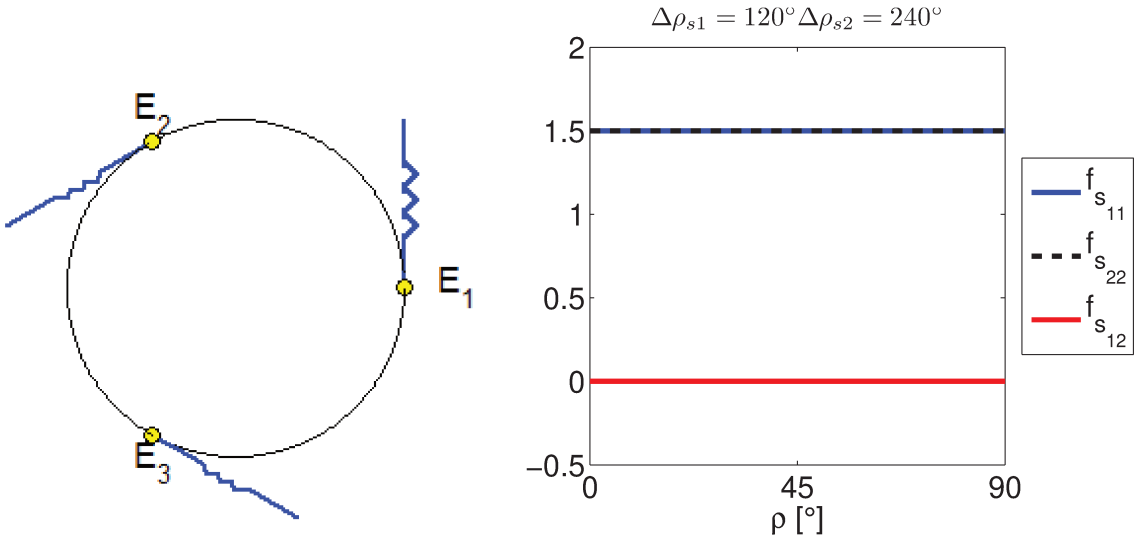

(a) (b)

Figure 11.5: Symmetric orientation for $\rho = 0°$ (Fig. 11.5(a)). Element functions for $\Delta\rho_{s_1} = 120°$ and $\Delta\rho_{s_2} = 240°$ (Fig. 11.5(b)).

As consequence from Eq. 11.23, the elements on the main diagonal from Eq. 11.17 are equal. The terms k_{12} and k_{21} are only related to friction efforts (Eq. 11.25).

$$k_{11} = k_{22} = (2R^2 + 2\mu^2 z_e h)k + \dot{\gamma}^2(I_{z'z'} - I) + \left(\frac{3}{2}\right)(k_t l)^2 \tag{11.24}$$

$$k_{21} = k_{12} = \left[2\mu kRh - 2\mu(h^2/R)kz_e\right] sign(\dot{\gamma}) \tag{11.25}$$

The system data was the same from Section 11.4.1. A consequence from the symmetry on the matrices (Eqs. 11.24 and 11.25) is that the natural frequencies of the modes behave in a similar manner (Figs. 11.7(a) and 11.7(b)). They both increase with the element stiffness. In this case, the real part from Fig. 11.7(c) requires greater values of k_t compared to the previous case (Fig. 11.6(c)). Stability is achieved only for very high values off stiffness, above 10^9 N/m (Fig. 11.7(d)). The real part of the stable eigenvalue becomes closer to zero with such amount of stiffness (Fig. 11.7(e)). This example leads to important verifications:

- a modification on the orientation must be carefully taken once that it can lead to very different stability conditions.
- without the non-diagonal terms ($k_{12} = k_{21} = 0$) the tangential stiffness involved could be prohibitive in terms of materials and design for a lightly damped system.

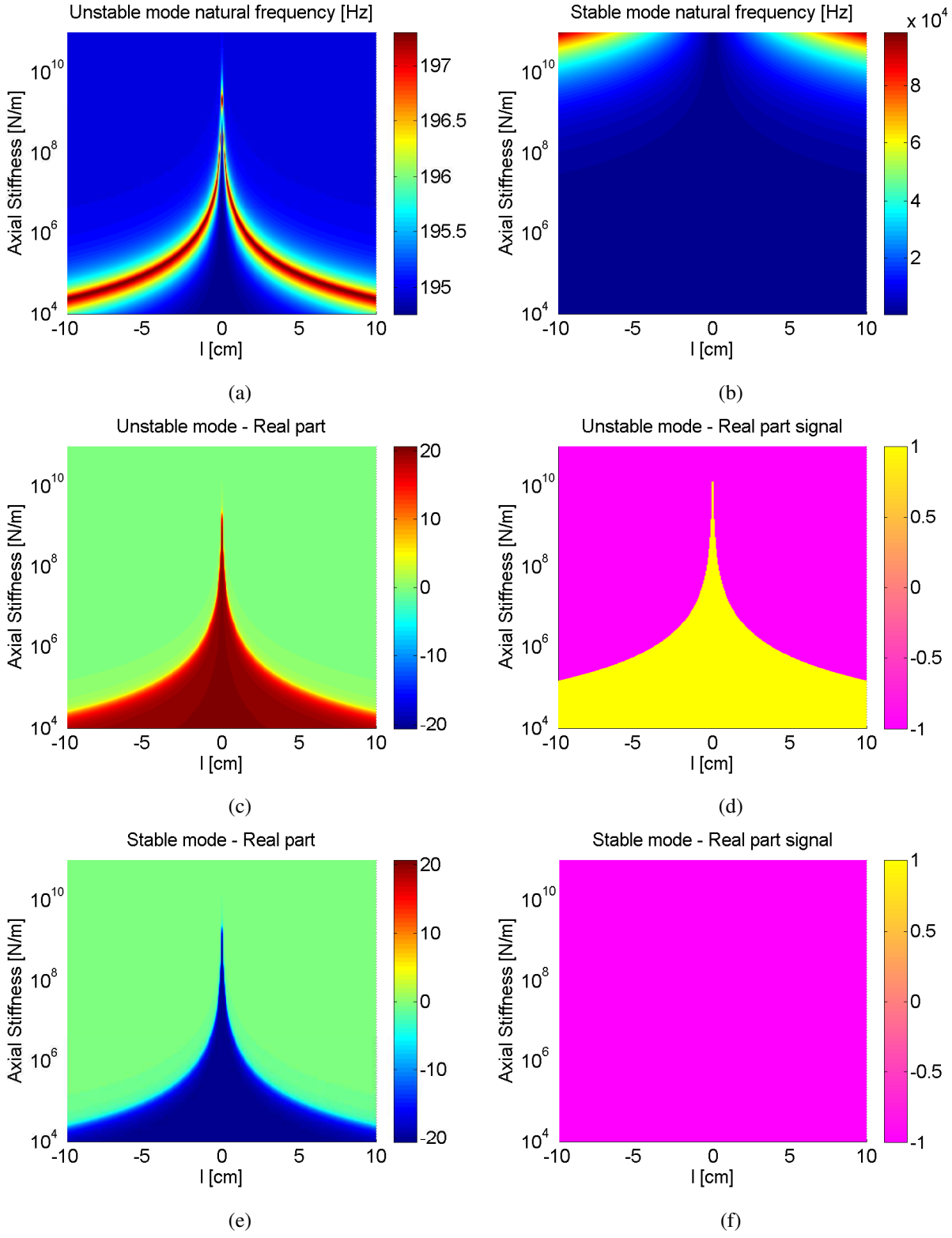

Figure 11.6: Results for $\Delta\rho_{s_1} = \Delta\rho_{s_2} = 0°$ and $\rho = 45°$. Natural frequencies (Figs. 11.6(a) and 11.6(b)), eigenvalue real parts (Figs. 11.6(c) and 11.6(e)) and their signals (Figs. 11.6(d) and 11.6(e)).

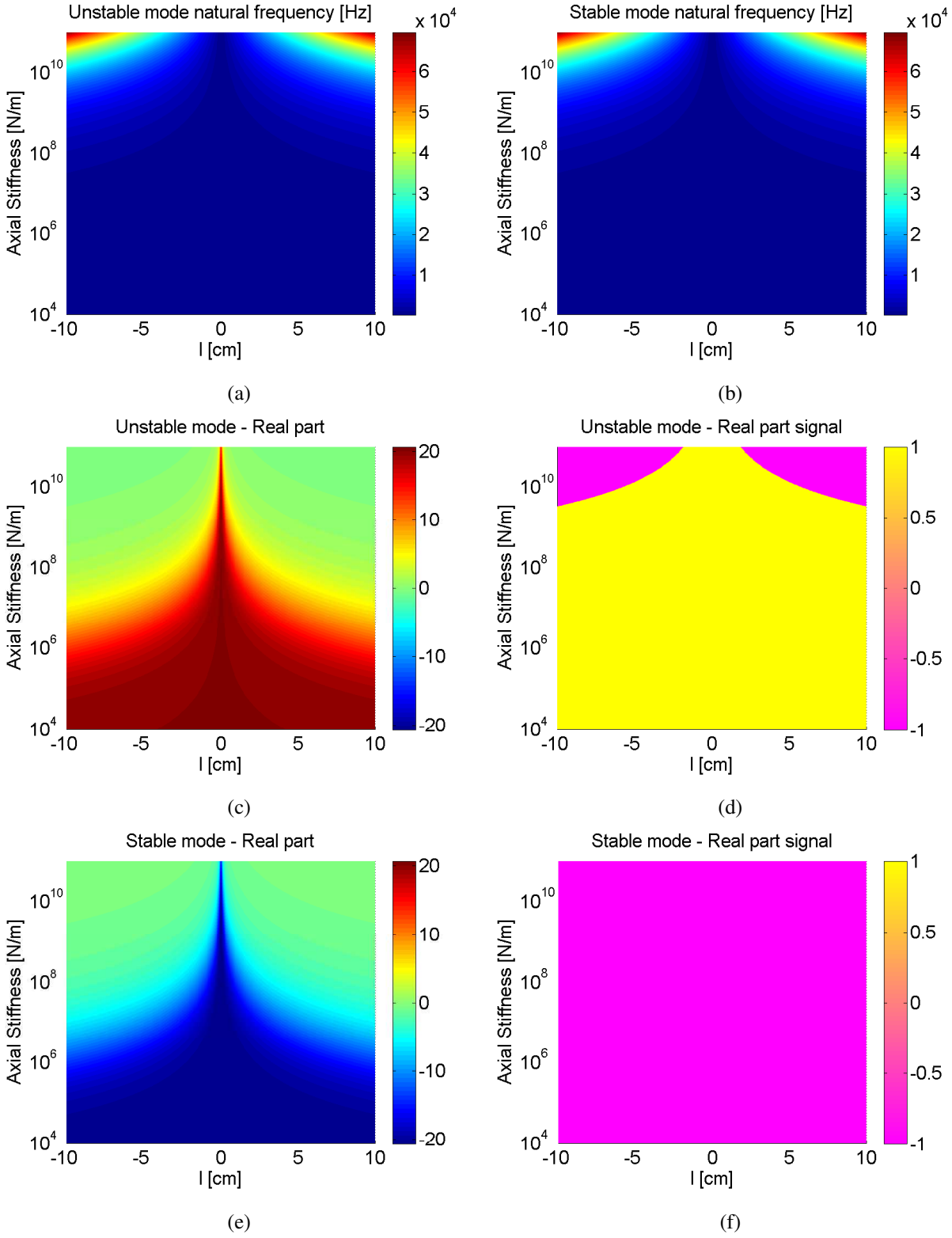

Figure 11.7: Results for $\Delta\rho_{s_1} = 120°$, $\Delta\rho_{s_2} = 240°$ and $\rho = 0°$. Natural frequencies (Figs. 11.7(a) and 11.7(b)), eigenvalue real parts (Figs. 11.7(c) and 11.7(e)) and their signals (Figs. 11.7(d) and 11.7(f)).

11.5 Using the preload matrix ($[K_{s_I}]_i$)

The combination of three inclined elements lead to the following contribution in terms accounting a common preload F_e and radius R_s (Eq. 11.26). Equation 11.27 presents the trigonometric functions f_{p11}, f_{p22}, f_{p12} and f_{p21} choosing a symmetrical distribution in relation to the disc ($\theta_r = 0$, 120 and 240° on Eq. 11.12). Angles $\Delta\rho_{s_1}$ and $\Delta\rho_{s_2}$ are used to define the orientation of those elements (Eq. 11.14) .

$$[K_{s_I}] = \sum_{i=1}^{3} [K_{s_I}]_i = F_e R_s \begin{bmatrix} f_{p11} & f_{p12} & 0 \\ f_{p21} & f_{p22} & 0 \\ 0 & 0 & 0 \end{bmatrix} \tag{11.26}$$

$$\begin{cases} f_{p11} = -\cos\rho_i \sin 0° - \cos(\rho + \Delta\rho_{s_1}) \sin 120° - \cos(\rho + \Delta\rho_{s_2}) \sin 240° \\ f_{p22} = \sin\rho_i \cos 0° + \sin(\rho + \Delta\rho_{s_1}) \cos 120° + \sin(\rho + \Delta\rho_{s_2}) \cos 240° \\ f_{p12} = -\sin\rho_i \sin 0° - \sin(\rho + \Delta\rho_{s_1}) \sin 120° - \sin(\rho + \Delta\rho_{s_2}) \sin 240° \\ f_{p21} = -\cos\rho_i \cos 0° - \cos(\rho + \Delta\rho_{s_1}) \cos 120° - \cos(\rho + \Delta\rho_{s_2}) \cos 240° \end{cases} \tag{11.27}$$

Figure 11.8(a) shows the functions from Eq. 11.27 with equal orientation angles $\Delta\rho_{s_1} = \Delta\rho_{s_2} = 0°$. Based on the previous picture, such configuration lead to the following conclusions:

- there is no effect of preload $f_{p11} = f_{p22} = f_{p12} = f_{p21} = 0°$
- the designer can only make modifications on the stiffness (Section 11.4.1)

A very different condition is presented by Eq. 11.8(a), where a symmetric orientation is used ($\Delta\rho_{s_1} = 120°$ and $\Delta\rho_{s_2} = 240°$). It results on a skew symmetric matrix. Figure 11.8(b) shows the trigonometric functions from Eq. 11.27 for different orientation references (ρ). The terms out from the main diagonal are greater for $\rho = 0°$ ($|f_{p12}| = |f_{p21}| = 1.5$) while $f_{p11} = f_{p22} = 0$. This orientation case allows modifications on preload and stiffness (Section 11.4.2) and is physically represented by Fig. 11.5(a).

$$[K_{s_{II}}] = \frac{3F_e R_s}{2} \begin{bmatrix} \sin\rho & -\cos\rho & 0 \\ \cos\rho & \sin\rho & 0 \\ 0 & 0 & 0 \end{bmatrix} \tag{11.28}$$

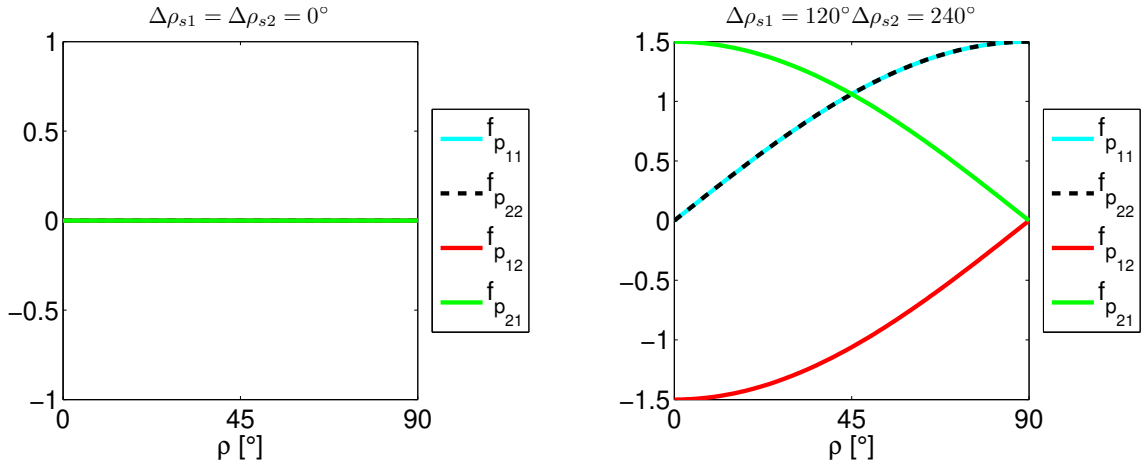

(a) (b)

Figure 11.8: Element functions for $\Delta\rho_{s_1} = \Delta\rho_{s_2} = 0°$ (Fig. 11.8(a)) and $\Delta\rho_{s_1} = 120°$ and $\Delta\rho_{s_2} = 240°$ (Fig. 11.8(b))

.

The inclusion Eq. 11.28 on the system from Eq. 11.17 results in $k_{11} = k_{22}$ on the main diagonal (Eq. 11.29) and $k_{21} = k_{12}$ (Eq. 11.30).

$$k_{11} = k_{22} = (2R^2 + 2\mu^2 z_e h)k + \dot{\gamma}^2(I_{z'z'} - I) + \left(\frac{3}{2}\right)(k_t l)^2 + \frac{3F_e R_s}{2}\sin\rho \tag{11.29}$$

$$k_{21} = k_{12} = \left[2\mu k R h - 2\mu(h^2/R)k z_e\right] sign(\dot{\gamma}) - \frac{3F_e R_s}{2}\cos\rho \tag{11.30}$$

The system data was the same from Section 11.4.1. The element distance was chosen as $l = 0.1$ m. The total tangential stiffness was varied between $10^4 < k_t < 10^{11}$ N/m while the preload was tested within $-8000 < F_e < 8000$ N.

Up to $\rho = 45°$ (Fig. 11.10(a)), the real parts from the eigenvalues (Figs. 11.9(a) and 11.9(b)) indicate that negative values of F_e does ot affect the stability of this system. For a positive value of F_e, there is a threshold where the stability between the stable/unstable modes are interchanged.

Such transition is shifted for $\rho = 45°$ (Fig. 11.10(b)) , where an increase on the positive preload resulted on a reduction of the total stiffness needed for stability (Figs. 11.9(c) and 11.9(d)).

Adopting $\rho = 90°$ (Fig. 11.10(c)), there is no influence of preload, only high values of tangential stiffness affected the stability (Figs. 11.9(e) and 11.9(f)).

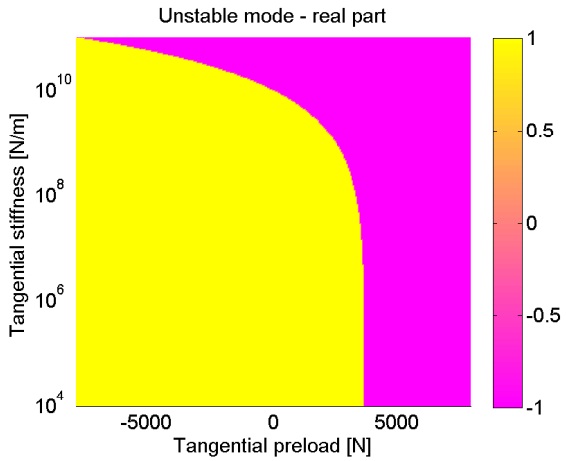

(a) $\rho = 45°$

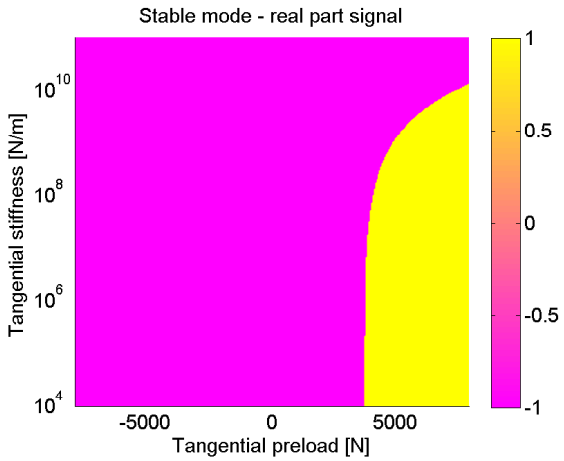

(b) $\rho = 45°$

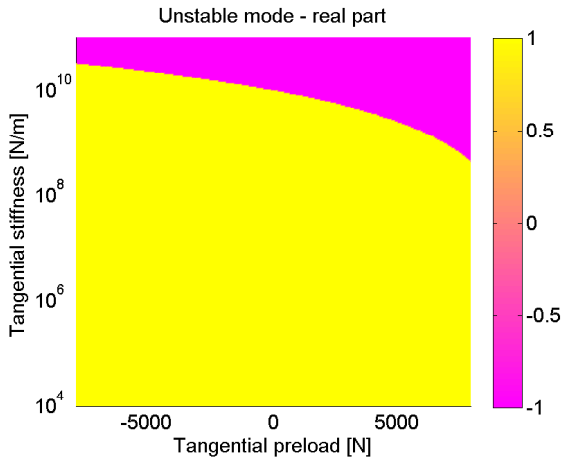

(c) $\rho = 75°$

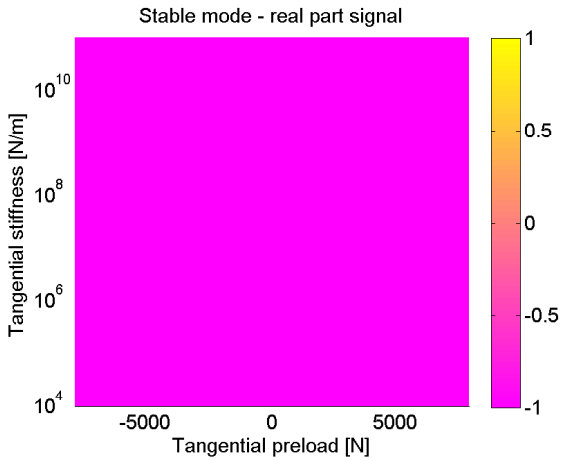

(d) $\rho = 75°$

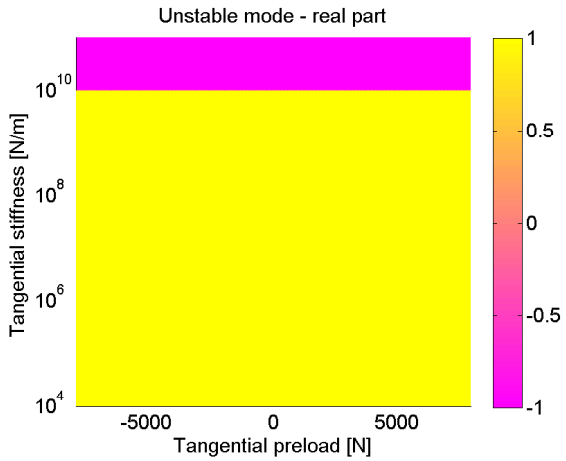

(e) $\rho = 90°$

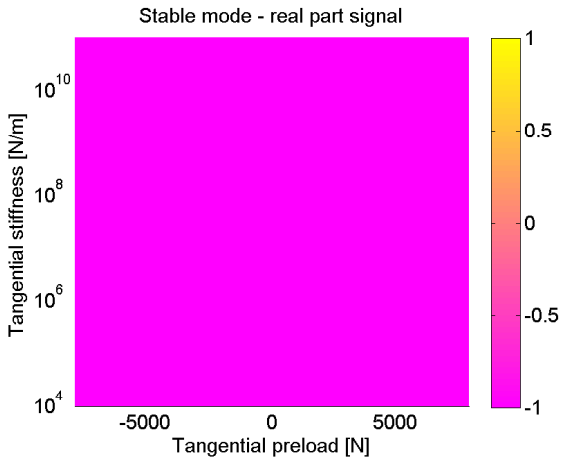

(f) $\rho = 90°$

Figure 11.9: Eigenvalue real parts for the unstable (Figs. 11.9(a),11.9(a) and 11.9(a)) and stable (Figs. 11.9(b),11.9(b) and 11.9(b)) mode shapes with $\rho = 45°$, $75°$ and $90°$.

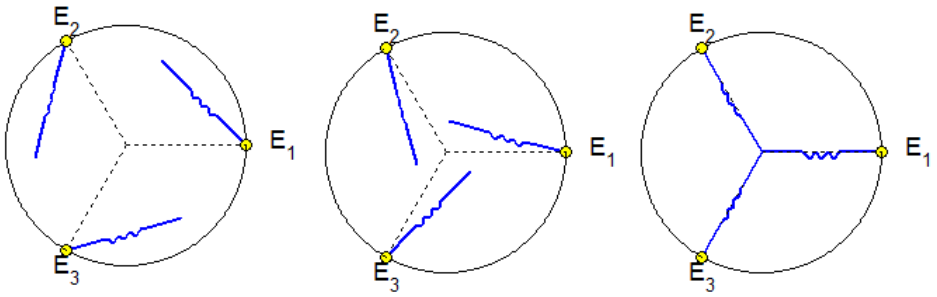

(a) $\rho = 45°$ (b) $\rho = 75°$ (c) $\rho = 90°$

Figure 11.10: Element configurations with symmetric orientation ($\Delta_{s1} = 120°$ and $\Delta_{s1} = 240°$).

11.6 Chapter summary

The leaf springs or straps were modelled on Section 11.2. It resulted in two matrices (Section 11.3) one representing the influence of the tangential stiffness (Eq. 11.12) and another account the spring preload (Eq. 11.13). All results are tied to the assumption that energy dissipation occurs only due to friction damping on the system.

- a greater distance from the centre of gravity required lower stiffness values for stabilization
- Elements with equal orientation angles required lower values of stiffness to achieve stability. The element matrices presented non-diagonal elements. Preload had no effect on this case.
- Symmetric oriented elements eliminated the non-diagonal terms of Eq. 11.12, resulting on very high stiffness values for stabilization. Preload could be used on this case, but with no significant effect on stability.

12 A device for pressure plate stabilization

This part of the work presents a device that was conceived to introduce damping to the pressure plate. It follows the initial idea from Tondl (1975), who linked an auxiliary mass to a self excited system through a spring and viscous elements. Such idea has not been tried yet on the literature (Chapter 3).

Section 12.1 contains the deduction of the connection elements. The device will be assumed to be another disc with annular shape. Their formulation was made to allow different distributions on the interface between the pressure plate and the device mass.

A numerical example will be tested on Section 12.3, showing that the stability range of this system is achieved on the condition of *curve veering* (Liu (2002) and Perkins and Mote Jr (1986)). There are in phase and out of phase wobbling movements on that will be discussed on Sections 12.3.4 and 12.3.4.

12.1 Stabilization device formulation

Figure 12.1(a) shows the pressure plate and device mass/inertia with centres of gravity G and G_d, respectively. The spring/damper element is placed between points S and T, with a linear stiffness and viscous damping coefficients k_{d_i} and c_{d_i}. The parameter R_i describes the radial distance while the angle ε_{d_i} is used to place the element. Equation 12.1 has the parameter d that indicates a position *above the point* G and while in Eq. 12.2 the variable a indicates a distance *bellow the point* G_d.

$$ {}_3\vec{r'}_{GT} = \begin{Bmatrix} R_i \cos\varepsilon_{d_i} & R_i \cos\varepsilon_{d_i} & d \end{Bmatrix}^T \tag{12.1} $$

$$ {}_3\vec{r'}_{G_dS} = \begin{Bmatrix} R_i \cos\varepsilon_{d_i} & R_i \cos\varepsilon_{d_i} & -a \end{Bmatrix}^T \tag{12.2} $$

The device may move according to two wobbling angles (θ_x,θ_y), with an additional vertical movement indicated by z_d (Fig. 12.1(b)). The pressure plate have similar degrees of freedom α, β and z. The coordinate system is detailed on Section 7.1.3, where the constant angular speed $\dot{\gamma}$ is maintained on the global reference frame.

The vertical displacement of the pressure plate at point T is given by Eq. 12.3 taking into account only angular movement. The complete expression (Eq. 12.4) requires the additional terms

from axial motion ${}_0r'_{OG_z}$:

$$ {}_0r'_{GT_z} = -\sin\beta R_i \cos\varepsilon_{d_i} + \sin\alpha\cos\beta R_i \sin\varepsilon_{d_i} + d\cos\alpha\cos\beta \tag{12.3} $$

$$ {}_0r'_{OT_z} = {}_0r'_{OG_z} + {}_0r'_{GT_z} = -(z - z_e) - \sin\beta R_i \cos\varepsilon_{d_i} + \sin\alpha\cos\beta R_i \sin\varepsilon_{d_i} + d\cos\alpha\cos\beta \tag{12.4} $$

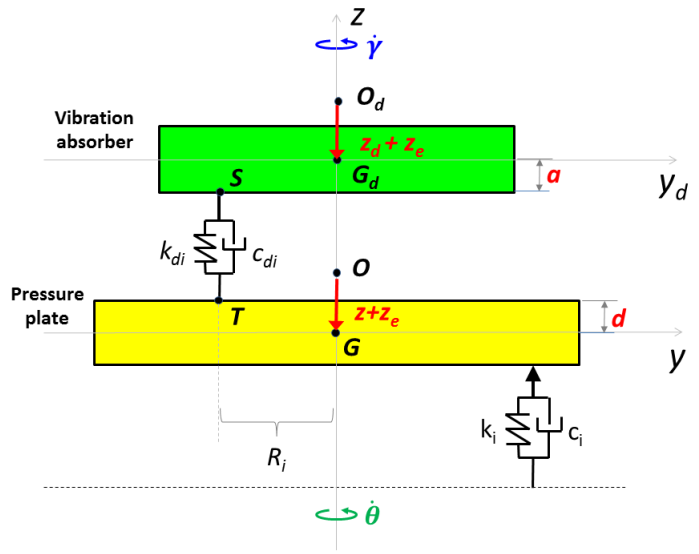

(a)

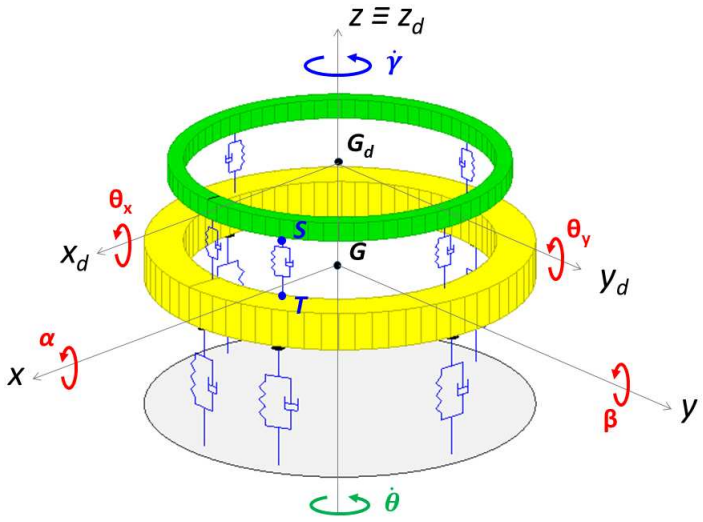

(b)

Figure 12.1: Geometric relations of the stabilization device (Fig. 12.1(a)). Spacial position of the device and wobbling angles (Fig. 12.1(b)).

The displacement on the device attachment point S (Eq. 12.6) is obtained by the combination of ${}_0r'_{G_dS_z}$ (Eq. 12.5) and the axial displacement ${}_0r_{O_dG_dz}$:

$$ {}_0r'_{G_dS_z} = -\sin\theta_y R_i \cos\varepsilon_{d_i} + \sin\theta_x \cos\theta_y R_i \sin\varepsilon_{d_i} - a\cos\theta_x \cos\theta_y \tag{12.5} $$

$$ {}_0r'_{O_dS_z} = {}_0r'_{O_dG_dz} + {}_0r'_{G_dS_z} = -z_d - \sin\theta_y R_i \cos\varepsilon_{d_i} + \sin\theta_x \cos\theta_y R_i \sin\varepsilon_{d_i} - a\cos\theta_x \cos\theta_y \tag{12.6} $$

The stiffness effort on the pressure plate (Eq. 12.7) is calculated using the total deformation between points S and T (Eqs. 12.8 and 12.9), considering $\Delta\,{}_0r'_{OT_z} > \Delta\,{}_0r'_{O_dS_z}$.

$$ {}_0\vec{F}'k_{i_{plate}} = -k_{d_i}\left[\Delta\,{}_0r'_{OT_z} - \Delta\,{}_0r'_{O_dS_z}\right]\vec{k} \tag{12.7} $$

$$ \Delta\,{}_0r'_{OT_z} = {}_0r'_{OT_z} - d \tag{12.8} $$

$$ \Delta\,{}_0r'_{O_dS_z} = {}_0r'_{O_dS_z} + a \tag{12.9} $$

The effort acting on the plate ${}_3\vec{F}'k_{i_{plate}}$ on the frame $x'_3y'_3z'_3$ is obtained as in Eq. 12.10. The moments are calculated on Eq. 12.11. Considering ${}_3\vec{F}'k_{i_{device}} = -\,{}_3\vec{F}'k_{i_{plate}}$, the stiffness moments on the device are calculated by Eq. 12.11.

$$ {}_3\vec{F}'k_{i_{plate}} = [R_{\gamma\beta\alpha}]^T\,{}_0\vec{F}'k_{i_{plate}} = {}_0\vec{F}'k_{i_{plate}} \begin{Bmatrix} -\sin\beta \\ \sin\alpha\cos\beta \\ \cos\alpha\cos\beta \end{Bmatrix} \tag{12.10} $$

$$ {}_3\vec{M}'k_{i_{plate}} = {}_3\vec{r}'_{GT} \times {}_3\vec{F}'k_{i_{plate}} \tag{12.11} $$

$$ {}_3\vec{M}'k_{i_{device}} = {}_3\vec{r}'_{G_dS} \times {}_3\vec{F}'k_{i_{absorber}} = {}_3\vec{r}'_{G_dS} \times \left[-\,{}_3\vec{F}'k_{i_{plate}}\right] \tag{12.12} $$

12.1.1 Connection matrices

A linearization on the torques from Eqs. 12.11 and 12.12 makes it possible to obtain the connection matrix $[K_{r_I}]$ (Eq. 12.13). The matrix $[P(\varepsilon_{d_i}, R_{d_i})]$, gives the stiffness state accord-

ing to the element angular position (ε_{d_i}) and radius (R_i). It is arranged for a state space $p = \begin{Bmatrix} \alpha & \beta & z & \theta_x & \theta_y & z_d \end{Bmatrix}^T$, where the upper positions refer to the motions of the pressure plate while the lower portion contains the degrees of freedom of the device. If a similar procedure from Section 12.1 is done to the damping forces and the dissipative part of the connection ($[C_{con}]_i$) is determined as Eq. 12.14. This connection will be responsible to introduce an external damping to the pressure plate.

$$[K_{con}]_i = k_{d_i}\left[P(\varepsilon_{d_i}, R_{d_i})\right] = k_{d_i}\begin{bmatrix} R_{d_i}^2\sin^2\varepsilon_{d_i} & -(R_{d_i}^2/2)\sin(2\varepsilon_{d_i}) & -R_{d_i}\sin\varepsilon_{d_i} \\ -(R_{d_i}^2/2)\sin(2\varepsilon_{d_i}) & R_{d_i}^2\cos^2\varepsilon_{d_i} & R_{d_i}\cos\varepsilon_{d_i} \\ -R_{d_i}\sin\varepsilon_{d_i} & R_{d_i}\cos\varepsilon_{d_i} & 1 \\ -R_{d_i}^2\sin^2\varepsilon_{d_i} & (R_{d_i}^2/2)\sin(2\varepsilon_{d_i}) & R_{d_i}\sin\varepsilon_{d_i} \\ (R_{d_i}^2/2)\sin(2\varepsilon_{d_i}) & -R_{d_i}^2\cos^2\varepsilon_{d_i} & -R_{d_i}\cos\varepsilon_{d_i} \\ R_{d_i}\sin\varepsilon_{d_i} & -R_{d_i}\cos\varepsilon_{d_i} & -1 \end{bmatrix} \begin{bmatrix} -R_{d_i}^2\sin^2\varepsilon_{d_i} & (R_{d_i}^2/2)\sin(2\varepsilon_{d_i}) & R_{d_i}\sin\varepsilon_{d_i} \\ (R_{d_i}^2/2)\sin(2\varepsilon_{d_i}) & -R_{d_i}^2\cos^2\varepsilon_{d_i} & -R_{d_i}\cos\varepsilon_{d_i} \\ R_{d_i}\sin\varepsilon_{d_i} & -R_{d_i}\cos\varepsilon_{d_i} & -1 \\ R_{d_i}^2\sin^2\varepsilon_{d_i} & -(R_{d_i}^2/2)\sin(2\varepsilon_{d_i}) & -R_{d_i}\sin\varepsilon_{d_i} \\ -(R_{d_i}^2/2)\sin(2\varepsilon_{d_i}) & R_{d_i}^2\cos^2\varepsilon_{d_i} & R_{d_i}\cos\varepsilon_{d_i} \\ -R_{d_i}\sin\varepsilon_{d_i} & R_{d_i}\cos\varepsilon_{d_i} & 1 \end{bmatrix} \tag{12.13}$$

$$[C_{con}]_i = c_{d_i}\left[P(\varepsilon_{d_i}, R_i)\right] \tag{12.14}$$

12.2 System matrices

The whole system comprehending the pressure plate and the device is written in Eq. 12.15. This formulation allows the creation of a wider range of possibilities in terms of connection elements distribution, as well as different configurations off the rotating friction elements from Section 7.4.

$$[M]_{sys}\{\ddot{p}\} + ([G]_{sys} + [C]_{sys})\{\ddot{p}\} + ([H(\dot{\gamma})]_{sys} + [K]_{sys})\{p\} = \{F\}_{sys} + \{F\}_{ext} \tag{12.15}$$

The elements from the matrices $[M]_{sys}$ (Eq. 12.16), $[G]_{sys}$ (Eq. 12.17) and $[H]_{sys}$ (Eq. 12.18) result from the composition of the following elements:

- mass matrices ($[M]_{plate}$ and $[M]_{device}$) based on Eq. 7.12. The total mass of the plate and device are defined as m_{plate} and m_{device} in Eq. 12.16, respectively.
- gyroscopic matrices ($[G]_{plate}$ and $[G]_{device}$) based on Eq. 7.13.
- inertial stiffness matrices $[H_1(\dot{\gamma})]_{plate}$ and $[H_1(\dot{\gamma})]_{device}$ are based on Eq. 7.14.

$$[M]_{sys} = \begin{bmatrix} \begin{bmatrix} [M]_{plate} & \begin{matrix} 0 \\ 0 \end{matrix} \\ \begin{matrix} 0 & 0 \end{matrix} & m_{plate} \end{bmatrix} & [0]_{3\times3} \\ [0]_{3\times3} & \begin{bmatrix} [M]_{device} & \begin{matrix} 0 \\ 0 \end{matrix} \\ \begin{matrix} 0 & 0 \end{matrix} & m_{device} \end{bmatrix} \end{bmatrix} \tag{12.16}$$

$$[G]_{sys} = \begin{bmatrix} \begin{bmatrix} [G]_{plate} & \begin{matrix} 0 \\ 0 \end{matrix} \\ \begin{matrix} 0 & 0 \end{matrix} & 0 \end{bmatrix} & [0]_{3\times3} \\ [0]_{3\times3} & \begin{bmatrix} [G]_{device} & \begin{matrix} 0 \\ 0 \end{matrix} \\ \begin{matrix} 0 & 0 \end{matrix} & 0 \end{bmatrix} \end{bmatrix} \tag{12.17}$$

$$[H]_{sys} = \begin{bmatrix} \begin{bmatrix} [H_1(\dot{\gamma})]_{plate} & \begin{matrix} 0 \\ 0 \end{matrix} \\ \begin{matrix} 0 & 0 \end{matrix} & 0 \end{bmatrix} & [0]_{3\times3} \\ [0]_{3\times3} & \begin{bmatrix} [H_1(\dot{\gamma})]_{device} & \begin{matrix} 0 \\ 0 \end{matrix} \\ \begin{matrix} 0 & 0 \end{matrix} & 0 \end{bmatrix} \end{bmatrix} \tag{12.18}$$

The damping matrix $[C]_{sys}$ (Eq. 12.19) is obtained by the combination of the device connection matrices $[C_{con}]_i$ (Eq. 12.14) with the rotating friction elements $[C_i']$ (Eq. 7.61). The same procedure has to be done for the stiffness component $[K]_{sys}$ (Eq. 12.20). A external effort array $[F]_{sys}$ (Eq. 12.21) takes into account all individual effort arrays $\{f_l'\}$ from Eq. 7.65.

$$[C]_{sys} = \sum_{i=1}^{n} [C_{con}]_i + \sum_{l=1}^{N} \begin{bmatrix} [C_l'] & [0]_{3\times3} \\ [0]_{3\times3} & [0]_{3\times3} \end{bmatrix} \tag{12.19}$$

$$[K]_{sys} = \sum_{i=1}^{n} [K_{con}]_i + \sum_{l=1}^{N} \begin{bmatrix} [K'_l] & [0]_{3\times3} \\ [0]_{3\times3} & [0]_{3\times3} \end{bmatrix} \tag{12.20}$$

$$[F]_{sys} = \begin{bmatrix} \sum_{l=1}^{N} \{f'_l\} \\ \{0\}_{3\times1} \end{bmatrix} \tag{12.21}$$

12.3 An applied numerical example

Equation 12.15 was simulated choosing a pressure plate with $m_{plate} = 2kg$, $h = 0.01m$, $R_{in} = 0.075m$ and $R_{out} = 0.1m$. The contact radius was considered as $R_i = 0.0875m$. The total cushion stiffness ($k_{cushion}$) was tested from 10^4 to 10^8 N/m and it was divided between 4 equally distributed friction elements using the model from Section 8.2. A common constant friction coefficient of 0.3 and a static displacement of 0.001 m were adopted.

Four connecting elements were placed between the pressure plate and the device, positioned by $\varepsilon_{d_i} = 0°$, 90°, 180° and 270° with $R_{d_i} = 0.0812m$. Damping and stiffness of each element were set as $c_{d_i} = 25Ns/m$ and $k_{d_i} = 1.75 \times 10^5 N/m$. The geometry of this device was a hollow cylinder with an inner and outer radius of 0.075 m and 0.0875 m, respectively. It has a total mass of 0.4 kg and a distance of 2 mm between its centre of gravity and the contact surfaces. A common constant rotating speed of 1800 rpm was adopted.

12.3.1 Natural frequencies, curve veering and stability range

As the cushion stiffness was increased, the natural frequencies of this system evolved as Fig. 12.2. Their values found for 10^4N/m and 10^8N/m are detailed in Table 12.1. From these data, it is possible to verify two distinct groups of mode shapes. Modes 1, 2 and 3 start at frequencies bellow 32 Hz and they reach maximum values nearby 212 Hz. Another group, of modes 4, 5 and 6 start at higher frequencies and increasing up to 1100 Hz.

From the literature, some definitions on curve veering can be found:

- Liu (2002): "*Mode localization and eigenvalue curve veering are the phenomena of rapid and even violent changes in dynamic modes.*".
- Perkins and Mote Jr (1986):"*An important characteristic of curve veering is that the eigenfunctions associated with the eigenvalues on each locus before veering are interchanged*

during veering in a rapid but continuous way. ”

Figure 12.2 presents such phenomenon, once that the curves from modes 1, 2 and 3 get really close to mode 4,5 and 6 within the region delimited by a “Stability range”. Apart from this situation, the frequencies from those groups are very different. Their associate mode shapes were carefully tracked using the Modal Assurance Criterion (Allemang, 2003) and their characteristics will be explained on Section 12.3.2

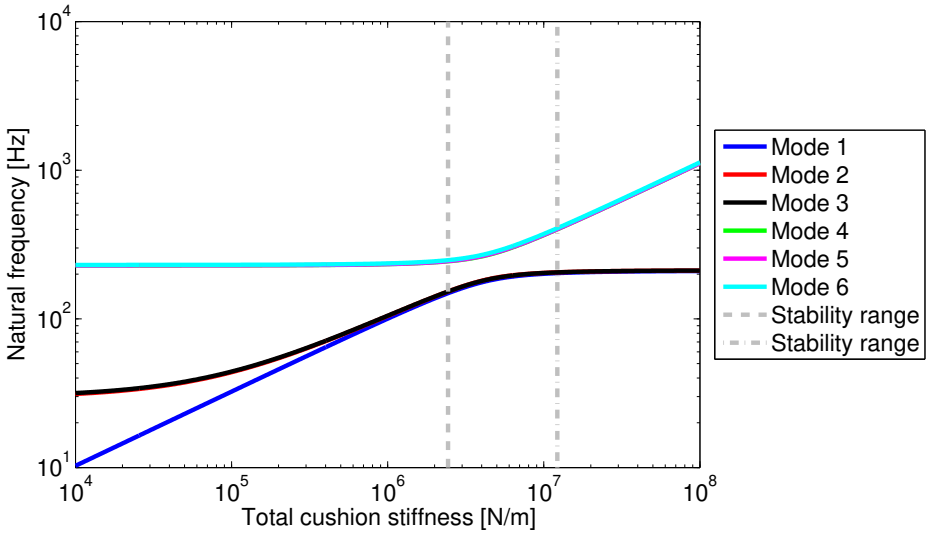

Figure 12.2: Natural frequencies for the example on Section 12.3.

Table 12.1: Mode shapes and the variation on its natural frequencies.

Mode	Initial frequency [Hz]	Final frequency [Hz]
1	10.2714	209.8114
2	31.2808	211.3844
3	31.7184	211.3953
4	228.8469	1113.193
5	228.9418	1113.9022
6	230.6833	1129.3153

The real part of the eigenvalues are displayed on Fig. 12.3. The stability rage was defined on the interval were all real parts were negative. The numerical simulation gave such results for cushion stiffness between 2.4×10^6 and 1.2×10^7 N/m. For low stiffness values, mode 2 presented the greater real part. Out from the upper limits of this curve, mode 4 had an increasing real part. It is possible to conclude that:

- *Within the stability range, the device modified the system to allow energy dissipation, avoiding the self excitation of the pressure plate*.

The modal damping on Fig. 12.4 show an increasing behaviour for modes 1, 2, 3 and a decreasing tendency for modes 4, 5 and 6. For both groups, maximum damping ratios occurred nearby 10 % for this group of parameters. Negative modal damping represents an unstable condition.

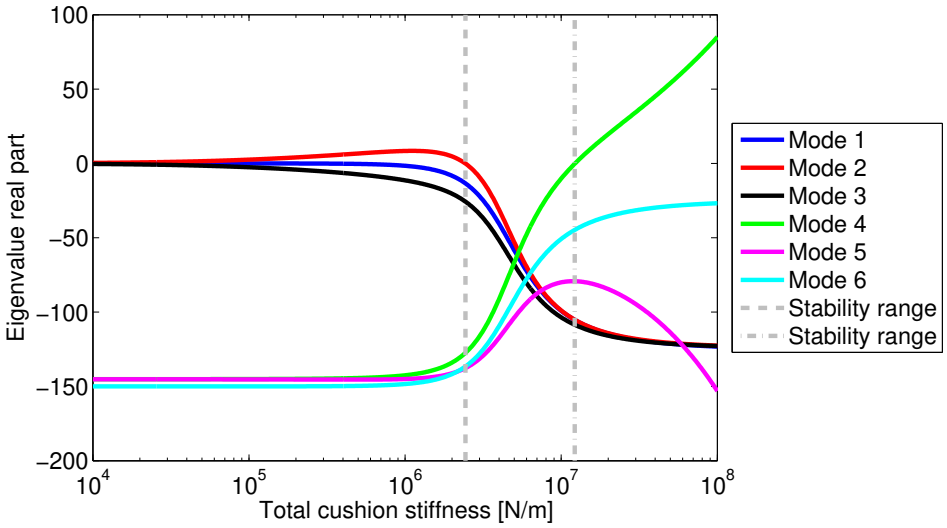

Figure 12.3: Real part of eigenvalues for the example on Section 12.3.

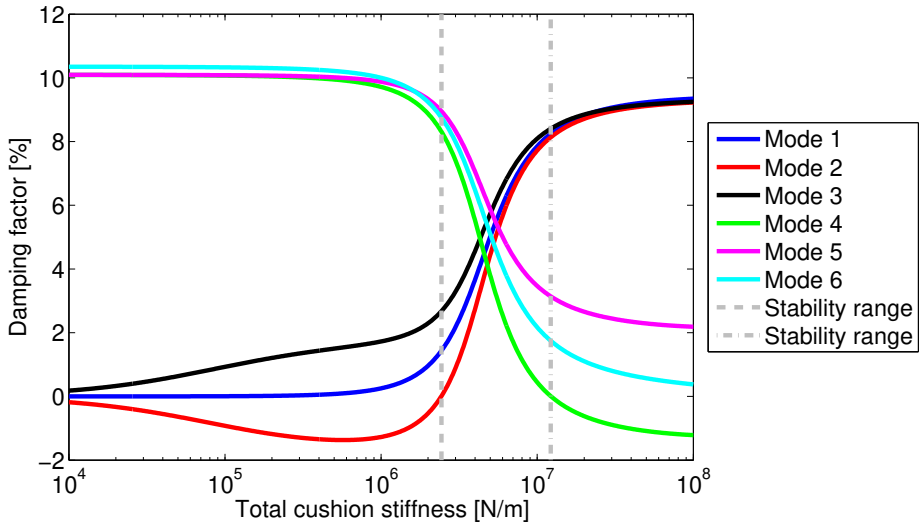

Figure 12.4: Damping factors for the example on Section 12.3.

12.3.2 Axial mode shapes

For the sake of clarification, all modes considered from Figs. 12.5 and 12.7 the angle α as reference for phase. Mode 1 (Figs. 12.5(a) and 12.5(b)) corresponds to an axial movement with lower natural frequency (Fig. 12.2). For high values of cushion stiffness ($k_{cushion}$), the device presents greater levels of vibration. In all cases , the pressure plate and the device have an in phase axial motion (Fig. 12.5(b)).

Mode 6 is a high frequency axial mode (Fig. 12.2). Even for low levels of cushion stiffness, for this case there is opposition of phase between z and z_d (Fig. 12.5(d)). On the other hand, if $k_{cushion}$ is too high, above the stability region found on the previous section, only the pressure plate vibrates at high frequencies (Fig. 12.5(c)).

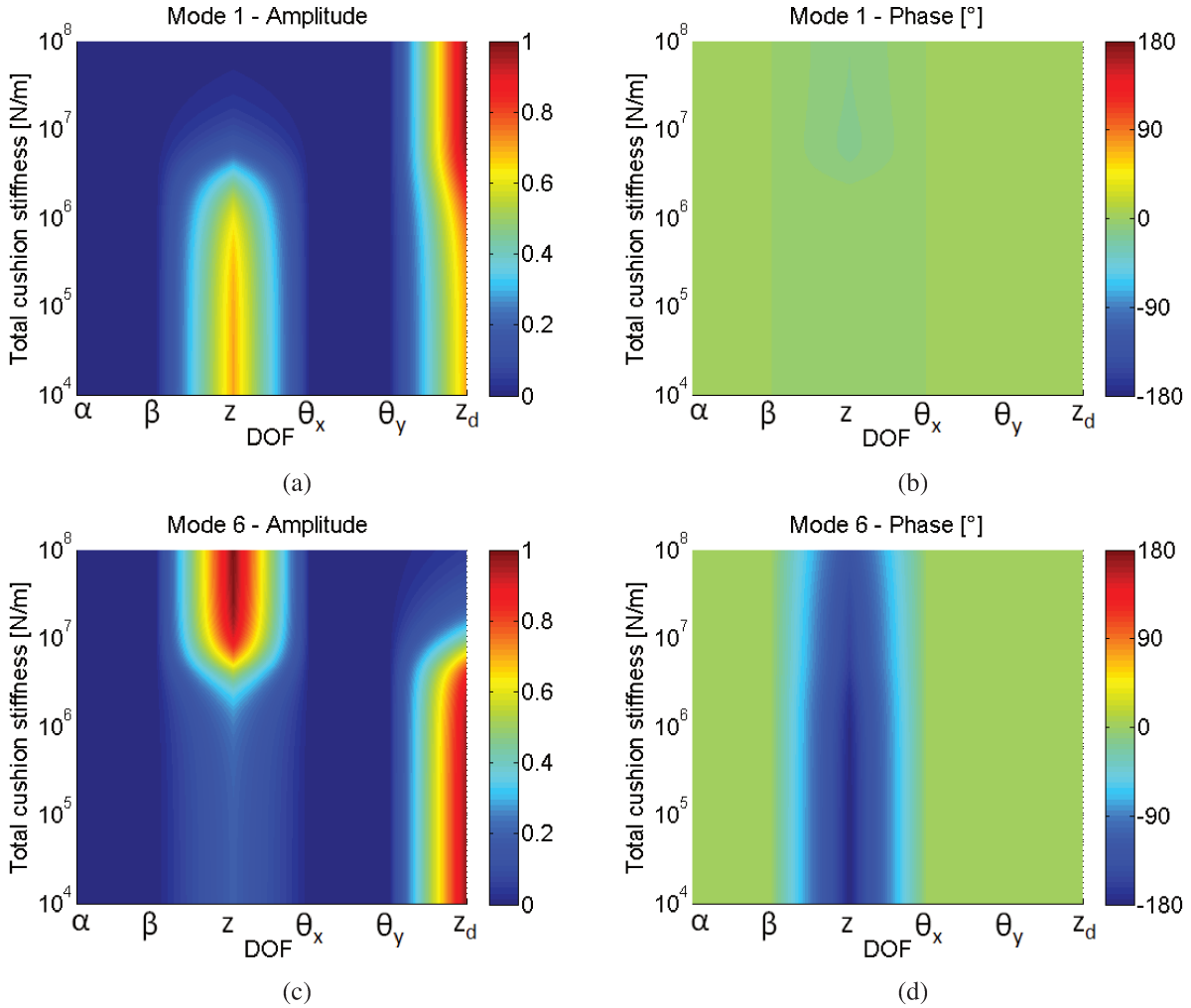

Figure 12.5: Axial mode shapes.

An important phenomenon occurs here and in all following situations. On the stability range (between 2.4×10^6 and 1.2×10^7 N/m for this case) both pressure plate (z) and device (z_d) vibrate *on the same mode shape* (Fig. 12.5(a) and 12.5(c)). A sequence of vibration on the stability range is detailed on Fig. 12.6. Out from this condition, vibration seems to be localized on one element only. This and the following results fit on the veering definition from Perkins and Mote Jr (1986). The stability range occurs on the *transition* of behaviour of these mode shapes.

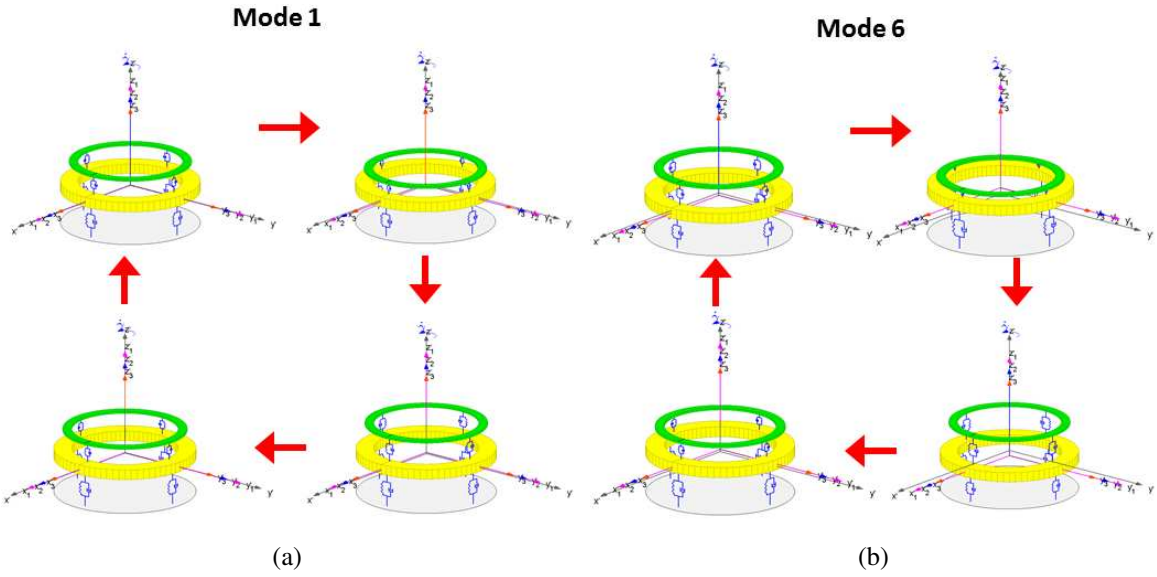

Figure 12.6: Axial modes 1 and 6 for a total cushion stiffness of 6×10^6 N/m.

12.3.3 In phase wobbling motion

Modes 2 and 3 occur with lower natural frequencies (Fig. 12.2). Based on Figs. 12.7(a) and 12.7(c), it is possible to observe wobbling on the pressure plate and on the device due to the non-zero amplitudes on α, β, θ_x and θ_y. On the transition (or stability range), there is a combination of movements of both elements. For high stiffness values, only the device vibrate (Figs. 12.7(a) and 12.7(c)).

For mode 2 (Fig. 12.7(b)), the phase relation between α and β is practically the same one found for θ_x and θ_y. Even for mode 3 (Fig. 12.7(d)) similar phase characteristics happen among these pairs. On important conclusion from this is that the pressure plate and the device perform *together* a forward or a backward wobbling (*in phase motion*). Vibration on the stability range is detailed on Fig. 12.8 ($k_{cushion} = 6 \times 10^6$ N/m). Mode 2 is represented as a forward wobbling, while mode 3 is a backward motion. Figure 12.8 agrees with the results on Fig. 12.7(a) and 12.7(c),

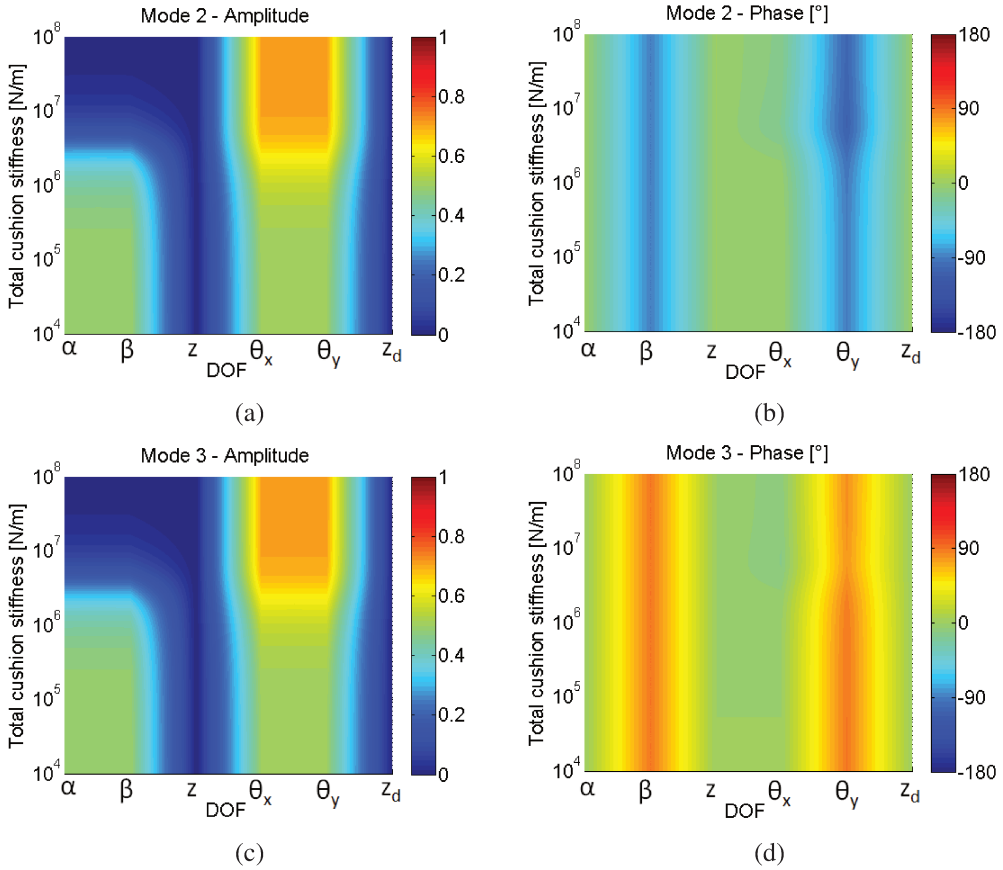

Figure 12.7: Lower frequency wobbling modes.

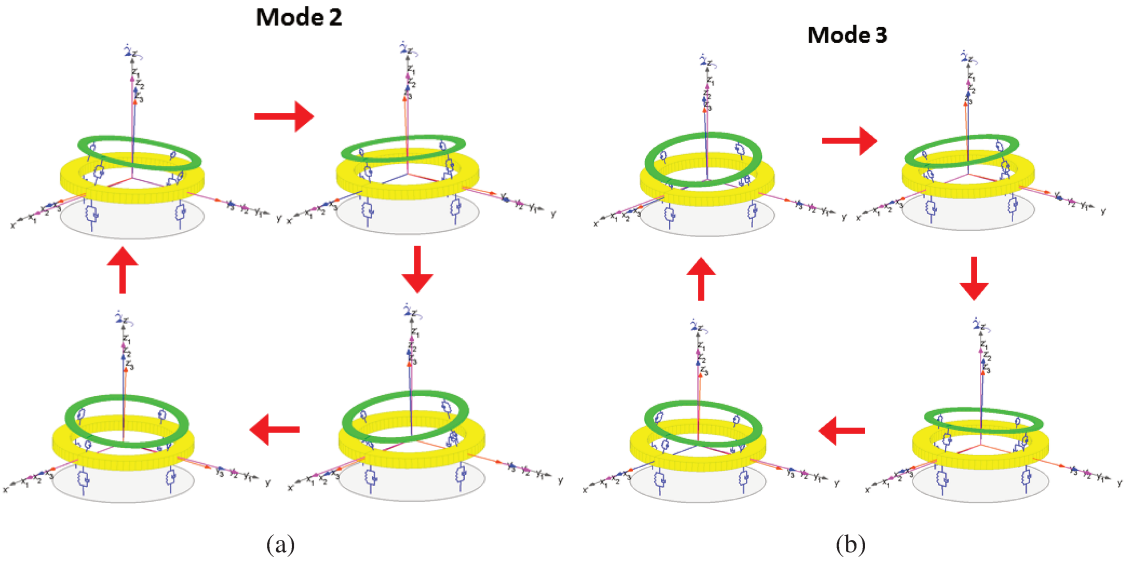

Figure 12.8: Wobbling modes 2 and 3 for a total cushion stiffness of 6×10^6 N/m.

presenting greater amplitudes on the device.

12.3.4 Out of phase wobbling motion

For stiffness bellow the stability range, Figures 12.9(a) and 12.10(a) shows that only the device presents wobbling. For high levels of cushion stiffness, there is motion on the pressure plate. Figures 12.9(b) and 12.10(b) presents a phase angle close to 180° between α and θ_x, indicating movement in *opposition of phase*. As a result, on the stability range, the following behaviour happen (Fig. 12.11):

- Mode 4: Figure 12.11(a) presents an *out of phase forward wobbling motion* between the pressure plate and device.
- Mode 5: Figure 12.11(b) presents an *out of phase backward wobbling motion* between the pressure plate and device.

Thinking on the constructive aspects from Fig. 12.1(b) it is possible to think that during out of phase wobbling the efforts on the connecting elements are greater. This is a strong mechanism for the working principle of this device.

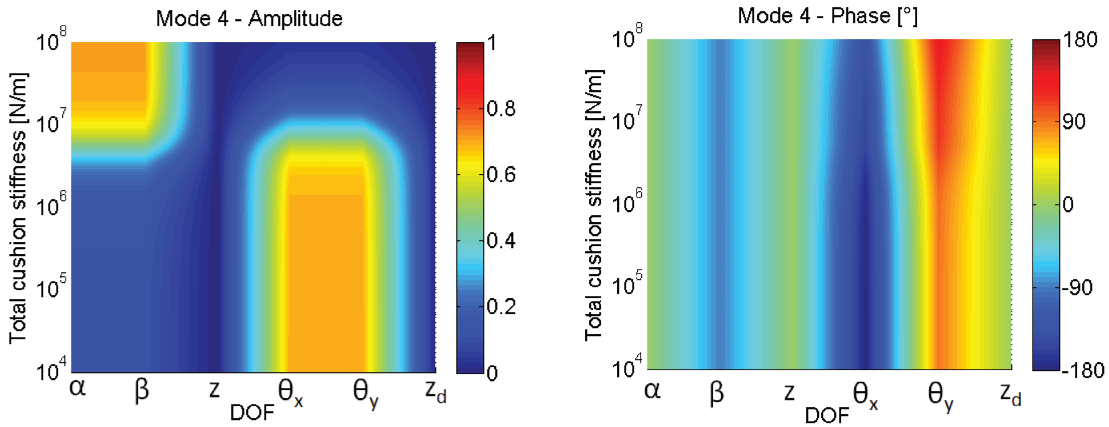

(a) (b)

Figure 12.9: High frequency wobbling modes.

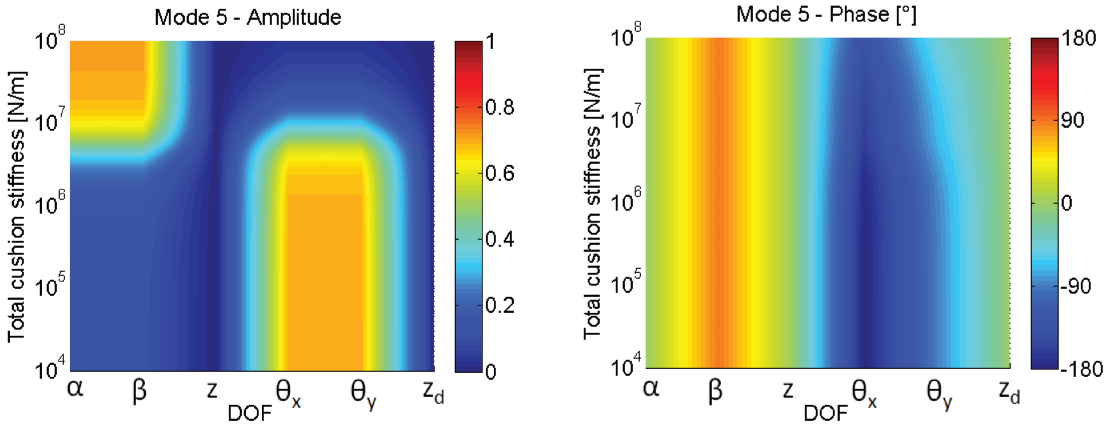

(a) (b)

Figure 12.10: High frequency wobbling modes.

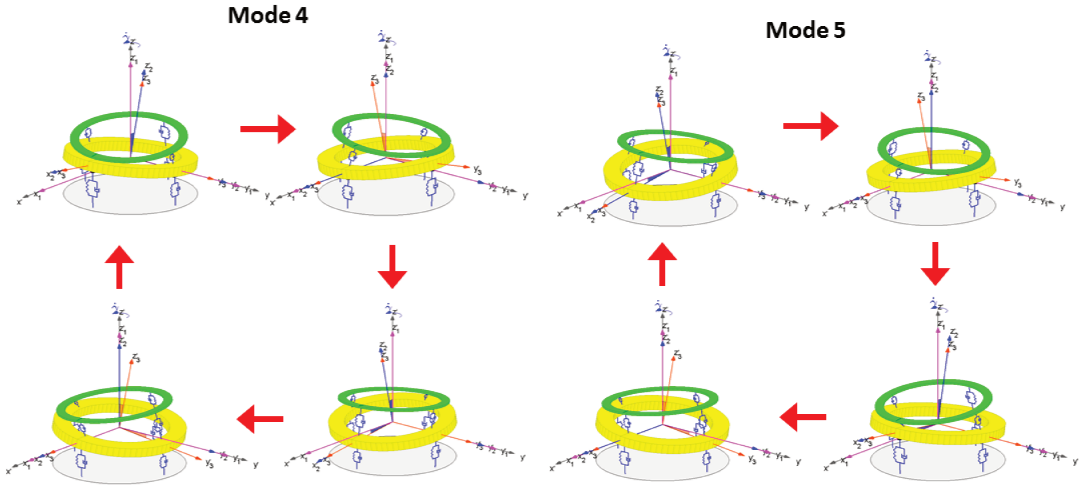

(a) (b)

Figure 12.11: Wobbling modes 4 and 5 for a total cushion stiffness of 6×10^6 N/m.

12.3.5 Time domain response of the system

Equations 12.22 and 12.23 represent the displacement and speed of the system under the conditions on Section 12.3 in case of free vibration. They take into account the contribution of the six modes presented in Sections 12.3.2, 12.3.3 and 12.3.4.

$$\left\{p(t)\right\} = \sum_{i=1}^{6} \left(d_i \left\{X_i\right\} e^{\lambda_i t} + d_1^* \left\{X_i^*\right\} e^{\lambda_i^* t}\right) \tag{12.22}$$

$$\left\{\dot{p}(t)\right\} = \sum_{i=1}^{6} \left(d_i \lambda_i \left\{X_i\right\} e^{\lambda_i t} + d_1^* \lambda_i^* \left\{X_i^*\right\} e^{\lambda_i^* t} \right) \tag{12.23}$$

Choosing $t = 0$ s, Equation 12.24 contains the relation between the initial conditions $\{p(0)\}$ and $\{\dot{p}(0)\}$ with the complex constants arranged on a array $\{d\}$ on Eq. 12.25 (Meirovitch, 2010). This system of equations can be solved for any desired initial state, resulting on specific values of $\{d\}$.

$$\begin{Bmatrix} \{p(0)\} \\ \{\dot{p}(0)\} \end{Bmatrix} = \begin{bmatrix} \{X_1\} & \{X_1^*\} & \dots & \{X_6\} & \{X_6^*\} \\ \lambda_1 \{X_1\} & \lambda_1^* \{X_1^*\} & \dots & \lambda_6 \{X_6\} & \lambda_6^* \{X_6^*\} \end{bmatrix} \{d\} \tag{12.24}$$

$$\{d\} = \begin{Bmatrix} d_1 & d_1^* & \dots & d_6 & d_6^* \end{Bmatrix}^T \tag{12.25}$$

Figure 12.12 highlights specific stiffness values on the eigenvalue real part previously shown in Fig. 12.3. The lower and upper limits of the stability range are indicated by stiffness $k_{lower\ limit}$ and $k_{upper\ limit}$, respectively. The parameter k_{stable} stand for eigenvalues with negative real part.

The parameter k_{bellow} was calculated as the mean value between the minimum stiffness considered (10^4 N/m) and $k_{lower\ limit}$. A greater value k_{above} was positioned between $k_{upper\ limit}$ and the maximum stiffness of 10^8 N/m. The numerical values for those parameters are presented in Table 12.2.

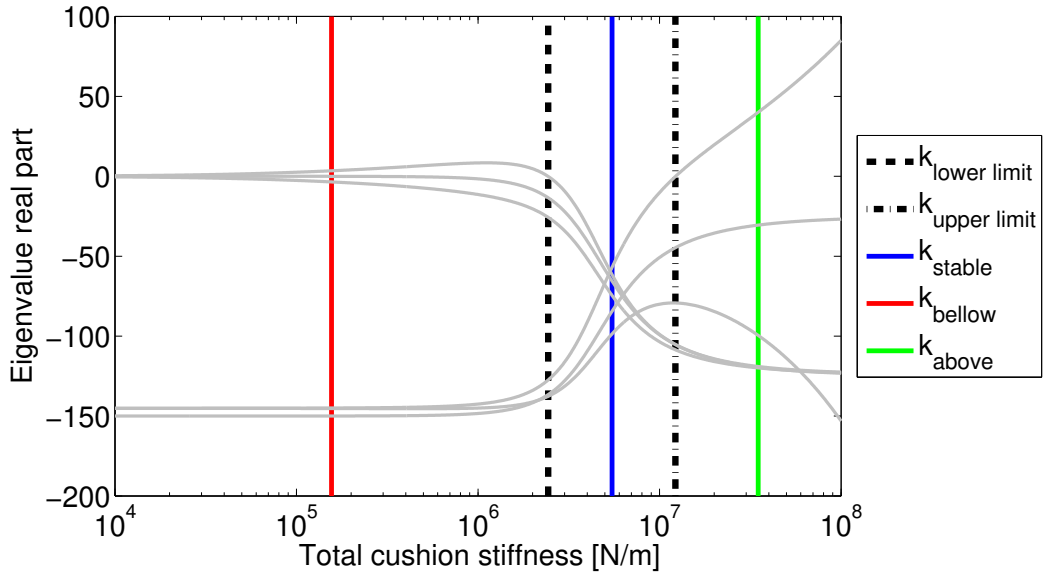

Figure 12.12: Stiffness values chosen for the time domain simulation.

Table 12.2: Stiffness values from Fig. 12.12 used for time domain simulations.

Parameter	**Value [N/m]**
k_{bellow}	1.56025×10^5
$k_{lower\ limit}$	2.43437×10^6
k_{stable}	5.47947×10^6
$k_{upper\ limit}$	1.22204×10^7
k_{above}	3.49578×10^7

The simulations considered $\{p(0)\} = \begin{Bmatrix} 0.01 & 0.01 & 0.01 & 0 & 0 & 0 \end{Bmatrix}^T$ as initial conditions. Figure 12.13 presents the results adopting k_{bellow} (Fig. 12.12). There is an in phase wobbling motion between the pressure plate and device that increases with time, indicated by the angles α and θ_x on Fig. 12.13(a), and by β and θ_y on Fig. 12.13(b). Vertical vibration amplitudes remain constant during the simulation (Fig. 12.13(c)).

Adopting $k_{lower\ limit}$ (Fig. 12.12), Figures 12.14(a) and 12.14(b) contains constant angular motions throughout the simulation. On the other hand, the vertical movement is damped, with a decrease of amplitude according to Fig. 12.13(c). In all cases, the vibration levels were greater on the device.

In the middle of the stability range (Fig. 12.12), a cushion stiffness k_{stable} results on a decay of amplitudes in all degrees-of-freedom on Fig. 12.15. One important characteristic on the signals is the out of phase motion between the pressure plate and device (Fig. 12.11), indicated by α and θ_x on Fig. 12.15(a) and by β and θ_y on Fig. 12.15(b).

On the upper limit of the stability range ($k_{upper\ limit}$ on Tab. 12.2), damping is still effective for reduction of vertical vibrations (Fig. 12.16(c)). In this situation, the out of phase motion persists, like in Fig. 12.15, but wobbling amplitudes remain practically constant during free vibration. Values for the pressure plate are greater in relation to the device (Figs. 12.16(a) and 12.16(b)).

The device is no longer effective for k_{above}, that is placed out of the stability range on Fig. 12.3. The unstable condition is presented by the exponentially increasing wobbling amplitudes on Fig. 12.16(a) and 12.17(b). Vertical vibrations are still reduced by damping (Fig. 12.17(c)).

Based on the previous results, k_{bellow} and k_{above} produced unstable responses. The free vibration for $k_{lower\ limit}$ or $k_{upper\ limit}$ is critical, once that vibrations on the pressure plate can be constant depending on the initial conditions. But it must be remembered that those are specific values, and, within the stability range, there is a decay on the wobbling responses of the pressure plate/device.

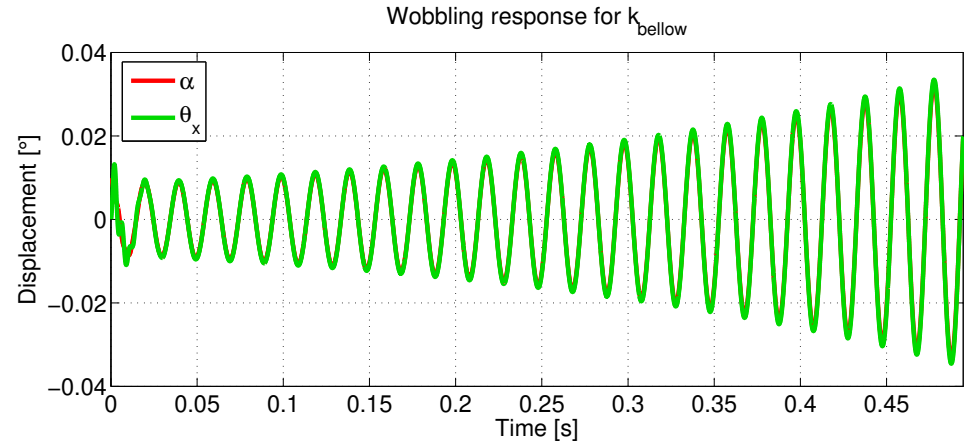

(a)

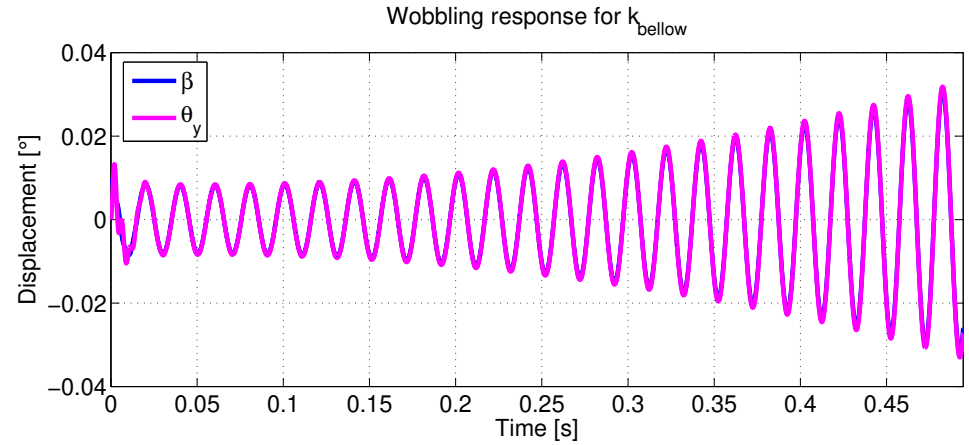

(b)

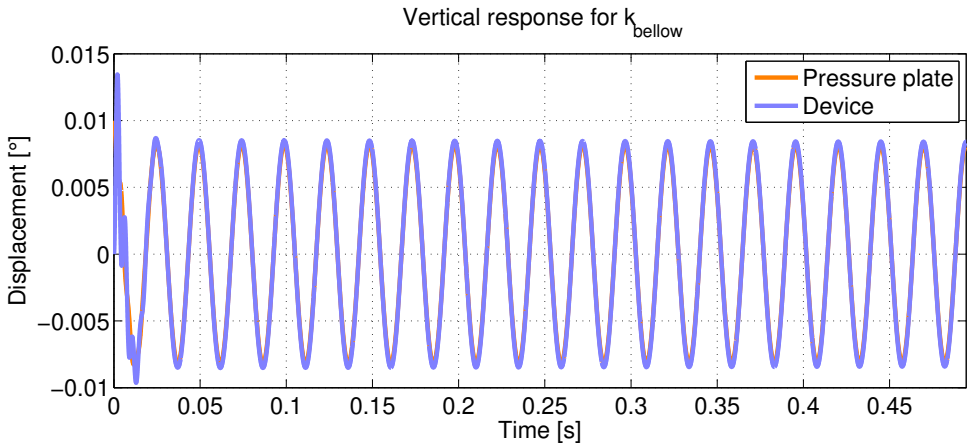

(c)

Figure 12.13: Wobbling responses (Fig. 12.13(a) and 12.13(b)) and vertical motion (Fig. 12.13(c)) for k_{bellow}.

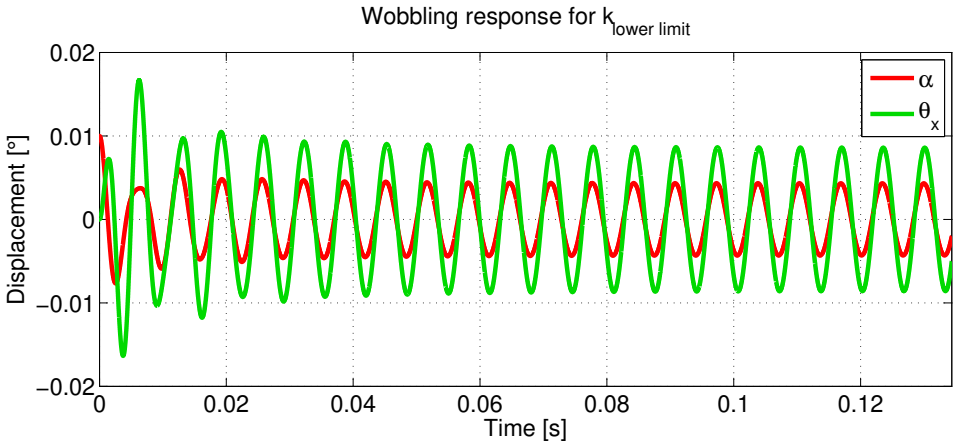

(a)

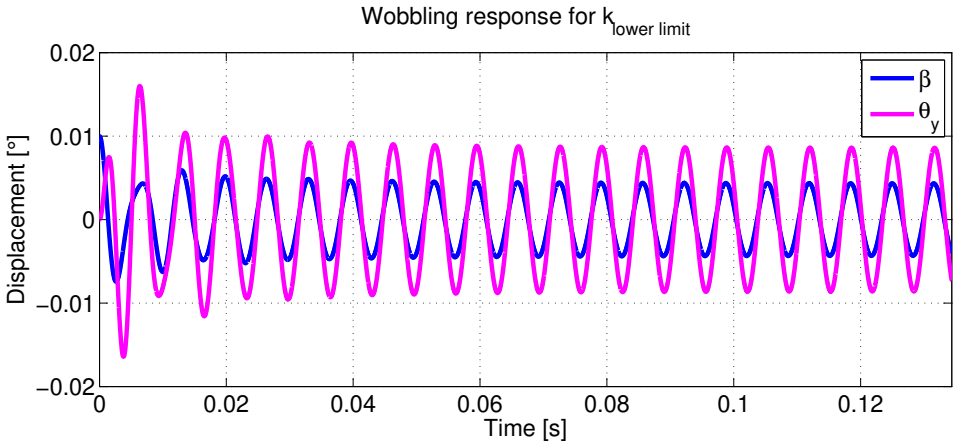

(b)

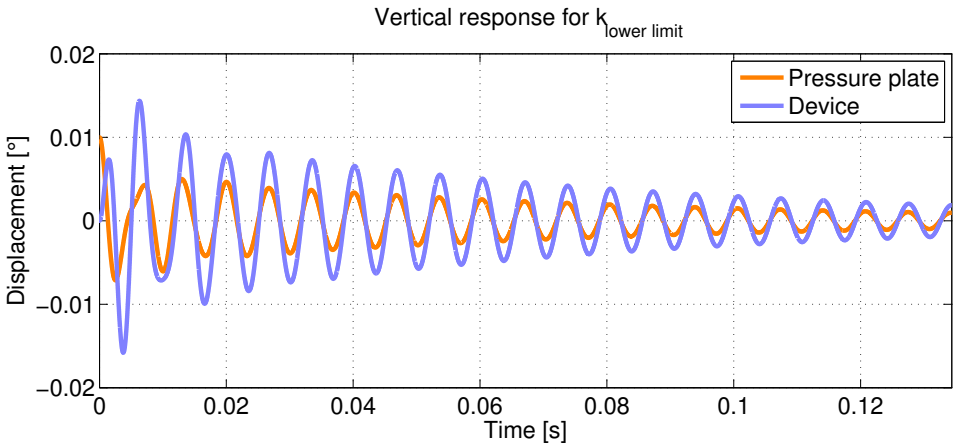

(c)

Figure 12.14: Wobbling responses (Figs. 12.14(a) and 12.14(b)) and vertical motion (Fig. 12.14(c)) for $k_{lower\ limit}$.

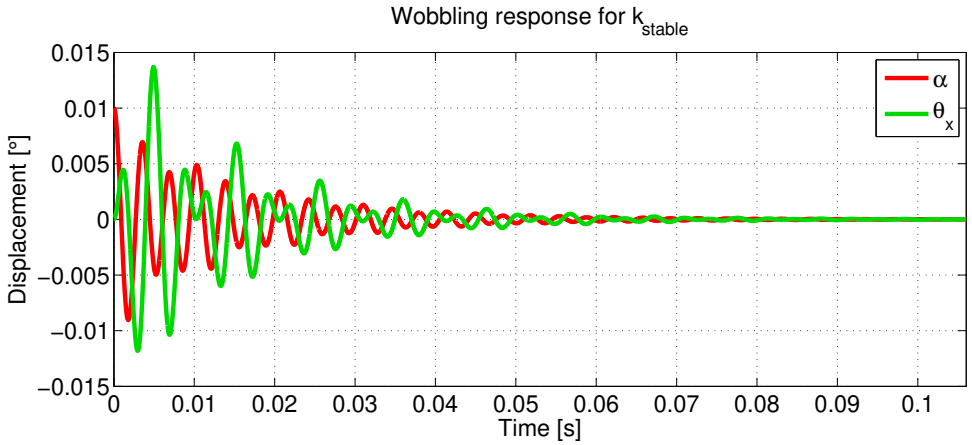

(a)

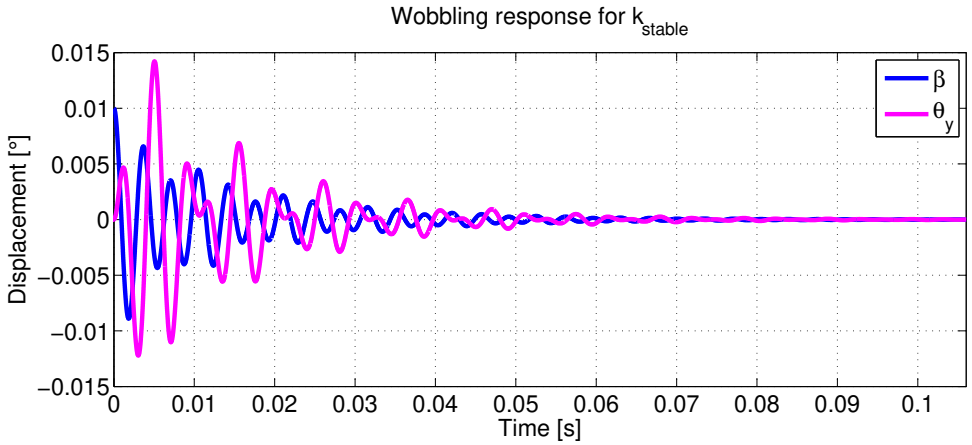

(b)

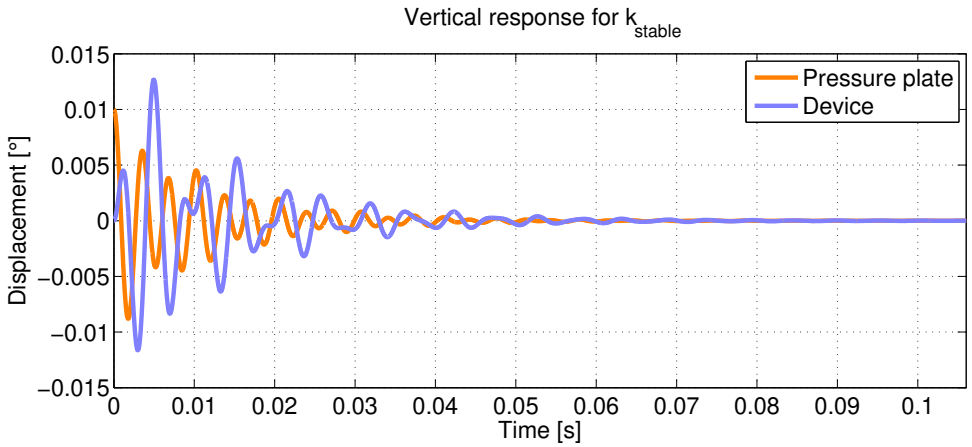

(c)

Figure 12.15: Wobbling responses (Figs. 12.15(a) and 12.15(b)) and vertical motion (Fig. 12.15(c)) for k_{stable}.

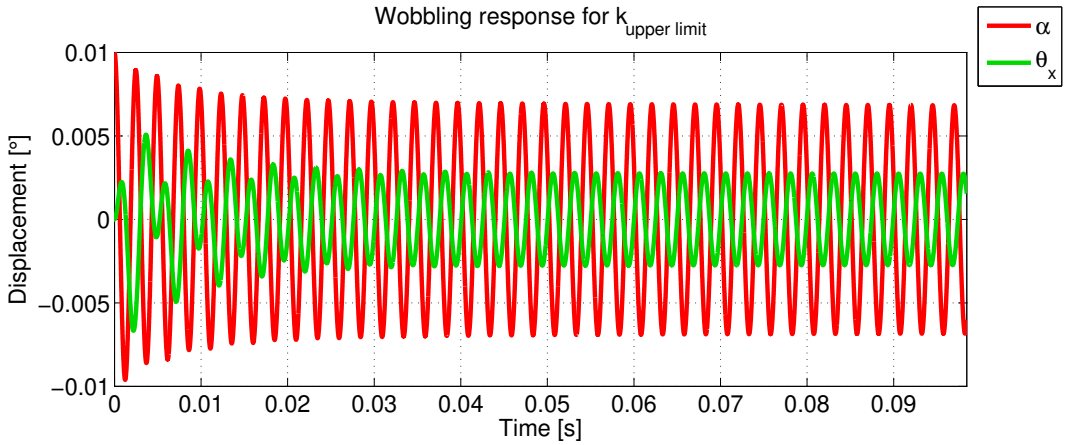

(a)

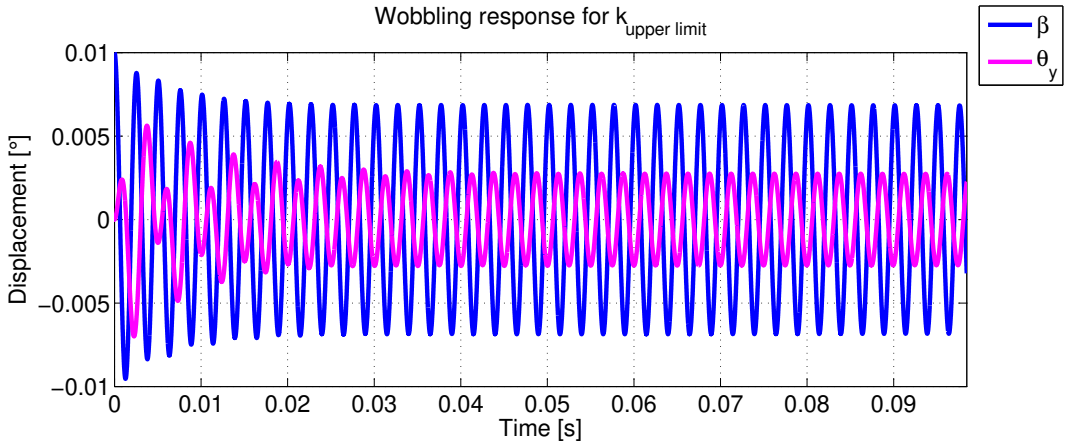

(b)

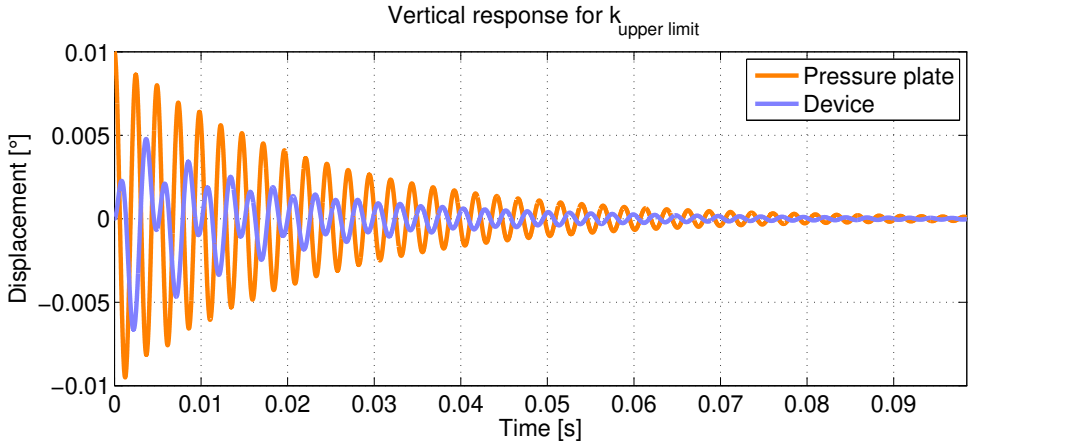

(c)

Figure 12.16: Wobbling responses (Figs. 12.16(a) and 12.16(b)) and vertical motion (Fig. 12.16(c)) for $k_{upper\ limit}$.

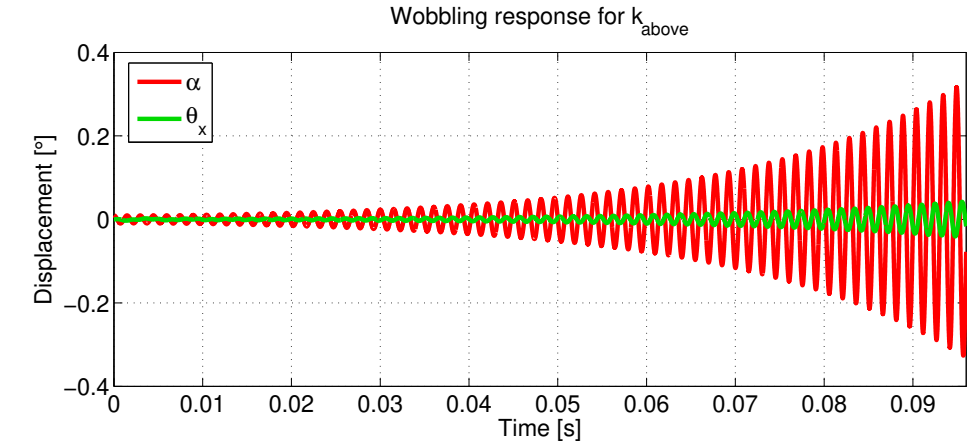

(a)

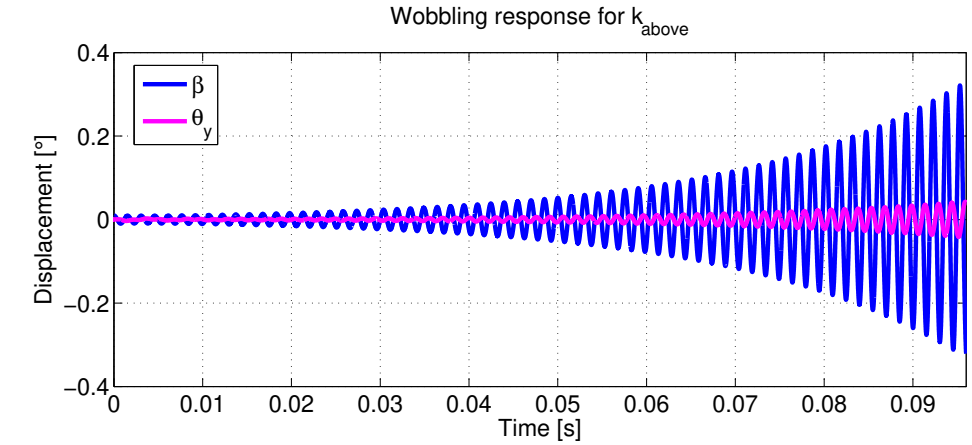

(b)

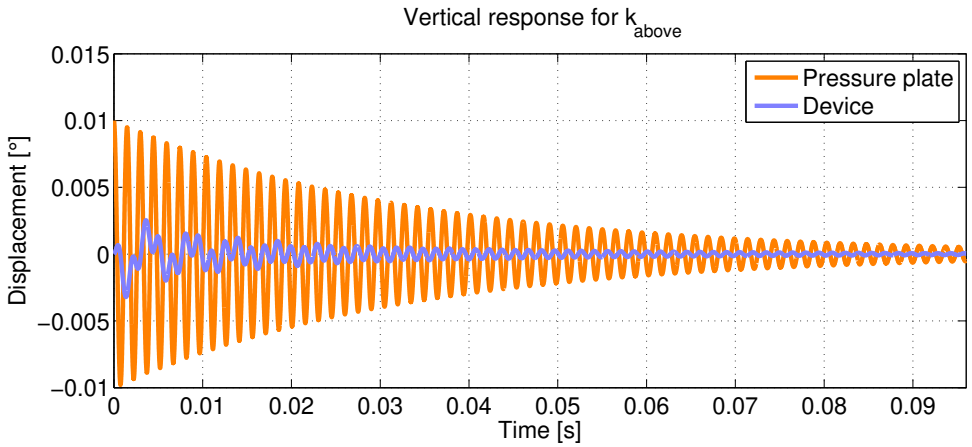

(c)

Figure 12.17: Wobbling responses (Figs. 12.17(a) and 12.17(b)) and vertical motion (Fig. 12.17(c)) for k_{above}.

12.3.6 Chapter summary

This chapter presented the formulation of a stabilization device for the pressure plate. It worked with the principle of veering, causing the stabilization of all mode shapes (Section 12.3.1). On the stable range, in phase and out of phase wobbling motions were detected (Sections 12.3.3 and 12.3.4). The out of phase wobbling motions between the lower and upper disc are a favourable condition for the use of the viscous damping. With this approach, damping is introduced on other elements than the cushion spring. The time domain responses under free vibration from Section 12.3.5 agreed with the stability range determined on Section 12.3.1, producing decaying time responses for cushion values within the stability range.

13 Conclusions and future work

13.1 Conclusions

13.1.1 Element formulation and possibilities

The system on Cardan coordinates (Chapter 6) presents greater modifications of its natural frequencies in relation to the pressure plate rotating speed than the model with the rotating speed on global coordinates (Chapter 8). The natural frequencies of the forward, backward and axial modes for the model under hypothesis 2 were close to each other for greater values of cushion stiffness. This thesis was innovative with assumption of relative displacement between the pressure plate and the flywheel in case of viscous damping (Sections 5.2 and 7.2). Sections 5.3, 7.3.1 discussed in detail that, due to the movement of this element, it is possible to generate vertical efforts when there is motion under a surface that changes its height or on the example of an inclined flat disc.

As a result, the model on Cardan coordinates (Hypothesis 1) presented a term of stiffness related to the contribution of rotating speed of the disc (Section 5.5.2), while the formulation with the rotating speed on global coordinates (Hypothesis 2) presented terms related to the element relative position angle (Section 7.4.2). Those terms resulted on instability under low levels of stiffness on Sections 6.4 and 8.4. The models assuming viscous damping have a dual characteristic, allowing instability due to the friction for higher values of contact stiffness and due to the effect of a moving viscous element when it is reduced. In both cases, the modification of the clutch disc rotating speed modified the real part of the eigenvalues of a viscously damped system (Sections 6.4 and 8.4). The whole literature (Chapter 3) takes into account structural damping, that do not produce this effect.

The results from Chapter 9 indicate that real clutch discs, that have variations on their properties due to several reasons (manufacturing tolerances, uneven wear, etc.) may cause vibrations on the pressure plate that cannot be directly associated to the existing literature. There was innovation on the possibility if inclusion of variations on the cushion spring using elements from Section 5.5. On the simulations with placement error on one element (Section 9.1), there was coupling between the angular coordinates with axial movement. It was shown that such errors change significantly the axial mode shape, decreasing the magnitude of vibration on axial direction and increasing the role of the angular displacements. Proportional changes according to the angular coordinates with symmetrical distribution (Section 9.2),did not cause a modification on the axial mode shape. When

the stiffness for one coordinate was greater than the other, the unstable mode shape presented higher amplitude. Only when the stiffness is equally distributed, the mode shape presents equal amplitudes between these coordinates.

13.1.2 Application

Chapter 10 included real measurements on the diaphragm spring lever model interacting with the cushion curve nearby the points of usage on a vehicle. Another important conclusion from this part of the work was that the diaphragm spring stiffness is negative for a new clutch disc and positive for an aged one. Any realistic model of clutch squeal will have to fulfill those technical requirements, matching the properties included on the model with the functional curves of the real system elements.

On Chapter 11 it was possible to conclude that attachment of the leaf springs at larger distances from the centre of gravity allowed the stabilization of the system with lower values of tangential stiffness. The orientation angles were very important, once that with all elements at 45° the non diagonal terms were maximized, requiring lower values of all parameters for stabilization. The preload had no effect to stabilize the eigenvalues.

Chapter 12 contains the formulation of a stabilization device for the pressure plate. In this formulation, stability was achieved during a situation of *veering* (Liu (2002) and Perkins and Mote Jr (1986)). On this situation, the upper and lower disc performed in phase and out of phase wobbling movements, which allowed energy dissipation on the connection between them. The time responses from Section 12.3.5 are related to the stability of the eigenvalues. For cushion stiffness bellow or upper the stabilization limits, there was a growing wobbling response. Within the stable region, such response presented a fast decay.

Clutch squeal is a very complex problem, once that up to know there is no complete explanation for the fact that this phenomenon has been focus of publications for just 10 years from now (Wickramarachi *et al.* (2005)). This thesis tried to deepen the research in terms of the comprehension of the clutch system itself in relation to the model, bringing the technical knowledge and including real measurements when possible (Chapter 10). Besides that, it tried to discuss pending questions on the matter on a equal basis. With the formulations proposed on this work, the analysis of clutch squeal is not restricted, allowing a simultaneous evaluation test contributions of different elements combined on the same model (cushion configurations, diaphragm spring, leaf springs, stabilization device, etc.).

13.2 Future works

Clutch squeal is an open field of study and it is on a early stage of development. There is still room for the following works:

- Study the equations from this work in terms of linear time varying systems.
- Produce simulations involving the interaction of the elements developed on this work
- Study the nonlinear behaviour of this system. Based on Chapter 10, it is possible to include the nonlinear stiffness profile of the diaphragm spring, that have parts with negative stiffness and friction hysteresis.
- Include characteristics of the clutch disc on the model.
- The Finite Element Method can contribute for the introduction of the more realistic characteristics on interaction between the cushion springs and the facings. But it is necessary to change the contact model to allow the presence of friction damping.
- Take the experience and analysis tools provided by the vast knowledge on brake squeal.
- There is a pending question about the comprehension of the role of charcateristics of the powertrain/vehicle on the threshold of squealing events.
- There is practically no available experimental data on the matter. Vehicular tests have already started in order to understand the occurrence of squeal. Modal analysis tests have been started too.

Bibliography

ALBERS, A. Advanced development of dual mass flywheel (dmfw) design-noise control for today's automobiles. In **5th LuK Symposium, Bühl, Germany**. 1994.

ALBERS, A. e HERBST, D. Chatter–causes and solutions. In **6th LuK Colloquium**. 1998.

ALLEMANG, R.J. The modal assurance criterion–twenty years of use and abuse. **Sound and vibration**, vol. 37, n. 8, 14–23, 2003.

BITTANTI, S. e COLANERI, P. **Periodic systems: filtering and control**, vol. 5108985. Springer, 2008.

BRANCATI, R.; ROCCA, E. e RUSSO, R. A gear rattle model accounting for oil squeeze between the meshing gear teeth. **Proceedings of the Institution of Mechanical Engineers, Part D: Journal of Automobile Engineering**, vol. 219, n. 9, 1075–1083, 2005.

CANTONI, C.; CESARINI, R.; MASTINU, G.; ROCCA, G. e SICIGLIANO, R. Brake comfort–a review. **Vehicle System Dynamics**, vol. 47, n. 8, 901–947, 2009.

CENTEA, D.; RAHNEJAT, H. e MENDAY, M. Non-linear multi-body dynamic analysis for the study of clutch torsional vibrations (judder). **Applied Mathematical Modelling**, vol. 25, n. 3, 177–192, 2001.

CHILDS, D.W. **Turbomachinery rotordynamics: phenomena, modeling, and analysis**. John Wiley & Sons, 1993.

CROLLA, D. e LANG, A. Paper vii (i) brake noise and vibration-the state of the art. **Tribology Series**, vol. 18, 165–174, 1991.

CROWTHER, A.R.; ZHANG, N. e SINGH, R. Development of a clunk simulation model for a rear wheel drive vehicle with automatic transmission. Technical report, SAE Technical Paper, 2005.

DREXL, H. **Motor Vehicle Clutches: Function and Design**. Verlag Moderne Industrie, 1999.

DROZDETSKAYA, O.; FIDLIN, A. e WALTERSBERGER, B. On the wobbling of friction discs. In **Proceedings of the 7th European Nonlinear Dynamics Conference(ENOC 2011)**. 2011.

FIDLIN, A. **Nonlinear oscillations in mechanical engineering**. Springer, 2006.

FIDLIN, A.; DROZDETSKAYA, O. e WALTERSBERGER, B. On the minimal model for the low frequency wobbling instability of friction discs. **European Journal of Mechanics-A/Solids**, vol. 30, n. 5, 665–672, 2011.

FIDLIN, A. e STAMM, W. On the radial dynamics of friction disks. **European Journal of Mechanics-A/Solids**, vol. 28, n. 3, 526–534, 2009.

FREITAG, J.; GERHARDT, F.; HAUSNER, M. e WITTMANN, C. The clutch system of the future. In **9th Schaeffler Symposium**. 2010.

GENTA, G. **Dynamics of rotating systems**. Springer, 2007.

GINSBERG, J.H. **Advanced engineering dynamics**. Cambridge University Press, 1998.

HERVÉ, B.; SINOU, J.; MAHÉ, H. e JÉZÉQUEL, L. Analysis of friction-induced self-generated vibrations originated from mode-coupling in clutches. **International Journal of Pure and Applied Mathematics**, vol. 42, n. 3, 369, 2008a.

HERVÉ, B.; SINOU, J.J.; MAHÉ, H. e JEZEQUEL, L. Analysis of squeal noise and mode coupling instabilities including damping and gyroscopic effects. **European Journal of Mechanics-A/Solids**, vol. 27, n. 2, 141–160, 2008b.

HERVÉ, B.; SINOU, J.J.; MAHÉ, H. e JEZEQUEL, L. Extension of the destabilization paradox to limit cycle amplitudes for a nonlinear self-excited system subject to gyroscopic and circulatory actions. **Journal of Sound and Vibration**, vol. 323, n. 3, 944–973, 2009.

HOCHLENERT, D. **Selbsterregte Schwingungen in Scheibenbremsen: Mathematische Modellbildung und aktive Unterdrückung von Bremsenquietschen**. Shaker, 2006.

HOFFMANN, N.; FISCHER, M.; ALLGAIER, R. e GAUL, L. A minimal model for studying properties of the mode-coupling type instability in friction induced oscillations. **Mechanics Research Communications**, vol. 29, n. 4, 197–205, 2002.

KIM, T.C. e SINGH, R. Dynamic interactions between loaded and unloaded gear pairs under rattle conditions. Technical report, SAE Technical Paper, 2001.

KIMMIG, K. The self-adjusting clutch sac of the 2nd generation. In **6th LuK Symposium**. 1998.

KINKAID, N.; O'REILLY, O. e PAPADOPOULOS, P. Automotive disc brake squeal. **Journal of sound and vibration**, vol. 267, n. 1, 105–166, 2003.

KIRCHNER, E.; KÖSTER, K.H.; LANGER, F.; NICOLA, A. e SAUER, B. Model-based analysis of the cold start squeal phenomenon of clutches. **ATZ worldwide**, vol. 107, n. 9, 38–40, 2005.

KRENZ, R.A. Vehicle response to throttle tip-in/tip-out. Technical report, SAE Technical Paper, 1985.

KUSHWAHA, M.; GUPTA, S.; KELLY, P. e RAHNEJAT, H. Elasto-multi-body dynamics of a multicylinder internal combustion engine. **Proceedings of the Institution of Mechanical Engineers, Part K: Journal of Multi-body Dynamics**, vol. 216, n. 4, 281–293, 2002.

LERESTRELO, L.T.R. Embreagem - sistema de acionamento, 2013. Lecturing slides.

LILES, G.D. Analysis of disc brake squeal using finite element methods. Technical report, SAE Technical Paper 891150, 1989.

LIU, X. Behavior of derivatives of eigenvalues and eigenvectors in curve veering and mode localization and their relation to close eigenvalues. **Journal of Sound and Vibration**, vol. 256, n. 3, 551–564, 2002.

MASSI, F.; BAILLET, L.; GIANNINI, O. e SESTIERI, A. Brake squeal: linear and nonlinear numerical approaches. **Mechanical Systems and Signal Processing**, vol. 21, n. 6, 2374–2393, 2007.

MEIROVITCH, L. **Methods of analytical dynamics**. Courier Dover Publications, 2010.

MENDAY, M.; RAHNEJAT, H. e EBRAHIMI, M. Clonk: an onomatopoeic response in torsional impact of automotive drivelines. **Proceedings of the Institution of Mechanical Engineers, Part D: Journal of Automobile Engineering**, vol. 213, n. 4, 349–357, 1999.

MICKNASS, W. **Kupplung, Gelenkwellen**. Der sichere Weg zur Meisterprüfung im Kfz-Handwerk. Vogel, 1993.

MIYASATO, H.H. **Simulation of the gear rattle phenomenon in automotive powertrain models**. 2011. Master thesis. University of Campinas.

MUSZYNSKA, A. **Rotordynamics**. CRC press, 2010.

NAYFEH, A.H. e BALACHANDRAN, B. **Applied nonlinear dynamics: analytical, computational and experimental methods**. John Wiley & Sons, 2008.

OUYANG, H.; NACK, W.; YUAN, Y. e CHEN, F. Numerical analysis of automotive disc brake squeal: a review. **International Journal of Vehicle Noise and Vibration**, vol. 1, n. 3, 207–231, 2005.

PAPINNIEMI, A.; LAI, J.; ZHAO, J. e LOADER, L. Brake squeal: a literature review. **Applied Acoustics**, vol. 63, n. 4, 391–400, 2002.

PERESTRELO, L.T.R. Automotive powertrain model for judder investigation. 2013.

PERKINS, N. e MOTE JR, C. Comments on curve veering in eigenvalue problems. **Journal of Sound and Vibration**, vol. 106, n. 3, 451–463, 1986.

SCHIEHLEN, W. e EBERHARD, P. Technische dynamik. **Teubner, Stuttgart**, pp. 87–89, 1986.

SENATORE, A.; HOCHLENERT, D.; DAGOSTINO, V. e VON WAGNER, U. Driveline dynamics simulation and analysis of the dry clutch friction-induced vibrations in the eek frequency range. In **ASME 2013 International Mechanical Engineering Congress and Exposition**, pp. V013T14A024–V013T14A024. American Society of Mechanical Engineers, 2013.

SFARNI, S.; BELLENGER, E.; FORTIN, J. e MALLEY, M. Numerical and experimental study of automotive riveted clutch discs with contact pressure analysis for the prediction of facing wear. **Finite Elements in Analysis and Design**, vol. 47, n. 2, 129–141, 2011.

SHAVER, R. e SHAVER, F. Manual transmission clutch systems. **Warrendale, PA: Society of Automotive Engineers, 1997. 200**, 1997.

SIMIONATTO, V. G. S. **Study of the influence of the parameters of the clutch disk's pre damper on shuffle and clunk phenomena in powertrains**. 2011. Master thesis. University of Campinas.

SIMIONATTO, V. G. S. **The Use of Centrifugal Pendulums for Torsional Vibration Control in Automotive Powertrains**. 2015. PhD Thesis. University of Campinas.

SINGH, R.; XIE, H. e COMPARIN, R. Analysis of automotive neutral grear rattle. **Journal of sound and vibration**, vol. 131, n. 2, 177–196, 1989.

SOOM, A.; SERPE, C.I. e DARGUSH, G.F. High frequency noise generation from components in sliding contact: flutter instabilities including the role of surface roughness and friction. **Tribology Series**, vol. 43, 477–485, 2003.

THOMPSON, D. e JONES, C. A review of the modelling of wheel/rail noise generation. **Journal of sound and vibration**, vol. 231, n. 3, 519–536, 2000.

TONDL, A. Quenching of self-excited vibrations equilibrium aspects. **Journal of Sound and Vibration**, vol. 42, n. 2, 251–260, 1975.

VON WAGNER, U.; HOCHLENERT, D. e HAGEDORN, P. Minimal models for disk brake squeal. **Journal of Sound and Vibration**, vol. 302, n. 3, 527–539, 2007.

WANG, M.; MANOJ, R. e ZHAO, W. Gear rattle modelling and analysis for automotive manual transmissions. **Proceedings of the Institution of Mechanical Engineers, Part D: Journal of Automobile Engineering**, vol. 215, n. 2, 241–258, 2001.

WICKRAMARACHI, P.; SINGH, R. e BAILEY, G. Analysis of friction-induced vibration leading to. **Noise control engineering journal**, vol. 53, n. 4, 138–144, 2005.

A Friction distribution near coupling

A.1 Cardan coordinates

Near coupling, it occurs that the terms which depend on the expression $\dot{\gamma} - \dot{\theta}\cos\alpha\cos\beta$ practically vanish on Equation 5.37. The approximate function for small angles is calculated by Eq. A.1.

$$ {}_3\vec{V}_{t_{rel}} \approx h \begin{Bmatrix} \left(\dot{\alpha}\sin\gamma - \dot{\beta}\cos\gamma\right) + \dot{\theta}\left(\beta\sin\gamma + \alpha\cos\gamma\right) \\ \left(\dot{\alpha}\cos\gamma + \dot{\beta}\sin\gamma\right) + \dot{\theta}\left(\beta\cos\gamma - \alpha\sin\gamma\right) \\ 0 \end{Bmatrix} \tag{A.1} $$

Assuming small angles, the norm of ${}_3\vec{V}_{t_{rel}}$ is calculated as Eq. A.1. It still depends on the wobbling angles (α and β). For $\gamma = 0°$ and $\dot{\alpha} = \dot{\beta} = 0$ the unitary vectors are calculated by Eq. A.3.

$$ \left|{}_3\vec{V}_{t_{rel}}\right| = h\sqrt{\dot{\alpha}^2 + \dot{\beta}^2 + 2\dot{\theta}(\dot{\alpha}\beta - \alpha\dot{\beta}) + \dot{\theta}^2(\beta^2 + \alpha^2)} \tag{A.2} $$

$$ {}_3\vec{\nu} = \frac{{}_3\vec{V}_{t_{rel}}}{\left|{}_3\vec{V}_{t_{rel}}\right|} \approx \frac{1}{\sqrt{\alpha^2 + \beta^2}} \begin{Bmatrix} \alpha \\ \beta \\ 0 \end{Bmatrix} \tag{A.3} $$

Adopting $\alpha = \gamma = 0°$ the unitary vector is given by Eq. A.4. Figure A.1 presents the distribution of the friction force and unitary relative speed when the element rotating speed ($\dot{\theta}$) is close to the values found for the pressure plate ($\dot{\gamma}$). Figure A.1(a) presents the pattern of friction forces tangent to the disc radius. As the difference decreases, there is a reorientation of the friction forces in Figs A.1(b) and A.1(c). Finally, for $\dot{\gamma} = 1000$ rpm and $\dot{\theta} = 999.9999$ rpm the unitary relative speed of all elements is the same, on the direction given by Eq. A.4.

$$ {}_3\vec{\nu} = \frac{1}{|\beta|} \begin{Bmatrix} 0 \\ \beta \\ 0 \end{Bmatrix} = sign(\beta) \begin{Bmatrix} 0 \\ 1 \\ 0 \end{Bmatrix} \tag{A.4} $$

Similar results are found imposing $\beta = \gamma = 0°$ (Eq. A.5). The modification on the unitary relative speed vector and friction forces is shown on Fig. A.2. Equation A.5 gives the direction of

${}_3\vec{\nu}$ (Figure A.2(d)), where all vectors are aligned with the axis y_3.

$$ {}_3\vec{\nu} = \frac{1}{|\alpha|} \begin{Bmatrix} \alpha \\ 0 \\ 0 \end{Bmatrix} = sign(\alpha) \begin{Bmatrix} 1 \\ 0 \\ 0 \end{Bmatrix} \tag{A.5} $$

Even if $\alpha = \beta = \gamma = 0^\circ$ the unitary speed is influenced by the angular speeds. Figure A.3 presents results for $\dot{\alpha} = \dot{\beta} = 1$ rad/s. If $\dot{\gamma} - \dot{\theta} = 100$ rpm (Fig. A.3(a)) and $\dot{\gamma} - \dot{\theta} = 10$ rpm (Fig. A.3(b)) the direction is not substantially changed. For $\dot{\gamma} - \dot{\theta} = 1$ rpm (Fig. A.3(c)) the field presents significant changes and are no more tangent to the radius if $x_3 \leqslant 0$ and $y_3 \leqslant 0$. (Fig. A.3(b)). The direction follows the direction given by Eq. A.6 on Fig. A.3(d) where $\dot{\alpha} = \dot{\beta} = 0.1$ rad/s. This degeneration of the friction forces in relation to the movement of the pressure plate is the physical explanation for the occurrence of friction damping Section 5.5.

$$ {}_3\vec{\nu} = \frac{{}_3\vec{V}_{t_{rel}}}{\left|{}_3\vec{V}_{t_{rel}}\right|} \approx \frac{1}{\sqrt{\dot{\alpha}^2 + \dot{\beta}^2}} \begin{Bmatrix} -\dot{\beta} \\ \dot{\alpha} \\ 0 \end{Bmatrix} \tag{A.6} $$

A.2 With the rotating speedon global coordinates

Near coupling condition, the terms that depend on $\dot{\gamma} - \dot{\theta}$ on Eq. 7.39 become too small. An approximation of the relative tangential speed is given by Eq. A.7. It depends on the wobbling angle α as well as the wobbling speeds $\dot{\alpha}$ and $\dot{\beta}$.

$$ {}_3\vec{V'}t_{rel} \approx \begin{Bmatrix} \dot{\beta}\left(-h\cos\alpha + \sin\alpha R_i \sin\psi_i\right) \\ \dot{\alpha}h - \dot{\beta}\sin\alpha R_i \cos\psi_i \\ 0 \end{Bmatrix} \tag{A.7} $$

Equation A.8 represents the normal vector near coupling adopting $\beta = 0^\circ$. It shows that the relative speed field will tends to align with the y_3' direction. Figures A.4 express such behaviour on tangential relative speed degrading from $\dot{\gamma} - \dot{\theta} = 10$ rpm (Fig. A.4(a)) to $\dot{\gamma} - \dot{\theta} = 0.1$ rpm (Fig. A.4(d)).

$$ {}_3\vec{\nu'} = \frac{{}_3\vec{V'}t_{rel}}{|\,{}_3\vec{V'}t_{rel}|} = \frac{\dot{\alpha}h}{|\dot{\alpha}|h} \begin{Bmatrix} 0 \\ 1 \\ 0 \end{Bmatrix} = sign(\dot{\alpha}) \begin{Bmatrix} 0 \\ 1 \\ 0 \end{Bmatrix} \tag{A.8} $$

Equation A.9 shows the case for $\alpha = 0°$. Figures A.4 shows ${}_3\vec{\nu}'$ aligning wit the $-x'_3$ for situations from $\dot{\gamma} - \dot{\theta} = 10$ rpm (Fig. A.5(a)) to $\dot{\gamma} - \dot{\theta} = 0.1$ rpm (Fig. A.5(d)).

$$ {}_3\vec{\nu}' = \frac{{}_3\vec{V}'t_{rel}}{|{}_3\vec{V}'t_{rel}|} = \frac{\dot{\beta}h}{|\dot{\beta}|h} \begin{Bmatrix} -1 \\ 0 \\ 0 \end{Bmatrix} = sign(\dot{\beta}) \begin{Bmatrix} -1 \\ 0 \\ 0 \end{Bmatrix} \tag{A.9} $$

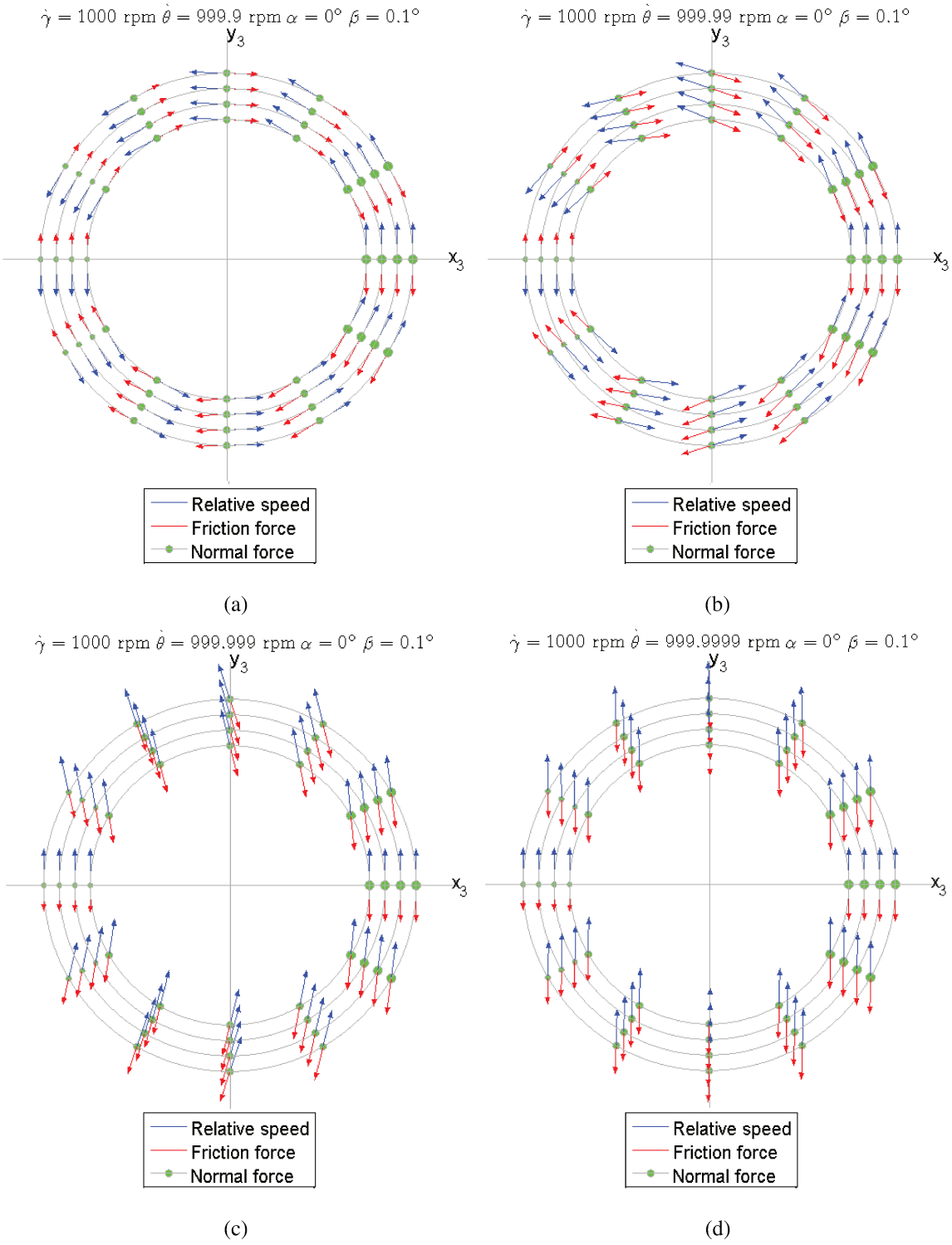

Figure A.1: Friction forces near coupling for $\alpha = 0°$.

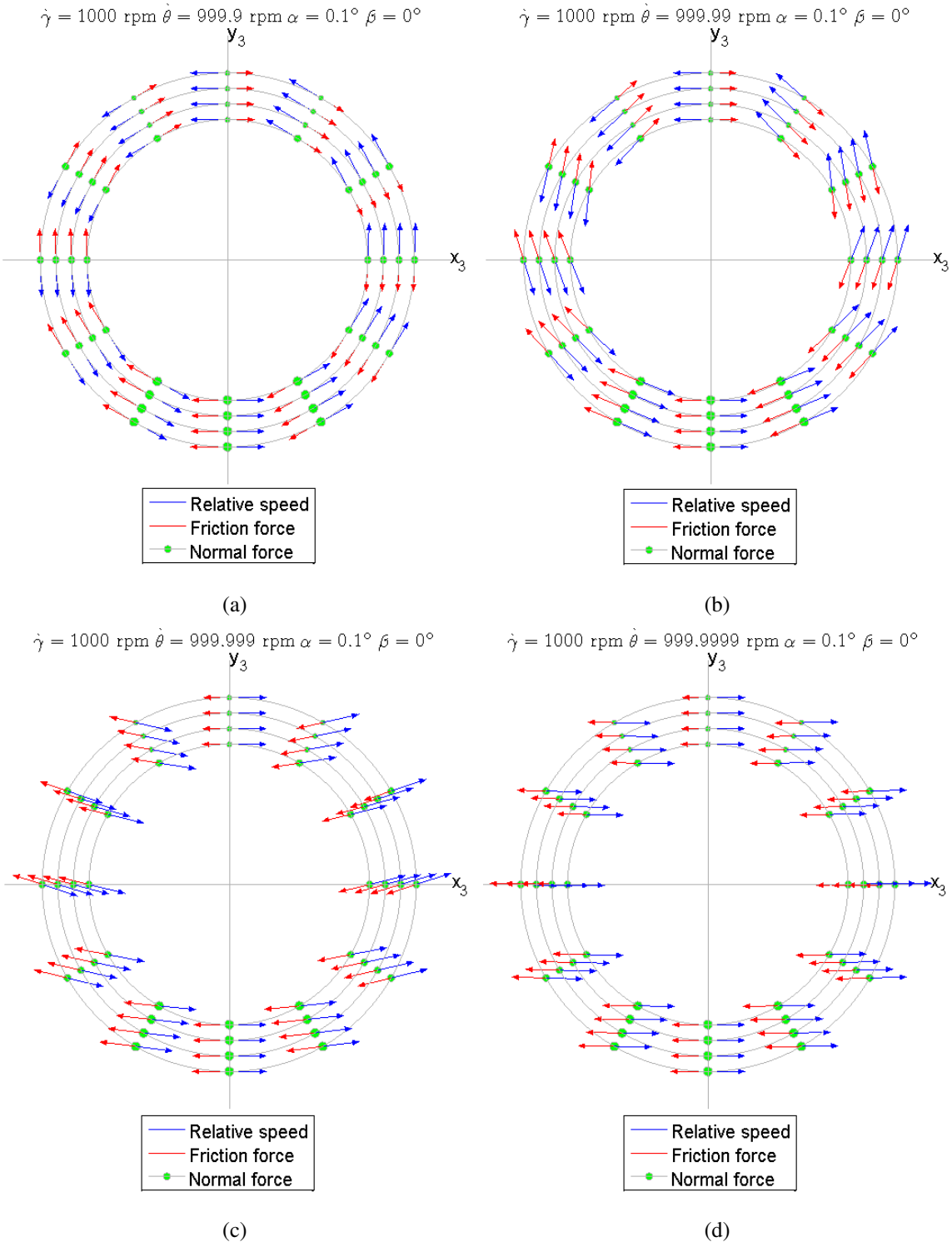

Figure A.2: Friction forces near coupling for $\beta = 0°$.

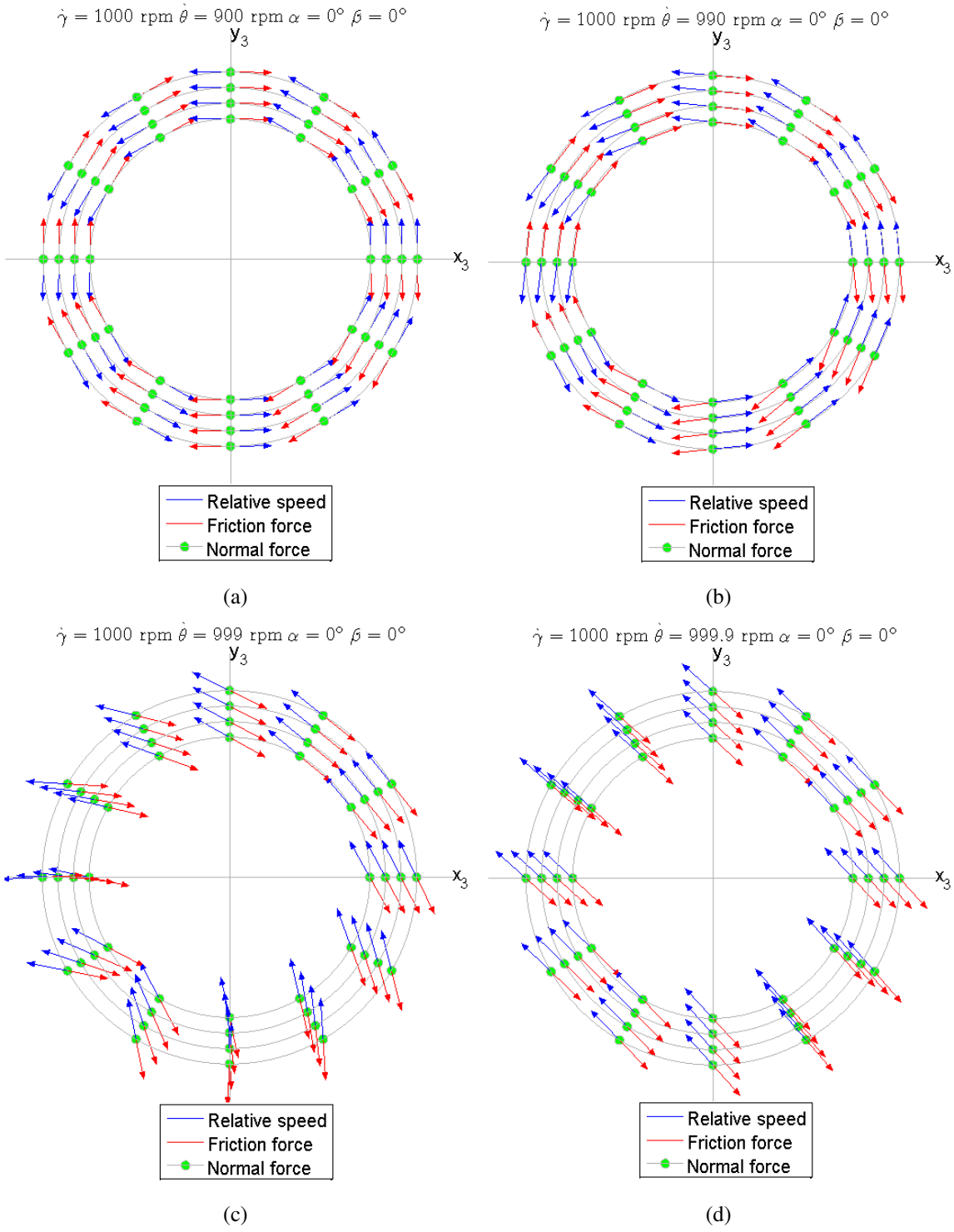

Figure A.3: Friction forces near coupling for $\dot{\alpha} = \dot{\beta} = 1 rad/s$.

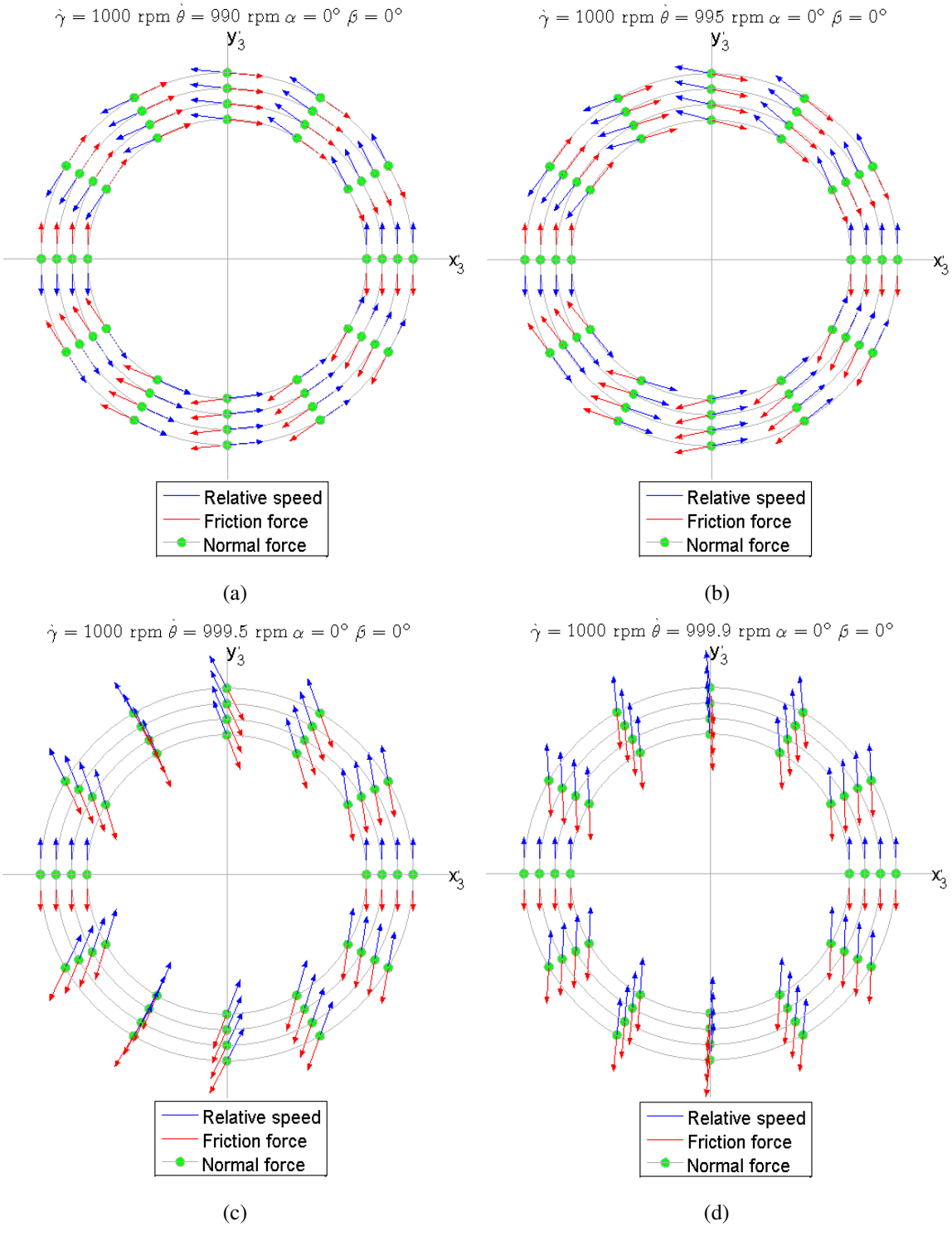

Figure A.4: Friction forces near coupling for $\dot{\alpha} = 1$ rad/s and $\dot{\beta} = 0$.

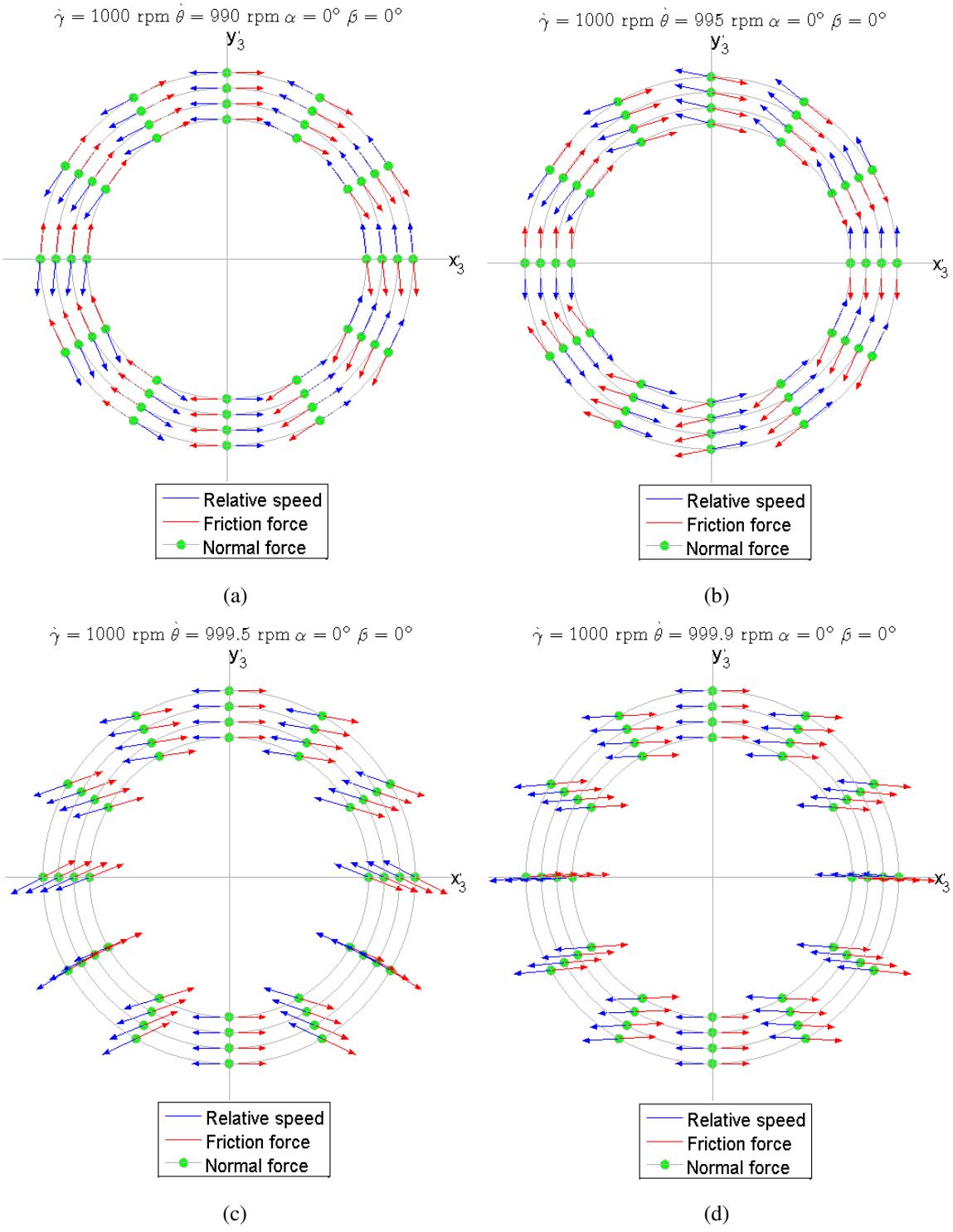

Figure A.5: Friction forces near coupling for $\dot{\beta} = 1$ rad/s and $\dot{\alpha} = 0$.

B Tangential speed error

B.1 Cardan coordinates

Having in mind the development of the previous section, it is possible to make a comparison on the physical representation of the original version of the unitary tangential relative speed (Eq. 5.37 and written here as ${}_3\vec{\nu}_{nonlinear}$) and its approximation (Eq. 5.42 noted here as ${}_3\vec{\nu}_{linear}$). The deviation from the nonlinear case is shown in Fig.B.1. The norm error was calculated by Eq. B.1:

$$\text{Norm error} = 100 \times \frac{\left|{}_3\vec{\nu}_{linear} - {}_3\vec{\nu}_{nonlinear}\right|}{\left|{}_3\vec{\nu}_{nonlinear}\right|} \tag{B.1}$$

For a greater relative angular speeds ($\dot{\gamma} = 1000$ rpm and $\dot{\theta} = 900$ rpm) the error is low, reaching 1.2% if α and β were chosen close to 1° Figs. B.1(a). When the system approaches the coupling, errors become more significant. With $\dot{\gamma} - \dot{\theta} = 10$ rpm (Fig. B.1(c)) a deviation of 14 % occurs for greater angular displacements. A critical point occur if $\dot{\gamma} - \dot{\theta} = 1$ rpm (Fig. B.1(c)), where errors above 180% were computed.

The direction error was calculated by Eq. B.2. The dot product between vectors give a measure of the relative angle between them. It was subtracted from 1 to verify how the approximation deviate from perfect alignment ($\cos 0^\circ$). As it is possible to see in Fig. B.1(b), B.1(d) and B.1(f), error on the orientation is extremely low no matter how close to coupling the system is.

$$\text{Direction error} = 1 - \frac{{}_3\vec{\nu}_{linear} \cdot {}_3\vec{\nu}_{nonlinear}}{\left|{}_3\vec{\nu}_{linear}\right| \left|{}_3\vec{\nu}_{nonlinear}\right|} \tag{B.2}$$

B.2 With the rotating speed on global coordinates

The norm and direction errors (Eqs. B.1 and B.2) from Section B.1 were applied here. As consequence of the formulation of the approximate unitary vector in Eq. 7.40, norm will present very low errors in terms of angles. Figure B.3 shows results assuming $\dot{\alpha} = \dot{\beta} = 0$ and angles within $10^{-4^\circ} < \alpha < 1^\circ$ and $10^{-4^\circ} < \beta < 1^\circ$. The element parameters were chosen as $\psi_{i0} = 45^\circ$, $h = 0.01$ m, $R = 0.0875$ m.

Norm errors for relative speeds equal to 100, 10 and 1 rpm (Figs. B.3(a), B.3(c) and B.3(e), respectively) have maximum errors near 0.14 % for wobbling angles near 1°. Maximum errors of direction error were very low (approximately 10^{-13} on Figs. B.3(b), B.3(d) and B.3(f)) if compared

to the case on Cardan coordinates (Figs. B.1(b), B.1(d) and B.1(f)). On that approach, both norm and direction errors increased for lower relative speeds (Figs. B.1).

On the other hand, the norm errors adopting $\dot{\alpha} = \dot{\beta} = 1$ rad/s were strongly affected by the relative speed, with maximum value nearby 1.65% on Fig. B.3(a) ($\dot{\gamma} - \dot{\theta} = 100$ rpm) that increases to 15.55% if $\dot{\gamma} - \dot{\theta} = 10$ rpm on Fig. B.3(c). This error trespasses 100 % if $\dot{\gamma} - \dot{\theta} = 1$ rpm (Fig. B.3(e)). The direction errors also increased with lower relative speeds on Figs. B.4(b), B.4(d) and B.3(f).

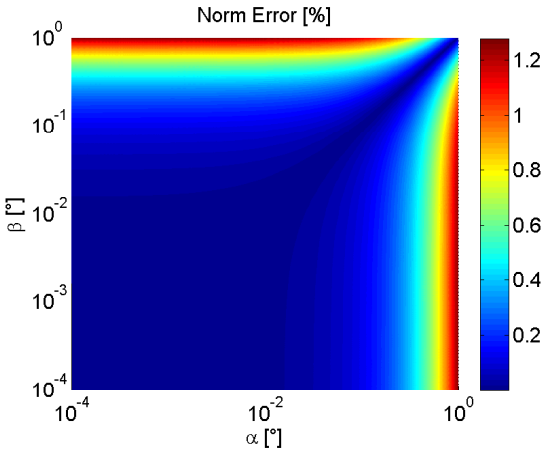

(a) Norm error for $\dot{\gamma} = 1000$ rpm and $\dot{\theta} = 900$ rpm

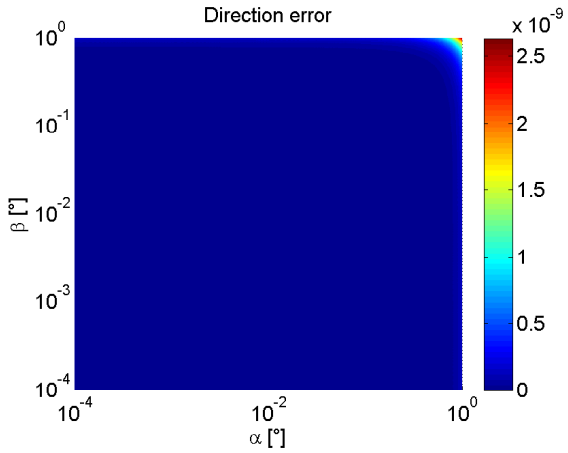

(b) Direction error for $\dot{\gamma} = 1000$ rpm and $\dot{\theta} = 900$ rpm

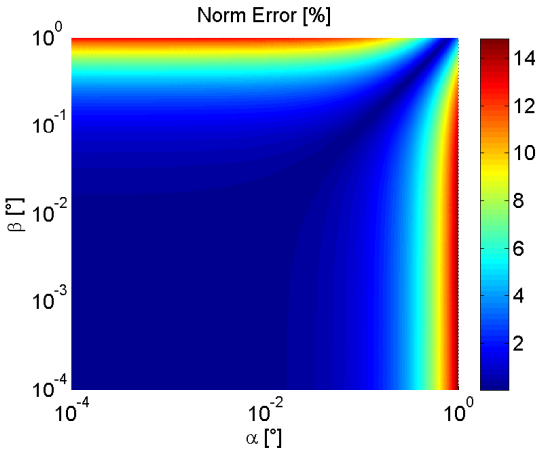

(c) Norm error for $\dot{\gamma} = 1000$ rpm and $\dot{\theta} = 990$ rpm

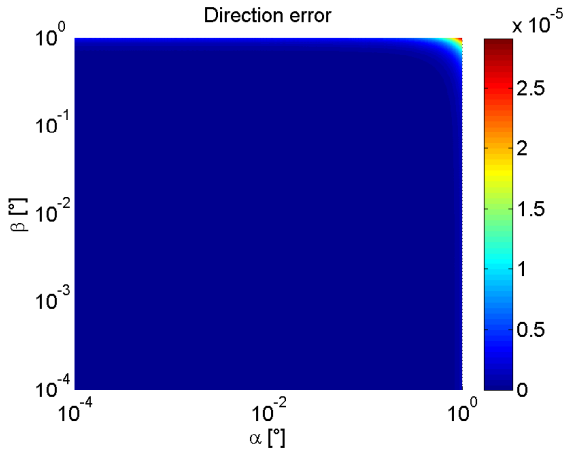

(d) Direction error for $\dot{\gamma} = 1000$ rpm and $\dot{\theta} = 990$ rpm

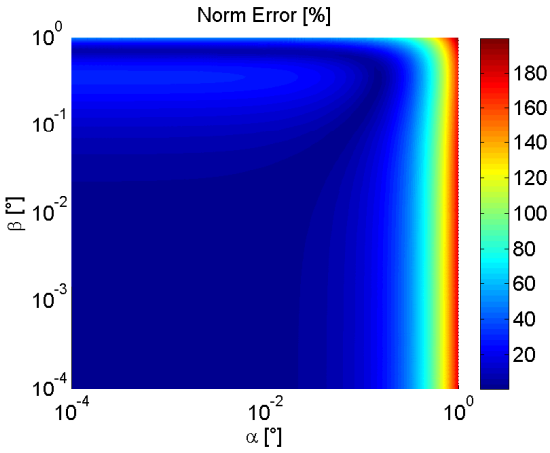

(e) Norm error for $\dot{\gamma} = 1000$ rpm and $\dot{\theta} = 999$ rpm

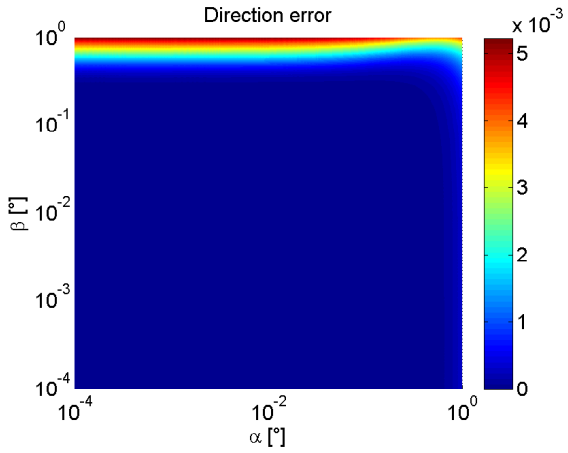

(f) Direction error for $\dot{\gamma} = 1000$ rpm and $\dot{\theta} = 999$ rpm

Figure B.1: Unitary vector error for $\psi_{i0} = 45°$, $\gamma = 0°$, $h = 0.01$ m, $R = 0.0875$ m and $\dot{\alpha} = \dot{\beta} = 0$ rad/s.

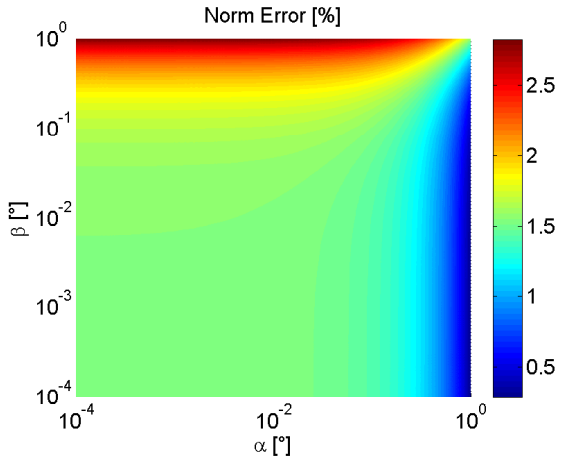

(a) Norm error for $\dot{\gamma} = 1000$ rpm and $\dot{\theta} = 900$ rpm

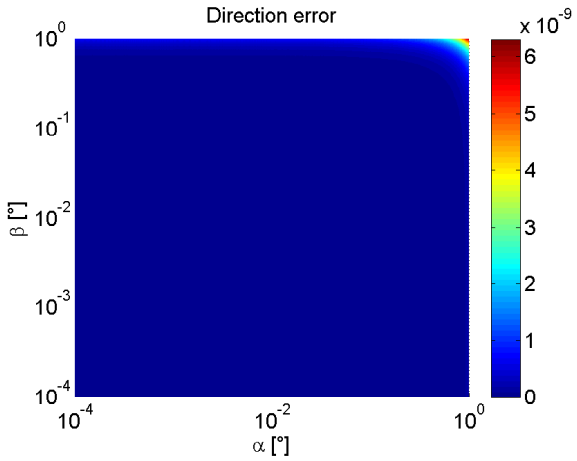

(b) Direction error for $\dot{\gamma} = 1000$ rpm and $\dot{\theta} = 900$ rpm

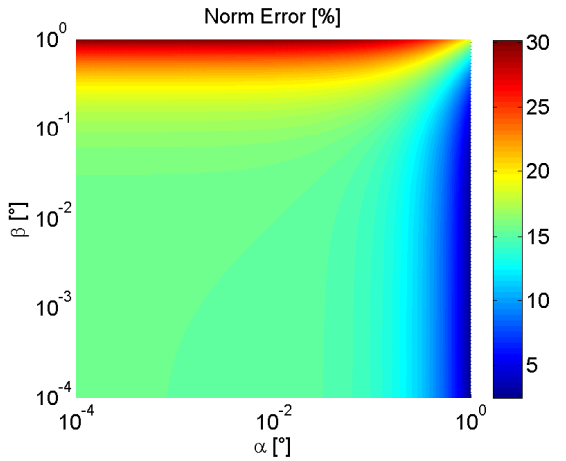

(c) Norm error for $\dot{\gamma} = 1000$ rpm and $\dot{\theta} = 990$ rpm

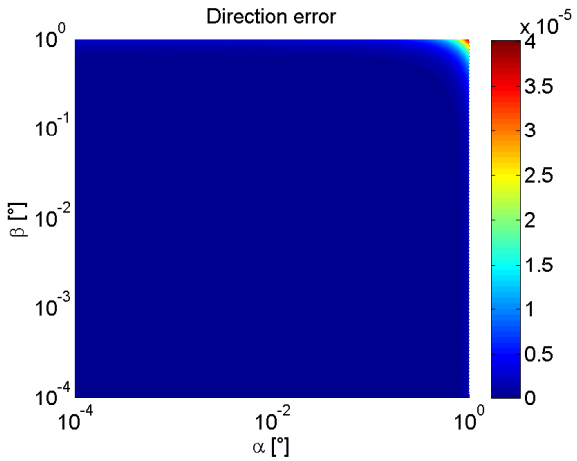

(d) Direction error for $\dot{\gamma} = 1000$ rpm and $\dot{\theta} = 990$ rpm

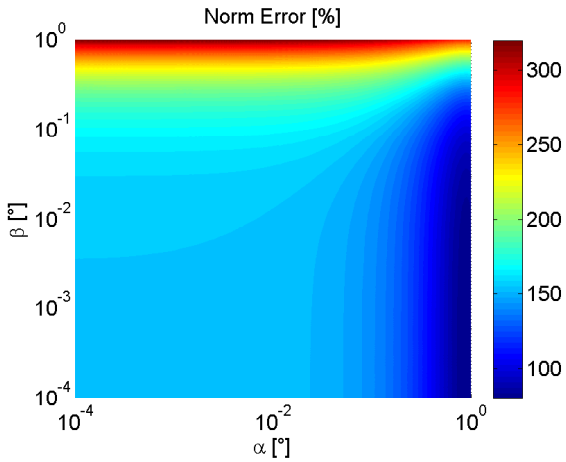

(e) Norm error for $\dot{\gamma} = 1000$ rpm and $\dot{\theta} = 999$ rpm

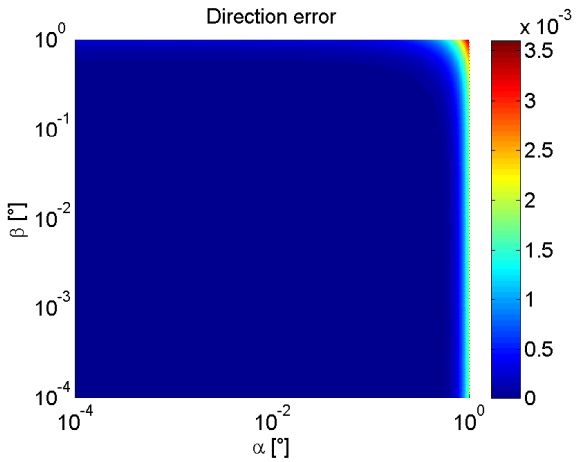

(f) Direction error for $\dot{\gamma} = 1000$ rpm and $\dot{\theta} = 999$ rpm

Figure B.2: Unitary vector error for $\psi_{i0} = 45°$, $\gamma = 0°$, $h = 0.01$ m, $R = 0.0875$ m and $\dot{\alpha} = \dot{\beta} = 1$ rad/s.

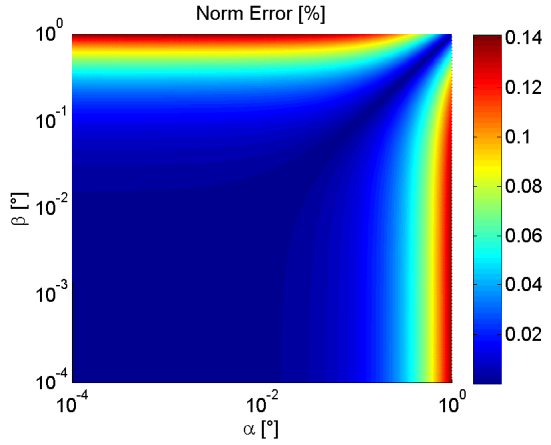

(a) Norm error for $\dot{\gamma} = 1000$ rpm and $\dot{\theta} = 900$ rpm

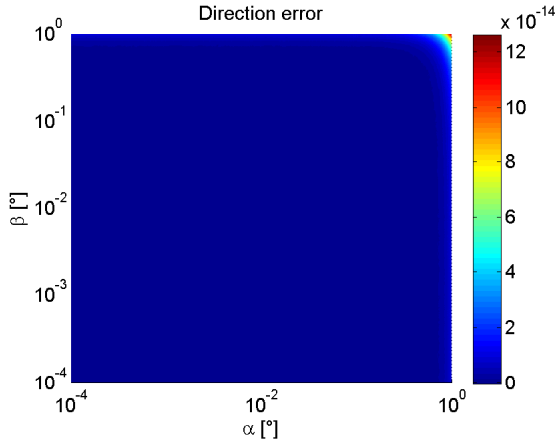

(b) Direction error for $\dot{\gamma} = 1000$ rpm and $\dot{\theta} = 900$ rpm

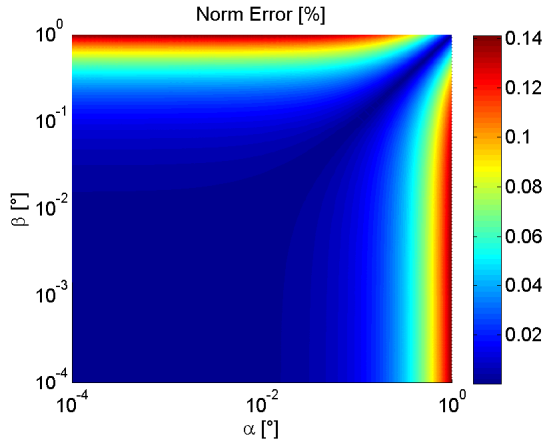

(c) Norm error for $\dot{\gamma} = 1000$ rpm and $\dot{\theta} = 990$ rpm

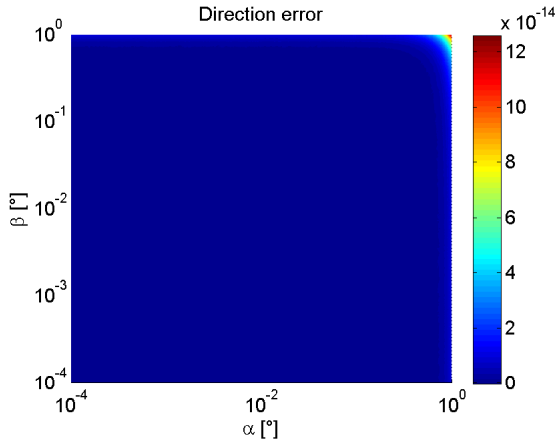

(d) Direction error for $\dot{\gamma} = 1000$ rpm and $\dot{\theta} = 990$ rpm

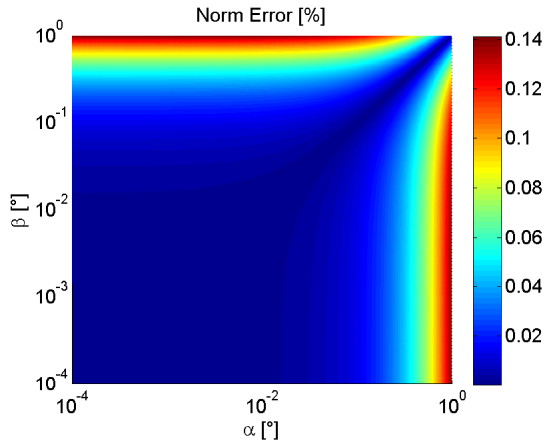

(e) Norm error for $\dot{\gamma} = 1000$ rpm and $\dot{\theta} = 999$ rpm

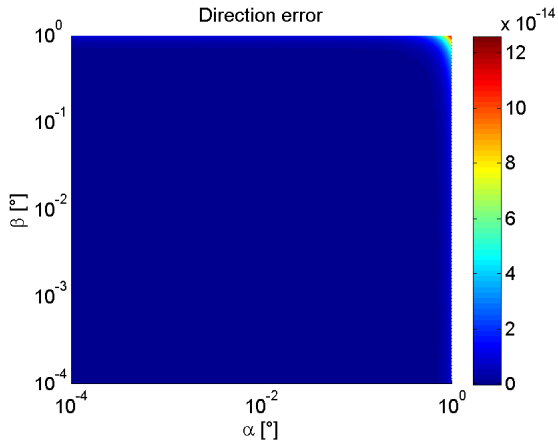

(f) Direction error for $\dot{\gamma} = 1000$ rpm and $\dot{\theta} = 999$ rpm

Figure B.3: Unitary vector error for $\psi_{i0} = 45°$, $\dot{\alpha} = \dot{\beta} = 0$ rad/s, $\gamma = 0°$, $h = 0.01$ m, $R = 0.0875$ m

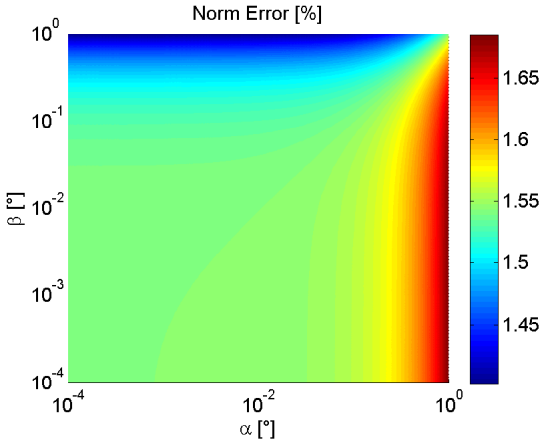

(a) Norm error for $\dot{\gamma} = 1000$ rpm and $\dot{\theta} = 900$ rpm

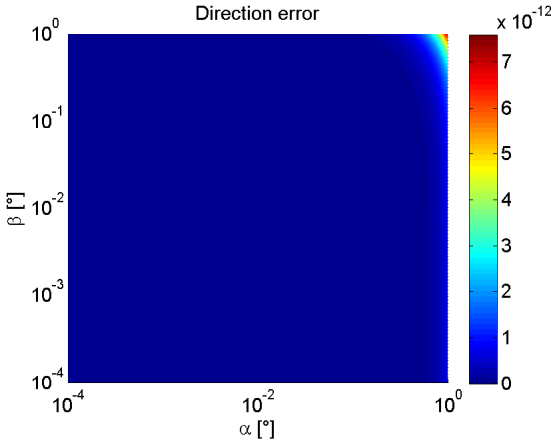

(b) Direction error for $\dot{\gamma} = 1000$ rpm and $\dot{\theta} = 900$ rpm

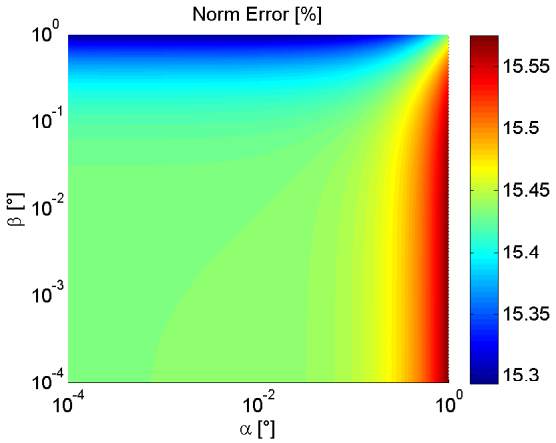

(c) Norm error for $\dot{\gamma} = 1000$ rpm and $\dot{\theta} = 990$ rpm

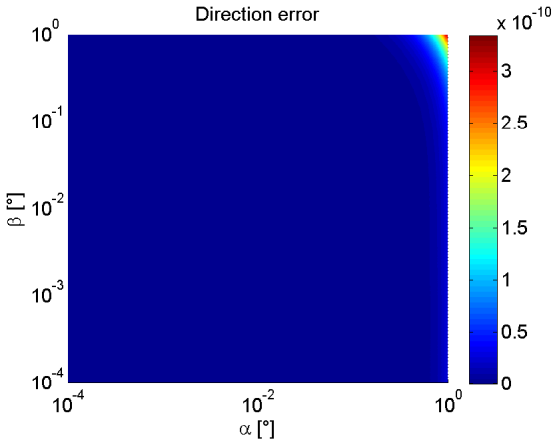

(d) Direction error for $\dot{\gamma} = 1000$ rpm and $\dot{\theta} = 990$ rpm

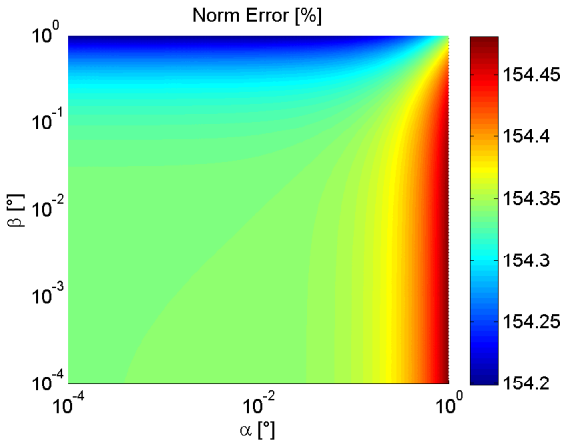

(e) Norm error for $\dot{\gamma} = 1000$ rpm and $\dot{\theta} = 999$ rpm

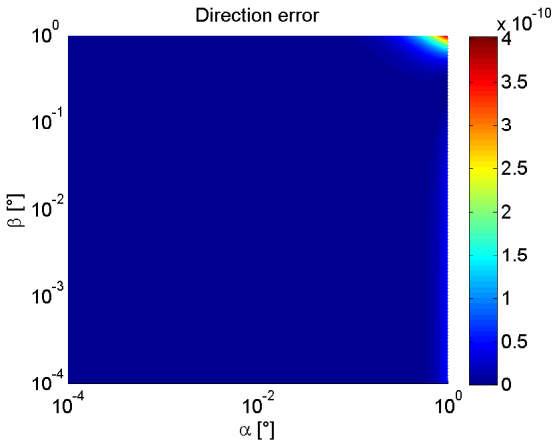

(f) Direction error for $\dot{\gamma} = 1000$ rpm and $\dot{\theta} = 999$ rpm

Figure B.4: Unitary vector error for $\psi_{i0} = 45°$, $\gamma = 0°$, $\dot{\alpha} = \dot{\beta} = 1$ rad/s, $h = 0.01$ m, $R = 0.0875$ m